



**HAL**  
open science

# Functionalized track-etched PVDF membrane-electrodes for toxic metal determination in water

Uliana Pinaeva

► **To cite this version:**

Uliana Pinaeva. Functionalized track-etched PVDF membrane-electrodes for toxic metal determination in water. *Polymers*. Université Paris Saclay (COmUE), 2019. English. NNT : 2019SACLX048 . tel-04227722

**HAL Id: tel-04227722**

**<https://theses.hal.science/tel-04227722>**

Submitted on 4 Oct 2023

**HAL** is a multi-disciplinary open access archive for the deposit and dissemination of scientific research documents, whether they are published or not. The documents may come from teaching and research institutions in France or abroad, or from public or private research centers.

L'archive ouverte pluridisciplinaire **HAL**, est destinée au dépôt et à la diffusion de documents scientifiques de niveau recherche, publiés ou non, émanant des établissements d'enseignement et de recherche français ou étrangers, des laboratoires publics ou privés.



# Functionalised track-etched PVDF membrane-electrodes for toxic metal detection in water

Thèse de doctorat de l'Université Paris-Saclay  
préparée à École polytechnique

Ecole doctorale n°573 INTERFACES: Approches Interdisciplinaires  
Fondements, Applications et Innovation  
Spécialité de doctorat: Chimie

Thèse présentée et soutenue à Palaiseau, le 3/10/2019, par

**ULIANA PINAEVA**

## Composition du Jury :

Remita Hynd Professor, Université Paris Sud (UMR 8000)	Présidente
Sébastien Balme Professor, Université de Montpellier (UMR 5635)	Rapporteur
Etienne Fleury Professor, INSA de Lyon (UMR 5223)	Rapporteur
Yvette Ngonon-Ravache CEA researcher, CIMAP Caen (UMR 6252)	Examinatrice
Marie-Claude Clochard CEA researcher, École Polytechnique (UMR 7642)	Directrice de thèse
Travis Lee Wade Ecole Polytechnique researcher, École Polytechnique (UMR 7642)	Co-directeur de thèse



# Résumé

Le greffage radio-induit de polymères fonctionnels, tels que le poly(acide acrylique) (PAA), la poly(4-vinyl pyridine) (P4VP) et le poly(bis[2-(methacryloyloxy)ethyl] phosphate (PB2MP), dans la structure nanoporeuse de membranes en poly(fluorure de vinylidène) (PVDF) à traces attaquées est ici rapporté, l'objectif étant la pré-concentration sélective des ions Pb(II), Hg(II) et U(VI) dans l'eau. Les membranes en PVDF à traces attaquées sont fabriquées par irradiation aux ions lourds rapides suivie par la révélation chimique des traces. L'irradiation du PVDF provoque la formation de zones endommagées, localisées autour du passage des ions. Ces zones, appelées traces latentes, peuvent être révélées par une solution oxydante conduisant à la formation de nanopores cylindriques traversant toute l'épaisseur des films de PVDF. L'ouverture et le rayon des pores sont contrôlés par la durée de l'attaque.

Les membranes nanoporeuses en PVDF ainsi créées sont ensuite fonctionnalisées dans la porosité grâce à la présence de radicaux résiduels à la paroi des nanopores. Il a été montré précédemment par Microscopie Confocale à Balayage Laser et des marqueurs fluorescents que le greffage du PAA est localisé à l'intérieur des pores. La spectroscopie RPE a été utilisée pour déterminer la quantité et la réactivité des radicaux piégés, notamment dans le cas d'une fonctionnalité nouvelle comme le PB2MP. Il a été montré que ces radicaux, alkyles et peroxy, étaient en quantité suffisante pour initier une polymérisation radicalaire du monomère B2MP. La décroissance radicalaire qui s'en est suivi témoigne du greffage du PB2MP. Le FESEM, le FTIR et une méthode moins conventionnelle comme le potentiel Zeta ont permis la caractérisation des groupes fonctionnels. Les états de charges à la surface des nanopores *versus* le pH de membranes en PVDF à traces attaquées se sont révélées négatives grâce aux espèces oxydées formées lors d'attaques chimiques. Lorsque des chaînes de P4VP greffées sont présentes, le potentiel Zeta négatif est complètement inversé et devient positif à faible pH. Le point isoélectrique a été atteint à pH 5, qui correspond au pKa du P4VP, montrant que le greffage a été relativement dense tout au long des canaux poreux.

L'objectif de ce travail étant de développer des capteurs électrochimiques innovants pour la détection des métaux toxiques, une étude en adsorption a confirmé des capacités de sorption très efficaces des membranes à traces en PVDF greffées dont les groupes fonctionnels facilitent les réactions de coordination. Les constantes d'équilibre  $b$  sont croissantes dans l'ordre suivant:  $b(\text{Pb(II)}\cdot\text{PAA}) < b(\text{U(VI)}\cdot\text{PB2MP}) < b(\text{Hg(II)}\cdot\text{P4VP})$  selon les différents mécanismes de complexation impliqués, partant d'une interaction électrostatique pure inhérente au PAA à la complexation chélatante avec la P4VP en passant par celle du PB2MP. L'effet complexant modéré du PB2MP dans le cas de l'adsorption de l'U(VI) est dû à la co-existence de groupements échangeurs d'ions et chélatants dans la structure du PB2MP.

Pour la détection électrochimique, les membranes en PVDF nanoporeuses radio-greffées sont converties en électrodes grâce à un dépôt d'or de 35 nm sur chaque face et intégrées dans une sonde de mesure pour détecter les ions toxiques piégés dans ces membranes suite à une immersion dans l'eau contaminée. Les membranes en PAA-g-PVDF ont été trouvées sélectives pour le Pb(II) avec une limite de détection (LOD) inférieure à 0.5  $\mu\text{g/L}$ ). Cependant, même si le PAA fonctionne bien pour certains cations divalents comme le Pb, le Cu, le Ni et peut être utilisé pour la détection multi-ion, un fort effet de matrice limite son application pour

l'analyse de l'eau réelle. Pour surmonter ces obstacles, les polymères sélectifs, notamment la P4VP et le PB2MP, ont été greffés dans la structure nanoporeuse des membranes en PVDF à traces attaquées. La LOD du P4VP-g-PVDF a été atteint à 0.01 ppb pour une fluence de  $10^{10} \text{ cm}^{-2}$  et 0.1 ppb pour  $10^9 \text{ cm}^{-2}$ . L'adsorption du mercure n'est affectée ni par le sel, ni par d'autres métaux. Pour acquérir les réactions globales de transfert de charge d'uranyle à l'électrode, étude de voltamétrie cyclique a été réalisée et optimisée par la suite pour la détection (LOD=10 ppb). Les données acquises en photoluminescence résolue en temps (TRPL) et en XPS ont approfondi la compréhension du mécanisme de coordination du complexe U(VI)·PB2MP. L'effet du pH et d'autres métaux sur l'adsorption des ions d'uranyle a été souligné, une explication possible a été suggérée.

La pré-concentration des ions d'uranyle adsorbés dans la nanoporosité de membranes en PB2MP-g-PVDF permet de diminuer la limite de sensibilité de la voltammétrie à redissolution à des concentrations sub-ppb par TRPL. La plus basse concentration d'uranyle constamment mesurée était aussi faible que 6 ppb. Les résultats acquis par TRPL sont en parfaite corrélation avec les études d'adsorption.

La méthodologie présentée apporte une approche efficace à la chimie sélective des nanopores basée sur le greffage radio-induit de polymères qui peut être appliqué non seulement à la rétention de métaux toxiques, mais aussi pour des recherches plus fondamentales sur les propriétés de transport. Cela ouvre une nouvelle classe de matériaux fonctionnalisés nanoporeux pour des applications variées.

# Acknowledgements

Undertaking this Ph.D has been indeed an invaluable experience for me which would not have been possible to acquire without the support and guidance that I received from many people. First of all, I want to thank Michèle Raynaud-Brun, director of LSI, for having me in the laboratory and our administration for helping with all questions and problems, not only administrative ones. I would like to express my sincere gratitude to my supervisors, Dr. Clochard and Dr. Wade, for their support during these past three years. Thank you for being so enthusiastic and kind, for all the insightful discussions we had and giving me enough freedom to proceed my work on this Ph.D project. I would also like to thank my Ph.D committee members, Pr. Etienne Fleury, Pr. Sebastien Balme, Pr. Remita Hynd, Dr. Yvette Ngonon-Ravache, for serving as my committee members, all the valuable comments as well as the hard questions which encouraged me to widen my research from various perspectives.

I am grateful to Bruno Boizot, Didier Lairez, Nadège Ollier and Olivier Cavani from LSI for their encouraging assistance in EPR, zeta-potential and TRPL measurements. Thanks for offering your help with instrumentation, discussions on the results and being always open to all my questions. I also thank CIMAP (GANIL, Caen) and SIRIUS (LSI) teams, Micaela Castellino (Politecnico di Torino) and Adeline Masset (CEA) for helping me in performing ion and electron-beam irradiation, XPS and ICP-MS measurements.

I will forever be thankful to our collaborator, Pr. Mohamad Al-Sheikhly, who has been providing both scientific and personal advice many times throughout my thesis. He was and remains my biggest role model for a scientist and mentor, whom I was lucky to meet. I really appreciate Travis Dietz from the group of Pr. Al-Sheikhly for his continuous guidance during my visit to their lab. I knew I could count on Travis to always provide helpful suggestions, assistance with instrumentation and general lab questions.

I want to thank my friends Quang, Mouad, Pierfrancesco, Simone, Annalisa, Mohamed, Imène, Ozlem and Karim from LSI for all lovely moments we had together. Thank you for listening, offering advice and supporting through the entire process. I am so happy to have met you!

Special thanks to my family. Words cannot express how grateful I am to my mother and father, who have sacrificed their lives for my sister and myself and provided unconditional love and care. I would not have completed my Ph.D without their support. I am so grateful to my darling sister, my best friend, who always was by my side and believed in me.

Last but not least, I would like to express my deepest appreciation to my beloved husband Ilia who spent sleepless nights with me and was always my support in the moments when there was no one to stand by me. These past several years have not been an easy time, both academically and personally. I truly thank you, Ilia, for sticking by my side no matter what, for your faith, care and love.



# Contents

<b>Introduction</b>	<b>1</b>
<b>I Background theory</b>	<b>5</b>
<b>1 Irradiation of polymers</b>	<b>7</b>
1.1 Interaction of ionizing radiation with matter . . . . .	7
1.1.1 Quantity of ionizing radiation . . . . .	7
1.1.2 Electron-beam irradiation . . . . .	8
1.1.3 SHI irradiation . . . . .	8
1.2 Radiation-induced defects in $\beta$ -PVDF . . . . .	11
1.2.1 $\beta$ -PVDF . . . . .	11
1.2.1.1 Polymorphism of PVDF . . . . .	11
1.2.1.2 $\beta$ -PVDF structure obtained by mechanical stretching . . . . .	12
1.2.2 Defect formation in irradiated PVDF . . . . .	13
<b>2 Selective ion-track etching of polymers</b>	<b>17</b>
2.1 Ion energy loss and track etching . . . . .	17
2.2 Track etching of PVDF . . . . .	20
<b>3 Radiation grafting of polymers</b>	<b>23</b>
3.1 Methods of RG . . . . .	23
3.2 Parameters affecting the RG . . . . .	25
3.3 Grafting front mechanism . . . . .	26
3.4 Radiation-induced grafting of PVDF . . . . .	27
3.4.1 Nature of radicals . . . . .	27
3.4.2 Difference between electron and ion irradiation . . . . .	28
3.5 Grafting inside track-etched PVDF . . . . .	29
<b>4 Electrochemical analysis</b>	<b>31</b>
4.1 Voltammetric methods . . . . .	31
4.1.1 Introduction . . . . .	31
4.1.1.1 Electrochemical cell . . . . .	32
4.1.1.2 Electrical Double Layer . . . . .	33
4.1.1.3 Electrode reactions . . . . .	34
4.1.2 Linear sweep voltammetry and cyclic voltammetry . . . . .	35
4.1.3 Square-wave voltammetry . . . . .	36
4.1.4 Stripping voltammetry . . . . .	38
4.2 Application of stripping voltammetry for metal analysis . . . . .	39
4.2.1 Mercury . . . . .	39
4.2.2 Uranium . . . . .	40

<b>II Results and discussion</b>	<b>43</b>
<b>5 Fabrication of membrane-electrodes</b>	<b>47</b>
5.1 Irradiation . . . . .	47
5.2 Track etching of PVDF . . . . .	48
5.3 Radiation grafting . . . . .	48
5.3.1 Acrylic acid (AA) . . . . .	49
5.3.1.1 Grafting of electron-beam irradiated PVDF . . . . .	49
5.3.1.2 Grafting of track-etched PVDF . . . . .	51
5.3.2 4-Vinylpyridine (4VP) . . . . .	52
5.3.2.1 Grafting of electron-beam irradiated PVDF . . . . .	52
5.3.2.2 Grafting of track-etched PVDF . . . . .	52
5.3.2.3 Zeta-potential measurement . . . . .	53
5.3.2.3.1 Origin of surface charge . . . . .	54
5.3.2.3.2 Principles of streaming potential . . . . .	55
5.3.2.3.3 Experimental set-up . . . . .	56
5.3.3 Bis[2-(methacryloyloxy)ethyl] phosphate (B2MP) . . . . .	57
5.3.3.1 Grafting of electron-beam irradiated PVDF . . . . .	57
5.3.3.2 Grafting of track-etched PVDF . . . . .	59
<b>6 Adsorption isotherm models</b>	<b>63</b>
6.1 Lead(II) . . . . .	64
6.2 Mercury(II) . . . . .	65
6.3 Uranium(VI) . . . . .	67
<b>7 Conversion into electrodes</b>	<b>71</b>
<b>8 Voltammetry detection</b>	<b>73</b>
8.1 Toxic metal preconcentration from water . . . . .	74
8.2 PAA-g-PVDF membrane-electrodes . . . . .	75
8.2.1 Lead(II) detection . . . . .	76
8.2.2 Multi-ion detection . . . . .	78
8.3 P4VP-g-PVDF for mercury(II) detection . . . . .	79
8.4 PB2MP-g-PVDF for uranium(VI) detection . . . . .	83
8.4.1 Square wave cathodic stripping voltammetry (SW-CSV) . . . . .	86
8.4.2 Time-resolved photoluminescence (TRPL) measurements . . . . .	88
<b>General conclusion</b>	<b>93</b>
<b>Bibliography</b>	<b>97</b>
<b>Appendix</b>	<b>113</b>

# Introduction

Although heavy metals are naturally existing elements in the earth's crust, main sources of water pollution come from antropogenic activities. Among all monitored pollutants, mercury is one of the priority substances identified by the Water Framework Directive (Directive 2000/60/EC) for which discharges have to be stopped before 2020. Furthermore, in the framework of nuclear plant site dismantlement, determination of a such hazardous element as uranium in nearby water and soils is required. The need for water quality monitoring therefore, in different environmental and health context demanded by European and national regulations, is increasing. It gives rise to large sampling campaigns with spot sampling, handling, preserving, shipping, storing samples and then time consuming laboratory analysis. Classic laboratory techniques for heavy metal analysis are usually performed either by atomic adsorption spectroscopy (AAS), or atomic fluorescence spectroscopy (AFS), or inductively coupled plasma mass spectroscopy (ICP-MS). These techniques have low limits of detection (LODs), but are expensive and, more importantly, are not portable.

The trend for some applications is towards real-time, on-site or *in situ* analyses to improve the reliability of monitoring. Quality standards are now in the very low  $\mu\text{g/L}$  (ppb), or even  $\text{ng/L}$  range. The objective of getting on-site or *in situ* information requires fast, portable, low-cost, environmentally friendly and sensitive instruments; however, few options are available. Unlike aforementioned classic laboratory techniques, stripping voltammetry is considered to be the most sensitive electrochemical technique for trace metal analysis. Mercury has historically been widely used as electrode material in polarography, primarily as dropping mercury electrode (DME). In a classical DME, mercury flows through the capillary by gravity and a drop grows until its weight exceeds the surface tension force holding it to the capillary. The hanging DME (with controlled drop lifetime) has been considered as the best working electrode in electrochemistry for a long time because of its extremely reproducible surface, amalgamation with most heavy metals and low capacitance. However, its toxicity has lead to a limited use. Therefore, there is a tendency to replace mercury-based electrodes with sensitive and portable but non-toxic ones. Solid electrodes made of platinum, gold or carbon can replace mercury-based electrodes for many voltammetric analyses. They are extensively utilized because of their broad potential range and low background currents. However, the common problem of electrochemical sensors for mercury analysis, for example, is a lack of repeatability due to memory effects resulting from the difficult removal of mercury from the working electrode. This serious drawback limits their implementation in chemical laboratories. Screen-printed electrodes (SPEs) is one of the examples of portable, cheap and mercury-free electrochemical sensors existing on market today. Despitess all advantages, extra steps of modification are needed to improve their LODs.

Nanostructured materials nowadays are becoming extensively utilized in water treatment technology due to their large specific area promoting efficient preconcentration effect. Various types of inorganic, carbon-based, cellulose, *etc.* materials have been developed for toxic metal removal. Among them functional, or chelate, polymers possessing donor atoms (ligands) are being increasingly used due to their enhanced selectivities. The radiation-induced grafting is one of the techniques to introduce functional copolymers to chemically inert polymers in form of films, fibers, or membranes by generation of free radicals under ionizing radiation.

Track-etched polymer membranes functionalised with functional polymers thus ensure the synergetic effect enabling the efficient preconcentration and high selectivities towards toxic metals in water. First ion track grafting has been reported by Monnin and Blanford in 1973 for track visualization. The authors utilized the high concentration of reactive chain ends and free radicals along tracks in polymer samples to initiate polymerization along particle tracks [1]. By using a monomer of a different polymer species they created a region of the new polymer by grafting onto the reactive sites at the track. A basic fluorescent dye was used then to visualize the tracks under a microscope with UV light illumination. Other methods of track visualization, performed using ion track etching, reported by Fleischer [2] and Samogyi [3] have become the entrance into the technology for many researchers since then. After this pioneer work, the team at Saclay was the leader one that has published results in the field of ion track grafting of polymers. Because of its remarkable mechanical strength, high chemical resistance, thermal stability and aging resistance, poly(vinylidene fluoride) (PVDF) has found extensive industrial applications and research interest, particularly in our laboratory. To go further towards membrane functionalisation, previous works of our team have demonstrated that radical polymerization of vinyl monomers is initiated from the residual in nanopore walls radicals using confocal laser scanning microscopy (CLSM) and fluorescence labeling.

Based on this approach, our team has already proposed functionalised track-etched PVDF membrane-electrodes sensitive and selective for heavy metal analysis. With their 3D nanostructure, which allows *in situ* sampling, these membrane-electrodes are ideal for self-monitoring of metals directly on-site. The manufacturing of these membrane-electrodes is so cheap that they can be used as disposable products. Gold electrodes deposited onto each side of the functionalised track-etched membranes, have already shown a remarkable stability towards Pb(II) and Hg(II) voltammetric detection. The proposed nanoporous electrodes combine not only the gold electrode nanostructuration but also the functionalisation inside of the cylindrical nanopores enabling efficient preconcentration of heavy metal ions dissolved in water by passive adsorption.

To address the environmental issues, following functional polymers, namely poly(acrylic acid) (PAA), poly(4-vinyl pyridine) (P4VP) and, attempted for the first time, poly(bis[2-(methacryloyloxy) ethyl] phosphate) (PB2MP) are intended to be grafted inside nanoporous structure of track-etched PVDF membranes and converted into electrodes for voltammetric detection of Pb(II), Hg(II) and U(VI) respectively in water. As the objective is to integrate these resulting electrochemical sensors in a portable device, a deeper understanding of metal ion adsorption mechanisms at solid-liquid interface inside the functionalised nanoporous structure is needed. Consequently, present work reports not only on the fabrication and characterization but also on investigation of adsorption mechanisms between PAA, P4VP and PB2MP grafted track-etched PVDF membranes and Pb(II), Hg(II) and U(VI). The thesis consists of two parts. Part I (chapters 1-4) is related to the theoretical and experimental background whereas part II (chapters 5-8) is focused on the acquired results and discussion following by a general conclusion.

The part I comprises state-of-the-art chapters following the multi-step electrochemical sensor fabrication and definition some physical concepts underlying the experimental set-ups used in this work. Indeed, PVDF films were first irradiated with accelerated heavy ions resulting in the formation of latent tracks. Radiolytically produced defects in solids with a particular focus on PVDF are described in chapter 1. Chemical etching was used to reveal latent tracks (chapter 2). The obtained track-etched PVDF membranes were then polymer grafted onto etched track walls through remained trapped radicals. Chapter 3 is devoted to radiation-induced grafting methods. Stripping voltammetry was performed on the functionalised track-etched PVDF membranes converted into electrodes for trace detection of metal

ions of interest. Chapter 4 describes basic theory on voltammetric techniques and their use for Hg(II) and U(VI) detection. In the part II, overall fabrication procedure of track-etched PVDF and optimization of radiation grafting conditions for PAA, P4VP and PB2MP are accordingly presented in chapter 5 following the characterization of nanopore surface charge by zeta-potential measurements. The adsorption experiments were carried out for each type of functionalisation and discussed in chapter 6. Conversion of functionalised membranes into electrodes (chapter 7), stripping voltammetry studies and results are presented in chapter 8 along with time-resolved photoluminescence (TRPL) measurements towards better understanding U(VI)-PB2MP mechanism.



## Part I

# Background theory



# Chapter 1

## Electron-beam and swift heavy ion irradiation of polymers

### 1.1 Interaction of ionizing radiation with matter

Radiation chemistry deals with the study of chemical changes induced by high energy charged particles or electromagnetic radiation, which is termed *ionizing radiation*, with energy in the range of  $10^2$ – $10^7$  eV. Radiation-matter interaction causes ionization and excitation of atoms of the substrate material by various possible pathways, resulting in the formation of a variety of chemically reactive species.

Several sources of irradiation can be used to produce the chemically reactive species. In this chapter, two types of irradiation used in present work will be considered: electron-beam and swift heavy ion (SHI) irradiation with respect to track-etched membrane fabrication. Both electrons and ions lose their energy through inelastic collisions with atom electrons and elastic scattering from atom nuclei. However, distribution of energy deposition in case of SHI irradiation is limited to the ion track, whereas it is homogeneous within the substrate when electron-beam irradiated.

#### 1.1.1 Quantity of ionizing radiation

A charged accelerated particle, passing through the substrate, losses its energy through interaction with atoms constituting this material. Let us first consider the basic definitions used to characterize the ionization radiation:

- The **electronic stopping power**,  $S(E)_{el}$ , also so-called *Linear Energy Transfer* (LET) is defined as the energy loss per unit of path of charged particles (or beam):

$$S(E)_{el} = \frac{dE}{dx}, \quad (1.1)$$

where  $dE$  is the energy loss of the charged particle due to electronic collisions while traversing a distance  $dx$ . The SI unit are joule per metre, however it is frequently expressed in  $\text{keV} \cdot \mu\text{m}^{-1}$ ,  $\text{MeV} \cdot \text{mm}^{-1}$ , or  $\text{MeV} \cdot \text{cm}^2 \cdot \text{mg}^{-1}$ .

- The **fluence**,  $n$ , is the number of ionizing particles per unit area. It is linked with the flux  $\Phi$  and exposition time,  $t$ , as follows:

$$n = \int_0^t \Phi dt \quad (1.2)$$

- The **absorbed dose**,  $D$ , expresses the quantity of energy transferred by the ionizing radiation to the target per unit of mass, measured in grays (Gy). According to SI, it equals to the absorbed dose at which the energy of 1 J is transferred to a target of 1 kg:  $1 \text{ Gy} = 1 \text{ J} \cdot \text{kg}^{-1}$ . The adsorbed dose corresponds to the stopping power, expressed in  $\text{MeV} \cdot \text{cm}^2 \cdot \text{mg}^{-1}$ , as follows:

$$D = C \cdot n \cdot \frac{dE}{dx}, \quad (1.3)$$

where  $C$  [ $\text{J} \cdot \text{mg} \cdot \text{MeV}^{-1} \cdot \text{kg}^{-1}$ ] is a conversion constant and equals to  $1.6 \cdot 10^{-7}$ .

- The **dose rate**,  $\dot{D}$  is the adsorbed dose per unit of time [ $\text{Gy} \cdot \text{s}^{-1}$ ]:

$$\dot{D} = \frac{dD}{dt} \quad (1.4)$$

### 1.1.2 Electron-beam irradiation

Unlike ion irradiation, where inelastic collisions with atom electrons are almost exclusively responsible for the energy loss causing excitation or ionization events, in case of light charged particles, *i.e.* electrons, there are two main processes contributing to the continuous energy loss: ionization and bremsstrahlung. The bremsstrahlung process is inversely proportional to the squared mass of the incident particle, thus it substantially accounts for radiation losses only for electrons. At the electron energies above a few tens of MeV, bremsstrahlung dominates completely other processes. Other rare but still probable processes causing energy loss when electron-beam irradiated are emission of Cherenkov radiation or nuclear reactions. The relative importance of each of these processes depends on the electron-beam energy.

Radiation emission is predominant at high electron energies, whereas elastic scattering and inelastic collisions predominate at low electron energies. The elastic scattering occurs when the electrons, passing close to the nucleus of an atom, are deflected by its electrostatic field. The inelastic collisions take place when electrons interact with the electrostatic field of atom electrons so that the atomic electrons are either raised to a higher energy level (*excitation*) or ejected from the atom (*ionization*). The incident primary electrons are gradually slowed down and cascades of secondary and tertiary electrons are produced. The overall absorption of ionizing radiation by matter results in the formation of chemically reactive species.

It is worth mentioning that the intensity of radiation decreases exponentially as it penetrates a substrate, *i.e.* the penetration depth depends on the electron-beam energy. Energy at keV is mainly used for surface treatment, while electrons at the energy of a few MeV can penetrate deeper in the material.

### 1.1.3 SHI irradiation

The character of ion-matter interaction depends not only on the projectile ion energy but also on its atomic number as well as substrate material properties. Contrary to electrons, heavy particles do not undergo neither bremsstrahlung nor Cherenkov radiation. Besides, they are not deflected as strong as electrons from the initial pathways making the elastic scattering events from the atom nuclei less probable. The inelastic collisions with atom electrons and further evolving secondary electronic collision cascade are essentially two energy loss processes that are needed to be considered in this case.

Generally, during the SHI irradiation energy is transferred from a projectile ion to the substrate atoms through elastic and inelastic interactions which is characterized by *stopping power*  $S(E) = \frac{dE}{dx}$ . The stopping power is divided into nuclear stopping power  $S_{\text{nuc}}(E)$  and electronic stopping power  $S_{\text{el}}(E)$ , *i.e.*  $S(E) = S_{\text{nuc}}(E) + S_{\text{el}}(E)$  (figure 1.1). For low or ion energies of the order of 1 keV/u, the dominating energy loss process is due to the elastic interaction

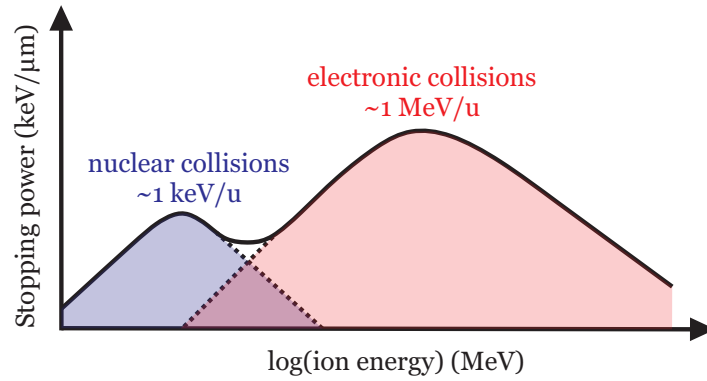


Figure 1.1: Schematic picture of the stopping power as a function of ion energy. Figure is extracted from [4].

with atom nuclei. This interaction is based on the direct kinetic energy transfer from the projectile ion to atoms of the substrate material resulting in dislocation phenomena. While at higher ion energies of the order of 1 MeV/u, inelastic collisions with electrons will prevail, leading to atom excitation or ionization all along the ion pathway leaving traces of modified material – *latent tracks*. There are two main models describing the possible mechanisms of ion track formation: the Coulomb explosion model based on electrostatic ion displacements from the ion pathway [2] and inelastic thermal spike model where latent tracks are regarded as originating from the heat transfer and rapid quenching process described elsewhere [5, 6].

The effect of SHI on polymers is characterized by a high LET value,  $(\frac{dE}{dx})_{el}$ , and a narrow spatial distribution of primary excitation and ionization events around the ion pathway (figure 1.2). A cylindrical zone of 5-10 nm in diameter along the ion trajectory is called the track

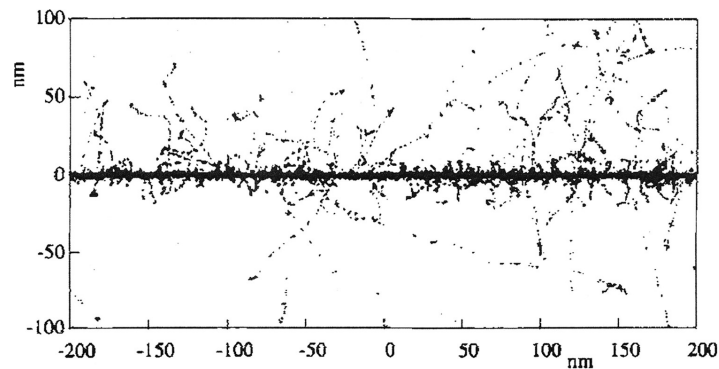


Figure 1.2: Distribution of the ionization events along the trajectory of a 60 MeV/u krypton ion in polyethylene [7].

*core*. The polymer undergoes a deep transformation due to the intense electronic damage caused by the mutual Coulomb repulsion of the ionized atoms, followed by a thermal spike [2]. The density of ionization events and size of the track core depend on the atomic number and energy of a projectile ion. In polymers, most of the pristine covalent bonds (both the backbone and side groups) in the track core are broken. This local zone is depleted of hydrogen atoms, and the polymer density is reduced. The experiments using small-angle X-ray scattering (SAXS), have shown a 60-70% density deficit in the uranium track core in polycarbonate and polyimide [8, 9]. The calculated distribution of electron density is presented in figure 1.3.

The most energetic of secondary electrons emitted from the core, *delta electrons*, dissipate their energy into the surrounding volume (of 100-1000 nm in diameter, strongly depends on material nature [10]) forming an outer cylindrical zone which is defined as the track *halo*.

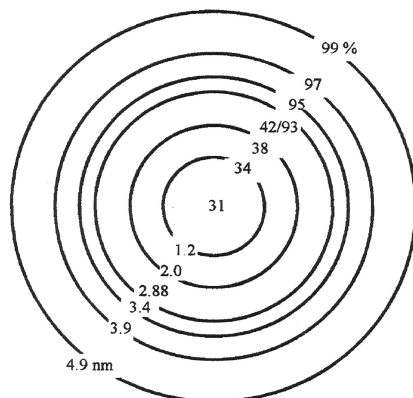


Figure 1.3: Residual electron density in 2.64 GeV uranium ion track as a function of radial distance (in nm) in polycarbonate [8].

In addition to commonly observed radiation defects under electron-beam or  $\gamma$ , SHI irradiation induces specific changes in polymers due to the inhomogeneous dose deposition radially spreading from the ion pathway by the energetic primary and secondary electrons. These specific changes are gas emission and unsaturated bond formation. Thus,  $H_2$  emission generally seen for almost all organic molecules, which increases as LET increases, however strongly depends on polymer structure [11]. For example, the presence of aromatic group in polystyrene (PS) with delocalised electrons confers to PS a much greater radiation resistance. After exceeding LET threshold, highly unsaturated groups (triple or cumulated bonds) are formed due to hydrogen depletion in the track core. For instance, in polyethylene (PE) alkynes [12, 13] and allenes [14] are created under SHI. However, alkynes and allenes are not the unique hydrogen depleted functions which can be formed. In nitrogen-containing polymers, such as poly(4-vinylpyridine), nitrile groups can also appear [15]. The nature of the defects depends not only on LET, but also on the environmental conditions during irradiation and storage. Irradiation under oxygen induces oxidation of radiolytically produced species (peroxy radicals,  $ROO^\bullet$ ). Vacuum or inert atmosphere ( $He$ ,  $N_2$ ) are usually used in order to prevent from oxidation when it is not desired.

Figure 1.4 shows the basic processes involved during irradiation of organic compounds. When an organic molecule  $A-B$  is exposed to high ionizing radiation, two processes occur simul-

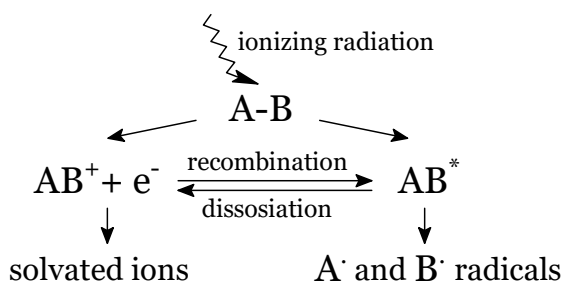


Figure 1.4: Scheme of radiation effect on polymers. Picture is adapted from [16].

taneously, namely: i) ionization of the molecule by expulsion of a low energy electron from the bonding orbital, resulting in the formation of ions  $AB^+$  and  $e^-$ , and ii) excitation of the molecule, which brings the  $A-B$  bond to a high energy state  $AB^*$ . For polymers other than conducting, in the absence of highly polar groups, the cation and electron are difficult to separate, therefore they tend to recombine rapidly resulting in excited species and subsequently a radical. At the same time, the  $AB^*$  species can either relax by energy emission or undergo homolysis leading to the formation of a pair of free radicals.

## 1.2 Radiation-induced defects in $\beta$ -PVDF

In order to get better understanding of the radiation grafting process that will be discussed in chapter 3, one would need to consider the material used in this work. This section reports on  $\beta$ -PVDF specific properties and radiation-induced changes formed as a result of SHI irradiation.

### 1.2.1 $\beta$ -PVDF

#### 1.2.1.1 Polymorphism of PVDF

PVDF,  $-(\text{CH}_2-\text{CF}_2)_n-$ , is a semicrystalline polymer which means that in a non-negligible part of polymer volume (generally around 35-40%) the polymer molecular chains is arranged in a regular order. The five crystal phases ( $\alpha$ ,  $\beta$ ,  $\gamma$ ,  $\delta$  and  $\epsilon$ ) have been reported for the PVDF [17]. The most commonly observed crystalline structure, obtained primarily by crystallization from the PVDF melt at moderate or high undercooling, is  $\alpha$ -PVDF. Because of the antiparallel packing of the dipoles, the  $\alpha$  and  $\epsilon$  phases are non-polar [18]. The other three PVDF polymorphs are polar and exhibit ferroelectric and piezoelectric properties [19, 20]. The  $\beta$ -PVDF constitutes all trans-planar zigzag conformation and can induce a significant total dipole moment. This phase is typically obtained by mechanical stretching of  $\alpha$ -PVDF films to several times their initial length (figure 1.5), resulting in highly oriented  $\beta$ -PVDF

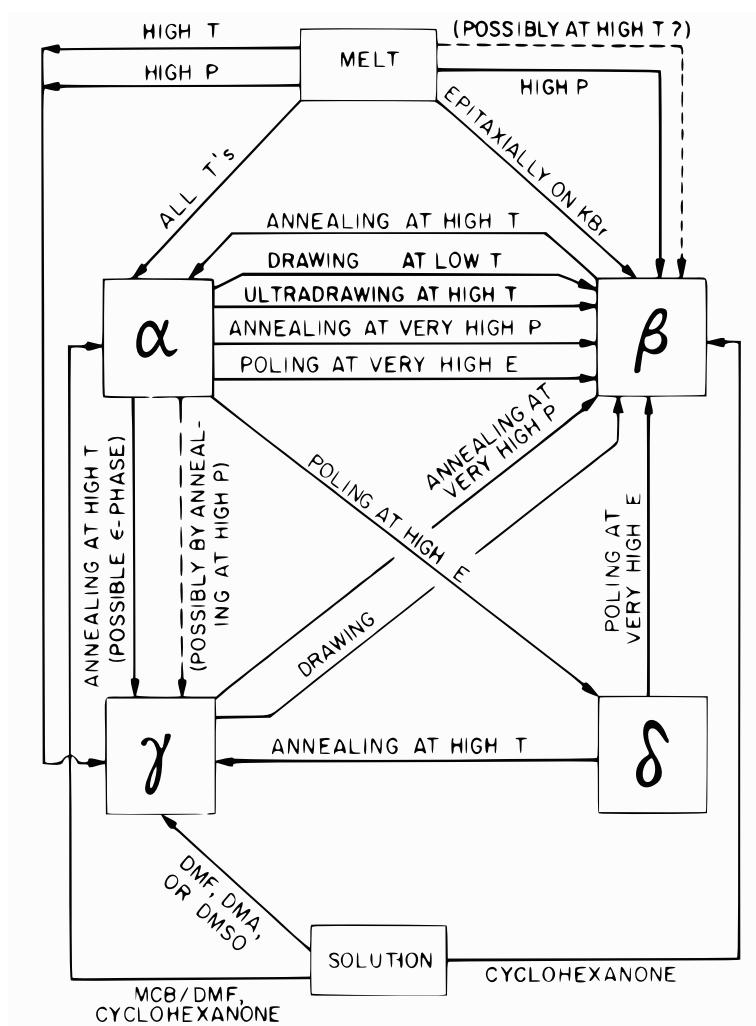


Figure 1.5: Schematic summary of interconversions of the polymorphic phases of PVDF [21].

films with a chain axis parallel to the stretching direction. Hasegawa [22] and Lando [23]

found unit cell parameters of an orthorhombic  $\beta$ -PVDF ( $a=8.47 \text{ \AA}$ ,  $b=4.90 \text{ \AA}$  and  $c=2.56 \text{ \AA}$ ); their unit cell configuration is depicted in figure 1.6.

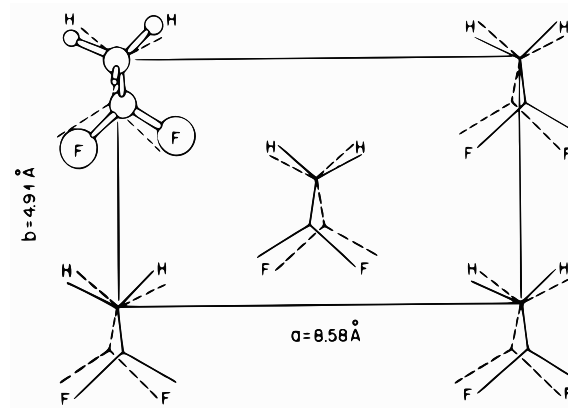


Figure 1.6: Unit cell of  $\beta$ -PVDF [21].

### 1.2.1.2 $\beta$ -PVDF structure obtained by mechanical stretching

Compared to  $\alpha$ -PVDF, the interest of biaxially stretched PVDF is an increase of the crystallinity up to ca. 40%. A higher crystallinity is herein a very important parameter not only for fabrication of symmetrical cylindrical nanopores (chapter 2) but also for further radical stabilization properties (chapter 3).

When semi-crystalline polymer crystallize, the polymer molecules typically form *lamellae* of the order of 10 nm thick and a stack of these lamellae form *spherulites*. The polymer molecular chains are oriented perpendicular to the surface of the lamellae and are folded in such a way as to penetrate the lamellae many times. Once mechanical stretching is applied on polymer, the transition region of crystalline structure started from the middle of spherulite (figure 1.7), where the polymer molecular chains are first extended along stretching direction.

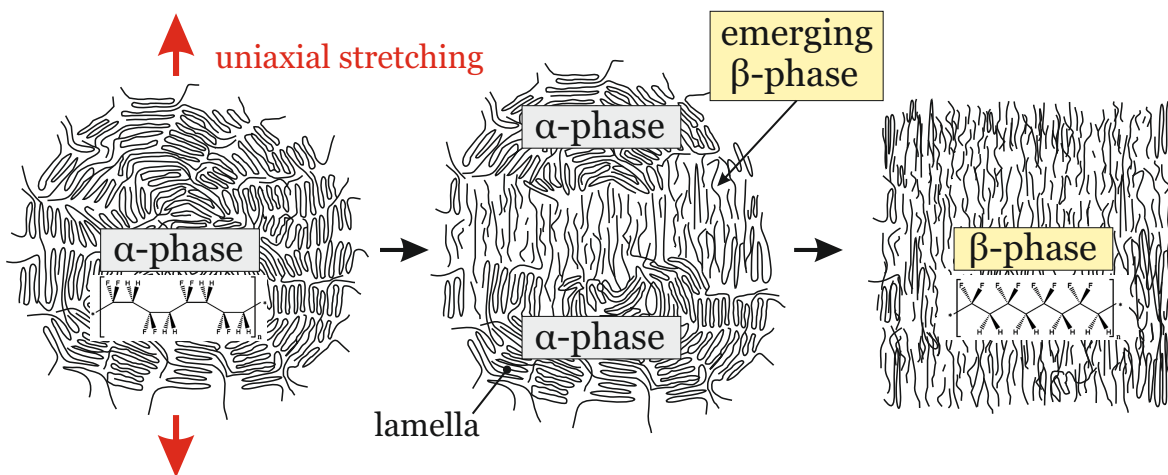


Figure 1.7: Schematic picture of PVDF crystalline phase transformation of the spherulitic  $\alpha$ -phase morphology to fibrillar  $\beta$ -phase, adapted from [24].

FESEM images (figure 1.8) demonstrate final polymer morphology obtained after uniaxial stretching resulting in transformation of entire spherulite ( $\alpha$ -PVDF) into the fibrillar structure ( $\beta$ -PVDF).

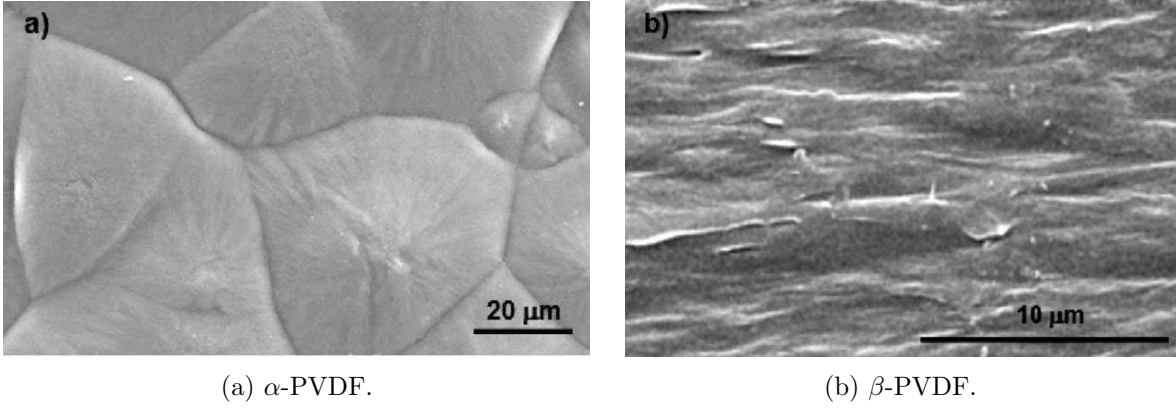


Figure 1.8: FESEM images (a) before and (b) after uniaxial stretching, extracted from [25].

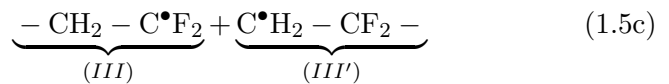
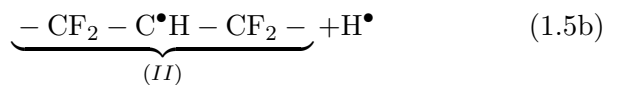
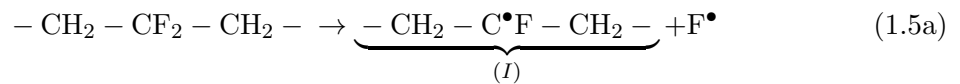
### 1.2.2 Defect formation in irradiated PVDF

Whatever the predominant crystalline phase, radiation-induced defects in PVDF are similar. Nevertheless, the higher the crystallinity degree, the more radiation-induced radicals will be trapped. Effectively, high energy ionizing radiation mainly breaks the lateral bonds of PVDF (C–H and C–F) leading to the formation of in-chain alkyl radicals (eqs. 1.5a and 1.5b), whereas a scission of C–C backbone of PVDF results in end-chain alkyl radicals (eq. 1.5c) [26, 27]. When put in contact with air, some of the alkyl radicals undergo oxidative reaction and the alkyl-peroxy radicals are formed (as for example, alkyl-peroxy  $-\text{CH}_2-\text{CFOO}^\bullet-\text{CH}_2-$ ).

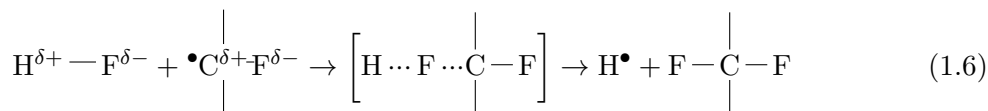
Equations 1.5a and 1.5b are also responsible for dehydrofluorination of PVDF by recombination of  $\text{H}^\bullet$  and  $\text{F}^\bullet$  radicals, i.e. formation of volatile species such as  $\text{F}_2$ , HF and  $\text{H}_2$  [28]. The process of the gas emission increases with the ion dose until the hydrogen and fluorine concentrations in the polymer decrease of about two orders of magnitude. The  $\text{H}_2$  is produced and ejected quickly due to its high diffusion coefficient in the PVDF ( $6 \cdot 10^{-6} \text{ cm}^2/\text{s}$ ) unlike HF which is ejected much slower ( $10^{-8} \text{ cm}^2/\text{s}$ ) [29].

Interesting phenomenon of the alkyl radical stabilization by evolving HF under irradiation was reported in [30] and the suggested model is discussed. It was found out that the decay of the alkyl radicals is faster in presence of evolving gases than in their absence. The mechanism, however, is not clear yet. Perhaps, lower diffusion coefficient of HF mentioned above is due to the interaction with (I) and (II) alkyl radicals, converting them into stable molecules. The polarity of the alkyl radical due to the high electronegativity of the covalently bonded fluorine atom would be expected to facilitate the HF attack upon the alkyl radicals as shown in equations 1.6 and 1.7a-1.7d.

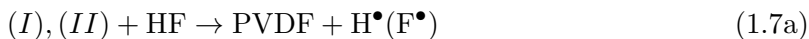
Radical formation and chain scission:



Model of alkyl radical stabilization by the evolved HF [30], an example of type (I) radical:



The tentative reaction scheme may be shown as following:



Crosslinking:



Unlike PE, for which crosslinking is a predominant radiation effect, PVDF undergoes both chain scission (eqs. 1.5a-1.5c) and crosslinking (eq. 1.8). The crosslinking is defined as the formation of a new covalent bond, which can occur in one single chain (*intrachain*) or between two nearby chains (*interchain*). The dose below which no insoluble fraction is measured, meaning that density of crosslinks is not sufficient to form a small insoluble piece of polymer, is called a *gel-dose*. The gel-dose of PVDF is known to be in the range from 9.9 to 35.1 kGy (corresponds to the fluence range from  $1.9 \times 10^9 \text{ cm}^{-2}$  to  $4.9 \times 10^9 \text{ cm}^{-2}$ ). The yield of crosslinking increases with dose, and the increase is not linear [31].

The equations 1.5a and 1.5b demonstrate induced scission that gives rise to the radicals and evolved gases. As a result of radical recombination, double bonds, conjugated or not, are created. FTIR was used to reveal the unsaturation formation by monitoring the C–H stretching vibration band at  $3304 \text{ cm}^{-1}$  in case of alkyne groups (namely,  $-\text{CH}_2-\text{C}\equiv\text{CH}$ ), and by the two C=C stretching vibration bands at  $1713 \text{ cm}^{-1}$  for  $-\text{CF}=\text{CH}-$  and at  $1754 \text{ cm}^{-1}$  for  $-\text{CF}_2-\text{CH}=\text{CF}_2$  [13]. The increase of  $-\text{CF}_2-\text{CH}=\text{CF}_2$  yield relative to the  $-\text{CF}=\text{CH}-$  takes place when changing from an electron-beam to krypton irradiation.

Figure 1.9 shows EPR experimental spectrum of electron-beam irradiated PVDF at 1.25 MeV dose (solid black line) under vacuum and subsequently put in contact with air for EPR measurements along with simulated spectra of free radical components. A large asymmetrical signal in the center corresponds to peroxy radicals (dotted red line). As was shown in [31], when the angle of PVDF stretching direction varies with direction of magnetic field, the peroxy structures show differences in their intensities indicating that the peroxy radicals are trapped in two zones of different mobilities. Indeed, after recombination of the initially formed radicals, stable radicals remain (not polyenyl [33, 34]). One would expect that it could be due to location of the radicals in a heavily crosslinked structure. Additionally, the crystallites of PVDF create sterical hindrances preventing radicals from free diffusion and further recombination. The five-line spectrum (dotted black line) is attributed to the in-chain alkyl radicals. The third component of the experimental signal is a triplet-line spectrum (dotted blue line) is due to the end-chain alkyl radicals.

Besides all aforementioned defects, at high energy irradiation (MGy doses), amorphisation, *i.e.* decrease of crystalline phase along damaged regions, of PVDF takes place. FTIR peak intensity corresponding to the  $\text{CH}_2$  bands at  $3025$  and  $2985 \text{ cm}^{-1}$  were used for evaluation of overall destruction of the polymer. The crystallinity is characterised by the bands at  $532$ ,  $614$ ,  $763$ ,  $796$  and  $975 \text{ cm}^{-1}$  [13]. Chailley et al. [35] reported the that crystallinity loss

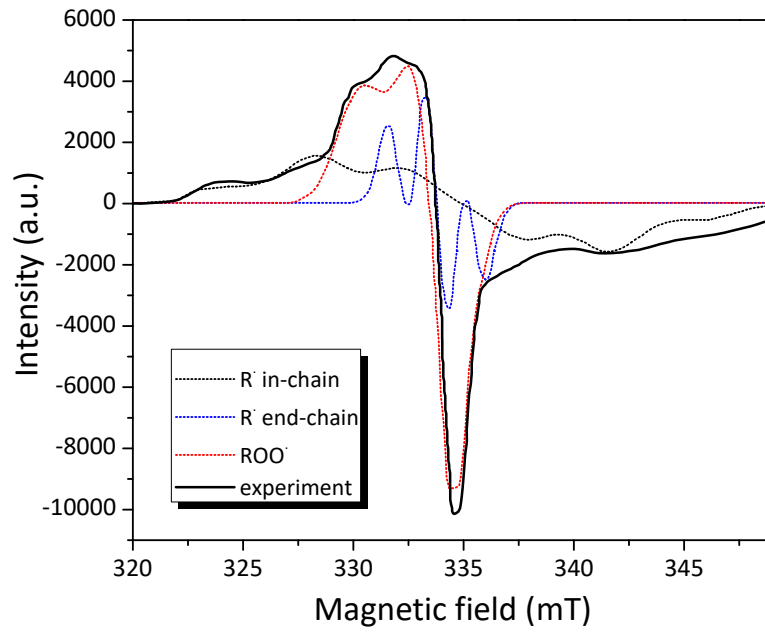


Figure 1.9: Typical EPR spectrum of electron-beam irradiated PVDF (1.25 MGy) at  $T=300$  K and simulated components corresponding to alkyl and peroxy radicals. Adapted from [32].

could result from different processes: at low  $(\frac{dE}{dx})_{el}$ , amorphization is retarded at low fluence. At high  $(\frac{dE}{dx})_{el}$ , the high densities of radicals in the ion track could be responsible for the direct amorphization of the crystal via chain scission and crosslinking. The dose required for transforming half the  $\alpha$ -PVDF varies between 3.5 and 7 MGy, and was found depending on the type of projectile.



## Chapter 2

# Selective ion-track etching of polymers

### 2.1 Ion energy loss and track etching

Due to a high local confinement of dissipated energy, SHI produce continuous damage trails (latent tracks) that consist of a highly degraded material with increased chemical reactivity. As a result, the polymers irradiated with heavy ions are anisotropic and highly heterogeneous on the nanometer scale. Chemical track-etching is used to further modify the structure of the ion irradiated polymers and to produce nanostructured membranes.

The energy transfer to the nuclei of target prevails at low values of ion energy (around 1 keV/u) and the energy transfer to electrons of the target prevails at higher ion energy (a few MeV/u) as was shown in previous section (figure 1.1). For the track-etched membrane fabrication, heavy ions with sufficiently high energy are used (from 2 MeV/u and higher). In this case, the transfer of energy in collisions with the nuclei may be neglected. Due to the large difference in masses of electrons and ions, the last do not change their direction in successive collisions and pass through material approximately along a straight line. The quantitative description of a heavy ion stopping in matter is the energy loss per unit of length (stopping power). The electronic energy losses to target electrons per length unit are described by Bethe-Bloch formula (eq. 2.1) from which the maximum energy transfer to target may be expressed as follows (eq. 2.2):

$$-\frac{dE}{dx} = Kz^2 \frac{Z}{A} \frac{1}{\beta^2} \left[ \frac{1}{2} \ln \frac{2m_e c^2 \beta^2 \gamma^2 T_{max}}{I^2} - \beta^2 - \frac{\delta}{2} \right], \quad (2.1)$$

$$T_{max} = \frac{2m_e c^2 \beta^2 \gamma^2}{1 + \frac{2\gamma m_e}{M} + \left(\frac{m_e}{M}\right)^2} \quad (2.2)$$

where  $A$  – atomic mass of target material,  $z$  and  $Z$  – atomic numbers of incidents particle and atom of target material,  $\beta$  – velocity of ion ( $\beta = \frac{v}{c}$ ),  $I$  – target ionization potential,  $T_{max}$  – maximum energy transfer to the target,  $m_e$  – electron mass,  $\gamma$  – relativistic factor ( $\gamma = \frac{1}{\sqrt{1-\beta^2}}$ ),  $\delta$  – density effect correction to ionization loss,  $M$  – ion mass.

The energy, deposited per length unit, is directly related to the density of damages in polymer chains all along the ion trajectory. However, the process of ion-matter interaction is statistical in nature, so there should be fluctuations in linear energy deposition. At sufficiently high values of the energy deposited per length unit, the fluctuations will be smoothed and the overlapping of damages can occur giving a continuous cylindrically damaged latent track prior etching. The *etching threshold* is defined as the minimum energy loss that is required for forming an etchable track. For making the continuous etchable latent tracks in polymer

films, the energy deposition per length unit should be higher than some threshold estimated at 720-900 eV/nm for polycarbonate, polyimide and poly(ethylene terephthalate) [36]. As the deposited energy is directly linked to the initial kinetic energy in MeV/u (where u is the atomic mass unit), the heavier the ion projectile, the more homogeneous the resulting latent tracks (figure 2.1).

Figure 2.1 gives theoretical curves of energy loss ( $\frac{dE}{dx}$ ) of different ions in Kapton as a function of their energy calculated by the TRIM code [37]. For open symbols ( $\frac{dE}{dx} < 180 \text{ eV/\AA}$ ) no

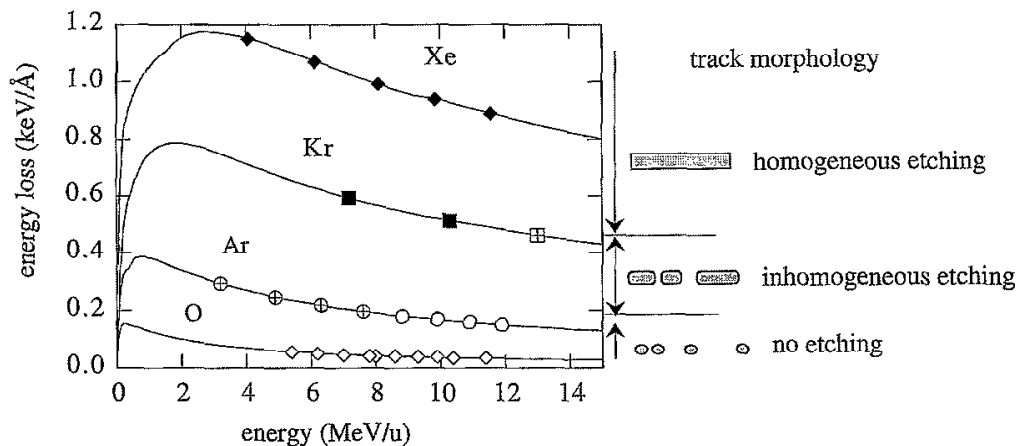


Figure 2.1: Calculated energy loss curves [37] of Xe, Kr, Ar, and O ions in polyimide (kapton) as a function of their specific energy. Picture is deduced from [36].

pores were observed. Obviously the damage density along the ion track was not sufficient to be etched, at least not within the given time limit. Filled symbols ( $\frac{dE}{dx} > 450 \text{ eV/\AA}$ ) correspond to the etched tracks with homogeneous pore size. In the case of crossed symbols ( $180 \text{ eV/\AA} \leq \frac{dE}{dx} \leq 450 \text{ eV/\AA}$ ), the ion tracks were etched but showed inhomogeneous properties.

Tracks in solid polymers may be revealed and become visible in an optical and/or electron microscope applying a chemical treatment properly chosen reagent. The free volume in the track core facilitates the penetration of the chemical reagent (etchant) along the particle pathway and accelerates the chemical degradation of the macromolecular parts located there. Though the free volume plays a main role in the preferential etchability of ion tracks [38]. The radiation-induced chemical modifications of the macromolecules, such as oxidation, also contribute. The distribution of material density in the track (figure 1.3) suggests that firstly etching occurs in the track core of a few nanometers in radius. Conductometric measurements of the local etching rate as a function of pore radius confirmed the dimensions of the selectively etchable track core [39].

Successful track etching requires that the damaged material is preferentially attacked at a higher rate along the track than in the surrounding undamaged matrix, *i.e.* the track etching rate  $v_t$  has to be larger than the bulk etching rate  $v_b$ . The ratio of  $\frac{v_t}{v_b}$  determines the geometry of the etched pores. In general,  $v_b$  remains constant for a given material and etchant applied under set etching conditions (concentration and temperature). In addition,  $v_t$  depends on the density of damages in the track and hence on the energy loss of the track-forming ion.

The simplest description of pore geometry in a homogeneous isotropic medium is based on two parameters –  $v_b$  and  $v_t$  (figure 2.2). It is applicable for large ( $\geq 1 \mu\text{m}$  in diameter) pores. The conical pore shape is transformed into a cylindrical one at  $v_t \gg v_b$ . The geometry of smaller pores is determined also by the size and structure of the damage zone around the

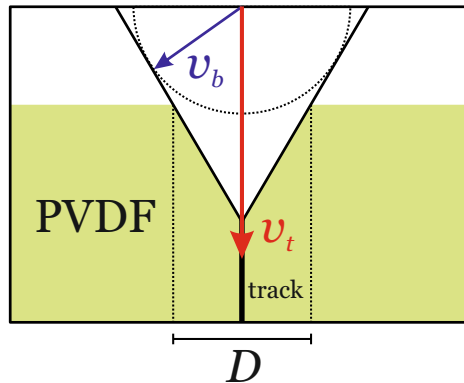


Figure 2.2: Schematic picture of an etched ion track. The opening angle is determined by the ratio of track etching rate  $v_t$  and bulk etching rate  $v_b$ .  $D$  is the final pore diameter.

particle path. The track core with the diameter determines the size of the channel that is etched out very quickly. Depending on the predominant process in the track halo – cross-linking or oxidation (degradation) – the local etch rate outside the track core may be lowered or increased with regards to the bulk etch rate [40].

The bulk etch rate depends on the material, etchant composition and temperature. The track etch rate depends on a much greater number of factors. They can be classified into a few categories: sensitivity of the material towards irradiation, irradiation conditions, post-irradiation conditions and etching conditions. The irradiation conditions include parameters of the bombarding particle ( $(\frac{dE}{dx})_{el}$  characterizes quite well the damaging ability of a particle [2]), atmosphere (vacuum, presence of oxygen) and temperature [41, 42]. The track etch rate generally increases with increasing of  $(\frac{dE}{dx})_{el}$ , however, at very high dissipated energy densities, the  $\frac{v_t}{v_b}$  ration *versus*  $(\frac{dE}{dx})_{el}$  function tends to saturation [43].

Chemically active products of radiolysis in heavy ion tracks undergo post-irradiation reactions, such as oxidation, photo-oxidation, etc. For this reason, storage of the irradiated PC or PET in air leads to a significant increase in the track etch rate [40, 44–46]. The acceleration of this process with an exposure to UV light is used in a technological process of track membrane fabrication to below aforementioned threshold and render possible the use of lighter ion projectiles [47].

In most cases, the variations of the etchant composition, component concentrations and temperature give a chance to vary the  $\frac{v_t}{v_b}$  ratio in a very wide range. For PET exposed to xenon ions, a change in the concentration of alkali in aqueous solutions may result in a gradual change of the etch rate ratio from units to thousands. The activation energy of the track etching process often differs from that of the bulk etching [40]. Thus, changing the temperature can be also used to increase or decrease the  $\frac{v_t}{v_b}$  ratio.

For the nanopore production, the parameters core and halo sizes are also of great importance. The heavier the ion, the larger the track core and halo are produced [48, 49]. At the same time, the heaviest ions do not necessarily provide the highest etch  $\frac{v_t}{v_b}$  ratio as they may also favor cross-linking reactions in the track halo limiting drastically  $v_b$ . From the comparison of the response function with the damage zone diameter *versus*  $\frac{dE}{dx}$ , the ions with moderate masses (krypton or xenon) are favored for production of nanopores in polymer films [43].

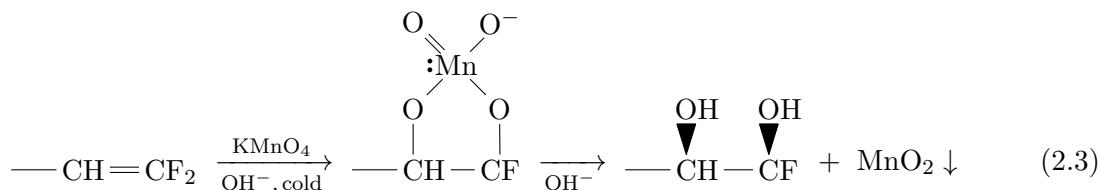
## 2.2 Track etching of PVDF

PVDF is an inert fluorinated polymer, known for its high resistance towards chemical etching. The first successful attempts to etch the SHI irradiated PVDF were made by Tretyakova and Jolos [50] and Komaki and Tsujimura [51]. Tretyakova et Jolos have studied the etching rates of PVDF using different etchants (NaOH,  $\text{KMnO}_4 + \text{NaOH}$ , and  $\text{KMnO}_4$ ) as a function of concentration and temperature. They have observed the highest etching rate for 13% NaOH + saturated  $\text{KMnO}_4$  solution and the lowest for 20% NaOH [52].

Grasselli and Betz investigated the effect of alkaline media strength and found the synergetical effect of mixing both KOH and  $\text{KMnO}_4$ . The solution of 9 M KOH and saturated  $\text{KMnO}_4$  was the best etching reactant [53]. At a given etchant composition, they have also found out that a temperature range between 55° C and 65° C was optimal to induce a cylindrical pore geometry in PVDF.

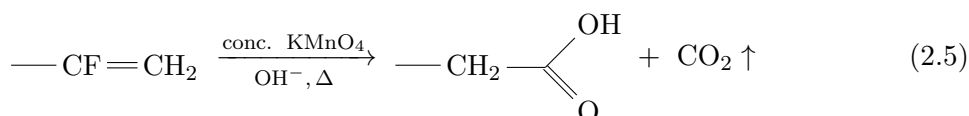
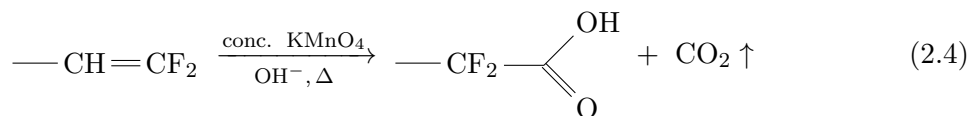
PVDF is known to have intermediate characteristics between those of crosslinked and degraded polymers after exposure to irradiation [13]. After SHI irradiation, following the reactions of radical recombination and disproportionation, C=C bonds are formed. Simultaneously, strong alkaline medium catalyses the dehydrofluorination of virgin PVDF and thus promoting  $-\text{CH}=\text{CF}_2$ ,  $-\text{CH}=\text{CF}-$  [54, 55], and  $-\text{CF}=\text{CH}_2$  [53] species formation (eq. 2.3).

In mild conditions (at low concentration of oxidative reagent, cold temperatures), alkaline  $\text{KMnO}_4$  can convert alkenes into glycols from less-hindered side of the double bond (*dihydroxy-addition*) [56, p. 1162]:



A cyclic manganese diester is an intermediate product in these oxidation conditions resulting in glycols formed by *syn addition*. Manganese dioxide formed is an insoluble brown precipitate due to changing its oxidation state from +7 (pink) to +4 (brown).

When more concentrated solutions of  $\text{KMnO}_4$  and higher temperatures are employed, the glycols are further oxidized, leading to the cleavage of the C=C bond and to the ketone (if C=C is internal) or carboxylic acid (if C=C is terminal) formation [56, p. 1732]. Certainly that carboxylic acids are the major oxidized species after oxidative cleavage for terminal C=C bonds (eqs. 2.4 and 2.5) as aldehydes and fluorinated acids are not stable under strong basic conditions (*Cannizzaro reaction*) [56, p. 1863]. However, there are multiple double bonds present in the track halo of SHI irradiated PVDF. These equations show only the terminal double bond cleavage and do not describe all possible oxidation reactions. Due to limited diffusion of etchant, non-cleaved internal C=C bonds are converted to ketones, diols, esters and other light oxidated products.



The oxidation cleavage of the C=C bonds by chemical etching mostly results in carboxylation of the inner nanopore surface. When put in contact with water, the carboxyl groups are

deprotonated ( $-\text{COO}^-$ ) making the nanopores negatively charged. This effect will help us to understand the results obtained by measuring of  $\zeta$ -potential in chapter 5.

As aforementioned, if  $v_t$  is not sufficiently higher than  $v_b$ , the obtained pores are not cylindrical (at a first approximation). Cuscito O. [57] has experimentally determined the track and bulk etch rates of 9.19 MeV/u krypton irradiated PVDF films to be equal to 18  $\mu\text{m}/\text{h}$  and 0.22  $\mu\text{m}/\text{h}$  respectively at 65° C using 9 M KOH and 0.25 M  $\text{KMnO}_4$  etching solution that permitted the cylindrical nanopore formation.



## Chapter 3

# Radiation grafting of polymers

For many decades, radiation-induced grafting has been used for surface functionalisation of polymers [58] so that they can be utilized in a variety of applications, such as biomedical, environmental and industrial [59]. Radiation grafting (RG) changes the surface of polymer by covalent bonding of monomers having different functional groups, for example,  $-\text{COOH}$ ,  $-\text{OR}$ ,  $-\text{OH}$ ,  $-\text{NH}_2$ , etc., to affect the surface properties without influence on the bulk. Ultra-violet (UV),  $\gamma$ -ray, electron-beam and swift heavy ion (SHI) irradiation are used to generate free radicals on the polymer surface and subsequently initiate grafting reaction.

Surface modification by the RG has several advantages over the conventional chemical methods. First, any polymer surface may be modified in the form of film, membrane, fiber, fabric or powder, and most free radical polymerisable monomers such as styrene, methacrylamides, methacrylates and arylates, vinyl acetates, vinyl chlorides, acrylic acid can be grafted. Additionally, the grafted copolymer is pure, with no initiator or any impurities remained. Second, the RG requires moderate heating of the system to initiate the RG reaction (important for temperature sensitive bio-polymers). And finally, the grafting yield can be tuned playing on reaction conditions and the irradiation exposure parameters.

The grafting efficiency is represented by *grafting yield* (GY), which is determined as the weight of grafted copolymer with respect to the initial weight of polymer substrate:

$$GY = \frac{m_f - m_i}{m_i} \times 100\%, \quad (3.1)$$

where  $m_i$  and  $m_f$  are masses of the polymer before and after grafting respectively.

### 3.1 Methods of RG

There are three methods to undertake the RG [58, 60]: 1) the *direct* (sometimes called *mutual*), 2) *peroxide*, and 3) *pre-irradiation*. The selection of one or other method depends on the polymer substrate, the monomer reactivity, the irradiation source and the GY required. Figure 3.1 summaries and illustrates similarities and differences in these methods.

Overall radiation-induced grafting comprises three main steps: initiation, chain propagation and termination. Depending on the grafting method used, initiation may involve peroxides/hydroperoxides decomposition at elevated temperature, primary or trapped radicals.

In the *direct method*, the polymer substrate is immersed in a monomer solution (or pure monomer) and exposed to ionizing radiation. The irradiation activates the polymer substrate, *i.e.* formation of free radicals occurs (eq. 5.4). The free radicals of the polymer backbone initiate polymerization reaction of monomer onto its surface (eq. 5.5). After the initiation, the propagation of monomer chains takes place (eq. 5.6). The process continues until the

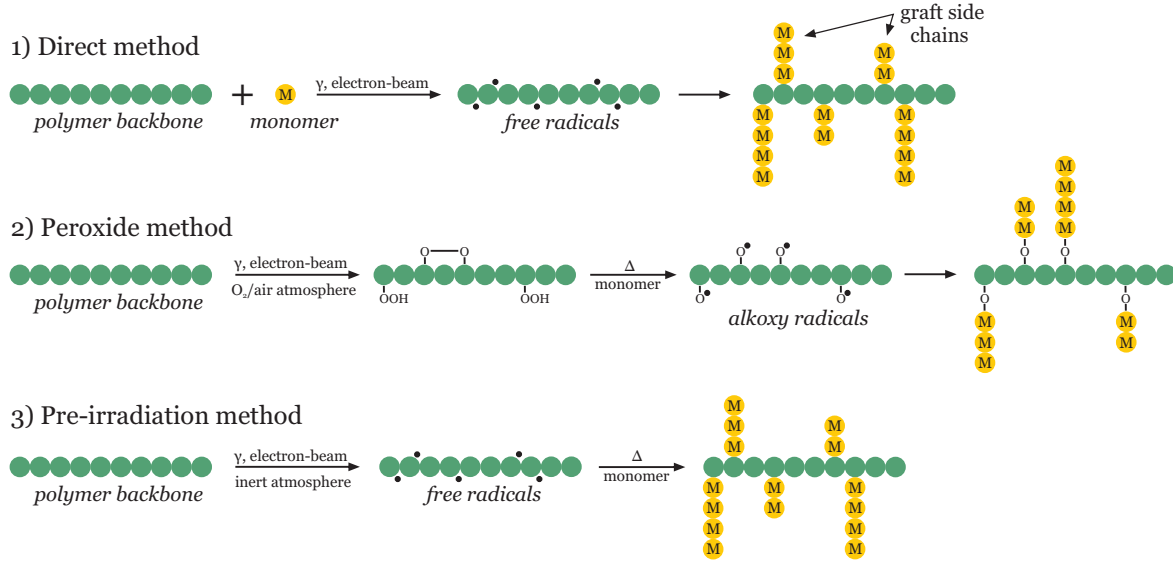
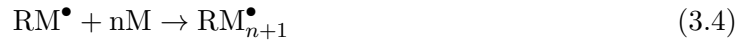


Figure 3.1: Three different methods of radiation-induced grafting of polymers.

growing macro-radicals meet each other (recombination) and thus terminate the chain growth (eq. 5.7).



Since the monomer solution is also exposed to irradiation, active sites are formed in it. The side reactions limit the GY due to i) increase of solution's viscosity as a result of homopolymerization (eqs. 3.6-3.8), and ii) monomer consumption by radicals other than those of the polymer substrate backbone.



In the *peroxide method*, the polymer substrate is irradiated under an oxygen or air atmosphere to form peroxides or hydroperoxides due to oxidation of alkyl radicals (eqs. 3.9-3.11). At high temperature, the peroxide bonds decompose on alkoxy and hydroxy radicals (eq. 3.12). The alkoxy radicals can then initiate the polymerization reaction when put in contact with monomer solution (eq. 3.13). In this method, the formation of homopolymer is negligible since the monomer is not exposed to irradiation.



In the *pre-irradiation method*, the grafting reaction is induced by trapped radicals and can be described by eqs. 5.4-5.7. In contrast to the peroxide method, which involves peroxides/hydroperoxides decomposition at elevated temperature, irradiation is carried out in vacuum or under an inert atmosphere to prevent oxidation reactions. Thus, heating is needed to

activate trapped radicals and initiate the RG reaction. In this method, in order to achieve a high concentration of radicals, the polymer substrate should be irradiated at high dose rates.

## 3.2 Parameters affecting the RG

The GY depends on many factors, such as type of polymer substrate, monomer to be grafted and its concentration, type of irradiation used, reaction temperature and atmosphere, concentration of the homopolymerization inhibitor and the type of solvent [61–63]. Therefore, the efficiency of grafting process can be controlled by the variation of these reaction parameters.

- **Effect of irradiation dose and dose rate.** Radiation-induced grafting by the direct method is usually performed using  $\gamma$ -rays in contrast to the pre-irradiation method, where the electron-beam is preferred [61, 64]. In general case, the higher the dose, the larger amount of radicals is formed, the higher the GY is expected. However, the increase of the GY as a function of dose may exhibit a non-linear dependence. At certain dose, no further growth in GY is observed. In the direct method, this phenomenon might be attributed to the restriction of monomer diffusion due to the increased viscosity of grafting solution (homopolymerization). In the pre-irradiation method, the decrease in GY may be explained by achieving the *gel-dose* threshold of polymer (defined in previous chapter). Crosslinking under irradiation can not only hinder the monomer diffusion inside the polymer but also the propagation of the grafting front. The inverse tendency is observed for the GY as a function of dose rate [65]. High dose rates produce higher density of radicals that favours their recombination and formation of gel.
- **Properties of polymer substrate.** GY strongly depends on the reactivity of radicals in the irradiated polymer substrate. Electron paramagnetic resonance (EPR) spectroscopy is often used to monitor the radical nature and their content in the irradiated samples and allows to predict the grafting behaviour. For instance, for polystyrene (PS), polypropylene (PP) and polyethylene (PE) irradiated at the same dose, the concentration of radicals stable at room temperature was found to be in the following order: PS<PP<PE [66]. Below a certain LET threshold, radical yield in PS is much lower in comparison to other polymers due to benzene ring protection effect. However, there is almost no LET effect for PP and PE [11]. PE is also known to be a polymer that effectively undergoes crosslinking during irradiation as well as formation of radicals in crystalline phase resulting in their higher stability. The irradiation conditions were: electron-beam irradiation, dose of 25 kGy, PS and PP under air whereas PE under vacuum (due to fast oxidation to peroxy radicals). Among many polymers, whose surfaces were modified by using RG, the larger group are polyolefins (PE and PP). There are also lots of reports on surface modification of polyamide (PA) [67, 68], poly(ethylene terephthalate) (PET) [69, 70], polyurethane (PUR) [71, 72], cellulose [73, 74], poly(tetrafluoroethylene) (PTFE) [75, 76] and poly(vinylidene fluoride) (PVDF) [77, 78].
- **Effect of monomer concentration.** The monomer reactivity is influenced by the type of solvent used for grafting as it involves the monomer diffusion. In general, the higher the monomer concentration, the greater the GY. However, both GY and rate of grafting tend to level off and at certain monomer concentration beyond which further increase causes sharp fall in both parameters. This decrease is often caused by the decrease in the monomer concentration and the diffusion rate in the grafting zone. In case of fluoropolymers, *e.g.* PTFE, which barely swell in the grafting mixtures, such decreasing effect is attributed to the suppression of the monomer diffusion by the increase in the viscosity of the grafting mixture close to the polymer surface [61]. This phenomenon is attributed to the grafting front mechanism [58] and will be described further.

- **Effect of solvent.** The nature of solvent determines not only the GY, but also location of grafting. If poor-swelling solvent for the growing grafted polymer chains is used, surface grafting is most likely to take place due to the slow down in monomer diffusion. When good-swelling solvent is utilized, bulk grafting is highly favored and homogenous grafting is most likely obtained. For example, PAA grafting preferentially occurs in the volume of PVDF film when water is used as a solvent [79]. Whereas THF promotes the surface grafting limiting the GYs [57]. In addition, properly chosen swelling solvent may affect not only the grafting efficiency but also the homogeneity of the grafted chains [61].
- **Effect of grafting temperature.** Increase of temperature enhances the RG by changing the kinetics of the reaction [80]. In the peroxide method, decomposition of the peroxides leads to the formation of active sites that initiate polymerization reaction. Heating of irradiated solution in the pre-irradiation method above  $T_g$  of polymer, enhances the mobility of chain segments, promoting the active sited migration to the surface and thus increasing the population of radicals involved in grafting process. At the same time, elevated temperature decreases viscosity of monomer solution, making the diffusion of monomer inside the polymer substrate easier.
- **Presence of inhibitor of homopolymerization.** In the direct method, in order to suppress the undesired homopolymerization, inorganic salts, such as iron(II) chloride, copper(II) chloride, copper(II) sulphate or ammonium iron(II) sulphate (Mohr's salt) may be used [81]. After dissolving, metal ions play a role of hydroxyl radical scavengers deactivating  $\bullet\text{OH}$  into inactive  $\text{OH}^-$  [82]. Therefore, less side reactions are involved in the system and more monomers available for grafting.

### 3.3 Grafting front mechanism

The first radiation-induced grafting of fluorinated polymer substrates had been reported in 1952 by Chapiro [58]. The author reported that styrene and methyl methacrylate (MMA) monomers could be grafted inside PTFE films using direct method at a low dose rate. Since PTFE substrates are not swelled in the monomer solution, the term *grafting front mechanism* was proposed. Afterwards, the concept of grafting front was shown by studying styrene or acrylic acid monomers onto PTFE or PVDF not only by direct method but also by pre-irradiation method [79, 83].

Monomer transport is made possible by swelling of the polymer substrate film and subsequent diffusion of monomer solution into the swollen zone. Grafting of monomer into the film proceeds by the grafting front mechanism [58, 84]. The graft polymerization occurs at the surface (eqs. 5.5 and 3.13), acting as the grafting front. The grafted layer swells in the monomer solution and polymerization continues in the swollen layer, resulting in chain growth. As a result of progressive diffusion of monomer through the swelling layer, the grafting front moves towards the middle of the film. A homogeneous distribution of the grafted copolymer across the film thickness can only be achieved when sufficient GY is obtained.

The grafting front mechanism was evidenced in PVDF electron-grafted with N-vinylpyrrolidone using differential interference contrast microscopy by Ellinghorst et al. [85]. This mechanism depends on various parameters among which the solubility properties of monomer and graft polymer. Ellinghorst et al. [86] also performed electron-grafting of PVDF with various monomers. In the case of AA, grafting-through could not be obtained in pure monomer at any temperature ranging from 50 °C to 80 °C. As the PAA is insoluble in its monomer, the grafted PAA layer hinders the diffusion of AA molecules to the inner part of the film. The absorbed dose used by Ellinghorst et al. was of 65 kGy which is about 3-fold less than the one used in Clochard et al. work [79]. Despite, Clochard et al. results are consistent with

Ellinghorst et al. as the grafting is localized on the PVDF surface in pure monomer where the mobility of the growing graft chains is substantially reduced by precipitation.

### 3.4 Radiation-induced grafting of PVDF

Essentially, the polymers used as substrates for RG have to meet certain requirements in order to produce efficient grafting with desirable and functional properties. These polymers have to possess an ability to easily generate stable free radicals upon exposure to ionizing radiation and high resistance towards radiolytic degradation [58]. Preferably, they are hydrophobic materials with high thermal, chemical and mechanical stability [87]. Both hydrocarbon (among them PE is frequently used) and fluorocarbon films have been used in RG technology. Compared to hydrocarbon, the fluorocarbon polymers have remarkable thermal and chemical stability [88]. These properties arise because the C–F bond is the strongest bond in organic chemistry. Due to their nucleophilicity, fluorine atoms can shield the carbon backbone of polymers from chemical attack. However, while the C–F bond is much stronger than the C–H bond, the G values for radical formation on high energy radiolysis of fluoropolymers are roughly comparable to those of their protonated counterparts.

The *G value* is the number of chemical changes induced by a deposited energy of 100 eV. For example, some typical G values for radical formation using  $\gamma$ -rays under vacuum at ambient temperature are: 0.14, PTFE [89]; 2.0, FEP [90]; 0.93, PFA [91]; 3.3, PVDF [92]. Besides the thermal and mechanical stability, these polymers have also shown the capability to produce highly stable radicals when exposed to irradiation [64]. Because of its resistance to irradiation and propensity to RG, PVDF was found to be a very good polymer substrate for fabrication of innovative membranes or nanoparticles leading in our laboratory to many applications [93–95].

#### 3.4.1 Nature of radicals

The exposure to ionizing irradiation results in formation of alkyl and peroxy radicals in polymer. There two types of irradiation used in this work: electron-beam and SHI. Regardless the type of irradiation, these radicals have identical nature. EPR spectroscopy is used for specification and quantification of the paramagnetic species. Signal amplitude (or integral intensity) increases with the increase of free radical content. At the resonance frequency and set magnetic field, g-value can be calculated. The g-value (also known as Landé g-factor) is used for identification of radical type. Figure 3.2 shows EPR spectra of  $\beta$ -PVDF films in air pre-irradiated by krypton ions (10 MeV/u) and electron-beam (absorbed dose of 50 kGy) under helium atmosphere. The EPR spectra of irradiated  $\beta$ -PVDF films show an overlap of characteristic signals of commonly occurring radicals in fluoropolymers [26, 31, 96]. As was depicted in chapter 1, there are various alkyl radicals formed in PVDF under irradiation, such as end-chain alkyls,  $-\text{CH}_2-\text{C}^\bullet\text{F}_2$  and  $-\text{CF}_2-\text{C}^\bullet\text{H}_2$ , in-chain alkyls,  $-\text{CH}_2-\text{C}^\bullet\text{F}-\text{CH}_2-$  and  $-\text{CF}_2-\text{C}^\bullet\text{H}-\text{CF}_2-$ , and corresponding peroxy radicals. The EPR parameters of identified

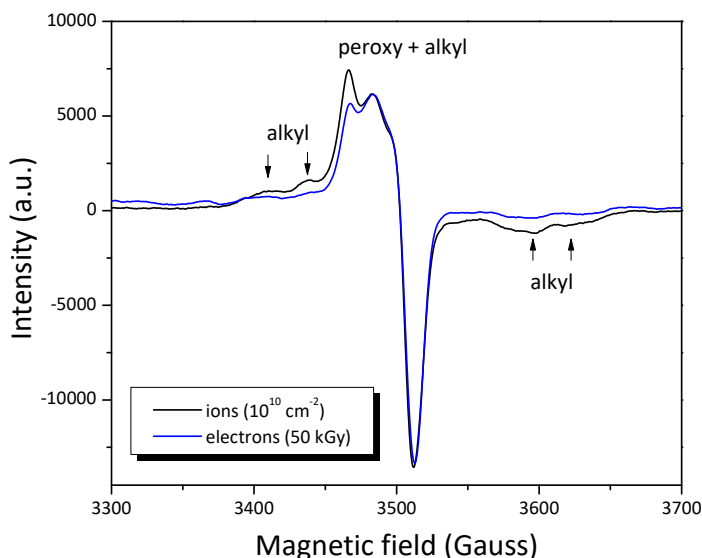


Figure 3.2: EPR spectra of  $9 \mu\text{m}$   $\beta$ -PVDF films irradiated by SHI of krypton (10 MeV/u), fluence of  $10^{10} \text{ cm}^{-2}$ , and electron-beam (50 kGy).

of irradiated  $\beta$ -PVDF films show an overlap of characteristic signals of commonly occurring radicals in fluoropolymers [26, 31, 96]. As was depicted in chapter 1, there are various alkyl radicals formed in PVDF under irradiation, such as end-chain alkyls,  $-\text{CH}_2-\text{C}^\bullet\text{F}_2$  and  $-\text{CF}_2-\text{C}^\bullet\text{H}_2$ , in-chain alkyls,  $-\text{CH}_2-\text{C}^\bullet\text{F}-\text{CH}_2-$  and  $-\text{CF}_2-\text{C}^\bullet\text{H}-\text{CF}_2-$ , and corresponding peroxy radicals. The EPR parameters of identified

radicals consistent with [32, 97, 98] are collected in Table 3.1. The irradiation conditions were: electron-beam irradiation at 1 MeV, dose of 1.25 MGy under vacuum. Peroxy radical species were subsequently formed when put in contact with air for EPR measurements.

As the pre-irradiation method of grafting was used in current work, precautions were made to ensure the absence of oxygen during irradiation and storage. After irradiation, however, the samples were exposed to air during transferring. As a result, some of alkyl radicals were converted into peroxy species.

Table 3.1: EPR spectral data for commonly observed radicals in irradiated PVDF.

Radical	$-\text{CH}_2-\text{CFOO}^\bullet-\text{CH}_2-$	$-\text{CF}_2-\text{C}^\bullet\text{H}-\text{CF}_2$	$-\text{CF}_2-\text{C}^\bullet\text{H}_2$
$g$ - value	$g_{\parallel} = 2.0327, g_{\perp} = 2.009$	$g_{iso} = 2.004$	$g_{iso} = 2.009$
$\Delta B_{pp}$ [Gauss]	$\Delta B_{pp}^{\parallel} = 20, \Delta B_{pp}^{\perp} = 18$	$\Delta B_{pp} = 33$	$\Delta B_{pp} = 12$
$A$ [Gauss]	-	$A_F = 43, A_H = 23$	$A_H = 16$

Aymes-Chodur et al. have shown that alkyl radicals are the major species that induce PS grafting in  $\gamma$ -irradiated PVDF [99]. The alkyl radicals were mainly attributed to in-chain  $-\text{CH}_2-\text{C}^\bullet\text{F}-\text{CH}_2-$  and end-chain  $-\text{CF}_2-\text{C}^\bullet\text{H}_2$  radicals. The crystalline fraction, remained in the polymer after SHI irradiation, significantly influences on radical trapping. At high dose, when the polymer is totally amorphous, no trapped radicals were observed [100]. At lower doses, the radicals formed after irradiation are trapped in zones of different mobilities (crosslinked zones, crystalline and amorphous regions, as well as interface of crystallites). The fact that alkyl radicals do exist under an air atmosphere indicates that they may be trapped in oxygen impermeable zones and consequently have less opportunities to react with monomer. Thus, depending on the zone, i) different times are needed for monomer to contact the radicals (different diffusion rates) and ii) some of the radicals may not be able to initiate grafting. Further works on PS grafting of SHI irradiated have shown that alkyl and peroxy radicals, initiating RG, are primarily located at the interface of crystallites and at the intra/intercrystalline amorphous zones of PVDF [99]. This assumption was confirmed by FESEM observation that revealed the grafted PS network essentially localized on the spherulite lamellae [101].

### 3.4.2 Difference between electron and ion irradiation

Despite the identical nature of radicals formed by ions and electrons, the distribution of energy deposition during irradiation is different. In the case of electron-beam, the energy is randomly deposited in polymer substrate and grafted copolymer chains are homogeneously distributed. Contrary, ions induce in their pathways continuous trails of excitations and ionizations leading to the formation of latent tracks. The deposited energy is highly localized along the ion trails, thus heterogeneous grafting occurs.

Small-angle X-ray scattering (SAXS) was used to investigate the location of PS grafting depending on type of irradiation in  $\alpha$ -PVDF [102]. It was found out that the grafting in  $\gamma$ -irradiated polymer takes place in the amorphous zone of while the grafting is located in the latent tracks after SHI irradiation. Betz [103] made a detailed study of ion track grafting of MMA and styrene in  $\alpha$ -PVDF. Following phenomenon was observed. When GY increases, the graft polymer spreads progressively around the track, destroying the crystalline structure in the bulk and covering the PVDF surface. Nevertheless, even at high GY, SHI-induced grafting remained more heterogeneous than  $\gamma$ -induced grafting.

Obtained GY in SHI irradiated PVDF depends on ion fluence. Absorbed dose and fluence are linked through equation 1.3 given in chapter 1. For example, for krypton irradiation that

has electronic stopping power of  $47.6 \text{ MeV} \cdot \text{cm}^2 \cdot \text{mg}^{-1}$  in PVDF, the fluence of  $10^9 \text{ cm}^{-2}$  is equivalent to the dose of 7.6 kGy. As the number of radicals is proportional to the dose [101], a way to increase the radical content is to increase the fluence. It has to be noted that at high ion fluences (greater than  $10^{10} \text{ cm}^{-2}$ ), overlapping of tracks takes place. It results in more homogeneous distribution of damages. Furthermore, high ion fluences promote degradation of PVDF films as a result of dehydrofluorination. As the purpose of this work is to exploit the SHI heterogeneity properties in PVDF films by creating track-etched membranes, we will limit the ion fluence to  $10^{10} \text{ cm}^{-2}$ .

### 3.5 Grafting inside track-etched PVDF

Due to a high value of LET during SHI irradiation, narrow cylindrical damaged regions are formed inside irradiated polymer (*latent tracks*, figure 3.3). The latent tracks are revealed by selective ion track etching (as described in chapter 2) in a highly oxidizing solution of KOH and  $\text{KMnO}_4$ . The etching process does not remove all the radicals. Due to the semi-crystalline structure of  $\beta$ -PVDF of about 40%, there is still a considerable amount of radicals trapped in the crystallites, and at the interfaces between the crystalline and amorphous regions. These radicals are capable to initiate grafting reaction in presence of vinyl monomer. Mazzei et al. performed grafting of PS inside track-etched  $\beta$ -PVDF by means of  $^{208}\text{Pb}$  (25.62 MeV/u) and  $^{35}\text{Cl}$  (115 MeV) irradiation [104]. It was the first report where the SHI active sites remained after chemical etching were assumed to graft styrene without using any supplementary irradiation source such as  $\gamma$ -rays or electron-beam. Likewise, PAA was grafted in the track-etched  $\beta$ -PVDF and optimal RG parameters have been determined [57, 105].

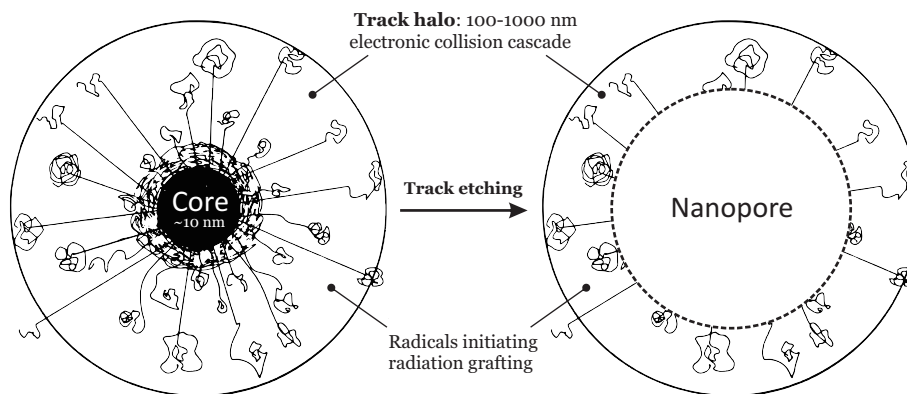


Figure 3.3: Schematic image of SHI irradiated polymer film before and after track etching.

Then, Cuscito et al. [57] proved, for the first time, that PAA grafting location is inside the nanopores and does not spread out to the bulk by confocal laser scanning microscopy (CLSM) and double labelling, confirming previous assumption. For CLSM two different fluorescent markers have been used: Alexa Fluor 488 hydrazide and fluorescein isothiocyanate. As was mentioned in chapter 2, chemical etching results in the formation of oxidated species, particularly carboxyl groups. Therefore, in track-etched and grafted PVDF there are carboxyl groups coming from PVDF surface oxidation and grafted PAA chains. To discriminate these two groups, before PAA grafting, carboxyl groups present in the track-etched PVDF were modified with ethylenediamine ( $\text{NH}_2\text{-CH}_2\text{-CH}_2\text{-NH}_2$ ) in presence of carbodiimide in accordance with the scheme in figure 3.4 to form primary amine groups. The track-etched membrane was then grafted with PAA by use of residual after chemical etching radicals. To visualize both chemical groups, the fluorescein isothiocyanate (FITC) and the Alexa Fluor hydrazide 488 were used to label amine groups of earlier modified PVDF (figure 3.5a) and carboxyl groups of grafted PAA chains (figure 3.5b) respectively.

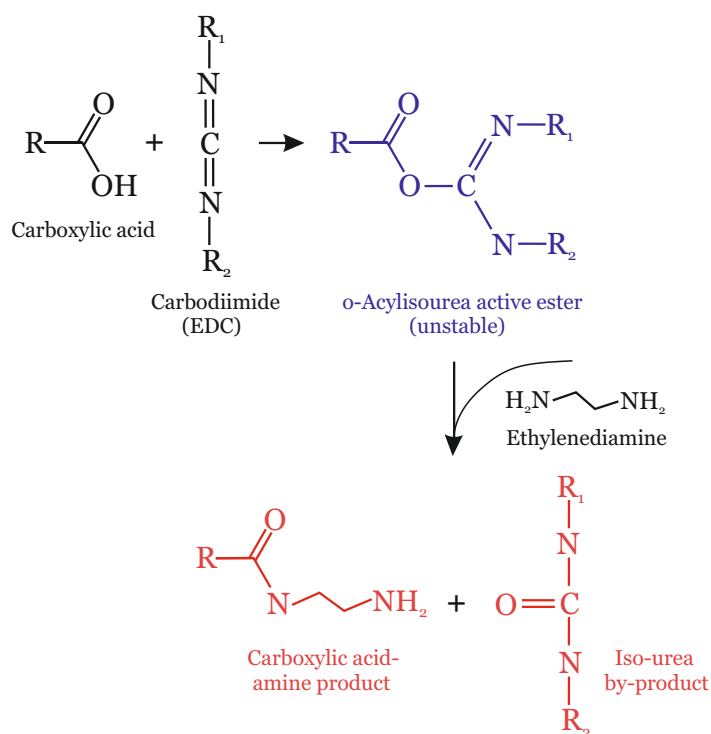
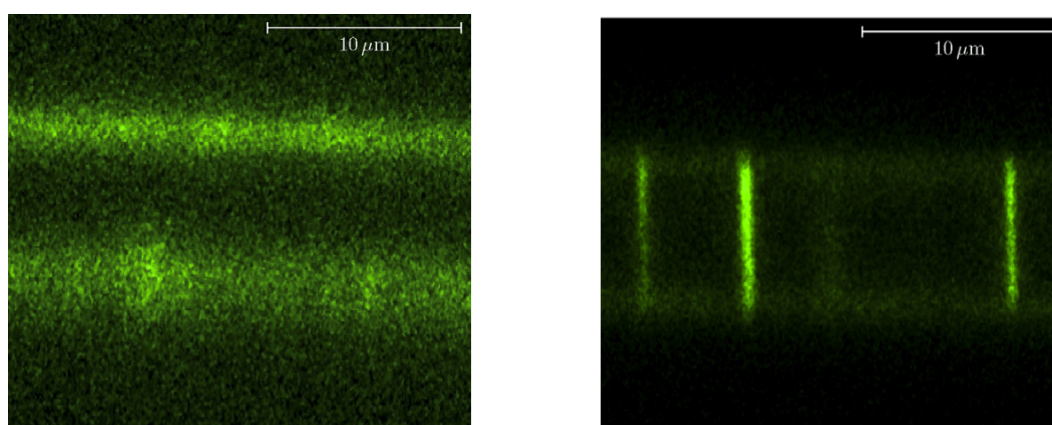


Figure 3.4: Scheme of PAA coupling with ethylenediamine.



(a) Fluorescein isothiocyanate (FITC) labeling reveals amine groups, i.e. surface oxydation.

(b) Alexa Fluor 488 hydrazide labeling reveals carboxyl group, i.e. PAA.

Figure 3.5: CLSM images of labeled PAA-g-PVDF membrane [57].

The presence of continuous fluorescence throughout the entire thickness of the membrane (figure 3.5b) indicates that the grafting is performed homogeneously inside track-etched PVDF. It also shows that the carboxyl groups of PAA remain chemically accessible and do not seem to be hindered by confined environment of the nanopores. This result emphasizes that radical polymerization of AA monomer is initiated from the residual radicals present in the pore walls. The PAA grafting did not diffuse inside the PVDF polymer bulk as the grafting conditions were tuned to keep a surface grafting process. Eight years later, the same group, succeeded to exploit even deeper this remarkable property of  $\beta$ -PVDF track-etched membranes to tune nanopore size of PAA grafted membranes using RAFT-mediated controlled radical polymerization [106].

# Chapter 4

## Electrochemical analysis

### 4.1 Voltammetric methods

#### 4.1.1 Introduction

Voltammetric techniques are based on application of a time-dependent potential to an electrochemical cell and measure the resulting current as a function of that potential. The resulting plot of current *versus* applied potential is called a *voltammogram*. It provides quantitative and qualitative information about the species involved in the oxidation or reduction reactions. The earliest voltammetric technique is polarography, developed by Jaroslav Heyrovský in 1922. Since then, many different forms of voltammetry have been developed, a few of which are highlighted in figure 4.1.

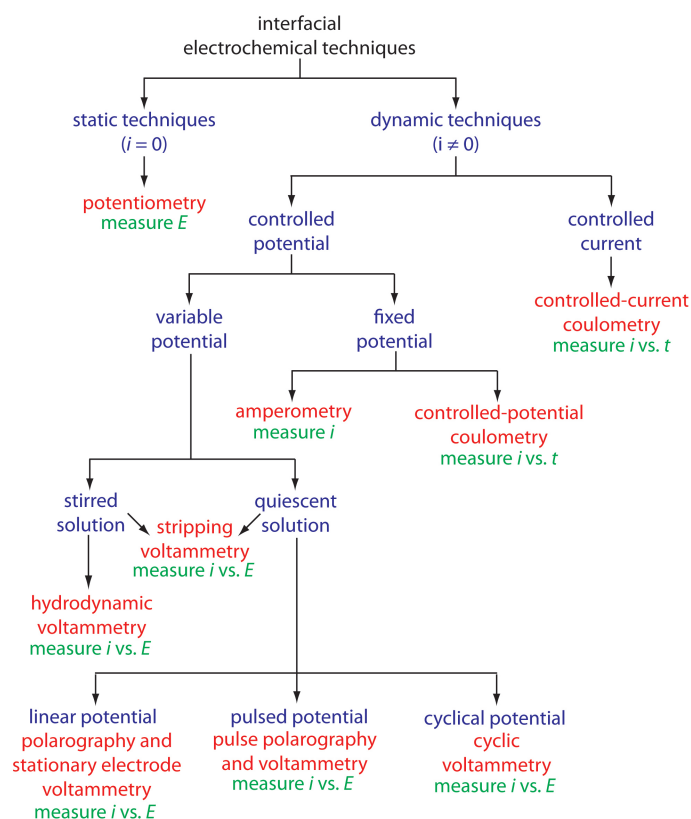


Figure 4.1: Scheme of various electrochemical techniques depending on the fixed variable.

Two dynamic voltammetric techniques have been used in current work: cyclic voltammetry and stripping voltammetry. In order to have a better understanding of basic electrochemical processes and terms, the following sections on electrochemical cell composition, double

electrical layer phenomenon and electrode reactions taking place during voltammetry analysis will be shortly presented first. Cyclic voltammetry based on linear sweep voltammetry following the stripping voltammetry will be described next.

#### 4.1.1.1 Electrochemical cell

Most common configuration for running dynamic electrochemical experiments involves the use of three-electrode cell consisting of a *working*, a *counter* (auxiliary) and a *reference* electrodes, all connected to a potentiostat (figure 4.2). The time-dependent potential signal is applied to the working electrode (WE), changing its potential relative to the fixed potential of the reference electrode (RE) and measure the current that flows between the WE and the counter electrode (CE). If, for example, oxidation reaction occurs at the surface of the WE, reduction with the same magnitude of current is sustained at the CE, hence there is no net current flow between WE and CE enabling to follow the changes in WE potential accurately. Potentiostat in this scheme is used for maintaining constant potential at the WE *versus* the RE and measuring the current between WE and CE.

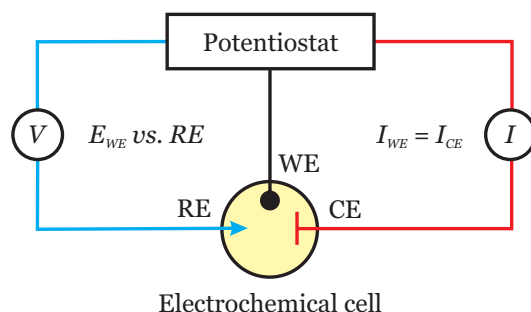


Figure 4.2: Scheme of a three-electrode cell and potentiostat. The potential of the working electrode (WE) is measured with respect to the reference electrode (RE). The input of the RE has a high-impedance forcing all current to flow through the counter electrode (CE).

The CE is typically a platinum or gold wire that provides a surface for a Ox/Red reaction to balance the one occurring at the surface of the WE. To support the current generated at the WE, the surface area of the CE must be equal to, or larger than, that of the WE. The reference electrode is usually a saturated calomel electrode (SCE) or a silver chloride electrode (Ag/AgCl) possessing a known and stable potential. The WE is the most important component of an electrochemical cell because at its interface the electron transfer of interest occurs. First, the WE must be a good conductor as it acts as a source or sink of electrons for exchange with analyte species in the interfacial region. Second, it must also be electrochemically inert (*i.e.*, does not generate a current in response to an applied potential) over a wide potential window. Commonly used WEs in voltammetry include platinum, gold, mercury, and glassy carbon. The choice of material depends upon the potential window required (*e.g.*, mercury can only be used for negative potentials, due to its oxidation at more positive potentials), as well as the rate of electron transfer (slow electron transfer kinetics can affect the reversibility of Ox/Red behavior of the system under study). The rate of electron transfer can vary considerably from one material to another, even for the same analyte, due to, for example, catalytic interactions between the analyte and active species on the electrode surface.

Mercury has historically been widely used as electrode material in polarography primarily as dropping mercury electrode (DME). In a classical DME, mercury flows through the capillary by gravity and a drop grows until its weight exceeds the surface tension force holding it to the capillary. The hanging DME (with controlled drop lifetime) has been considered as the best working electrode in voltammetry for a long time because of its extremely reproducible surface, amalgamation with most heavy metals and low capacitance [107]. However, its toxicity has led to a limited use. Therefore, there is a tendency to replace mercury-based electrodes

with sensitive but non-toxic ones.

Solid electrodes made of platinum, gold, silver, or carbon can replace mercury-based electrodes for many voltammetric analyses. They are widely used primarily because of their broad potential range and low background currents [108]. Even though their use is mainly limited by the surface oxidation and memory effects, they are extensively utilized in environmental and pharmaceutical applications.

#### 4.1.1.2 Electrical Double Layer

Electrochemical processes take place at the electrode/electrolyte interface. At the interface, the properties of the two neighboring phases differ significantly from those of the bulk. The processes at the interface are of central interest and depend on the potential drop across the interface.

In general, the metal surface carries an excess of charge, which is compensated by ions of opposite charge from the electrolyte. This means that there is an excess or lack of electrons on the electrode surface and an excess of either cations or anions in the solution in the vicinity of the electrode surface. This can be viewed as a capacitor. The charge in the electrode resides in a surface region about 1 Å thick. In the solution, the charge carrier concentration is lower than in a piece of metal. Thus, the charge in the solution extends over a larger region, typically 5-20 Å thick. The resulting charge distribution (two narrow regions of equal and opposite charge) is known as the *electrical double layer* (EDL) and is a central issue in electrochemistry.

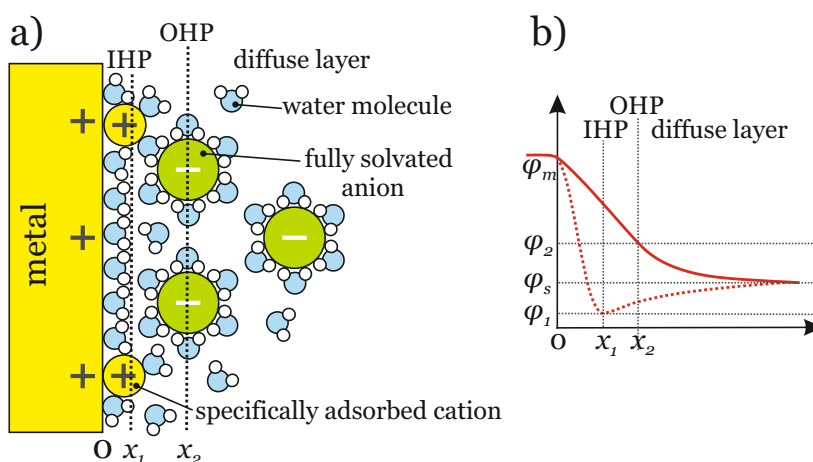


Figure 4.3: (a) Model of the metal/electrolyte interface (IHP: inner Helmholtz plane; OHP: outer Helmholtz plane). (b) Potential distribution across the electrical double layer for nonspecifically adsorbed anions (solid line) and specifically adsorbed anions (dotted line) [109].

Figure 4.3 a schematically shows the structure and the potential distribution of the metal/electrolyte interface for the case of a positively charged metal surface. The layer closest to the surface consists of ions that have partially lost their solvation shell and are in contact with the surface. They are held in place by chemical interactions with the surface and are referred to as *specifically adsorbed*. They form the inner Helmholtz plane (IHP) at a distance  $x_1$ . Anions usually have a weak solvation shell and can adsorb specifically. Most cations and some anions have a stronger solvation shell, which they retain upon adsorption. Solvated ions can approach the surface only to a distance  $x_2$ . Their interaction with the surface is purely electrostatic, thus essentially independent of the chemical properties of the ions. They are called *nonspecifically adsorbed* and form the outer Helmholtz plane (OHP) at  $x_2$ . From the OHP the diffuse layer extends into the bulk of the solution. In this three-dimensional region the nonspecifically adsorbed ions are distributed by an interplay of electrostatic interactions

and thermal motion. The thickness of the diffuse layer depends on the ionic strength of the solution and the applied potential to the electrode.

The potential profile across the double-layer region is shown in Figure 4.3 b in the absence (solid line) and presence (dotted line) of specific adsorbing ions. For only nonspecifically adsorbing ions the potential drop between the metal surface and the OHP is generally assumed to be linear, as for a plate capacitor. This potential does not drop completely to the solution value  $\varphi_S$ , but only to some residual value  $\varphi_2$ . Across the diffuse layer the potential drops in an almost exponential form to  $\varphi_S$ . In the case of specifically adsorbed ions more charge is accumulated at the surface than required by electrostatics. This overcharging leads to a steeper potential gradient and the potential at the IHP  $\varphi_1$  drops below the solution value. For charge compensation countercharge is brought into the double layer.

#### 4.1.1.3 Electrode reactions

There are several different processes can happen at electrode surface at once [110]. Among them adsorption/desorption and the formation of the EDL are processes where no charge is transferred across the metal/electrolyte interface and are called *nonfaradaic* processes. Even though no charge crosses the interface, external currents can flow, when the potential or solution composition changes. Processes where charges are transferred across the metal/electrolyte interface are called *faradaic* processes. The electron transfer causes oxidation or reduction to occur, which are reactions governed by Faraday's law. Thus, the flowing current is directly proportional to the concentration of electroactive species in the solution. The electrode potential allows the control of the rate and the direction of the interfacial electron transfer. Figure 4.4 summarises all the processes occurring at the surface of WE.

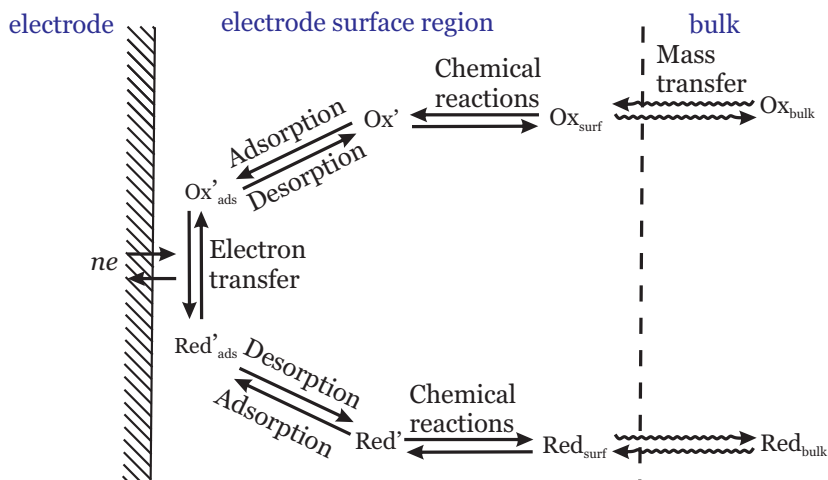


Figure 4.4: General electrode reaction pathway.

The potentials at which electron transfer occurs are related to the standard potentials  $E^0$  of the specific chemical species in the system. The electrode potential under standard conditions of a given half-reaction:



is called the *standard potential* of the Ox/Red couple,  $E^0_{Ox/Red}$  (where  $n$  is the number of transferred electrons). By convention these electrode potentials are referred to the normal hydrogen electrode, which has by definition an electrode potential of zero.

The Nernst equation describes the dependence of the equilibrium potential  $E_{eq}$  of the Ox/Red electrode reaction on the thermodynamic activities  $a_i$  of the components:

$$E_{eq} = E^0_{Ox/Red} + \frac{RT}{nF} \ln \frac{a_{Ox}}{a_{Red}} \quad (4.2)$$

with the universal gas constant  $R$ , the temperature  $T$  and the Faraday constant  $F$ .

For practical reasons the thermodynamic activities can be replaced by concentrations  $c_i$  and eq. 4.2 transforms to give

$$E_{eq} = E_{Ox/Red}^{0'} + \frac{RT}{nF} \ln \frac{c_{Ox}}{c_{Red}} \quad (4.3)$$

where  $E_{Ox/Red}^{0'}$  is the experimentally determined formal potential and can be described with activity coefficients  $\gamma_i$  as

$$E_{Ox/Red}^{0'} = E_{Ox/Red}^0 + \frac{RT}{nF} \ln \frac{\gamma_{Ox}}{\gamma_{Red}} \quad (4.4)$$

where  $E_{Ox/Red}^0$  is the standard electrode potential, the activity is defined through  $a_i = \gamma_i \times c_i$ . The  $E_{Ox/Red}^{0'}$  varies from medium to medium, because the ionic strength affects the activity coefficients.

In most cases, electrode reactions are multistage processes and the electron transfer is only one step in the mechanism. Other steps, like mass transfer and chemical reactions, which precede or follow the electron transfer, influence the electrode reaction as well. The overall rate of a reaction (the current through the electrode) depends on the rate constants of these processes. The rate constants of some processes (*e.g.*, electron transfer at the electrode surface) depend on the applied potential.

#### 4.1.2 Linear sweep voltammetry and cyclic voltammetry

Linear sweep voltammetry (LSV) and cyclic voltammetry (CV) are the most commonly used potential sweep techniques. In both LSV and CV the potential is varied with a constant *scan*

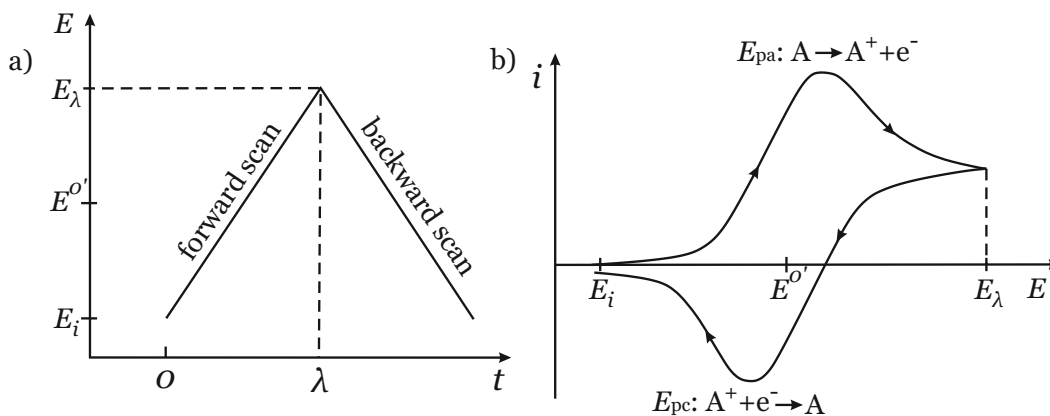


Figure 4.5: Cyclic voltammetry of a simple electron transfer reaction, where  $A$  species in solution are oxidized to  $A^+$  and subsequently reduced back to  $A$ . (a) Single potential scan and (b) resulting cyclic voltammogram.

rate  $v = \frac{dE}{dt}$  (typically between  $1 \text{ mV} \cdot \text{s}^{-1}$  and  $1 \text{ V} \cdot \text{s}^{-1}$  [111, 112]) and the resulting current  $i$  is recorded as a function of the potential  $E$ . In LSV, the explored potential region is scanned from the initial potential  $E_i$  to the final potential  $E_f (= E_\lambda)$ . CV however, is an extension of LSV since the direction of the potential scan is reversed at the end of the scan, which then becomes the switching potential  $E_\lambda$  (figure 4.5a).

Figure 4.5b shows the CV of a Ox/Red species  $A$  in solution. The starting potential is negative of  $E^{0'}$ , the formal potential of the  $A^+/A$  couple. During scanning the potential towards more positive values, first only a nonfaradaic current flows. When the electrode potential  $E$  approaches  $E^{0'}$ , oxidation of  $A$  starts and a faradaic current begins to flow ( $A \rightarrow A^+ + e^-$ ). The resulting concentration gradient leads to depletion resulting in diffusion of  $A$  from the bulk towards the surface. As the potential continues to become more positive, the surface

concentration of A drops resulting in the flux increase to the surface. As the potential passes  $E^{0'}$  the surface concentration of A drops nearly to zero and mass transfer of A to the surface reaches a maximum rate. The continued flux of A leads to an expansion of the depletion zone. Thus, the slope of the concentration profile at the surface declines and the current decreases. The result is a peak in the voltammogram  $E_{pa}$ . After reaching the return potential  $E_{\lambda}$  the sweeping direction is reversed. Now, in the vicinity of the electrode, is a large concentration of the generated  $A^+$ . During this backward scan of the potential, the electrochemical balance at the surface becomes more and more favorable toward the neutral A species. The  $A^+$  is reduced and a cathodic current flows ( $A^+ + e^- \rightarrow A$ ). Again a peak  $E_{pc}$  is observed, essentially for the same reasons.

In this context,  $E_{pa}$  and  $E_{pc}$  correspond to the anodic and cathodic potential peaks, respectively. The formal electrode potential  $E^{0'}$  for a reversible couple can be readily estimated using eq. 4.5.

$$E^{0'} = \frac{1}{2}(E_{pa} + E_{pc}) \quad (4.5)$$

The separation between the peak potentials is given by

$$\Delta E_p = E_{pa} - E_{pc} = \frac{0.059}{n} \text{ V} \quad (4.6)$$

Thus, the peak separation can be used to determine the number of electrons transferred, and as a criterion for a Nernstian behavior. Accordingly, a fast one-electron transfer process exhibits a  $\Delta E_p$  of about 59 mV. Both the cathodic and anodic peak potentials are independent of the scan rate.

We must always remember that current response in voltammetry is composed of two different currents

$$I = I_F + I_c = I_F + v \times C_d \quad (4.7)$$

while  $I_c \propto v$  (the interfacial capacitance  $C_d$  is the proportionality constant),  $I_F \propto C_s v^{1/2}$ , where  $C_s$  corresponds to the concentration of the electroactive species in electrolyte.

First one corresponds to a flow resulting from the electron transfer process (faradaic current  $I_F$ ). The magnitude of the faradaic current depends of the analyte concentration in solution and all kinetic steps occurring on the electrode. Another current is generated due to formation of the electrical double layer (see section 4.1.1.2), that produces the capacitive current  $I_c$ . It is not related to the electron transfer process, contributing in most cases only to background signals in the measurement. The capacitive current can be significantly higher than the faradaic one, when the concentration of analyte is very low (*e.g.*,  $\mu\text{M}$  bulk concentration). Thus, the capacitive current is the limiting factor in terms of the sensitivity of voltammetry in general.

In order to separate the capacitive current from the faradic, microelectrodes and/or step potential techniques (*e.g.*, pulse techniques, see 4.1.3) can be used. In practice in LSV or CV, the capacitive contribution in eq. 4.7 is eliminated by subtraction of the blank response (electrolyte without analyte species). In this way, detection limits are around  $10^{-5}$  M [113]. Trace analysis concerns with concentrations lower than  $10^{-8}$  M.

### 4.1.3 Square-wave voltammetry

There are variety of pulse techniques have been developed as ways to diminish the contribution of the capacitive current and as a consequence to ensure the lowering of the detection limits. This can be achieved by replacing the continuous potential scan (figure 4.5 a) with a stair-like potential waveform as a function of time. Measuring the current at the end of each

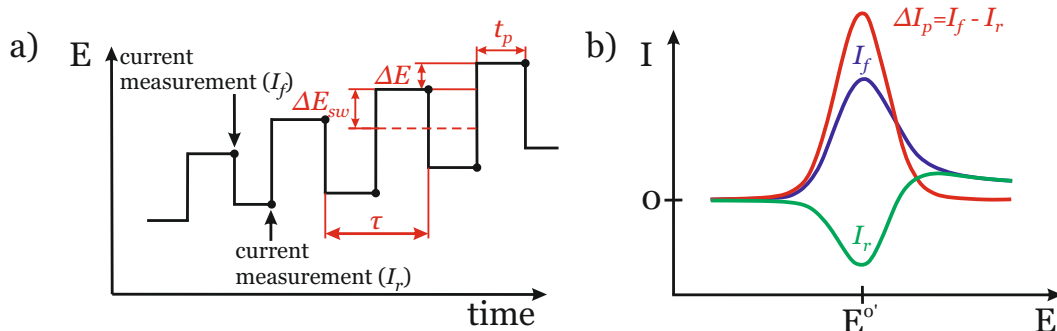


Figure 4.6: a) Potential wave-form of SWV and b) the resulting net peak current. Figures are extracted from [114].

potential diminishes the capacitive current contribution significantly, thus profoundly improving the sensitivity and quality of the voltammetric data. Pulse voltammetry techniques include normal-pulse voltammetry (NPV), differential-pulse voltammetry (DPV), staircase voltammetry (SV), and square-wave voltammetry (SWV). This section only involves one of them, which has been used for all voltammetric measurements in current work, it is *square-wave voltammetry*.

SWV is a large-amplitude differential technique in which a wave-form composed of a symmetrical square wave, superimposed on a base staircase potential, is applied to the WE (figure 4.6a). To understand the overall potential modulation, let us consider the potential variation during a single potential step. Indeed, at each potential step, two small, oppositely oriented potential pulses are imposed. The duration of the two pulses is identical, designated as  $t_p = \frac{\tau}{2}$ , where  $\tau$  is the duration of the potential step. The height of a single pulse is termed as square-wave amplitude ( $E_{sw}$ ). Thus, the main parameters of the SW potential modulation are the step height  $\Delta E$ , the SW amplitude ( $E_{sw}$ ) and the duration of the potential pulse  $t_p$ . Often, the later parameter is expressed in terms of the SW frequency  $f = \frac{1}{2t_p}$ . One of the advantages of SWV is its speed. The effective scan rate is given by  $v = f\Delta E$ . Frequencies of 1 to 100 cycles per second permit the use of extremely fast potential scan rates. For example, if  $\Delta E = 10$  mV and  $f = 50$  Hz, then the effective scan rate is  $0.5 \text{ V} \cdot \text{s}^{-1}$ . As a result, the analysis time is drastically reduced; a complete voltammogram can be recorded within a few seconds, as compared with about 2-3 minutes in DPV.

For the sake of improved sensitivity the current is measured at the end of each potential pulse only (figure 4.6a). The series of current values measured at the end of each forward and reverse pulse constitute the forward ( $I_f$ ) and reverse components ( $I_r$ ) of the SW voltammetric response, respectively (figure 4.6b). Obviously, at each potential step two current values are measured. Moreover, another voltammetric curve can be constructed by subtracting the corresponding values of the forward and reverse current values, termed as *net current*,  $\Delta I_p = I_f - I_r$ .

The peak-like shape of the net current in SWV is advantageous in analytical context as it provides readily measurable parameters peak height and peak position, thus improving the resolution of the technique. The intensity of the  $\Delta I_p$  is higher compared to the forward and backward components, which is another important feature. Finally, the contribution of the charging current to the net current may be even less significant than in particular forward and reverse components, for most cases. The reason is that the charging current measured at the end of the pulse is generally small. When small amplitudes are used ( $nE_{sw} \leq 50$  mV;  $n$  is the stoichiometric number of electrons), the small charging current at two neighbouring pulses is identical in the sign and vary close in the magnitude. Thus, the subtraction procedure in calculating  $\Delta I_p$  diminishes further contribution of the charging current, making SWV one of

the most sensitive voltammetric techniques [115–118].

#### 4.1.4 Stripping voltammetry

Stripping analysis is an extremely sensitive electrochemical technique for measuring trace metals, the limit of detection (LOD) is about  $10^{-11}$  M or sub-parts per billion, ppb [119, 120]. Its remarkable sensitivity is attributed to the combination of an effective preconcentration step with advanced measurement procedures that generate an extremely favourable signal-to-background ratio.

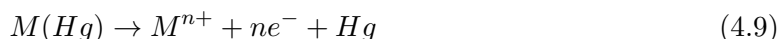
Essentially, stripping analysis is a two-step technique. In case if mercury electrode is used, the analysis may be described as follows. The first step, *deposition*, involves the electrolytic deposition of a small portion of the metal ions in solution into the mercury electrode to preconcentrate the metals. This is followed by the *stripping step*, which involves the dissolution (stripping) of the deposit. Different versions of stripping voltammetry can be employed, depending upon the nature of the deposit and measurement steps.

*Anodic Stripping Voltammetry* (ASV) is the most widely used form of stripping analysis. In this case, the metals are preconcentrated by electrodeposition into a small-volume mercury electrode (a thin mercury film or a hanging mercury drop). The preconcentration is done by cathodic deposition at a controlled time and potential. The deposition potential is usually 0.3–0.5 V more negative than  $E^0$  for the least easily reduced metal ion to be determined. The metal ions reach the mercury electrode by diffusion and convection, where they are reduced and concentrated as amalgams:



The convective transport is achieved by electrode rotation or stirring of the solution. The rotating disc electrode (RDE) is the classical hydrodynamic electroanalytical technique used to limit the diffusion layer thickness and therefore allowing the study of the steady-state electrode reaction kinetics [121]. The RDE includes a conductive disk (*e.g.* of Pt, Au, glassy carbon, graphite, *etc.*) embedded into an inert insulating material (*e.g.*, Teflon). When the electrode is rotating, the solution will run from the bulk to the surface, and then be flushed out along the direction parallel to the disk surface. Quiescent solutions however can be used when using mercury ultramicroelectrodes. The duration of the deposition step is selected according to the concentration of the metal ions in question, from less than 0.5 min at the  $10^{-7}$  M to about 20 min at the  $10^{-10}$  M [115].

Following the preselected time of the deposition, the forced convection is stopped, and the potential is scanned anodically, either linearly or in a more sensitive potential wave-form that discriminates against the capacitive background current (square-wave or differential-pulse ramps). During this anodic scan, the amalgamated metals are re-oxidized, stripped out of the electrode (in an order that is a function of each metal standard potential), and a current flows:



The potential-time sequence used in ASV, along with the resulting stripping voltammogram, is shown in figure 4.7. The voltammetric peak reflects the time-dependent concentration gradient of the metal in the mercury electrode during the potential scan. Peak potentials serve to identify the metals in the sample. The peak current depends on various parameters of the deposition and stripping steps, as well as on the characteristics of the metal ion and the electrode geometry.

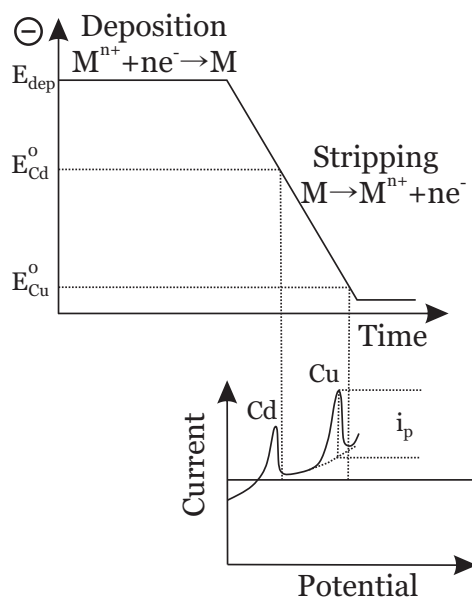
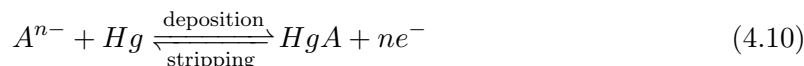
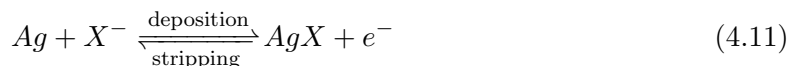


Figure 4.7: ASV: the potential-time wave-form (top) along with the resulting voltammogram (bottom).

*Cathodic stripping voltammetry* (CSV) is the “mirror image” of ASV. It involves anodic deposition of the analyte, followed by stripping in a negative-going potential scan:



CSV is used to measure a wide range of organic and inorganic compounds capable of forming insoluble salts with mercury. Among these are various thiols, as well as halide ions, cyanide, and sulfide. Anions (*e.g.*, halides) that form insoluble silver salts can be measured at a rotating silver disk electrode. In this case, the deposition and stripping steps involve the reaction:



where  $X = Cl^{-}, Br^{-}$ . Copper-based electrodes can also be employed for the same task.

Shortly, *adsorptive stripping voltammetry* (AdSV) is based on the accumulated adsorption of a complex between the analyte and a complexing agent at the electrode surface, often at an applied potential chosen so as to help the adsorption process. Either the metal ion or the ligand can be measured in the presence of an excess of the other component in bulk solution. Usually, the determination step involves reduction of the metal ion from the adsorbed complex.

## 4.2 Application of stripping voltammetry for metal analysis

In current work, gold was used as electrode material for the analysis of mercury and uranium. Thus, literature review will be given in two separate subsections with respect to the electrode material and technique chosen (excluding all mercury-based electrodes).

### 4.2.1 Mercury

Different types of gold electrodes have been used for the determination of mercury(II). Solid gold electrodes [122] are less commonly used than fiber gold [123] and plated gold electrodes [124, 125]. The main disadvantages of solid gold electrodes are well-known phenomenon

of structural changes caused by amalgam formation and complex electrochemical pretreatments that are needed to achieve reproducibility [125]. The former, however, only applies when bulk deposition of mercury takes place [126]. There is a great difference in the behavior of the gold electrode when bulk deposition and when ASV are concerned. When ASV is applied, the fractional surface coverage during the deposition step is typically less than 1% [127–129]. Under such experimental conditions some metal ions form a uniform adlayer, a process referred to as underpotential deposition (UPD) [130]. The phenomenon of the UPD refers to the deposition of metals on foreign metal substrates at potentials that are more positive than the potential of reduction ( $E_{\text{upd}} > E_{\text{Red}}^0$ ) because of the strong interactions between the deposited metal and the substrate surface structure [131]. In the UPD region, the metal is deposited as a monolayer on the substrate through self-limiting deposition [132]. Thus, during repetitive deposition and dissolution of mercury on gold electrode (as is the case when ASV is applied under typical conditions of concentrations below  $10^{-7}$  M and relatively short deposition times, or by deposition from higher concentrations of mercury in the UPD region), excellent reproducibility is reached starting from the first run. This indicates that there are no structural changes under mentioned conditions. The absence of structural changes has also been demonstrated by Inukai et al. [126], by applying *in situ* scanning tunneling microscopy and cycling the electrode in the potential region in which a UPD layer is formed.

Indeed, Bonfil et al. [133] reported determination of mercury(II) on a rotating gold disk electrode and marked excellent electrode stability. No structural changes on the gold electrode were observed for moderate mercury(II) concentrations, as opposed to electrochemical measurements performed at high concentrations of mercury(II), where amalgamation caused profound changes. Different variations of gold-based electrodes using ASV for mercury(II) analysis were reported in literature. Among them, for example, gold nanoparticle-modified glassy carbon electrode [134] and screen-printed electrode modified with gold film [135]. Many electrochemical strategies are based on the modification of the working electrode surface by chemicals reagents, such as monomolecular ligands [136, 137] or functional polymers [138, 139]. The actual trend is the nanostructuring of electrodes for both diminishing the limit of detection (LOD) and enhancing their robustness. Zinoubi et al. [140] reported the development of a modified glassy carbon electrode with nanocellulosic fibers for trace heavy metal ions determination using DP-ASV. Carbon cloth composite electrode modified with gold nanoparticles was prepared by a facile *in situ* electrodeposition method and applied to the continuous detection of mercury ions in water by Guan et al. [141]. The most recently reported sensitive sensors made up of three-dimensional gold nanoelectrode ensembles, prepared by gold deposition inside the parallel pores of a porous template, had been successfully applied in electrochemical determination of mercury(II) by Bahari et al. [142].

### 4.2.2 Uranium

Over the past few decades, many studies have been focused on the coordination chemistry of uranyl ion both for extracting and determination of the toxic analyte in different environments. Trace levels of uranium can be determined and quantified by stripping voltammetry mainly with modified gold electrodes. Becker et al. [143] developed a new type of calix[6]arene modified gold electrode showing a high selectivity towards uranyl ions. Before examining the effect of the surface modification however, a series of SWV were recorded and the LOD for dissolved uranyl was found to be equal to  $10^{-6}$  M (1 ppm). Five years ago, Peled et al. [144] reported the determination of uranyl using gold microelectrodes by ASV, the LOD was found to be  $10^{-9}$  M.

Even though AdSV is the most common electrochemical technique for determination of low concentrations of uranyl in aqueous media [119] and a great number of articles concern with AdSV of uranium [145], electrochemical sensors based on chemically modified electrodes with high affinity toward uranyl ions are considered to be favoured in terms of robustness and re-

sponse time. Since the modification process of the electrode surface is carried out before the interaction with uranyl is taking place, the main challenge for researchers is to find an agent that can be efficiently bound to the electrode surface, and, at the same time, can interact rapidly with the uranyl ions, assuring fast detection.

Recent electrode modification approaches include ion imprinted polymers with specific binding sites for uranyl [146] and selective host molecules such as calixarenes, bound to the electrode surface [147, 148]. Phosphate-based uranyl selective electrodes, *i.e.*, chemically modified electrodes with phosphate (or phosphine) derivatives terminal groups, are likely to serve as more adequate on-site rapid detection tools for uranium. The known properties of phosphates to form fast and stable complexes with uranyl [149] has driven researchers to develop a uranyl sensor based on organophosphorus compounds which are usually anchored to the electrode surface through an aliphatic residue.

Since the important work by Manning et al. [150], who studied the function of several organophosphorus compounds bound to a poly(vinyl chloride)(PVC) matrix as uranyl sensors, many groups have dealt with the attempts to design a phosphate-based uranyl selective electrode, by different approaches. Notable studies were published by Goldberg and Meyerstein [151], who applied phosphite ligands as uranyl complexing agents bound to PVC based electrode, Chang et al. [152] who introduced tri-n-octylphosphine oxide based electrodes, and Slater et al. [153] who have employed organo-phosphorus based electrodes to form bis(di[4-(1,1,3,3-tetramethylbutyl)phenyl] phosphate) salts with uranyl ions. All these results have lead to work of Becker et al. [154], demonstrating  $\mu\text{M}$  analysis of uranyl by a phosphate-based self-assembled monolayer on gold electrode by means of SWV.



## Part II

# Results and discussion



# Preface

Part II of the thesis reports on acquired results and discussion. Some of the results related to mercury(II) and uranium(VI) detection were recently published in the journals of Hazardous Materials (2019) [155] and Reactive&Functional Polymers (2019) [156], will be joined in appendix. The results on time-resolved photoluminescence measurements for trace uranyl detection by PB2MP grafted track-etched PVDF membranes, provided in chapter 8, are for the forthcoming publication.



## Chapter 5

# Fabrication of functionalised track-etched PVDF membrane-electrodes

This chapter reports on the fabrication procedure of functionalised PVDF track-etched membrane-electrodes synthesized for toxic metal preconcentration. The synthesis was a multi-step process adapted and optimized for each functional copolymer to be grafted. Each section will give a description of the particular step. Overall fabrication procedure is shown in figure 5.1. First, 9  $\mu\text{m}$  thick PVDF films are irradiated with SHI resulting in latent track formation. Following the chemical etching, the obtained track-etched PVDF membrane is copolymer grafted onto etched track walls through the remained trapped radicals.

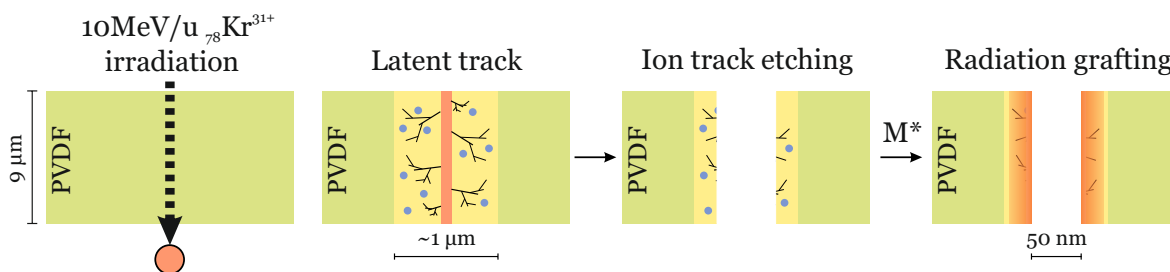


Figure 5.1: Scheme of fabrication procedure of functionalised track-etched PVDF membranes.

### 5.1 Irradiation

Swift-heavy ion (SHI) irradiation was performed at GANIL, France.  $\beta$ -PVDF 9  $\mu\text{m}$  thick PVDF films were irradiated at room temperature with  ${}_{136}\text{Xe}^{48+}$  or  ${}_{78}\text{Kr}^{31+}$  at energies of 7.46 and 10.37 MeV/u under He atmosphere. As long as only  $\beta$ -PVDF was used in present work, it will be further referred as PVDF implying its  $\beta$ -phase. For irradiation, PVDF films of  $4 \times 30\ \text{cm}^2$  area were anchored on movable sample holders perpendicular to ion beam. The ion fluence was adjusted taking into account number of passages and ion beam flux. Studied fluences were  $10^9$  and  $10^{10}\ \text{cm}^{-2}$ .

Electron-beam irradiation was performed at the SIRIUS facility of the Laboratoire des Solides Irradiés, Ecole Polytechnique, France. Films were irradiated at room temperature under He atmosphere with accelerating voltage of 2.5 MeV and machine current of 1.4  $\mu\text{A}$ . Doses were 5, 7.5, 10, 50 and 100 kGy.

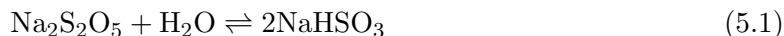
Regardless the type of irradiation, all irradiated samples were immediately sealed and stored

at  $-20^{\circ}\text{C}$  under anaerobic conditions to prevent from oxidation and to prolong radical lifetimes.

## 5.2 Track etching of PVDF

SHI irradiated PVDF films were chemically etched using 10 M KOH and 0.25 M  $\text{KMnO}_4$  solutions at  $65^{\circ}\text{C}$  for 25 min. The mechanism of track etching of PVDF is described in the details in chapter 2. Shortly, in mild conditions, alkaline solution of  $\text{KMnO}_4$  converts  $\text{C}=\text{C}$  into glycols (reaction of *dihydroxy-addition*). Highly concentrated alkaline  $\text{KMnO}_4$  solution at elevated temperature results in terminal  $\text{C}=\text{C}$  bond cleavage and subsequent carboxylic acid formation. Simultaneously, multiple oxidated products, such as ketones, diols, etc. are produced in heavily crosslinked track halo of PVDF.

The etched membranes were washed with 7.5 wt.% sodium metabisulfite ( $\text{Na}_2\text{S}_2\text{O}_5$ ) aqueous solution to reduce the excess of  $\text{KMnO}_4$ . In water, hydrolysis of  $\text{Na}_2\text{S}_2\text{O}_5$  to sodium bisulfite ( $\text{NaHSO}_3$ ) occurs



Sodium bisulfite reacts with potassium permanganate resulting in the formation of insoluble brown precipitate of manganese dioxide



The membranes were then vigorously rinsed with deionized water.

The diameter of resulting nanopores is proportional to the etching time, however linear relationship is dependent on fluence [105, 157]. For instance, for the fluence of  $5 \cdot 10^8 \text{ cm}^{-2}$ , nanopore radii  $r$  equals to  $r=0.8 \times t$  (nm), where  $t$  is the etching time (min). For the fluence of  $10^{10} \text{ cm}^{-2}$ , the  $r=1.6 \times t$ .

## 5.3 Radiation grafting

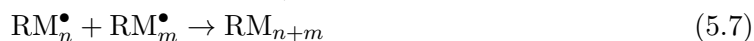
Radiation grafting is a sophisticated method to introduce the chelating properties to chemically inert polymers such as PVDF in form of films, fibers or membranes. Chelate polymers, often referred as resins, exhibit high selectivities towards toxic metals and may be grafted inside nanoporous structure of the membrane. Resulted confinement is expected to facilitate complexation reactions between the chelate polymer and metal ions. To selectively adsorb ions of interest, two concepts were addressed: i) ion-exchange complexation and ii) chelation with donor atoms (ligands). Pearson acid-base classification (1968) is generally used to predict the stability of metal complexes and mechanism of their reaction. This principle will be described in more detail in chapter 8.

For radiation grafting, electron-beam irradiated films or track-etched PVDF membranes were placed in purgeable glass tubes containing vinyl monomer solutions. Pre-irradiation method of grafting was used in order to i) avoid undesired homopolymerization reactions, ii) in case of track-etched PVDF, to control the grafting location (inside the nanopores and not on the membrane surface). The purgeable glass tubes were then connected to a Schlenk line for oxygen elimination. After 15 min of  $\text{N}_2$  purging at room temperature, they were then sealed and put into a thermostat water bath at experimentally set temperature for radiation grafting reaction. The grafted samples were then washed, dried and weighted. Gravimetric grafting yields (GYs) were calculated by eq. 5.3.

$$\text{GY} = \frac{m_f - m_i}{m_i} \times 100\% \quad (5.3)$$

where  $m_i$  and  $m_f$  are masses of the polymer before and after grafting, respectively.

Radiation-induced grafting in presence of vinyl monomer is undertaken according to the free-radical polymerization mechanism that comprises initiation (eqs. 5.4 and 5.5), chain propagation (eq. 5.6) and termination reactions (eq. 5.7 and 5.8). There are two types of radicals formed under either electron-beam or ion irradiation in PVDF capable of initiating radiation grafting reactions. These radicals are in-chain ( $-\text{CH}_2-\text{C}^\bullet\text{F}-\text{CH}_2-$ ,  $-\text{CF}_2-\text{C}^\bullet\text{H}-\text{CF}_2-$ ) and end-chain alkyls ( $-\text{CH}_2-\text{C}^\bullet\text{F}_2$ ,  $-\text{CF}_2-\text{C}^\bullet\text{H}_2$ ) which in contact with air can be converted to corresponding peroxy radicals ( $\text{ROO}^\bullet$ ). Besides the grafting reaction, homopolymerization and various transfer reactions may occur between the growing polymer chains and molecules of monomer, or solvent affecting the GY.



### 5.3.1 Acrylic acid (AA)

Radiation grafting with AA was undertaken at 60 °C within 1 hour in 50 vol.% AA aqueous solutions with addition of 0.25 wt.% Mohr's salt following 48 hours Soxhlet extraction in boiling water.

#### 5.3.1.1 Grafting of electron-beam irradiated PVDF

At this temperature, two chemical reactions take place: i) thermal homopolymerization of AA and ii) grafting reaction onto PVDF surface. Since water is a solvent for both the grafted polymer and homopolymer, when the latter is formed in solution, it can diffuse into the grafted copolymer. Therefore, addition of inhibitor of the AA homopolymerization is needed in order to suppress reactions in solution and make the grafting reaction predominant. Clochard et al. [79] investigated the effect of Mohr's salt concentration on GY for electron-beam irradiated  $\beta$ -PVDF films irradiated at 150 kGy doses using 70 vol.% AA aqueous solutions. The authors confirmed the presence of AA homopolymerization. They have also demonstrated that presence of 0.25 wt.% of Mohr's salt lowers the GY twice due to the suppression of homopolymer diffusion inside grafted PAA and its further increase does not affect significantly on GY. Thus, 0.25 wt.% of Mohr's salt was added to all monomer solutions prior grafting to eliminate the thermal homopolymerization of AA.

Figure 5.2 shows the variation of GY as a function of AA concentration in water [79]. It can be seen that with increase of monomer concentration, the GY steadily increases up to approximately 40 wt.% at 50 vol.% of AA due to an increase of the polymerization rate. Then a rapid rise up to more than 120 wt.% at 80 vol.% of AA where the maximum GY is obtained. For higher AA concentrations (90 vol.% and 100 vol.%), a sharp decrease of the GY occurs.

Aymes-Chodur [158] has shown that the increase in the polymerization rate is accompanied by a consumption of radicals. PVDF has a semicrystalline nature (see chapter 1), thus the stability of the radicals produced under irradiation depends on their location in the polymer. The least stable radicals are located in the amorphous parts of PVDF and will be consumed quickly. The crystalline phase contains the most stable and least accessible radicals. It is perturbed by the growing chains and water, being a solvent, accompanies them, thus gradually

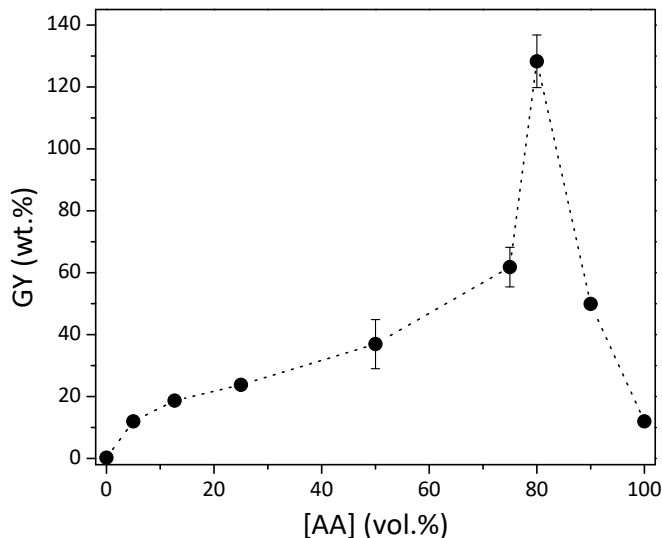


Figure 5.2: GY as a function of AA concentration for electron-beam irradiated  $\beta$ -PVDF films at doses of 150 kG [79]. Grafting conditions: 1 hour at 60 °C, 0.25 wt.% Mohr’s salt.

liberating the radicals which furthermore initiate grafting. In these conditions, the growth of PAA chains strongly depends on the solvent which plays a key role facilitating the monomer migration into polymer matrix and consequently increasing the grafting rate. However, existence of this GY maximum at 80 vol.% AA due to the *Trommsdorff-Norrish effect* (or, also so-called *gel effect*), which results in a self-acceleration of the polymerization, cannot be totally excluded. This effect means that at certain monomer concentration, termination reactions become diffusion controlled which results in increase of polymerization rate [159, 160]. To reduce this effect, less concentrated AA solutions should be used for grafting.

Cuscito [57] has demonstrated the effect of AA concentration on the mechanical deformation of the grafted electron-beam irradiated PVDF films at 100 kGy doses. It was also observed that the degree of deformation (GY *versus* volume or surface deformation) is not the same for  $\alpha$  and  $\beta$  phases of PVDF. In case of  $\alpha$ -PVDF, the deformation occurs in three dimensions for [AA] < 80 vol.% whereas  $\beta$ -PVDF deforms only in thickness regardless the AA concentration. This is reasonable as long as the  $\beta$ -PVDF is made by stretching of the  $\alpha$ -PVDF resulting in an aligned crystalline structure along the stretching direction. It enables a parallel to the crystallites orientation of the grafted PAA chains, thus leading to the thickness evolution of the grafted  $\beta$ -PVDF films and not the surface.

As abovementioned, solvent greatly affects on grafting process. Chapiro and Dulieu [161] have investigated the effect of different solvents on AA polymerization kinetics and introduced the term *matrix effect*. Solvents of the first group, such as water, methanol, dioxane stabilize the oligomeric auto-associated structures of AA (type II, figure 5.3). Solvents of the second group, such as hydrocarbons and chlorinated derivatives, do not associate with AA, shifting the equilibrium from oligomers to cyclic dimers (types I, figure 5.3). Both structures are in dynamic equilibrium. In the first group solvents, grafted PAA chains possess the “matrix effect” through a link the oligomeric aggregates by H-bonds to form an organized structure in which fast “zip” propagation takes place enabling progressive penetration of linear oligomeric AA structures inside PVDF matrix (type III, figure 5.3). In the second group solvents, the auto-associated oligomers are replaced by cyclic dimers which no longer form oriented structures with PAA and the “matrix effect” disappears.

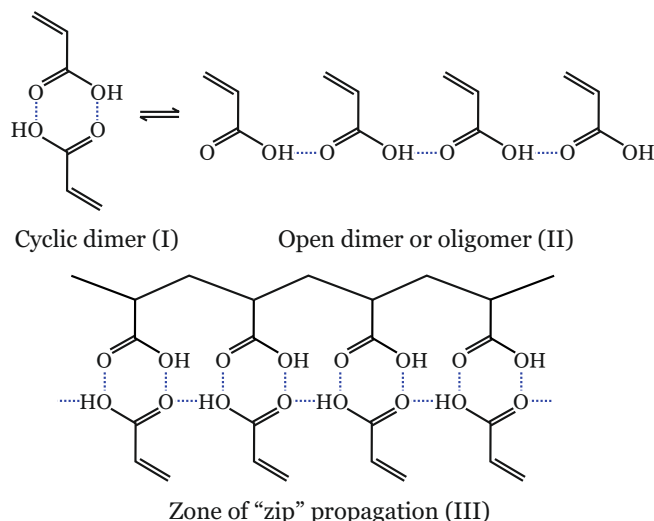


Figure 5.3: Association of carboxylic acids via hydrogen bonds in different solvents and "matrix effect" of PAA introduced by Chapiro and Dilieu [161].

Indeed, Grasselli et Betz [162] have demonstrated the effect of solvent on GY, surface and thickness evolution of electron-beam irradiated  $\alpha$ -PVDF films at 0.25 vol.% AA concentration. According to these results, some solvents, such as water and methanol, significantly deform the PVDF while others, such as THF, have an insignificant effect on all these parameters. As PAA is only partially soluble in its monomer, the use of solvent will allow swelling of the grafted areas and promoting migration of the monomer into the volume of the polymer. Furthermore, Cuscito [57] has shown that the use of a non-solvent, THF, mainly facilitates surface grafting whereas water promotes bulk grafting of PAA acting as a plasticizer of the soaked PAA-g-PVDF [79].

### 5.3.1.2 Grafting of track-etched PVDF

Using confocal laser scanning microscopy (CLSM) and double labeling method, it has been demonstrated that the localization of PAA grafted chains is inside the nanopores and not on the membrane surface nor in the inter-porous region (see chapter 3), thus, emphasizing that the radical polymerization of AA is initiated from the residual radicals present in the pore walls.

The presence of PAA functional polymer inside cylindrical nanopores was verified by FTIR in transmission mode (figure 5.4). The FTIR spectrum primarily demonstrates the characteristic absorption bands of PVDF with a doublet corresponding to the  $\text{CH}_2$  sym and asym vibrations at  $2985$  and  $3025\text{ cm}^{-1}$  respectively, a multiplet with spectral absorption bands at  $1453$ ,  $1424$ ,  $1403$  and  $1385\text{ cm}^{-1}$  attributed to a mixture of  $\text{CH}_2$  and  $\text{C-C}$  vibrations, two of the most intense absorption bands of  $\text{CF}_2$  at  $1211$  and  $1183\text{ cm}^{-1}$  and PVDF skeleton vibration region between  $900$  and  $400\text{ cm}^{-1}$  [12]. The latter region is attributed to the crystalline structure of PVDF. A well-defined peak at  $840\text{ cm}^{-1}$  represents  $\beta$ -phase of PVDF.

A characteristic band of  $-\text{C}=\text{O}$  stretching at  $1710\text{ cm}^{-1}$  is assigned to the  $-\text{COOH}$  group of the grafted PAA. The corresponding OH vibration gives rise to a broad band in the  $2500\text{-}3500\text{ cm}^{-1}$  region in which are superimposed with the  $\text{CH}_2$  sym and asym stretching absorption bands of PVDF at  $3025\text{ cm}^{-1}$  and  $2985\text{ cm}^{-1}$ , respectively [79].

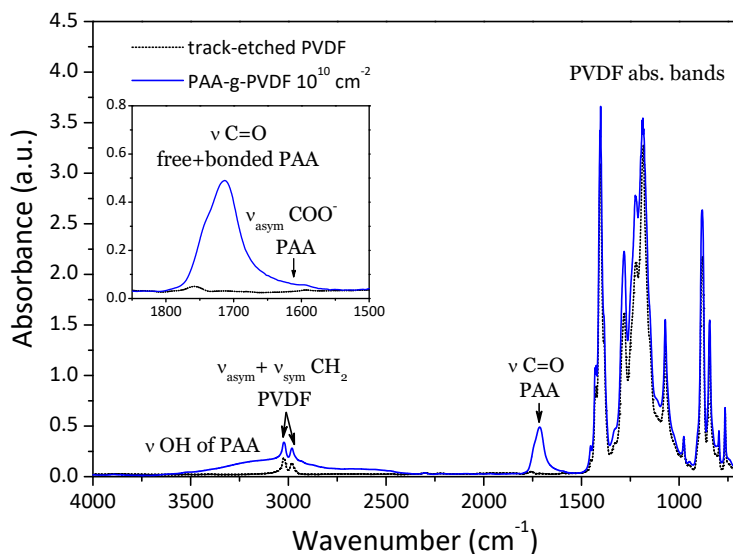


Figure 5.4: PAA-g-PVDF membrane of  $10^{10} \text{ cm}^{-2}$  fluence, 1 hour of RG at  $60^\circ\text{C}$  with 50 vol.% AA aqueous solution.

### 5.3.2 4-Vinylpyridine (4VP)

Radiation grafting with 4VP was undertaken at  $65^\circ\text{C}$  within 15 min in 100 vol.% 4VP solutions without addition of any inhibitor following rigorous washing with ethanol and soaking in  $10^{-2} \text{ M HCl}$  for 24 hours.

#### 5.3.2.1 Grafting of electron-beam irradiated PVDF

In order to establish the aforementioned grafting procedure, electron-beam irradiated PVDF films were grafted first. The films were immersed in a oxygen free 4VP solutions of various concentrations (from 25 to 100 vol.%) in N-methylpyrrolidone (NMP) as a solvent. At a set reaction temperature of  $65^\circ\text{C}$ , 100 kGy dose and 1 hour of grafting time, GY was proportionally increasing with 4VP concentration. Pure monomer solution was found to give the highest GY (ca. 80 wt.%) [157]. For the nanopore size system, the GY has to be lowered to ca. 10 wt.% to prevent from the pore blockage. A way to do it is to diminish grafting time or play on reaction temperature. Bessbousse et al. [157] have shown that 10 wt.% GY may be easily achieved at low doses (5-10 kGy) in pure 4VP during 10 min of grafting. The dose and ion fluence are linked through equation 1.3 given in chapter 1 (fluences of  $10^9$  and  $10^{10} \text{ cm}^{-2}$  correspond to the doses of 7.6 and 76 kGy respectively).

#### 5.3.2.2 Grafting of track-etched PVDF

Upon the chemical etching, radical content present in PVDF after irradiation decreases as a function of pore radii ( $\frac{1}{r^2}$ ) [105, 106]. The etching temperature and time thus are other important parameters for grafting of the track-etched PVDF because different vinyl monomers have not the same reactivity towards initiation step. Bessbousse et al. [157] demonstrated that considering grafting parameters set for electron-beam irradiated PVDF, such as 100 vol.% 4VP, 10 min,  $65^\circ\text{C}$  after 15 min of chemical etching, the amount of remained radicals was not sufficient to achieve considerable GYs. However, the reduced etching time (12 min) was found enough to reach 6.25 wt.% for  $10^{10} \text{ cm}^{-2}$  fluence. Indeed, a higher density of radicals can be directly tuned playing on the etching time. Despite, considering the objective of getting a

good compromise between GY + adsorption/release of toxic metal ions, it was decided to fix etching time at 30 min to intentionally limit the radiation grafting for well-open functionalized nanopores ( $\sim 40\text{-}50$  nm in diameter).

Figure 5.5 shows a FTIR spectrum of synthesized P4VP-g-PVDF membrane. Besides afore-

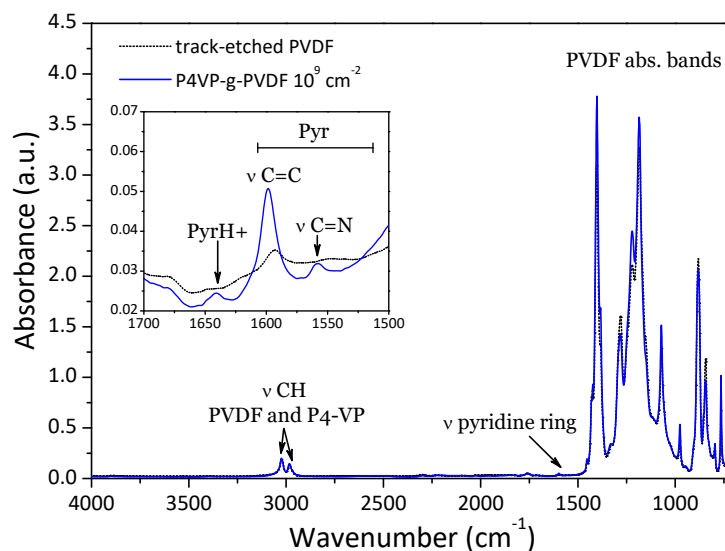


Figure 5.5: FTIR spectra of PVDF before and after grafting with P4VP;  $10^9 \text{ cm}^{-2}$  fluence, 15 min grafting time at  $65^\circ\text{C}$  100 vol.% P4VP. Inset: zoom of 1598 and 1558  $\text{cm}^{-1}$  peaks assigned to the C=C and C=N stretching vibrations in the pyridine ring.

mentioned characteristic absorption bands of PVDF described in section 5.3.1, the peaks appeared at 1598 and 1558  $\text{cm}^{-1}$  are assigned to the C=C and C=N stretching vibrations of uncharged pyridine ring of P4VP [163, p. 169]. Because of the soaking in  $10^{-2}$  M HCl, a part of neutral P4VP chains become protonated (pKa of P4VP is around 5 [164]) as exhibited in figure 5.6 and a weak peak at 1641  $\text{cm}^{-1}$  assigned to protonated pyridine ring appears which

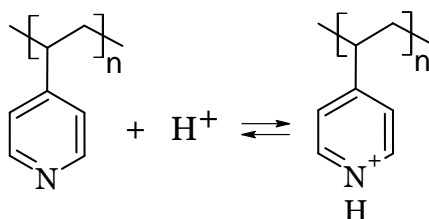


Figure 5.6: P4VP protonation at  $\text{pH} < \text{pKa}$ .

is in accordance with literature [165]. The C–H stretching vibrations of the pyridine ring at 3100–3010  $\text{cm}^{-1}$  are superimposed with those of PVDF.

### 5.3.2.3 Zeta-potential measurement

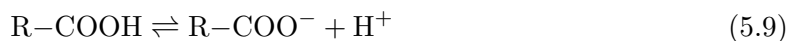
Surface charge properties have a significant influence on membrane performance. Zeta potential, which provides useful information about the surface charge properties of the membrane in solution, is an important parameter with regards to membrane retention and fouling properties. A number of techniques for measuring the zeta-potential have been developed based on one of three electrokinetic effects, electrophoresis, electro-osmosis, and streaming poten-

tial, out of which streaming potential (or streaming current) is the most suitable for flat membrane surfaces [166].

**5.3.2.3.1 Origin of surface charge** When brought into contact with an aqueous electrolyte solution, polymer membrane can have electrically charged surfaces. The surface charge characteristics are dependent on the chemical properties of the membrane and the chemicals present in the solution. There are various mechanisms through which polymer membranes can acquire surface charge. These mechanisms are dissociation (ionization) of surface functional groups; adsorption of ions from solution; and adsorption of polyelectrolytes, ionic surfactants, and charged macromolecules.

*Dissociation of surface functional groups*

Different polymer membranes contain ionizable surface groups, such as carboxylic ( $\text{R}-\text{COO}^-$ ), amine ( $\text{R}-\text{NH}_3^+$ ), and sulfonic ( $\text{R}-\text{SO}_3^-$ ). Surface charge arises from the deprotonation of these functional groups as shown in eqs. 5.9-5.11.



The surface charge depends on the degree of ionization and, hence, the pH of the aqueous solution. As seen from the above reactions, at low pH values, a membrane surface with amine functional groups can be positively charged, while at moderate to high pH values, a membrane with carboxyl functional groups can be negatively charged.

*Adsorption of ions from solution*

Even in the absence of ionizable functional groups, polymeric membrane surfaces can acquire a surface charge through the adsorption of anions from solution [167–169]. Preferential adsorption of anions has been suggested as a source of surface with no ionizable functional groups, such as hydrocarbon droplets [167, 168] and hydrophobic polystyrene latex colloids [170–172]. It has been postulated that anions can approach more closely to nonpolar or hydrophobic surfaces because they are less hydrated than cations. In this process a surface will acquire a negative electrokinetic potential due to the presence of anions beyond the plane of shear. Jacobasch and Schurz [173] have developed expressions for determining the adsorption free energy of ions onto polymeric surfaces by means of zeta-potential measurements. In addition, they unequivocally demonstrated that, in the presence of 1:1 simple electrolytes, such as NaCl, the zeta-potential of various polymers becomes more negative as the contact angle of the polymer increases (*i.e.*, as the polymer is more hydrophobic).

*Absorption of surfactants, polyelectrolytes, and charged macromolecules*

Membrane surfaces can also acquire a surface charge through the adsorption of polyelectrolytes, ionic surfactants, and charged macromolecules [173–175]. The free energy of adsorption,  $\Delta G_{ads}$ , of a solute is given by

$$\Delta G_{ads} = \Delta G_{surf} + \Delta G_{solv} \quad (5.12)$$

where  $\Delta G_{surf}$  represents the surface affinity for the solute and  $\Delta G_{solv}$  is the solvent affinity for the solute. Thus, a solute that is hydrophobic in character will readily adsorb onto a solid surface. For polyelectrolytes adsorption arises from London-van der Waals interactions, hydrophobic bonding of nonpolar segments, hydrogen bonding, electrostatic attraction, and chemical reaction with surface functional groups. If the polyelectrolyte and the membrane surface are similarly charged, adsorption occurs if the non-electrostatic attraction is greater than the electrostatic repulsion. In this case adsorption is enhanced by increasing the ionic

strength or by the presence of polyvalent counterions. If the polyelectrolyte and the surface are oppositely charged, then adsorption is dominated by electrostatic attraction.

**5.3.2.3.2 Principles of streaming potential** As aforementioned, polymer membranes acquire a surface charge when brought into contact with an aqueous solution. The surface charge is compensated by counterions in the solution close to the surface, forming the so-called *electrical double layer*. The distribution of ions at the solid-liquid interface can be described by several models, which are discussed in detail elsewhere [176, 177].

The electrical double layer (EDL) was previously described in chapter 4. Briefly, the EDL is a region close to the charged surface in which there is an excess of counterions to neutralize the surface charge. In the solution layer near the solid surface, termed *Stern layer* (also referred as outer Helmholtz plane), ions are strongly attracted to the surface charge and are immobile. Further away from the surface of in the *diffuse layer*, ions are less affected electrostatic interactions near the solid surface and the net charge density gradually decreases to that of the bulk solution. The diffuse layer can flow under the influence of tangential stress and the shear plane is defined where the diffuse layer slips (flows past) the charged surface. The electrical potential at the shear plane, which can be measured experimentally, is defined as the zeta-potential,  $\zeta$  (figure 5.7).

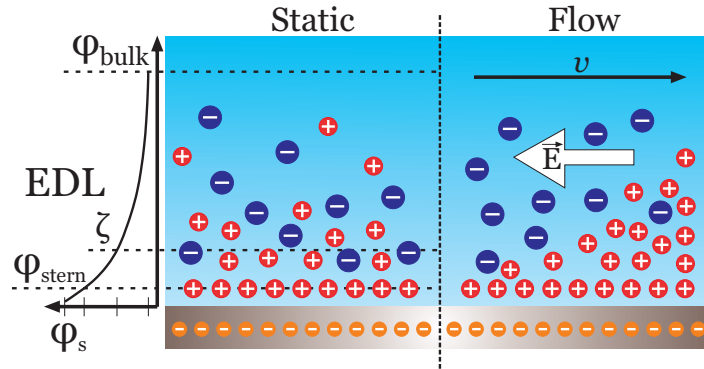


Figure 5.7: Streaming potential appearance due to the flow of diffuse layer.

In streaming potential technique, a pressure difference,  $\Delta P$ , is applied between the ends of a channel containing electrolyte to induce hydrodynamic flow. The ions in the diffuse layer of the EDL are carried in the direction of the flow, resulting in an electrical current defined as the streaming current,  $I_s$ . The streaming current can be measured when the electrical potential difference between two ends of the channel is zero. At open circuit, the streaming potential,  $E_s$ , generated by the hydrodynamic flow of electrolyte is the potential difference between the ends of the channel which induces a flow of ions in the opposite direction of the flow, defined as the conduction current,  $I_c$ . Streaming potential is measured when the flow reaches a steady state and the conduction current equals the streaming, making the total electrical current in the channel zero.

The Smoluchowski equation describes the relationship between zeta-potential and  $E_s$  (eq. 5.13) or  $I_s$  (eq. 5.14)

$$\zeta = \frac{dE_s}{dP} \frac{\eta}{\varepsilon\varepsilon_0} \sigma \quad (5.13)$$

$$\zeta = \frac{dI_s}{dP} \frac{\eta}{\varepsilon\varepsilon_0} \sigma R \quad (5.14)$$

where  $\frac{dE_s}{dP}$  is the change in streaming potential with pressure,  $\frac{dI_s}{dP}$  is the change of streaming current *versus* pressure,  $\sigma$  is the electrolyte conductivity,  $R$  is the resistance of the measuring

cell,  $\eta$  is the electrolyte viscosity,  $\epsilon_0$  is the vacuum permittivity, and  $\epsilon$  is the dielectric constant of the electrolyte.

**5.3.2.3.3 Experimental set-up** Measurements were performed using a home-made cell depicted in figure 5.8. A piece of membrane is placed between two cell compartments with inserted Ag/AgCl electrodes, sealed by tightening screw and filled with 0.1 M KCl electrolyte.

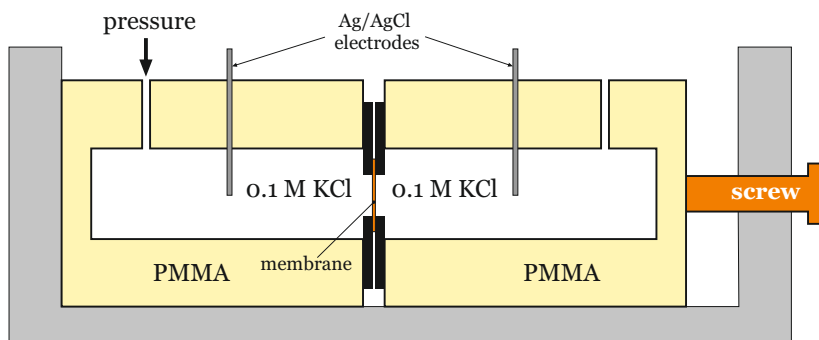


Figure 5.8: Schematic image of the experimental cell for  $\zeta$ -potential measurement.

The electrolyte pH was adjusted using HCl and KOH. One compartment of the cell is connected to a syringe-pump to vary the pressure whereas another one is under atmosphere pressure. The pressure difference ranging between  $\pm 0.3$  bar is measured with a differential-pressure transducer while the feedback voltage is automatically applied, and so measured, using an Axopatch-200B amplifier operating in the  $I=0$  mode. The experiment is controlled by a computer software and can perform measurements continuously.

For the measurement membranes were cut into around  $5 \times 5$  cm<sup>2</sup> pieces to fit the cell aperture and rinsed thoroughly with deionised water. Once placed into the cell and filled with electrolyte, it was pumped in alternating directions several times (typically less than 10) until achieving a good reproducibility.

The streaming potential ( $E_s$ ) is measured as a function of pressure ( $P$ ) by applying a transmembrane potential  $E = -E_s$  to maintain zero current in the cell. From the slope of  $\Delta E_s$  versus  $\Delta P$  one gets  $\zeta$ -potential (according to eq. 5.13) for the electrolyte solution with known  $\sigma$ ,  $\eta$  and  $\epsilon$ .

Figure 5.9 displays zeta-potential values of track-etched PVDF membrane before and after being grafted with P4VP as a function of pH. Nanopore walls of track-etched PVDF were found to be negatively charged within a whole pH range. This negative charge can be attributed to the presence of oxidized species formed at the nanopore surface during chemical etching in strong alkaline  $\text{KMnO}_4$  medium. As was shown in chapter 2, along with ketones, diols and other oxidized species, carboxylic acids are mainly formed during etching in accordance with the Cannizzaro reaction. In PVDF, these carboxylic acids can be fluorinated or not. Given that pKa of a hydrogenated carboxylic acid is 4.8,  $\zeta$ -potential evolution with pH for track-etched PVDF membrane must be observed. The mean  $\zeta$ -potential of -7 mV was roughly constant whatever the pH of the electrolyte pointing out that pKa of species present in the etched tracks should be very low if not negative. A fluorine atom, being much more electronegative than hydrogen, is able to pull electron density towards itself, away from the carboxyl group making it stronger acid (see *Bronsted acid-base concept*). The stronger the Bronsted acid, the more easily it gives up its proton, the lower the pKa. Thus, fluorinated acids and alcohols are much more acidic than equivalent non fluorinated ones. For example, pKa of  $\text{CF}_3\text{COOH}$  equals to -0.2 [178]. The unchanging with pH  $\zeta$ -potential value emphasizes that fluorinated molecules are predominantly formed after etching compare to non fluorinated ones, possessing pKa value as low as 1.2 [179].

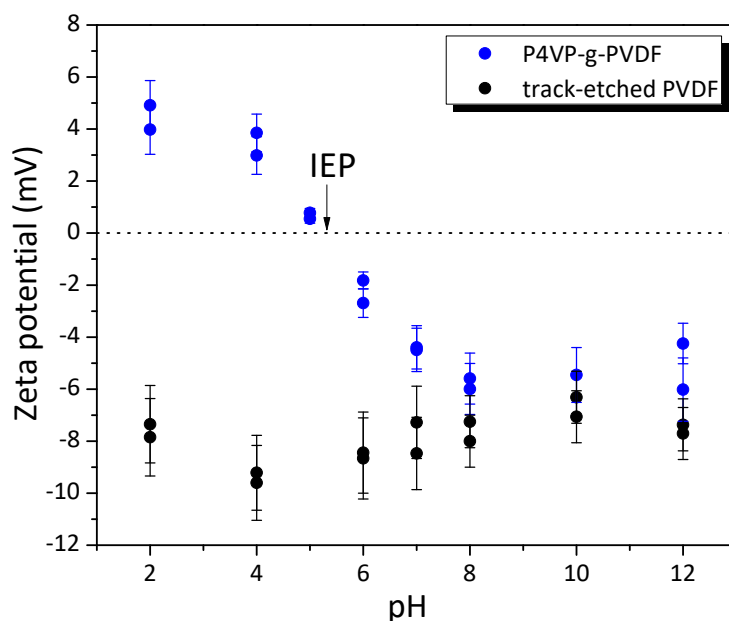


Figure 5.9: Zeta-potential as a function of pH for the track-etched PVDF before and grafting with P4VP,  $10^9 \text{ cm}^{-2}$  fluence,  $\text{GY}=0.35 \text{ wt.}\%$ .

When grafted with P4VP, the functionalised membrane exhibited a different behaviour. The nanopore charge was completely inverted into positive at low pH due to protonation of P4VP chains (figure 5.6). The isoelectric point (IEP), at which the total charge of polymer is zero, was reached at approximately pH 5 which corresponds to the  $\text{pK}_a$  of P4VP [155, 164, 180]. The nanopore diameter of the utilised membrane was ca. 60 nm and GY of 0.35 wt.%. This result demonstrates that the  $\zeta$ -potential determination *via* the streaming potential is a powerful technique for accurate characterization of the charge state of functionalized nanoporous membranes. It also gives information on the grafted polymer chain density along the nanopores. Effectively, the P4VP protonation at low pH was sufficient to completely counterbalance the underneath negative charges of oxidized walls of track-etched PVDF membrane. It means that the grafting coverage is uniform and relatively dense all along the nanopores.

### 5.3.3 Bis[2-(methacryloyloxy)ethyl] phosphate (B2MP)

Radiation grafting with PB2MP was undertaken at  $65^\circ\text{C}$  within 2 hours in 300 mM B2MP solutions in 50 vol.% water and 50 vol.% ethanol as a solvent with the addition of 0.25 wt.% Mohr's salt following rigorous washing with ethanol.

#### 5.3.3.1 Grafting of electron-beam irradiated PVDF

In order to determine the optimal radiation grafting parameters for radiation grafting of PB2MP, electron-beam irradiated PVDF films were studied first. Figure 5.10 shows variation of GY as a function of B2MP monomer concentration for electron-beam irradiated PVDF films at 100 kGy dose. The grafting time was set at 18 hours and grafting temperature of  $65^\circ\text{C}$  with addition of 0.25 wt.% Mohr's salt to prevent from gel formation. Even though pre-irradiation method was used and homopolymerization was not expected, gel was observed. This may be due numerous transfer reactions occurring in monomer solution. It is also known that B2MP is frequently used as a crosslinker [181]. Addition of 0.25 wt.% Mohr's

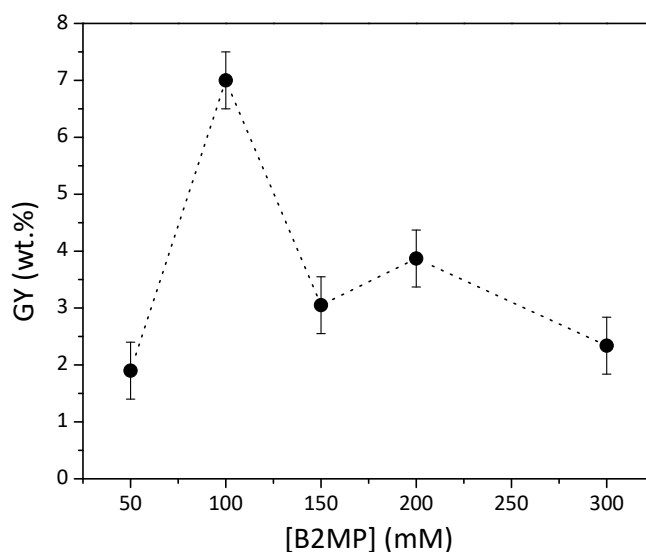


Figure 5.10: GY as a function of B2MP concentration for electron-beam irradiated  $\beta$ -PVDF films at doses of 100 kGy. Grafting conditions: 18 hours at 65 °C, 0.25 wt.% Mohr's salt, 50 vol.% water and 50 vol.% ethanol as a solvent.

suppressed gel formation and allowed to obtain considerable GYs. It is important to note that generally, B2MP polymerizes at various temperatures (from 60 to 100 °C), however the effect of grafting temperature has not been studied in this work. As aforementioned, all grafting reactions were held at 65 °C. The increase of the B2MP concentration up to 100 mM resulted in the increase of grafting rate and the maximum GY was reached at 7 wt.%. Further growth of B2MP concentration up to 300 mM, however, did not affect the GY greatly. This can be interpreted by the fact that after exceeding of 100 mM B2MP, the electron transfer reactions between the growing grafting chains and the monomer become predominant, leading to a faster termination of the polymerization grafting reaction [156].

It is known in literature that B2MP polymerizes in alcoholic and aqueous solutions [182, 183]. Therefore, the effect of solvent was studied using 100 vol.% water, 100 vol.% ethanol, and 50 vol.% water and 50 vol.% ethanol at a fixed dose of 100 kGy. First two solvent compositions gave similar GYs (around 5 wt.%) whereas a mixture of water and ethanol unexpectedly resulted in the increase of GY up to 7.5 wt.%. The role of solvent in polymerization process is to enhance the swelling of polymer substrate during polymerization through the growing polymer chains. Consequently, a good solvent should be both a good solvent for the monomer and its polymer facilitating the monomer accessibility to radical sites. Possibly, due to amphiphilic nature of B2MP molecule, the mixture of 50 vol.% water and 50 vol.% ethanol solvent enhances monomer solubility and consequently results in a higher GY.

In order to estimate the lower dose for B2MP grafting and dose-GY dependence, the electron-beam irradiated PVDF films at various doses were grafted prior track-etched PVDF. The grafting parameters were: 100 mM B2MP, 18 hours at 65 °C, 50 vol.% water and 50 vol.% ethanol, 0.25 wt.% Mohr's salt. As pre-irradiation method was used, the GY is expected to be proportionally increasing with dose as the amount of radicals increases. Figure 5.11 shows the dependence of GY as a function of dose indicating that chosen solvent composition and monomer concentration indeed promote better monomer solubility making B2MP grafting reaction driven by the number of available for polymerization radicals within this dose range.

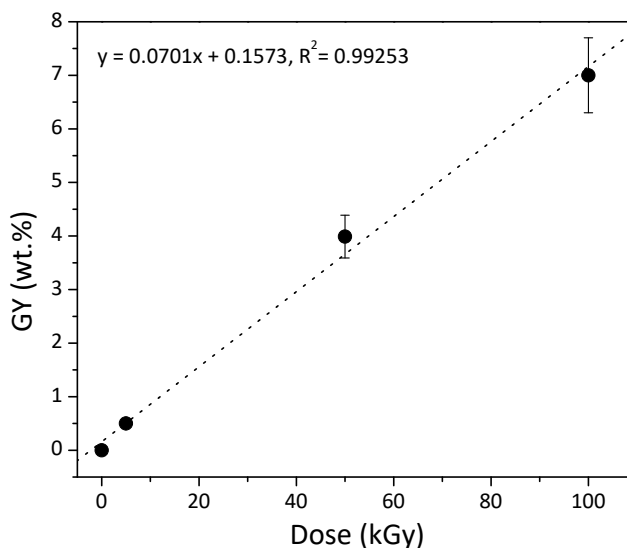


Figure 5.11: GY as a function dose for electron-beam irradiated PVDF films. Grafting conditions: 100 mM B2MP, 18 hours at 65 °C, 50 vol.% water and 50 vol.% ethanol, 0.25 wt.% Mohr's salt.

### 5.3.3.2 Grafting of track-etched PVDF

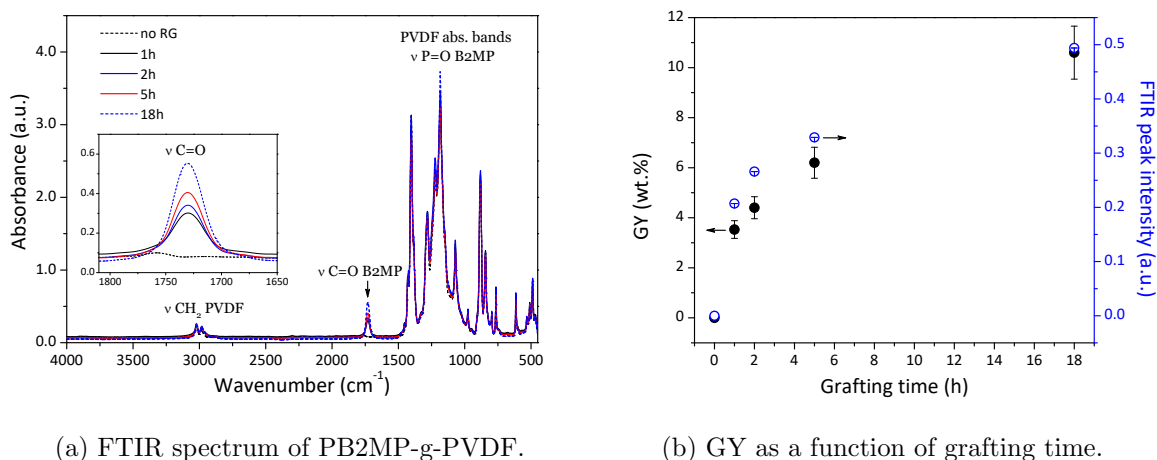
The chemical etching does not remove all the radicals from the track formed under ion irradiation. Even though its amount is relatively low, a localized radiation grafting occurs from the nanopore walls [105, 106]. The optimal parameters, established for electron-beam irradiated PVDF films, were subsequently applied to track-etched PVDF of  $10^{10} \text{ cm}^{-2}$  fluence. However, 100 mM B2MP concentration was found insufficient to reach significant GYs due to dose and radical density difference between electron-beam and track-etched membranes. The increase of B2MP concentration by the factor of three (300 mM) recovered same grafting behaviour, therefore was fixed as optimal for PB2MP-g-PVDF membrane fabrication.

This may be attributed to following phenomenon. Because the grafting reaction starts at the surface, where contact with monomer solution takes place, a higher monomer concentration is needed for monomer diffusion to the radical sites inside the membrane, which are less accessible for the monomer. In this situation, monomer is consumed mainly at the surface region and does not almost penetrate inside resulting in tiny GYs. The 300 mM B2MP was found to be an optimal monomer concentration for both reaching a considerable GYs and not enhancing the gel formation (Table 5.1).

Table 5.1: GYs of track-etched PVDF under various irradiation and grafting conditions.

Fluence $\text{cm}^{-2}$	Grafting time h	[B2MP] mM	Solvent	GY <i>wt.</i> %
$10^9$	18	100	EtOH/water	0.08
		300		1.04
		600		0.63
$10^{10}$	1	300	EtOH/water	3.53
	2			4.4
	5			6.2
	18			10.6

Presence of PB2MP inside cylindrical nanopores was verified by FTIR (figure 5.12a). The



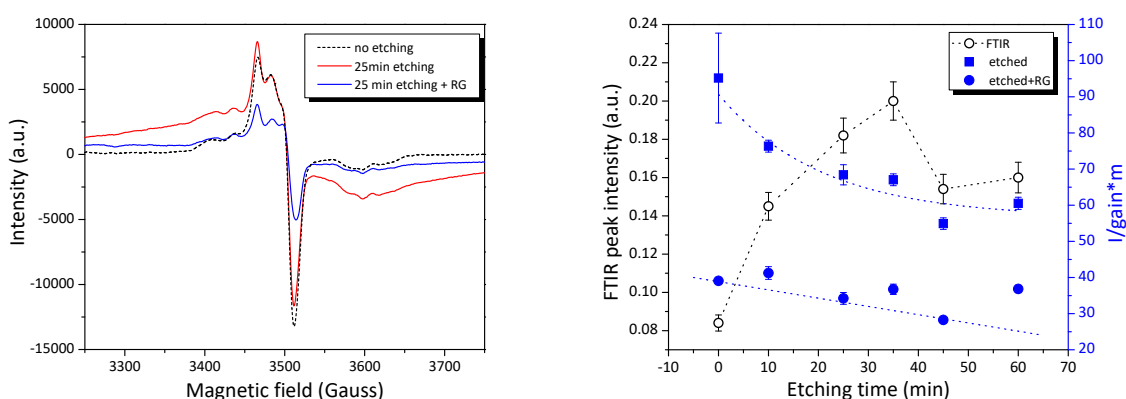
(a) FTIR spectrum of PB2MP-g-PVDF.

(b) GY as a function of grafting time.

Figure 5.12: Grafting kinetics of PB2MP inside track-etched  $\beta$ -PVDF of  $10^{10} \text{ cm}^{-2}$  fluence. Grafting conditions: 300 mM B2MP,  $65^\circ\text{C}$ , 0.25 wt.% Mohr's salt, 50 vol.% water and 50 vol.% ethanol as a solvent.

spectrum demonstrates aforementioned PVDF vibration bands described in section 5.3.1 along with  $-\text{C}=\text{O}$  stretching vibration of PB2MP at  $1725 \text{ cm}^{-1}$ . The stretching vibration of  $-\text{P}=\text{O}$  that typically appears at  $1350\text{--}1250 \text{ cm}^{-1}$  is not observable due to overlapping with intense absorption bands of PVDF [181]. Figure 5.12b shows grafting kinetics of PB2MP inside track-etched PVDF of  $10^{10} \text{ cm}^{-2}$  fluence. GY rapidly increases within 4 hours and reaches a plateau after 18 hours due to the diminution of monomer diffusion through the grafted amorphous part of PVDF [155]. The  $1725 \text{ cm}^{-1}$  FTIR absorption peak is in coherence with quantitative GY obtained gravimetrically.

Figure 5.13a shows EPR spectra of track-etched  $\beta$ -PVDF membranes of  $10^{10} \text{ cm}^{-2}$  fluence before and after grafting with PB2MP. The spectra represent an overlap of characteristic



(a) EPR spectra of track-etched  $\beta$ -PVDF before and after grafting with PB2MP.

(b) Decay of radicals as a function of etching time plotted versus FTIR peak height.

Figure 5.13: Radical consumption by B2MP. Grafting time is 1 hour.

signals of commonly occurring radicals in PVDF under irradiation [26, 31, 96] (see chapter 3). Taking the central resonance peak intensity normalized by the receiver gain and mass of the sample, the relative decay of radical content is obtained (figure 5.13b). Clearly, amount of paramagnetic species decreases with etching time. It is reasonable since the longer the etching time, the larger pores are obtained, the less trapped radicals in PVDF halo are re-

mained. Around 60% decrease of EPR signal intensity is observed when put grafted with PB2MP within to 1 hour. The same tendency is seen for membranes with the nanopores of different diameters but still having sufficient amount and density of radicals capable of initiating B2MP polymerization reaction, pointing out that observed radical consumption is accompanied by PB2MP grafting.

Black empty dots represent FTIR  $1725\text{ cm}^{-1}$  peak intensity which is proportional to GY of PB2MP at a given etching time. It shows that up to a certain etching time (corresponding to a certain pore diameter), grafting reaction is facilitated whereas longer etching causes lowering the GY due to pore overlapping. This dependence, however, is not straightforward. Since the amount of radicals remained after etching (blue squares) does not drop off sharply, one would expect that other reactions such as radical recombination, disproportionation favoured by grafting temperature or reactions occurring in monomer solution can occur affecting the GY.

## Conclusion

In this chapter, fabrication procedure of functionalized track-etched  $\beta$ -PVDF membranes was described. The radiolytically produced free radicals in PVDF under irradiation initiate radiation grafting reaction when put in contact with monomers. Different functional polymers having vinyl groups such as PAA, P4VP and difunctional allyl PB2MP were grafted inside the nanoporous structure of PVDF membranes for selective complexation with Pb(II), Hg(II) and U(VI) ions dissolved in water.

To establish the radiation grafting protocol, electron-beam irradiated films were grafted first and subsequently applied to track-etched PVDF membranes. Both electrons and ions produce radicals of identical nature (alkyl in-chain and end-chain along with corresponding peroxy radicals). Pre-irradiation method of grafting was used in present work. By means of EPR spectroscopy, it has been shown that amount and density of trapped radicals were sufficient to reach considerable GYs. The radical decay observed for nanopores of different sizes was accompanied by PB2MP grafting. The stability of these radicals was mainly attributed to semicrystalline structure of PVDF. The least stable radicals are located in the amorphous parts of PVDF are consumed quickly. While the crystalline phase contains the most stable and least accessible radicals. Therefore, properly chosen grafting conditions such as grafting temperature, monomer concentration, solvent, *etc.* can drastically influence not only GY, but also on grafting location and density of grafted polymer chains.

Notably, in case of PAA, AA monomer concentration and solvent greatly affected the grafting rate and location. The role of solvent is to facilitate monomer migration into substrate polymer matrix and subsequently to increase the grafting rate. The type of solvent is of great importance for PAA since it is only partially swelled in its monomer. The radiation grafting therefore using 50 vol.% AA aqueous solutions within 1 hour with addition of 0.25 wt.% Mohr's salt to suppress AA thermal homopolymerization was found to be optimal. Unlike AA, pure 4VP monomer solution was found to give the highest grafting rate. Radiation grafting with P4VP was undertaken at 65 °C within 15 min in 100 vol.% 4VP solutions without addition of any inhibitor.

Effect of B2MP concentration, solvent and dose were studied using electron-beam irradiated PVDF films. The optimal grafting conditions for electron-beam irradiated PVDF at 100 kGy were: 100 mM B2MP, 18 hours at 65 °C, 0.25 wt.% Mohr's salt, 50 vol.% water and 50 vol.% ethanol as a solvent. The 100 mM B2MP concentration, however, was found insufficient for reaching considerable GY in the track-etched membranes. This effect may be interpreted by the difference in absorbed dose and radical density between electron-beam and ions as well as by grafting front mechanism observed for PAA grafting onto PVDF. Because PVDF barely swells in B2MP monomer solution, the monomer is mainly consumed at the surface region resulting in less monomer available for migration. In these conditions higher monomer concentration is needed for monomer diffusion to the inhomogeneously distributed radicals of track-etched membrane. Indeed, 300 mM B2MP recovered same grafting behaviour for PB2MP-g-PVDF membranes.

For the first time, non-conventional  $\zeta$ -potential measurements were applied for characterization of nanopore surface charge state. The mean  $\zeta$ -potential of track-etched PVDF was found to be negative and roughly constant (-7 mV) over all investigated pH range (2-12). It was assigned to oxidized species (namely fluorinated ones) formed during track etching in strong alkaline  $\text{KMnO}_4$  medium. The P4VP presence inside the nanopores, however, has completely inverted  $\zeta$ -potential into positive at low pHs. The isoelectric point of P4VP-g-PVDF at GY of 0.35 wt.% was reached at pH 5, which corresponds to pKa of pure P4VP, pointing out that density of the grafted P4VP chains is relatively high all along the nanopore channels.

## Chapter 6

# Adsorption isotherm models

This chapter reports on application of basic two-parameter isotherm models for describing the acquired experimental data. The adsorption isotherm represents the relationship between the amount of solute adsorbed by a unit mass of solid sorbent and remained in the solution at equilibrium. The equilibrium concentrations vary as a function of temperature, therefore, the adsorption equilibrium relationship at a given temperature is referred as adsorption isotherm.

Langmuir (1918), Freundlich (1906) and Temkin (1941) are the most widely applied two-parameter isotherm models for toxic metal adsorption. Langmuir isotherm model is based on the assumption that binding sites are homogeneously distributed over the adsorbent surface. These binding sites have the same affinity for adsorption of a single molecular layer. This model assumes that there is no interaction between adsorbed molecules. The mathematical representation for a single solute adsorption is

$$q_{eq} = \frac{q_{max}bc_{eq}}{1 + bc_{eq}} \quad (6.1)$$

where  $q_{eq}$  is the equilibrium sorption capacity ( $\text{mg g}^{-1}$  or  $\text{mmol g}^{-1}$ ), *i.e.* mass of retained species at equilibrium per mass of the membrane,  $q_{max}$  is the saturated monolayer sorption capacity ( $\text{mg g}^{-1}$  or  $\text{mmol g}^{-1}$ ),  $b$  is the sorption equilibrium constant ( $\text{L mol}^{-1}$ ) and  $c_{eq}$  is an equilibrium (final) concentration ( $\text{mg L}^{-1}$  or  $\text{mmol L}^{-1}$ ).

Freundlich isotherm model is an empirical equation describing non-ideal, reversible adsorption on the basis of an assumption of the surface energetic heterogeneity. It is often applied to multilayer adsorption. This model assumes that as the adsorbate concentration increases so does the concentration of adsorbate on the adsorbent surface and can be expressed as

$$q_{eq} = K_F c_{eq}^{\frac{1}{n}} \quad (6.2)$$

where  $K_F (\text{mol g}^{-1})(\text{mol L})^{-1/n}$  is a constant characterizing the adsorption capacity and  $n$  (dimensionless) is a constant depicting the adsorption intensity.

Temkin isotherm is based on the assumption that heat of adsorption would decrease linearly with the increase in coverage of the adsorbent. Similarly to Freundlich model, it has been applied to describe adsorption on heterogeneous surface.

$$q_{eq} = \frac{RT}{b_T} \ln(K_T \cdot c_{eq}) \quad (6.3)$$

where  $K_T$  is the equilibrium binding constant corresponding to the maximum binding energy,  $b_T$  is the Temkin isotherm constant,  $T$  is the absolute temperature (K), and  $R$  is the ideal gas constant. For all the models presented, the constants can also be determined from the linearised plots.

## 6.1 Lead(II)

For adsorption, PAA-g-PVDF membranes were placed into aqueous solutions ( $V = 50$  mL) of various Pb(II) concentrations ( $c_0$  from 0 to 36 ppb) at pH 7. All experiments were performed at room temperature ( $20 \pm 5$  °C) according to the established laboratory adsorption protocol (30 min adsorption in stirring solutions). The concentration before and after adsorption were determined using the PAA-g-PVDF membrane-electrodes and calibration curve obtained for the same batch of membranes.

The mass  $q_{eq}$  of Pb(II) fixed at equilibrium per gram of the membrane ( $\text{mg g}^{-1}$ ) was calculated as follows

$$q_{eq} = \frac{(c_0 - c_{eq})V}{m} \quad (6.4)$$

where  $c_0$  and  $c_{eq}$  are initial and equilibrium concentrations of Pb(II) in the solution ( $\text{mg L}^{-1}$ ), respectively (molar mass of lead is  $207.2 \text{ g mol}^{-1}$ ).  $V$  is a volume of solution (L),  $m$  is the mass of the dry PAA-g-PVDF membrane (g).

The adsorption isotherms of Pb(II) ions by PAA-g-PVDF are presented in figure 6.1a. The Pb(II) adsorption isotherms may be considered to consist of two major parts: i) a rapidly

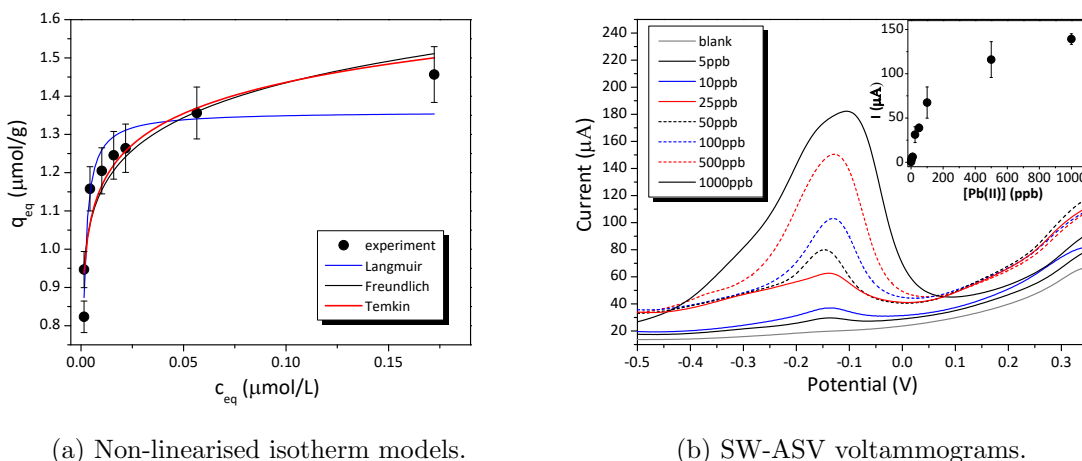


Figure 6.1: Pb(II) adsorption by PAA-g-PVDF membranes, fluence is  $10^9 \text{ cm}^{-2}$ .

increasing phase at low  $c_{eq}$  where Pb(II) uptake increases almost proportionally with  $q_{eq}$ , suggesting that the number of binding sites is sufficient, and ii) a saturation phase at higher  $c_{eq}$  where metal uptake is no longer increasing proportionally with equilibrium concentrations. This indicates that the number of available adsorption sites onto PAA surface becomes a limiting factor that controls further Pb(II) adsorption.

Tables 6.1 and 6.2 include estimated parameters obtained from both non-linearised isotherms and their linearised plots. To verify which of the models fits better, linearised plots were built. The parameters obtained from the linearised plot of Langmuir isotherm correlate with those acquired by non-linearised one. Even though the correlation coefficient is high for linearised plot, the Langmuir model cannot be applied at this concentration range as saturation is not yet achieved. According to the previous SW-ASV measurements in a larger concentration range, it starts after exceeding 100 ppb (figure 6.1b). Freundlich and Temkin models seem to be more adequate for experimental data description. Both models do not limit the adsorption to a monolayer adsorbate formation, which seems to be reasonable since PAA possess cation-exchange character. The Pb(II)-PAA interaction is governed mainly by ionized at pH close to neutral. This interaction can be considered as electrostatic, thus indirect adsorbate-adsorbate interactions cannot be excluded. Therefore, Freundlich and Temkin isotherm models appear

to describe better the Pb(II) adsorption process by PAA-g-PVDF membranes than Langmuir taking into account a larger concentration range. Despite, in dilute regime as all three isotherm models describe very well the experimental data, Langmuir isotherm parameters can be considered to discuss later on lead adsorption affinity to PAA.

Table 6.1: Two-parameter non-linearised isotherm models.

Model	Equation	Parameters		
Langmuir	$q_{eq} = \frac{q_{max}bc_{eq}}{1+bc_{eq}}$	$q_{max}$ (mol g <sup>-1</sup> ) 1.36·10 <sup>-6</sup>	$b$ (L mol <sup>-1</sup> ) 1.24·10 <sup>6</sup>	$R^2$ 0.89751
Freundlich	$q_{eq} = K_F c_{eq}^{\frac{1}{n}}$	$K_F$ (mol g <sup>-1</sup> )(mol L) <sup>-1/n</sup> 6.62·10 <sup>-6</sup>	$n$ 10.53	$R^2$ 0.86436
Temkin	$q_{eq} = \frac{RT}{b_T} \ln(K_T \cdot c_{eq})$	$K_T$ (L mol <sup>-1</sup> ) 2.0·10 <sup>12</sup>	$b_T$ (J g mol <sup>-2</sup> ) 2.10·10 <sup>10</sup>	$R^2$ 0.9005

Table 6.2: Linearised adsorption isotherm models.

Model	Equation	Parameters		
Langmuir	$\frac{c_{eq}}{q_{eq}} = \frac{c_{eq}}{q_{max}} + \frac{1}{bq_{max}}$	$q_{max}$ (mol g <sup>-1</sup> ) 1.47·10 <sup>-6</sup>	$b$ (L mol <sup>-1</sup> ) 4.60·10 <sup>8</sup>	$R^2$ 0.99936
Freundlich	$\ln q_{eq} = \ln K_F + \frac{1}{n} c_{eq}$	$K_F$ (mol g <sup>-1</sup> )(mol L) <sup>-1/n</sup> 1.31·10 <sup>-6</sup>	$n$ 9.62	$R^2$ 0.8428
Temkin	$q_{eq} = \frac{RT}{b_T} (\ln K_T + \ln c_{eq})$	$K_T$ (L mol <sup>-1</sup> ) 1.93·10 <sup>12</sup>	$b_T$ (J g mol <sup>-2</sup> ) 8.5·10 <sup>6</sup>	$R^2$ 0.90073

## 6.2 Mercury(II)

For adsorption, P4VP-g-PVDF membranes, initially weighted ( $m \approx 2.24$  mg), were placed into aqueous solutions ( $V = 100$  mL) of various Hg(II) concentrations ( $c_0$  from 0 to 100 ppb, 1 ppb equals to 1  $\mu\text{g L}^{-1}$ ) at pH 7. All experiments were performed at room temperature ( $20 \pm 5$  °C) temperature according to the established laboratory adsorption protocol (4 hours adsorption in stirring solutions). The concentration before and after the adsorption were determined using P4VP-g-PVDF membrane-electrodes and calibration curve obtained for the same batch of the membranes.

Table 6.3 includes the estimated parameters obtained from non-linearised Langmuir, Freundlich and Temkin isotherm models.

Table 6.3: Two-parameter non-linearised isotherm models.

Model	Equation	Parameters		
Langmuir	$q_{eq} = \frac{q_{max}bc_{eq}}{1+bc_{eq}}$	$q_{max}$ (mol g <sup>-1</sup> ) 5.53·10 <sup>-7</sup>	$b$ (L mol <sup>-1</sup> ) 7.0·10 <sup>7</sup>	$R^2$ 0.94959
Freundlich	$q_{eq} = K_F c_{eq}^{\frac{1}{n}}$	$K_F$ (mol g <sup>-1</sup> )(mol L) <sup>-1/n</sup> 1.04·10 <sup>-5</sup>	$n$ 5.10	$R^2$ 0.82746
Temkin	$q_{eq} = \frac{RT}{b_T} \ln(K_T \cdot c_{eq})$	$K_T$ (L mol <sup>-1</sup> ) 6.0·10 <sup>9</sup>	$b_T$ (J g mol <sup>-2</sup> ) 3.60·10 <sup>10</sup>	$R^2$ 0.94736

The mass  $q_{eq}$  of Hg(II) fixed at equilibrium per gram of the membrane (mg g<sup>-1</sup>) was calculated as follows

$$q_{eq} = \frac{(c_0 - c_{eq})V}{m} \quad (6.5)$$

where  $c_0$  and  $c_{eq}$  are initial and equilibrium concentrations of Hg(II) in the solution ( $\text{mg L}^{-1}$ ), respectively (molar mass of mercury is  $200.59 \text{ g mol}^{-1}$ ).  $V$  is a volume of solution (L),  $m$  is the mass of the dry P4VP-g-PVDF membrane (g).

Table 6.3 includes the estimated parameters obtained from non-linearised models. The correlation coefficient for Langmuir isotherm shown in figure 6.2 is the highest one. In order to verify if the model fits well, linearised plot was built (inset in figure 6.2). The parameters obtained from the linearised plot are presented in Table 6.4. The correlation coefficients

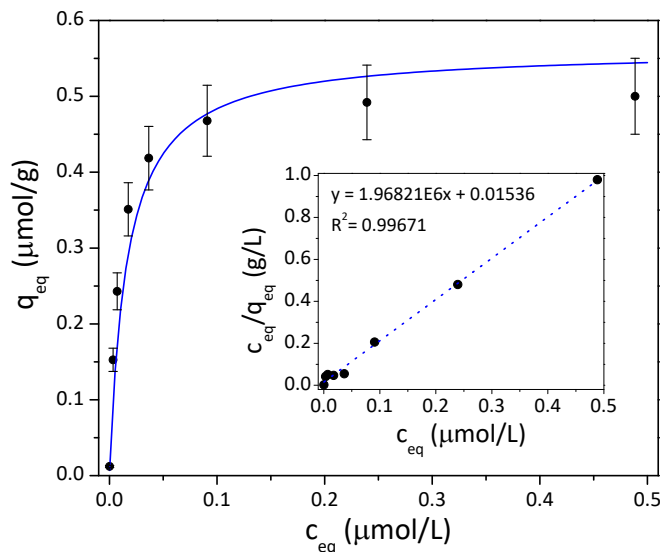


Figure 6.2: Langmuir isotherm of Hg(II) adsorption by P4VP-g-PVDF membranes, fluence is  $10^9 \text{ cm}^{-2}$ . Inset: linearised plot of Langmuir isotherm model.

close to 1 and almost identical  $q_{max}$  values acquired in non-linearised (Table 6.3) and linearised (Table 6.4) plots confirm that Langmuir model properly describes Hg(II) adsorption by P4VP-g-PVDF membranes, which is in agreement with the results obtained by Bessbousse et al. [184, 185]. This also confirms that the adsorption process involves Hg(II)-P4VP complexation which is limited by the number of available adsorption sites. Indeed, non-ionized P4VP chains at the pH studied can coordinate only with a particular amount of Hg(II), and once adsorbed, no Hg(II)-Hg(II) interactions are expected as there is no charge involved (solvated ions are normally surrounded with water molecules, thus coordination interaction in this case is considered as interaction of neutral species, see chapter 8).

Table 6.4: Parameters of the linearised Langmuir isotherm model.

P4VP-g-PVDF membrane	Hanes-Woolf plot parameters		
	$q_{max}$ ( $\text{mol g}^{-1}$ )	$b$ ( $\text{L mol}^{-1}$ )	$R^2$
	$5.081 \cdot 10^{-7}$	$12.814 \cdot 10^7$	0.99671

The loading capacity of P4VP-g-PVDF membranes ( $q_{max}$ ) was estimated to be  $0.55 \mu\text{mol g}^{-1}$ . It is worth mentioning that these results correlate with those acquired by stripping voltammetry (see chapter 8), according to which the membrane saturation starts at 10 ppb ( $c_{eq}$  of  $0.05 \mu\text{mol L}^{-1}$ ), explaining the observed deviation from the linearity of Hg(II) calibration curves [155].

### 6.3 Uranium(VI)

For adsorption, PB2MP-g-PVDF membranes, initially weighted ( $m \approx 6.40$  mg), were placed into aqueous solutions ( $V = 100$  mL) of various U(VI) concentrations ( $c_0$  from 0 to 658 ppb), at pH 7. All experiments were performed at room temperature ( $20 \pm 5$  °C) during 17 hours of adsorption in stirring solutions. The concentration before and after adsorption were determined by ICP-MS provisionally calibrated. The masses of retained U(VI) at equilibrium per gram of the membrane,  $q_{eq}$ , were calculated using eq. 6.5.

Table 6.5 includes the estimated parameters obtained by three different two-parameter models and shown in figure 6.3.

Table 6.5: Two-parameter non-linearised isotherm models.

Model	Equation	Parameters		
Langmuir	$q_{eq} = \frac{q_{max}bc_{eq}}{1+bc_{eq}}$	$q_{max}$ (mol g <sup>-1</sup> ) 6.73·10 <sup>-6</sup>	$b$ (L mol <sup>-1</sup> ) 9.850·10 <sup>6</sup>	$R^2$ 0.8886
Freundlich	$q_{eq} = K_F c_{eq}^{\frac{1}{n}}$	$K_F$ (mol g <sup>-1</sup> )(mol L) <sup>-1/n</sup> 4.950·10 <sup>-4</sup>	$n$ 3.050	$R^2$ 0.71497
Temkin	$q_{eq} = \frac{RT}{b_T} \ln(K_T \cdot c_{eq})$	$K_T$ (L mol <sup>-1</sup> ) 1.050·10 <sup>8</sup>	$b_T$ (J g mol <sup>-2</sup> ) 1.964·10 <sup>9</sup>	$R^2$ 0.84265

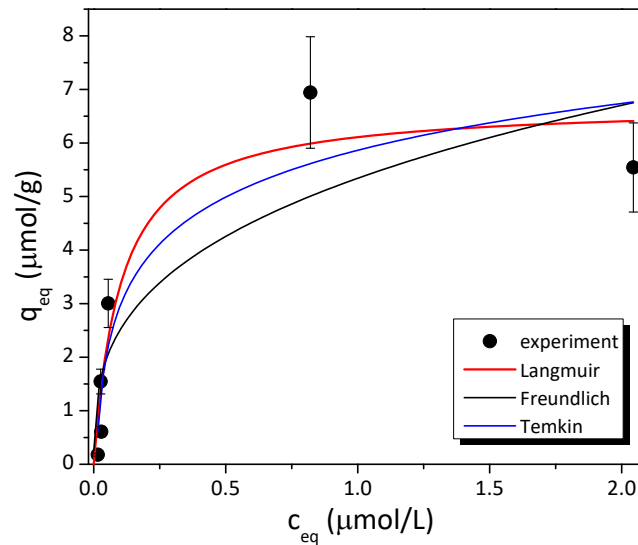


Figure 6.3: Non-linearised Langmuir, Freundlich and Temkin isotherm models of U(VI) adsorption by PB2MP-g-PVDF membranes, fluence is  $10^{10}$  cm<sup>-2</sup>.

To verify which of these models fits better, linearised plots were built. The parameters determined through the linearised plots are presented in Table 6.6.

Unlike Langmuir and Freundlich models, Temkin isotherm model takes into account the adsorbent-adsorbate interactions and is based on the assumption that free energy of sorption is a function of the surface coverage [186]. This model in principle might be used for describing U(VI) adsorption data for a given system. It is worth mentioning that there are no data in literature related to the U(VI) adsorption isotherm onto PB2MP. Among considered two-parameter isotherm models, Langmuir model gave the best correlation coefficient, the closest  $q_{max}$  and  $b$  values for non-linearised and linearised plots. The results showed that Langmuir

Table 6.6: Linearised adsorption isotherm models.

Model	Equation	Parameters		
Langmuir	$\frac{c_{eq}}{q_{eq}} = \frac{c_{eq}}{q_{max}} + \frac{1}{bq_{max}}$	$q_{max}$ (mol g <sup>-1</sup> ) 6.0·10 <sup>-6</sup>	$b$ (L mol <sup>-1</sup> ) 1.150·10 <sup>7</sup>	$R^2$ 0.96865
Freundlich	$\ln q_{eq} = \ln K_F + \frac{1}{n} c_{eq}$	$K_F$ (mol g <sup>-1</sup> )(mol L) <sup>-1/n</sup> 1	$n$ 1.760	$R^2$ 0.60278
Temkin	$q_{eq} = \frac{RT}{b_T} (\ln K_T + \ln c_{eq})$	$K_T$ (L mol <sup>-1</sup> ) 1.0452·10 <sup>8</sup>	$b_T$ (J g mol <sup>-2</sup> ) 7.93·10 <sup>5</sup>	$R^2$ 0.84265

isotherm model could fit the data better than Temkin and Freundlich models. Despite the fact that Langmuir isotherm model was found to be the most appropriate, the adsorption behaviour may be more complex than a simple monolayer adsorption since one of the group of PB2MP possess ion-exchange interaction whereas another one owns chelating effect at pH close to neutral.

## Conclusion

In this chapter, adsorption characteristics of track-etched PVDF membranes grafted with PAA, P4VP and PB2MP towards Pb(II), Hg(II) and U(VI) selective preconcentration were demonstrated. Adsorption study confirmed that adsorption capacities of the grafted track-etched PVDF membranes are due to presence of functional groups inside the nanopores facilitating complexation reactions.

In case of PAA grafted membranes, the Pb(II)·PAA interaction is governed mainly by complexation between ionized at pH close to neutral carboxylic groups and metal ions. If so, indirect interaction of adsorbed species, or adsorbed layer re-organization, cannot be excluded. Therefore, Freundlich and Temkin isotherm models appeared to describe better the adsorption of lead by PAA-g-PVDF membranes than Langmuir isotherm model at high concentrations (after exceeding 100 ppb).

When functional polymers are used, namely P4VP and PB2MP, as no ion-exchange is involved, Hg(II) and U(VI) uptakes must be limited by the number of available adsorption sites (functional groups). This hypothesis was confirmed by experimental results, for which Langmuir isotherm model gave the most adequate fitting. Indeed, non-ionized P4VP chains at investigated pH can coordinate only with a particular amount of Hg(II), and once adsorbed, no interaction between adsorbed species is expected. The U(VI) adsorption mechanism onto PB2MP, however, may differ from that of Hg(II) onto P4VP, since phosphate group of PB2MP can possess both ion-exchange character and chelating effect at pH close to neutral. Although Langmuir isotherm model was proved to be the most appropriate for describing the experimental data among considered two-parameter isotherm models, it nevertheless may be more complex than a simple monolayer adsorption. To strengthen the latter observation, obtained Langmuir sorption equilibrium constants  $b$ , representing metal ion binding affinity to the given adsorption sites, can be compared between these three different adsorbing systems as follows:  $b(\text{Pb(II)}\cdot\text{PAA}) < b(\text{U(VI)}\cdot\text{PB2MP}) < b(\text{Hg(II)}\cdot\text{P4VP})$ . The higher the  $b$  values, the greater affinity of the ions studied towards adsorbent. The ascending order demonstrates a transition from pure inherent to PAA electrostatic nature of interaction to metal-ligand coordination in case of P4VP, and PB2MP complexation character in between. To find out the extent of two possible complexation mechanisms of uranyl and validate adsorption isotherm results, XPS and TRPL measurements were performed of uranyl adsorbed membranes (see chapter 8).



## Chapter 7

# Functionalised nanoporous membranes conversion into electrodes

The purpose of the present work is to develop novel electrochemical sensors for toxic metal detection. To do so, the functionalised track-etched PVDF membranes must be transformed into electrodes. The first step in developing an electroanalytical method is the selection of working electrode material. Gold was chosen as it was already used for low concentrations measurements of many metal ions, notably mercury [122, 124, 125] and uranium [143, 144, 154].

As long as we deal with nanometer pore radii, thickness of the gold layer should be thin enough to prevent from pore blockage, and thick enough to carry sufficient conductivity. To determine an optimal electrode thickness, various thickness gold layers were deposited using a cathodic evaporator Quorum Q 150R S. Figure 7.1a shows obtained electrode resistance measured along with SW-ASV peak current of mercury(II) according to the established

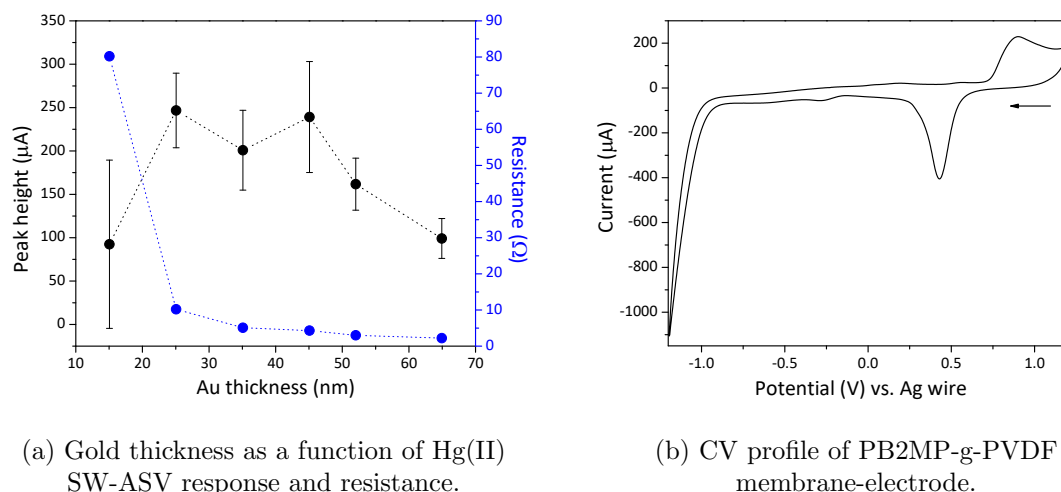


Figure 7.1: Functionalised membrane conversion into electrodes.

voltammetry protocol (see chapter 8). The 35 nm gold thickness was found to give better sensor response and represented a low resistance, thus was chosen as optimal. Despite the fact that gold thickness is only 35 nm (0.8 cm in diameter), a typical cyclic voltammetry profile of amorphous gold electrode was registered. The voltammogram was recorded in 50 mM acetate buffer and 100 mM  $\text{KNO}_3$  (pH3) at a scan rate of  $100 \text{ mV}\cdot\text{s}^{-1}$  (figure 7.1b).

Once track-etched PVDF membranes are grafted, a 35 nm thick gold layer is deposited on each side of the membrane through a mask. Figure 7.2 shows FESEM images before and after gold deposition. As can be seen from the images, this layer thickness does not block the nanopores and does not affect significantly the pore radii.

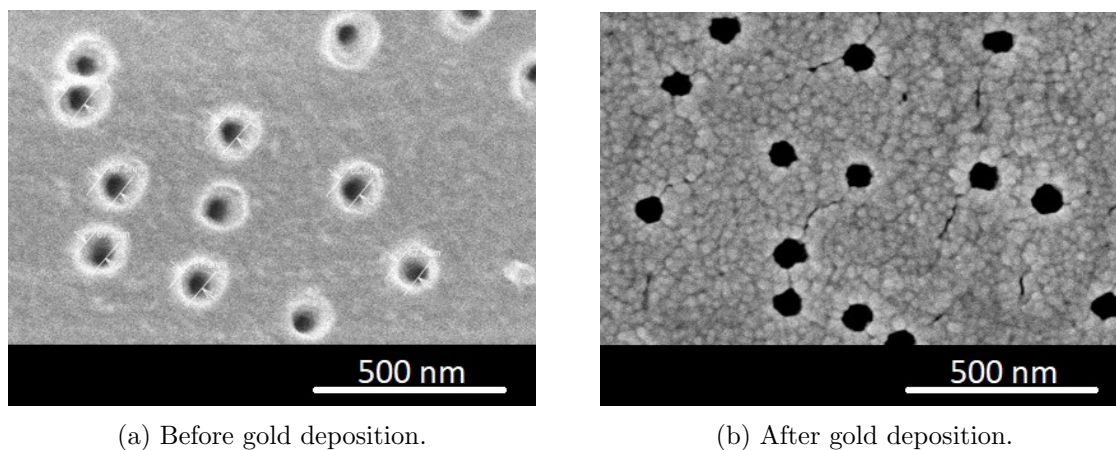


Figure 7.2: FESEM images of P4VP-g-PVDF membranes a) before and b) after deposition of 35 nm gold layer using a cathodic evaporator Quorum Q 150R S.

## Conclusion

For electrochemical determination, track-etched membranes grafted with functional polymers were converted into electrodes by depositing a 35 nm thick gold layer onto each side through a mask. FESEM investigations revealed no considerable effect on nanopore radii. Despite the gold thickness of only 35 nm, a typical cyclic voltammetry profile of amorphous gold electrode was registered.

The functionalisation is a crucial characteristic for sensor determining its selectivity towards toxic metal ions of interest. Chapter 8 will be mainly focused on complexation mechanisms between PAA, P4VP, and PB2MP grafted inside the nanopores of track-etched PVDF membranes with Pb(II), Hg(II) and U(VI) ions dissolved in aqueous solutions and their subsequent detection by stripping voltammetry.

## Chapter 8

# Voltammetry detection

This chapter reports on mechanisms of selective toxic metal preconcentration by functionalised track-etched PVDF membrane-electrodes and their subsequent detection by stripping voltammetry. The PAA grafted membrane-electrodes were used for Pb(II) trace detection. Despite their low limits of detection (LODs) in deionized water of 0.3 ppb for  $10^9 \text{ cm}^{-2}$  and 0.13 ppb for  $10^{10} \text{ cm}^{-2}$  [187], these sensors were found to have a strong matrix and pH effect due to cation-exchange character of PAA. To go beyond these limitations, the sensors were functionalised with selective polymers, namely P4VP and PB2MP (chapter 5) and used herein for Hg(II) and U(VI) detection.

For adsorption, the membrane-electrodes were placed in glass or plastic bottles containing aqueous metal-spiked solutions and stirred using an orbital shaker or magnetic stir bar during equilibrium adsorption time (figure 8.1). Adsorption is passive meaning that application of potential is not needed to preconcentrate ions from solution. During adsorption, solvated

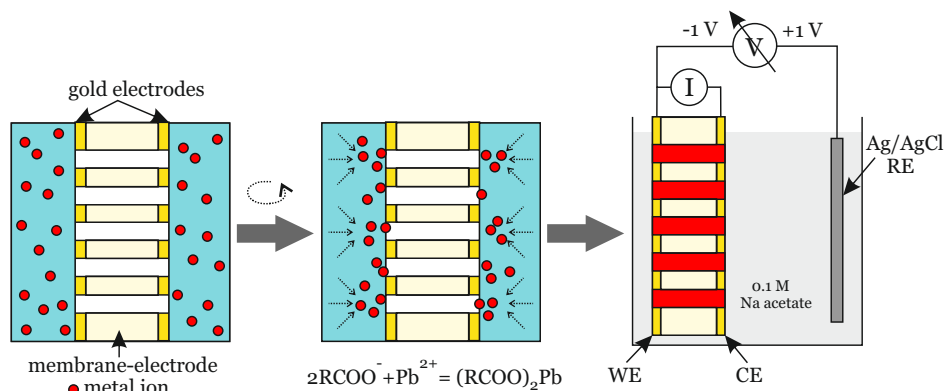
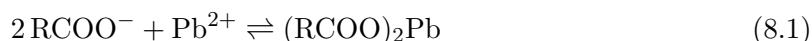


Figure 8.1: Working principle of sensor.

metal ions interact with functional groups in the nanoporous region of grafted track-etched PVDF membrane. When PAA grafted, metal cations electrostatic interaction with ionized carboxyl groups takes place:



After adsorption, each membrane-electrode is transferred into a electrochemical cell for measurement. Stripping voltammetry (SV) technique combined with square-wave potential waveform (further will be referred as SW-ASV) was used for toxic metal detection as it is the most sensitive technique for trace concentration analysis (see chapter 4). The experimentally determined parameters for Pb(II), Hg(II), and U(VI) differ one from another, thus will be presented in three separate sections.

To connect the membrane-electrodes to a potentiostat, a home-made clip was utilized (figure 8.2). The clip is made of poly(methyl methacrylate) (Plexiglas) with two inserted gold

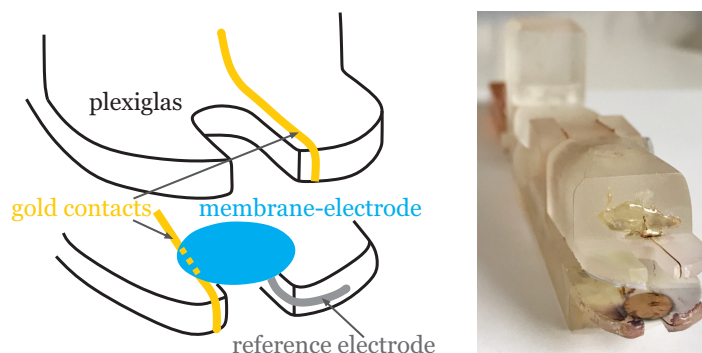


Figure 8.2: Schematical image and photo of a home-made clip used for membrane-electrode connection to a potentiostat.

wires to provide an electrical contact between gold surfaces of the membrane-electrode and potentiostat. A silver wire played the role of pseudo-reference electrode. The PalmSens (The Netherlands) potentiostat arranged with the home-made clip was used for all lab-scale tests.

## 8.1 Toxic metal preconcentration from water

The selective preconcentration of certain heavy metal ions and not the others is a key issue for any sensor, especially if concentration of the analyzed contaminant is low. For this purpose various functional polymers can be used. This work concerns mainly PAA, P4VP, and PB2MP for selective preconcentration of Pb(II), Hg(II), and U(VI) ions from aqueous solution.

Conventionally, functional polymers can be classified into three main divisions: i) cation-exchangers, ii) anion-exchangers, and iii) chelating polymers. The choice of an effective chelating polymer is dictated by its physical-chemical properties (acid-base character of the metal ion species and the polymer, selectivity, adsorption capacity, kinetic and stability characteristics). One of the rules of selection is based on the concept of hard and soft acids and bases. The functional groups (more precisely, donor or ligand atoms) in chelating polymers usually act as bases (oxygen-containing are hard, sulphur-containing are soft, and nitrogen-containing have an intermediate character).

Table 8.1 shows the Hard and Soft Acids and Bases (HSAB) classification according to Pearson [188]. It gives a preliminary guide for donor atom selection. A *base* here is an electron-pair donor, and an *acid* is an electron-pair acceptor. In other words, “hard” bases hold their electrons tightly (they are of high electronegativity and low polarizability) whereas “soft” bases are easily oxidized (conversely, of low electronegativity and high polarizability). The typical acid-base reaction is



The coordination compound or acid-base complex A:B is formed through *coordinate covalent* bond. All metal ions are Lewis acids; they are frequently found coordinated to several bases, or ligands, simultaneously since they are polyvalent. A general simple rule proposed by Pearson in 1963 says: *hard acids bind strongly to hard bases and soft acids bind strongly to soft bases*. For instance, if it was decided to design a ligand specific for Fe<sup>3+</sup>, which is hard acid, and thus a hard donor atom (base) such as the negatively charged oxygen donor would be chosen.

Normally, metal ions exist in water as hydrated ions or as a complex species in association with various anions (Cl<sup>-</sup>, CO<sub>3</sub><sup>2-</sup>, HPO<sub>4</sub><sup>2-</sup>, etc.). To convert a metal ion into an extractable

Table 8.1: A classification of Acids and Bases according to the HSAB principle of Pearson [188].

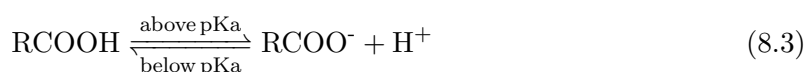
<b>Acids</b>	
<b>Hard</b> H <sup>+</sup> , Li <sup>+</sup> , Na <sup>+</sup> , K <sup>+</sup> Be <sup>2+</sup> , Mg <sup>2+</sup> , Ca <sup>2+</sup> , Sr <sup>2+</sup> , Ba <sup>2+</sup> Al <sup>3+</sup> , Sc <sup>3+</sup> , Ga <sup>3+</sup> , In <sup>3+</sup> , La <sup>3+</sup> Gd <sup>3+</sup> , Lu <sup>3+</sup> , Cr <sup>3+</sup> , Co <sup>3+</sup> , Fe <sup>3+</sup> , As <sup>3+</sup> Si <sup>4+</sup> , Ti <sup>4+</sup> , Zr <sup>4+</sup> , Hf <sup>4+</sup> , Th <sup>4+</sup> , U <sup>4+</sup> Pu <sup>4+</sup> , Ce <sup>4+</sup> , WO <sup>4+</sup> , Sn <sup>4+</sup> UO <sub>2</sub> <sup>2+</sup> , VO <sup>2+</sup> , MoO <sup>3+</sup>	<b>Soft</b> Cu <sup>+</sup> , Ag <sup>+</sup> , Au <sup>+</sup> , Tl <sup>+</sup> , Hg <sup>+</sup> Pd <sup>2+</sup> , Cd <sup>2+</sup> , Pt <sup>2+</sup> , Hg <sup>2+</sup> CH <sub>3</sub> <sup>+</sup> Hg, Co(CN) <sub>5</sub> <sup>2-</sup> , Pt <sup>4+</sup> Te <sup>4+</sup> , Br <sup>+</sup> , I <sup>+</sup>
<b>Borderline</b>	
Fe <sup>2+</sup> , Co <sup>2+</sup> , Ni <sup>2+</sup> , Cu <sup>2+</sup> , Zn <sup>2+</sup> , Pb <sup>2+</sup> Sn <sup>2+</sup> , Sb <sup>3+</sup> , Bi <sup>3+</sup> , Rn <sup>3+</sup> , Ir <sup>3+</sup> , B(CH <sub>3</sub> ) <sub>3</sub>	
<b>Bases</b>	
<b>Hard</b> H <sub>2</sub> O, OH <sup>-</sup> , F <sup>-</sup> , CH <sub>3</sub> CO <sub>2</sub> <sup>-</sup> , PO <sub>4</sub> <sup>3-</sup> SO <sub>4</sub> <sup>2-</sup> , Cl <sup>-</sup> , CO <sub>3</sub> <sup>2-</sup> , ClO <sub>4</sub> <sup>-</sup> , NO <sub>3</sub> <sup>-</sup> ROH, RO <sup>-</sup> , R <sub>2</sub> O, NH <sub>3</sub> , RNH <sub>2</sub> NH <sub>2</sub> NH <sub>2</sub>	<b>Soft</b> R <sub>2</sub> S, RSH, RS <sup>-</sup> , I <sup>-</sup> , SCN S <sub>2</sub> O <sub>3</sub> <sup>2-</sup> , R <sub>3</sub> P, R <sub>3</sub> As, (RO) <sub>3</sub> P CN <sup>-</sup> , RNC, CO, C <sub>2</sub> H <sub>4</sub> , H <sup>-</sup> , R <sup>-</sup>
<b>Borderline</b>	
C <sub>6</sub> H <sub>5</sub> NH <sub>2</sub> , C <sub>5</sub> H <sub>5</sub> N, N <sub>3</sub> <sup>-</sup> , Br <sup>-</sup> , NO <sub>2</sub> <sup>-</sup> , N <sub>2</sub> , SO <sub>3</sub> <sup>2-</sup>	

species, its charge must be neutralized and some or all of its water molecules from hydration shell replaced. Suppose a M<sup>z+</sup> is a hard acid, which is in water already associated with hard H<sub>2</sub>O ligands. If there was a soft base, the ligand substitution will not be favourable. Thus, the nature of the functional group of chelate polymer and/or its donor atom capable of forming complexes with the metal ions in solution are greatly significant for successful toxic metal extraction.

## 8.2 PAA-g-PVDF membrane-electrodes

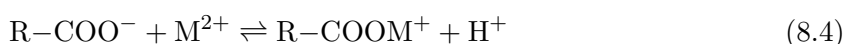
This section reports on using PAA-g-PVDF membrane-electrodes for Pb(II) determination, its advantages and possible limitations since PAA is known to retain not only such divalent cations as Pb<sup>2+</sup>, Cu<sup>2+</sup>, Ni<sup>2+</sup> and Cd<sup>2+</sup> [189, 190], but also some trivalent and even tetravalent cations [191]. For this reason it is often used as a cation-exchanging polymer in ultrafiltration membranes.

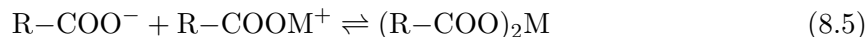
High retention capacity of PAA is attributed to its ability electrostatically interact with metal ions through complex formation with carboxylates. The carboxyl group (-COOH) of PAA is a weak acid and partially dissociates in water (eq. 8.3). The pKa of PAA is 4.5 [192], meaning that at pH values below 4.5 functional groups are predominantly protonated whereas, at pH higher than pKa, degree of



dissociation  $\alpha$  of carboxyl groups sharply increases ( $\alpha=0.97$ ) and reaches 1 at pH 9 [193].

Tomida et al. [194] expressed a complexation model between carboxylate and divalent metal cations as follows





### 8.2.1 Lead(II) detection

PAA-g-PVDF membrane-electrodes were used for trace determination of Pb(II) as previously reported [187]. The first step is a passive adsorption during which the solvated Pb(II) ions interact with carboxylates of PAA-g-PVDF membrane-electrode and become adsorbed (coordinated). For adsorption, the PAA-g-PVDF membrane-electrodes were immersed into Pb(II)-spiked solutions of various concentrations for 30 minutes. Once adsorbed, each membrane-electrode was transferred into electrochemical cell for measurement. As aforementioned, each membrane-electrode was connected to a potentiostat through a home-made clip shown in figure 8.2 and immersed into 0.1 M sodium acetate electrolyte (pH 4.5). SW-ASV is a two-step analysis (see chapter 4). SW-ASV parameters were: deposition potential  $E_{dep} = -0.8$  V,  $t_{dep} = 100$  seconds, SW frequency  $f = 25$  Hz, SW amplitude  $E_{SW} = 25$  mV step amplitude and potential modulation  $\Delta E = 4$  mV. During deposition step, a difference of potential of  $-0.8$  V is applied between a gold working electrode (WE) and the silver wire pseudo-reference electrode (RE) during 100 sec in order to reduce Pb(II) ions insoluble species. Coordinated by carboxylates Pb(II) ions driven by negative electrode potential migrate to the electrode surface and reduce



forming a lead metallic species onto gold. To determine the amount of the deposited lead, the potential is then switched in a positive direction and SW potential waveform scan is applied enabling oxidation of the metallic lead back to the electrolyte



while measuring current, which corresponds to the electron flow from the deposited lead oxidation. Redox potential of this reaction is seen at  $-0.05$  V *versus* a silver wire. Figure 8.3 shows a calibration curve acquired from PAA-g-PVDF membrane-electrodes adsorbed

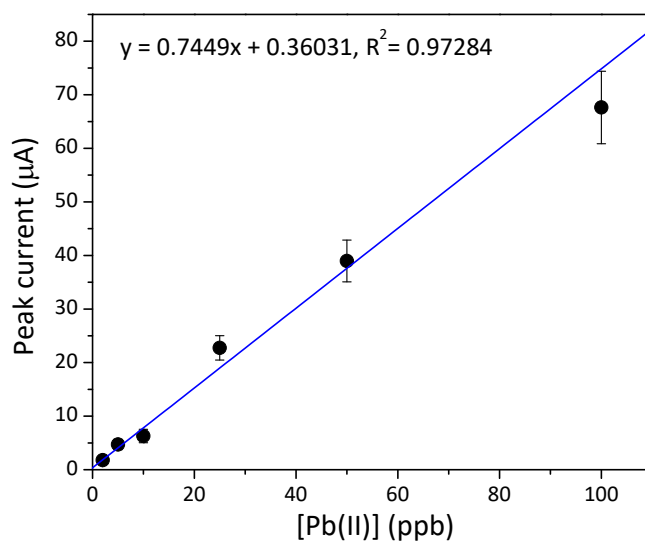


Figure 8.3: Calibration curve for PAA-g-PVDF membrane-electrodes adsorbed in solutions of various Pb(II) concentration, fluence is  $10^9$   $\text{cm}^{-2}$ .

in solutions of various Pb(II) concentrations (each point corresponds to three independent membrane-electrodes). The estimated LOD ( $3\sigma/\text{slope}$ ) equals to 1.5 ppb.

Figure 8.4 represents the coordination scheme of Pb(II) ions by the two carboxylates of PAA. When deprotonated, the carboxylate groups can be more accurately depicted by a pair of reso-

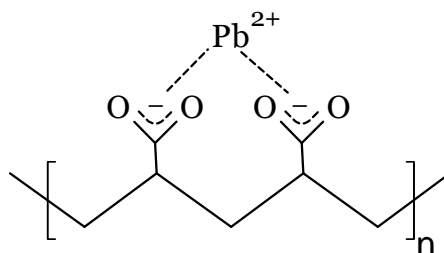


Figure 8.4:  $(R-COO)_2Pb$  complex formation with carboxylates of PAA.

nance structures or alternatively by a single structure, representing the resonance-delocalized  $\pi$  bond and the negative charge located between two oxygens.

The optimization of the  $E_{dep}$ ,  $t_{dep}$ , and adsorption time for Pb(II) was done in the following way [187]: the  $E_{dep}$  was determined by immersing a membrane-electrode in 50 ml of stirred 3 ppb Pb(II) solution for 10 minutes followed by SW-ASV measurement. The charge was increasing with decreasing deposition potential (figure 8.5a). The local minimum at  $-0.9$  V is likely due to the hydrogen gas bubbles from proton reduction at the electrode surface that could impair Pb(II) deposition:



For potentials more negative than  $-0.8$  V there was a problem with the gold electrode adhesion due to the formation of hydrogen gas bubbles. Therefore, a  $E_{dep} = -0.8$  V was used

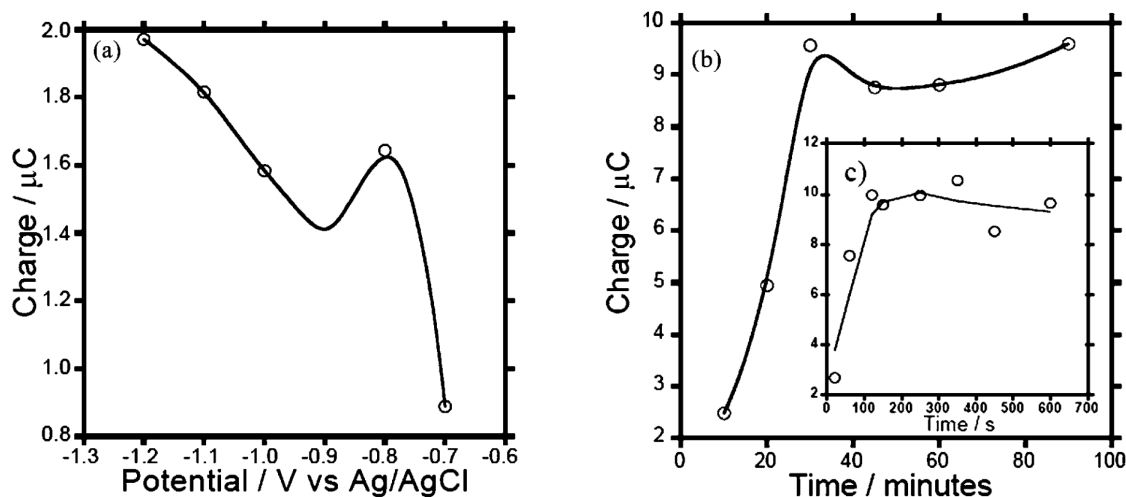


Figure 8.5: (a) SW-ASV of PAA-g-PVDF membrane-electrodes after immersion into 50 ml of stirred 3 ppb Pb(II) samples for 10 minutes at various  $E_{dep}$ ; (b) charge versus adsorption time ( $E_{dep} = -0.8$  V); (c)  $t_{dep}$  versus charge after 30 minutes adsorption into 3 ppb Pb(II) ( $E_{dep} = -0.8$  V) [187].

for all measurements. The absorption time was determined by immersing a PAA-g-PVDF membrane-electrode in 50 ml of a 3 ppb Pb(II) solution for different times followed by SW-ASV using  $E_{dep} = -0.8$  V (figure 8.5b). After 30 minutes equilibrium was established. Figure 8.5c shows the charge as a function of  $t_{dep}$ . After 100 seconds a plateau was reached, thus a minimum  $t_{dep}$  of 100 seconds was fixed for all measurements.

### 8.2.2 Multi-ion detection

Figure 8.6 shows the SW-ASV voltammogram obtained by PAA-g-PVDF membrane-electrode adsorbed in a multi-ion solution of 25 ppb of Co(II), Ni(II), Pb(II) and Cu(II) versus Ag/AgCl electrode. This is an example of aforementioned PAA capability of complexing with different

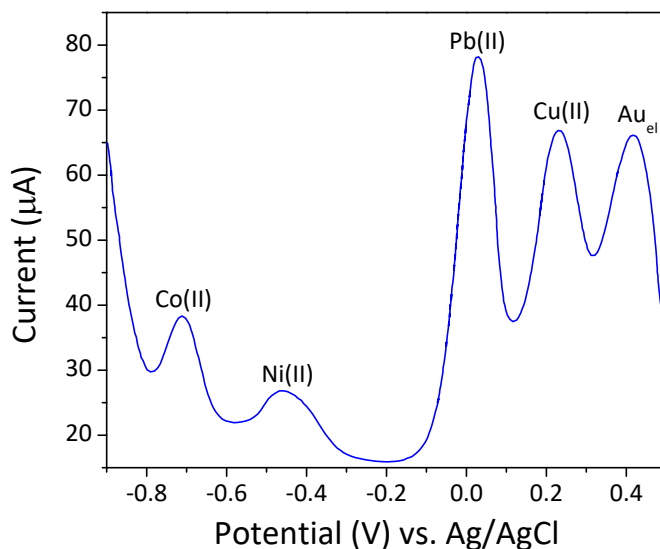


Figure 8.6: SW-ASV voltammogram of PAA-g-PVDF membrane-electrode adsorbed in multi-ion solution 25 ppb of Co(II), Ni(II), Pb(II) and Cu(II). Fluence is  $10^{10} \text{ cm}^{-2}$ .

divalent metal cations. At  $E_{dep} = -0.8 \text{ V}$  several different metal ions can be reduced and subsequently determined. It is, on the one hand, advantageous because these membrane-electrodes can be used for multi-ion detection, which could be ideal from practical point of view. On the other hand, it causes complex issue because there is always a competitive complexation of various metals and strong matrix effect is expected.

The effect of the matrix and co-adsorption of several metals is very complex. Attempts were made to understand the adsorption process in simulated seawater solutions for some of those shown in figure 8.6. Figure 8.7 demonstrates calibration curves obtained by SW-ASV from PAA-g-PVDF of  $10^{10} \text{ cm}^{-2}$  fluence adsorbed in saline solutions containing Cu(II) or Pb(II). The saline solution compositions were: 9 g (solution of 10 g/L salt) or 49 g (solution of 50 g/L salt) of NaCl, 0.77 g of KCl, 0.11 g of CaCl<sub>2</sub>, 0.20 g of MgCl<sub>2</sub>, 0.01 g of Na<sub>2</sub>SO<sub>4</sub> and 0.09 g of NaHCO<sub>3</sub>. All the solutions were spiked with petroleum (total organic carbon, TOC) of 185 mg/L or 59 mg/L. As can be seen in figure 8.7 (left), the presence of salt and TOC regardless the concentration decreases the Pb(II) uptake. It can be due to Pb(II) chloride complex formation since the presence of salts in such concentrations changes its speciation compare to that in deionized water (Pb(OH)<sub>2</sub>) and coordination with carboxyl groups of PAA becomes unfavourable. Simultaneously, as pH is slightly more basic (due to NaHCO<sub>3</sub>), most carboxyl groups are ionized (deprotonated). The K<sup>+</sup>, Na<sup>+</sup>, Mg<sup>2+</sup> and Ca<sup>2+</sup> ions will be competitively attracted by  $-\text{COO}^-$  until reaching the equilibrium. Karppi et al. [195] studied K<sup>+</sup> and Mg<sup>2+</sup> adsorption using PAA-g-PVDF membranes. The authors found out that addition of Ca<sup>2+</sup> and Na<sup>+</sup> to the adsorption medium reduces the of K<sup>+</sup> and Mg<sup>2+</sup> uptake due to co-adsorption competition. Divalent Ca<sup>2+</sup> reduces more efficiently than monovalent Na<sup>+</sup>. As a result, the affinity of the PAA-g-PVDF membranes was determined to be increasing in the order  $\text{Na}^+ < \text{K}^+ < \text{Mg}^{2+} < \text{Ca}^{2+}$ . It is in accordance with previous studies of other authors [196]. This means that tightly binded Ca<sup>2+</sup> competes Pb<sup>2+</sup>, limiting its uptake. In case of Cu(II) adsorption (figure 8.7, right), however, higher ionic strength caused

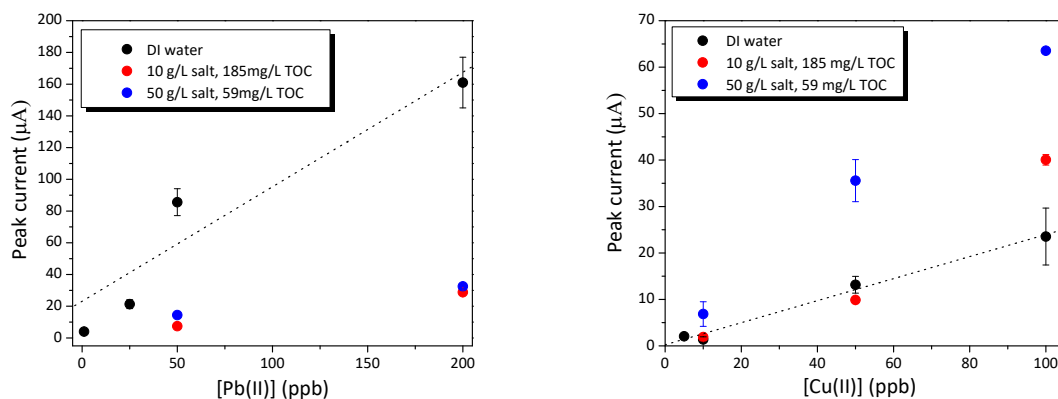


Figure 8.7: Calibration curves for PAA-g-PVDF membrane-electrodes adsorbed in solutions of various Pb(II) or Cu(II) concentration at different salinity and TOC content, fluence is  $10^{10}$   $\text{cm}^{-2}$ .

higher peak currents, *i.e.* enhanced Cu(II) uptake. The enhanced  $\text{Cu}^{2+}$  adsorption, possibly, is due to the more favoured ion-exchange between coordinated cations of salts and  $\text{Cu}^{2+}$ . Several authors reported high  $(\text{R}-\text{COO})_2\text{Cu}$  complex stability, which in presence of other divalent metals decreases in the order  $\text{Cu(II)} > \text{Pb(II)} > \text{Zn(II)} > \text{Ni(II)}$ ,  $\text{Co(II)}$  [191, 197]. Although there are many reports on PAA retention ability, there is still no clear idea why  $\text{Cu}^{2+}$  has superior affinity to carboxylates of PAA. Perhaps, it is assigned to similar ionic radii which allows to Cu(II) with less sterical hindrance to be coordinated. Indeed, salinity affects the PAA swelling behaviour. When counterbalanced with cations present in salted solution, chain shrinking takes place. Metal ions, even those having superior affinity like Cu(II), have to have comparable ionic radii for successful cation-exchange. Also, if a complex formation involves ligand substitution, in case when metal cation is coordinated with anions present in the solution, for certain metal cations the ligand substitution may be slow or unfavourable. Nevertheless, these encouraging results require a deeper study and might be a goal for further research, which is beyond the subject of present work.

Even though PAA possesses a high cation-exchange capacity and can retain various toxic metals, its use as a functionalisation for the sensor may bring complex results in real water samples due to co-adsorption and matrix effect, which have to be better understood. Therefore, chelating polymers containing donor atoms seem to be more successful way towards selective preconcentration of toxic metals from water.

### 8.3 P4VP-g-PVDF for mercury(II) detection

In accordance with Pearson classification,  $\text{Hg}^{2+}$  is a soft acid which complex formation with a soft base will be favoured. Besides thiols which form stable complexes with Hg(II), nitrogen-containing polymers is another type of compounds widely used in mercury extraction processes [198–202]. Nitrogen, owning a lone pair of electrons, shares them with Hg(II) ion forming a covalent coordinate bond as schematically shown in figure 8.8.

Figure 8.9 shows mercury speciation at  $[\text{Hg(II)}]=10$  ppb over all pH range in deionized water, predicted by a commercial software (Hydra-Medusa Equilibrium Diagrams). According to the diagram,  $\text{Hg(OH)}_2$  are predominant species at neutral and basic pHs. Solution pH affects both the metal ion speciation and the ionization state of the P4VP functional groups. As was demonstrated in section 5.3.2.3 on zeta-potential measurements of P4VP-g-PVDF, at strong acidic conditions, surface functional groups are protonated, thus interaction with positively charged species may be inhibited. When pH increases, the P4VP deprotonated and therefore

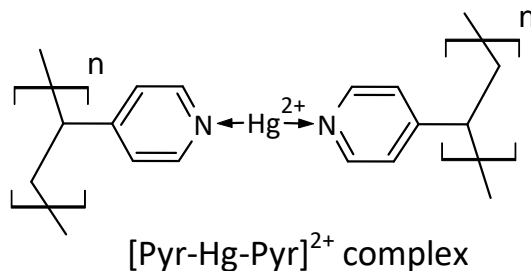


Figure 8.8: Scheme of Hg(II) coordination with P4VP (two associated hydroxyl groups are not shown).

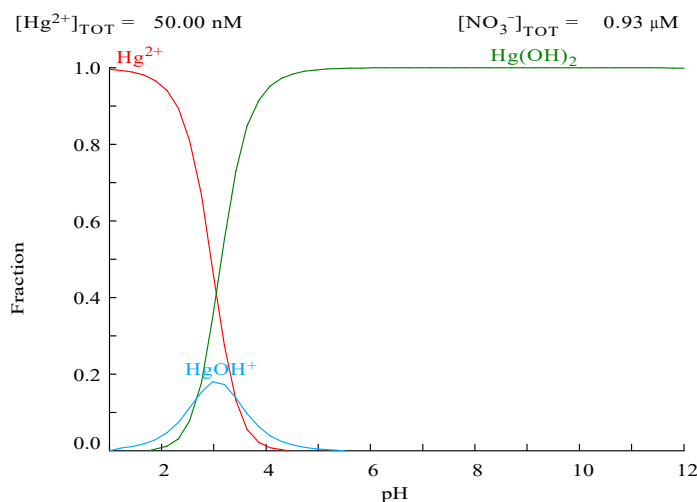


Figure 8.9: Mercury speciation as a function of pH in deionized water,  $[\text{Hg}^{2+}] = 10$  ppb.

the interaction with  $\text{Hg}(\text{OH})_2$  species is promoted.

For the adsorption, the P4VP-g-PVDF membrane-electrodes were immersed into the Hg(II)-spiked solutions for 4 hours of various concentrations according to the established laboratory protocol for the analysis. The concentration range was from 0.5 to 100 ppb. After adsorption, each P4VP-g-PVDF membrane-electrode was connected to a potentiostat for measurement. Similarly to Pb(II), SW-ASV was used for determination of adsorbed Hg(II) species. SW-ASV parameters were: deposition potential  $E_{dep} = -0.8$  V,  $t_{dep} = 50$  seconds, SW frequency  $f = 75$  Hz, SW amplitude  $E_{SW} = 30$  mV step amplitude and potential modulation  $\Delta E = 3$  mV. The solution of 10 mM  $\text{HNO}_3$  and 10 mM NaCl was used as electrolyte. During deposition, Hg(II) species chelated by P4VP migrate to the electrode surface and reduction occurs



Stripping, *i.e.* oxidation of the deposited mercury, is carried out by scanning the potential anodically from  $-0.8$  V to  $+1$  V:



Figure 8.10 displays SW-ASV results using the aforementioned parameters for the fluence of  $10^9 \text{ cm}^{-2}$ . The two calibration curves were plotted using oxidation peak current (left axis) and charge (right axis). One can see that a good linearity for both may be achieved only within the 10 ppb range. A deviation from the linearity was observed for the Hg(II) concentrations higher than 10 ppb pointing out the saturation of the membrane, reaching a maximum membrane uptake. Simultaneously, this is caused by the oxidation peak broadening (inset in figure 8.10) which is common phenomenon for solid electrodes.

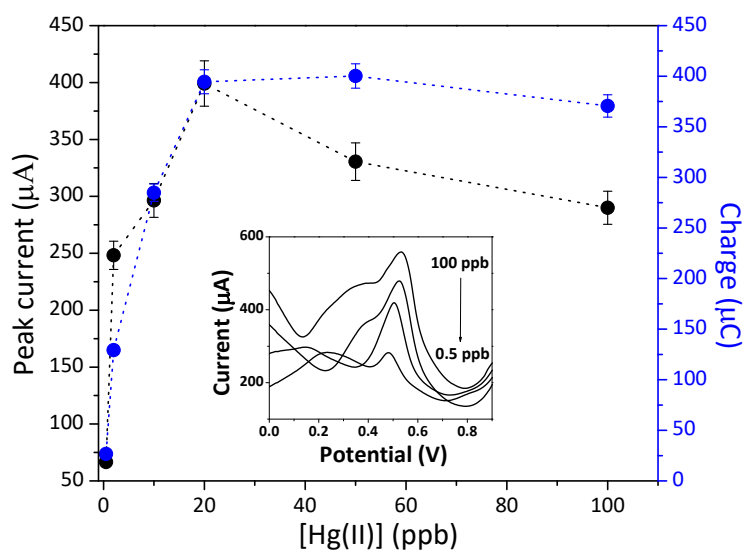


Figure 8.10: Peak current and charge *versus* various Hg(II) concentrations, fluence is  $10^9 \text{ cm}^{-2}$ .

The shoulder-like peak appears when concentration exceeds 10 ppb. It may be explained as follows. During deposition, Hg(II) cations are reduced to their metallic state forming *adatoms* of mercury on gold. At some Hg(II) concentration, the gold surface becomes completely covered with a monolayer of mercury and deposition of the second monolayer starts over the first. It should be noted here that there is no amalgam formation because in this case gold structure would be changed. In our case, oxidation peak of gold remains the same in all voltammograms confirming no structural changes. When deposition is complete, stripping of deposited mercury goes in two steps: i) mercury oxidation from mercury (left shoulder); ii) mercury oxidation from gold (right peak). This leads to appearance of a pre-peak at more negative potential and primary peak broadening. Considering the area under the peak instead of peak height gives better linearity, however the calibration curve still remains bimodal. Nevertheless, the peak height measurement is much simpler from a practical point of view which is more important for sensor's application.

The calibration curves of two various fluences are shown in figure 8.11. One can see that ten times higher fluence (from  $10^9$  to  $10^{10} \text{ cm}^{-2}$ ) gives ten times lower sensitivity (from 0.1 to 0.010 ppb) of the P4VP-g-PVDF membrane-electrodes. Thus, there is a capability to get linear response in a wide concentration range only by varying the membrane density of pores (*i.e.*, fluence).

The imposed limit for mercury in water is 0.015 ppb (French water norms of 27 October 2011). In order to evaluate the quantitative limits of the sensor at very low concentrations, long adsorption times are required, so P4VP-g-PVDF membrane-electrodes were placed in solutions of various Hg(II) concentrations in the range of 0.005–0.100 ppb for 24 hours. The sensors were found to be very sensitive with a LOD of 0.005 ppb [157].

In the presence of numerous metal cations, such as Ni(II), Zn(II), Cd(II), Cu(II), Mg(II), Pb(II) and Ca(II), Hg(II) peak did not exhibit significant interference (figure 8.12a). The studied concentrations were: 5 ppb of Hg(II) in presence of 100 ppb of Ni(II), Zn(II), Cd(II), Cu(II), Mg(II), Ca(II), and 1 ppm of Pb(II). Neither Hg(II) peak area nor peak height was affected within experimental error, except when Fe(II) was present. The interference with Fe(II) ions is in agreement with Bessbousse et al. [157] due to a well-known complex formation between Fe(II) and Hg(II) species in the solution [203]. As a matter of fact, this

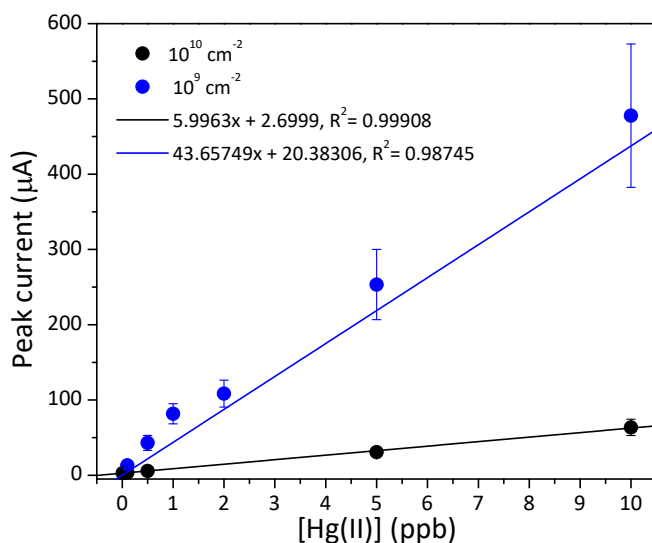
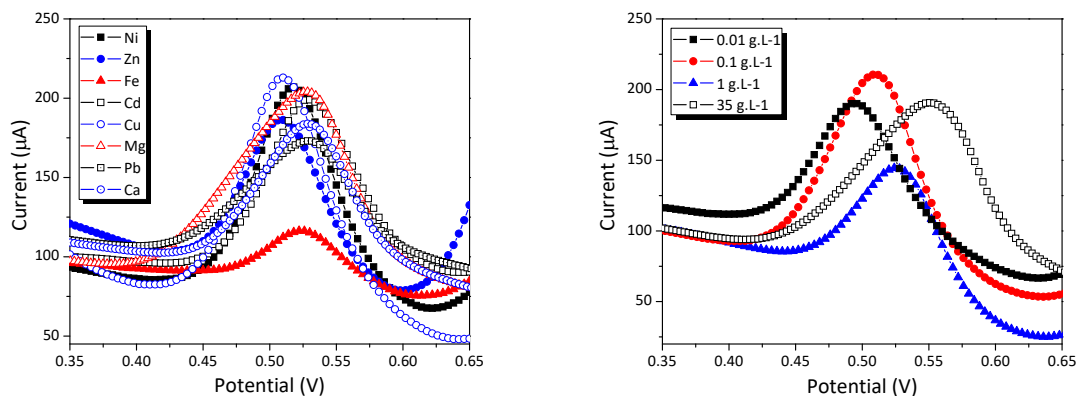


Figure 8.11: Calibration curves after 4 hours of adsorption at two various fluences:  $10^9 \text{ cm}^{-2}$  and  $10^{10} \text{ cm}^{-2}$ . Electrolyte composition is 10 mM  $\text{HNO}_3$  and 10 mM  $\text{NaCl}$ .

complex formation decreased the  $\text{Hg(II)}$  content prior the adsorption by the P4VP-g-PVDF membrane-electrode. The pH effect in the range from 3 to 9 has no impact on  $\text{Hg(II)}$  peak intensity [157].



(a) SW-ASV of 5 ppb  $\text{Hg(II)}$  adsorbed membrane-electrode in presence of 100 ppm interfering metals.

(b) SW-ASV 5 ppb  $\text{Hg(II)}$  adsorbed membrane-electrode in presence of salt of various concentrations.

Figure 8.12:  $\text{Hg(II)}$  interference with other metals and effect of salt [155]. Fluence is  $10^9 \text{ cm}^{-2}$ .

The effect of salt content varying from 0.01 to  $35 \text{ g L}^{-1}$  was also investigated (figure 8.12b). The concentration of  $35 \text{ g L}^{-1}$  of  $\text{NaCl}$  was herein chosen to simulate seawater. As can be seen from the figure, increase of ionic strength slightly shifts the  $\text{Hg(II)}$  oxidation peak towards more positive potentials. This can be caused by change of the gold electrode state during adsorption. Such small potential variations (around 50 mV) are not a problem for the sensor application as far as peak height and area remain unchanged. The electrolyte composition (10 mM  $\text{HNO}_3$  and 10 mM  $\text{NaCl}$ ) used in this study was chosen in purpose. Nitric acid helps to strip adsorbed  $\text{Hg(II)}$  while  $\text{NaCl}$  facilitates mercury chloride complex formation preventing from amalgamation with gold. As chloride concentration changes only in the solutions for

passive adsorption and remains constant in the electrolyte, it affects only on Hg(II) speciation and not to the water insoluble calomel formation during deposition (which is often reported in literature [204–206]). In saline solutions at pH close to neutral, mercury is found in the form of chloride anions  $\text{HgCl}_3^-$  and  $\text{HgCl}_4^{2-}$ . Successful adsorption of the anionic mercury complexes may be assigned to an anion-exchange effect of P4VP [207]. Soaking of P4VP-g-PVDF in  $10^{-2}$  M HCl after grafting promotes P4VP protonation ( $\text{pyrH}^+$ ), which can bind negatively charged species. These results emphasize high selectivity of P4VP toward Hg(II) ions allowing the detection compatible to seawater environment.

Figure 8.13 illustrates the effect of salt and TOC on Hg(II) adsorption by P4VP-g-PVDF

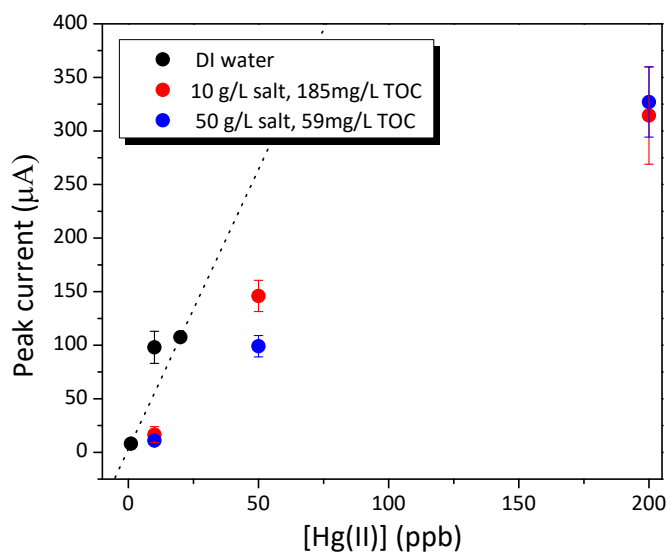


Figure 8.13: Calibration curves for P4VP-g-PVDF membrane-electrodes adsorbed in solutions of various Hg(II) concentration at different salinity and TOC content, fluence is  $10^{10}$   $\text{cm}^{-2}$ .

membrane-electrodes. The solutions represent simulated seawater and are similar to those used in section 8.2.2. As can be seen from the figure, presence of both salts and TOC decrease the Hg(II) peak height. It was demonstrated above that 35 g/L of NaCl content has insignificant effect on Hg(II) uptake. Thus, we can assume that both salt concentrations do not affect greatly on this peak decrease. Based on the preference of a cation for complexation with ligands, mercury is classified as a metal cation with a soft sphere of highly polarizable electrons in its outer shell. Soft metals like mercury show a pronounced preference for such ligands as sulfur, the less electronegative halides, and nitrogen over ligands containing oxygen [208]. In fact, the name “mercaptan” for sulfhydryl compounds (that are contained in small concentrations in petroleum) came from its affinity for mercury. Therefore, a strong interaction between mercury and organic matter is expected. Indeed, addition of 59 mg/L of TOC results in a SW-ASV peak current decrease. Higher TOC content, however, has not proportionally decreased the Hg(II) peak intensity. This issue definitely needs further investigations. A collaboration with a petroleum industrial partner has been recently signed to pursue the study.

## 8.4 PB2MP-g-PVDF for uranium(VI) detection

In the framework of nuclear plant site dismantlement, there is a need of sensitive on-site determination of U(VI) in nearby water and soils. Uranium naturally exists in various oxidation states, namely +2, +3, +4, +5, and +6. The most common and thermodynamically stable

form of dissolved uranium is uranyl ion,  $\text{U}^{\text{VI}}\text{O}_2^{2+}$ . The uranyl ion has a linear structure with two nonreactive double uranium-oxygen bonds, and it tends to create a complex with six ligands at the most, leaving the  $\text{U}=\text{O}$  bonds unaltered [209]. According to Pearson classification, being a hard acid, uranyl has more affinity for hard bases. The compounds, containing oxygen or nitrogen atoms, as well as phosphate or carbonate anions, are good candidates for uranium preconcentration [210–213]. Phosphate containing B2MP shown in figure 8.14a, has

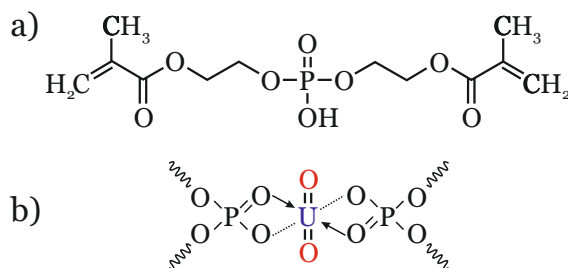


Figure 8.14: (a) Chemical structure of B2MP; (b) scheme of  $\text{U}(\text{VI})$  interaction with a phosphate group of PB2MP (two associated hydroxyl groups are not shown).

been chosen in this work as uranyl chelating polymer. During the past decade, phosphates have proven their selectivity towards uranyl preconcentration [154, 214] and very recently PB2MP [215, 216].

Figure 8.14b schematically shows  $\text{UO}_2^{2+}$  coordination with oxygens of phosphate groups of B2MP. This complex formation, however, was not reported in literature yet. One of the goals of this work is to find out the  $\text{U}(\text{VI})$ -PB2MP coordination mechanism. The  $\text{pK}_a$  value of phosphate diester equals to 1.5 meaning that at pH close to neutral (or, at seawater  $\text{pH}=8.3$ ),  $\text{P}-\text{OH}$  is deprotonated ( $\text{pK}_a < \text{pH}$ ). Thus, two types of interactions are expected: uranyl coordination with  $\text{P}=\text{O}$  and ion-exchange with  $\text{P}-\text{O}^-$ .

Figure 8.15 shows uranyl speciation at 10 ppb concentration in deionized water as a function of pH, predicted by a commercial software (Hydra-Medusa Equilibrium Diagrams). Accord-

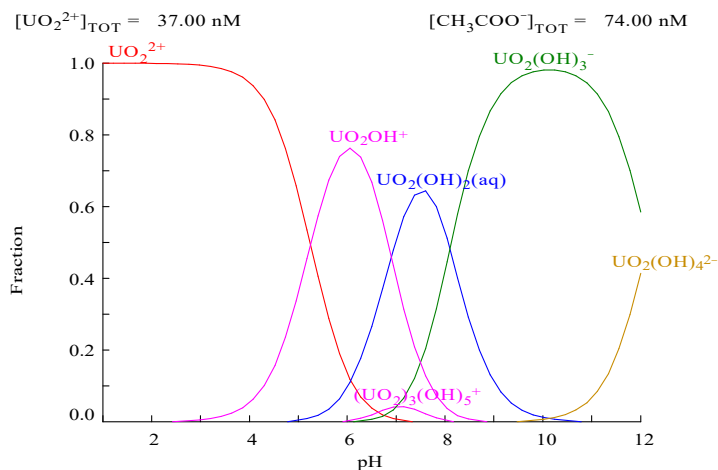


Figure 8.15: Uranium speciation as a function of pH in deionized water,  $[\text{U}(\text{VI})]=10$  ppb.

ing to the diagram, uranyl hydroxide complexes  $\text{UO}_2\text{OH}^+$ ,  $\text{UO}_2(\text{OH})_2$  and  $(\text{UO}_2)_3(\text{OH})_5^+$  are the major species at pH 6-8. While in seawater, containing carbonates, the dominant species of uranyl in aqueous solutions are  $\text{UO}_2\text{OH}^+$ ,  $\text{UO}_2\text{CO}_3$ , and  $\text{UO}_2(\text{CO}_3)_2^{2-}$  [217].

XPS was used to confirm the presence of phosphate groups after radiation grafting of PB2MP and its capability of adsorbing uranyl. Figure 8.16 shows XPS survey spectrum of the PB2MP-g-PVDF membranes of  $10^{10} \text{ cm}^{-2}$  fluence after adsorption in 2 mM uranyl acetate

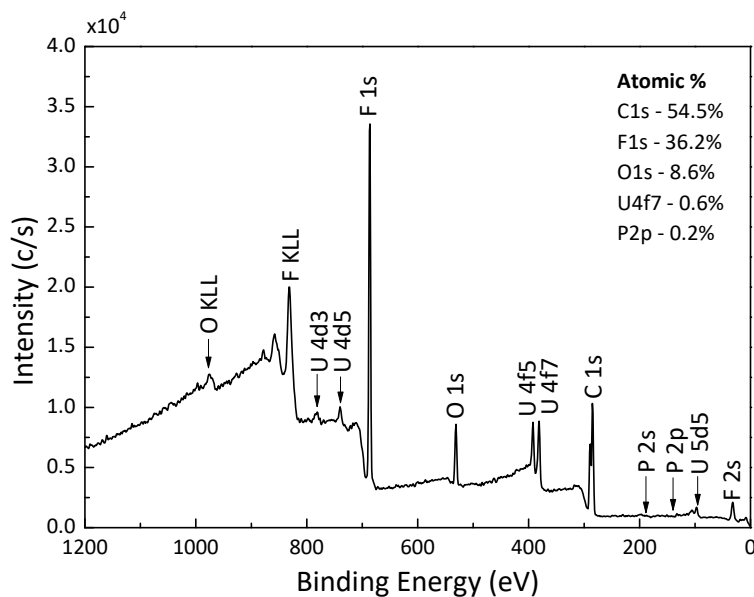
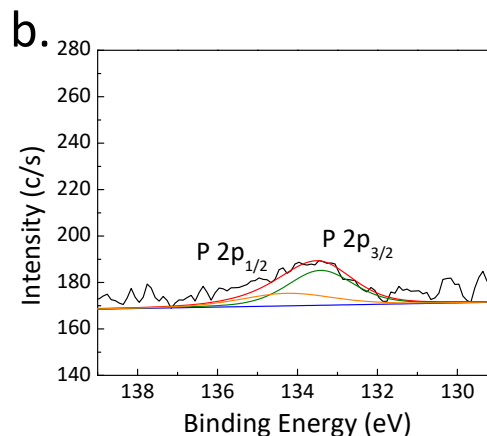
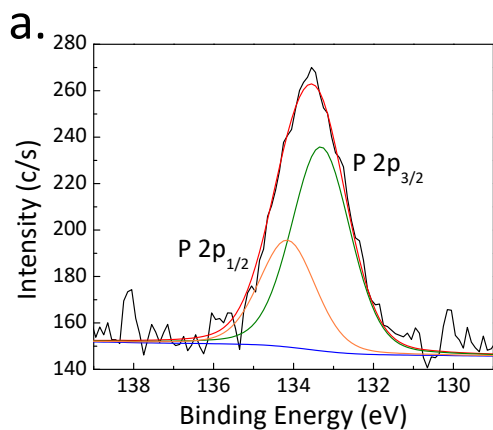


Figure 8.16: XPS survey spectrum of PB2MP-g-PVDF membrane after immersion into 2 mM uranyl acetate solution for 18 hours. Fluence is  $10^{10} \text{ cm}^{-2}$ , GY=3.5 wt.%.

solution for 18 hours. An intense peak of F 1s arises from PVDF. Two main peaks with binding energies of 285.6 eV and 290.1 eV for  $\text{CH}_2$  and  $\text{CF}_2$  species, respectively, assigned to the PVDF main chains. Others, less intense, arise from C-C/H, -C=O, -C-O and -O-C=O groups of grafted PB2MP. The revealed peak at 133 eV (figure 8.17a) confirms the presence of the phosphate groups of PB2MP whose position is in agreement with previous studies [143, 218]. Evidently, no signal of uranium was observed before adsorption (figure 8.17c). After adsorption, oxygen atoms from the uranyl ion shield the phosphate group as they are more electronegative than phosphorus, causing a decrease of the P 2p peak intensity (figure 8.17b) and thus affirming U(VI)-PB2MP complex formation. Figure 8.17d shows the U 4f XPS spectrum of uranyl after the PB2MP-g-PVDF membrane adsorbed uranyl ions. Two peaks at 381.8 and 392.7 eV assigned to the U  $4f_{7/2}$  and U  $4f_{5/2}$  possessing spin orbit splitting of 10.9 eV were detected [219–221], which are attributed to hexavalent uranium state [220, 222–231]. The 381.8 eV is close to 382.3 eV reported by Drot et al. [232] for U(VI) sorbed onto phosphate surfaces.



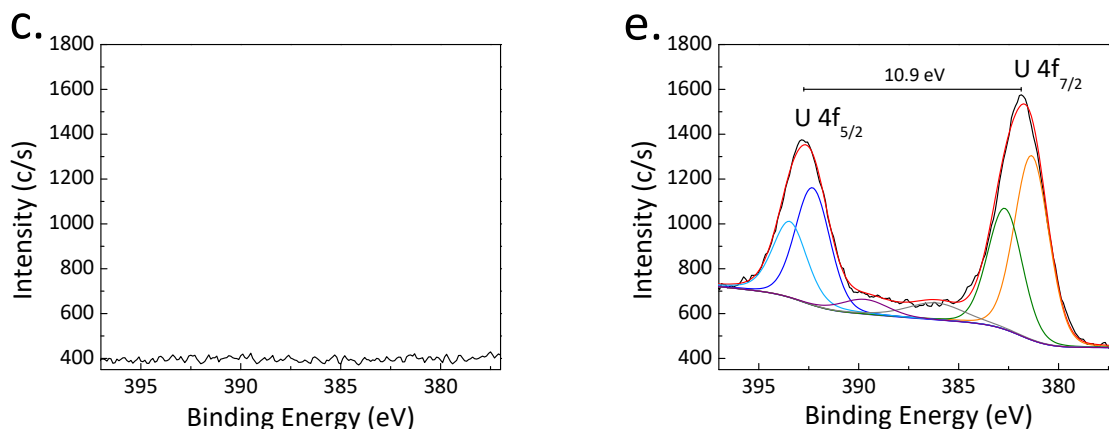
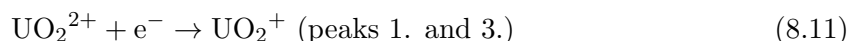


Figure 8.17: (a, b) P 2p peak and (c, d) U 4f peak before and after uranyl adsorption, respectively.

#### 8.4.1 Square wave cathodic stripping voltammetry (SW-CSV)

Uranium(VI) determination was run inversely to aforementioned Pb(II) and Hg(II) procedures. Cathodic stripping voltammetry is advantageous in case of strongly complexing uranium in aqueous media. For adsorption, the PB2MP-g-PVDF membrane-electrodes were immersed into U(VI)-spiked solutions for 7 hours of various concentrations according to the established laboratory protocol. After adsorption, each PB2MP-g-PVDF membrane-electrode was connected to a potentiostat for measurement. SW-CSV was performed as follows. Applying a potential of  $E_{dep} = +1.2$  V during  $t_{dep} = 300$  seconds permits oxidation of adsorbed species on the anode. Square-wave potential scan from +1.2 V to -1.2 V is then performed in order to reduce the oxidated uranyl species. The SW frequency  $f = 20$  Hz, SW amplitude  $E_{SW} = 30$  mV step amplitude and potential modulation  $\Delta E = 3$  mV were utilized. Electrolyte and its pH are important parameters, which have a significant effect on redox mechanism of uranyl [233, 234]. The measurements are preferably to be conducted at  $\text{pH} > 2.5$  to ensure that the limiting current of  $\text{UO}_2^{2+}$  reduction is only dictated by diffusion. Peled et al. [144] reported that a solution of 50 mM acetate buffer (pH3) with 0.1 M  $\text{KNO}_3$  is the best medium for low concentration detection of uranyl in water. Thus, this mixture was used as electrolyte.

Overall redox behaviour of uranium is more complex compare to those of divalent cations. Therefore, cyclic voltammetry was performed first using not adsorbed B2MP-g-PVDF membrane-electrode immersed into uranyl containing electrolyte for initial electrochemical studies of the system and for acquiring qualitative information about the redox reactions. Figure 8.18 shows electron transfer reactions occurring at the electrode surface of PB2MP-g-PVDF membrane-electrode. The black dotted line represents blank CV (electrolyte), the black, red, blue solid lines correspond to 3, 10, and 20 ppm U(VI) concentrations in electrolyte recorded at 100 mV/s scan rate. Arrow indicates the direction of potential scan. The intensive peaks at ca. 0.4 and 0.8 V are associated with reduction of hydrous gold and its oxidation. The first reduction wave at -0.03 V and oxidation at 0.054 V *versus* Ag wire correspond to one-electron reduction and oxidation of uranyl (eq. 8.11) [235].



This gives a standard electrode redox potential of  $E^{0'} = \frac{E_{Ox} + E_{Red}}{2} = 0.026$  mV *versus* Ag wire. The peak-to-peak separation  $\Delta E_{pk} = 51$  mV is smaller than expected for one-electron transfer (69 mV), which can be explained by known disproportionation of the  $\text{UO}_2^+$  into  $\text{UO}_2^{2+}$  and  $\text{UO}_2$  [236]. The second reduction peak seen at -0.5 V is associated with the reduction of  $\text{UO}_2^+$  to the insoluble  $\text{U}^{4+}$ , or  $\text{UO}_2$ , species (eq. 8.12).



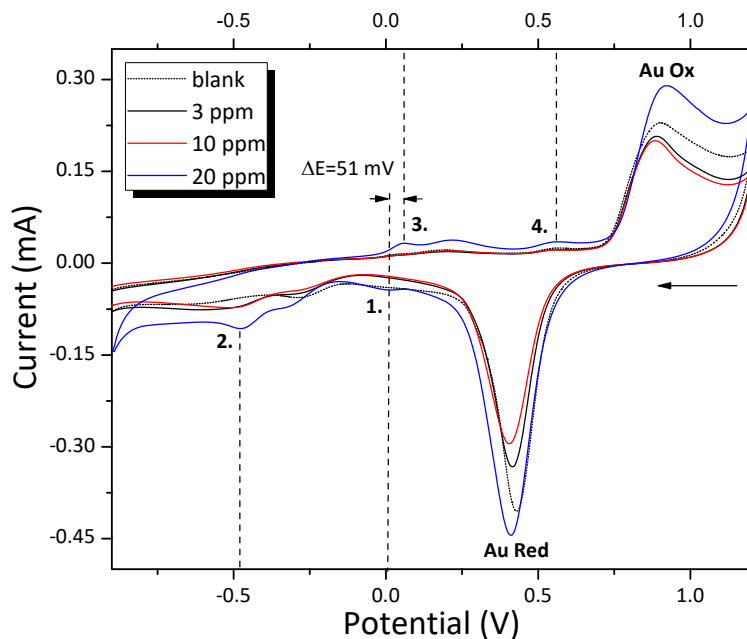


Figure 8.18: Cycling voltammetry of PB2MP-g-PVDF membrane-electrode immersed in U(VI)-spiked 50 mM acetate buffer (pH3) + 0.1 M KNO<sub>3</sub>. Scan rate is 100 mV/s.

The second oxidation peak at 0.5 V is attributed to direct two-electron oxidation of UO<sub>2</sub> to UO<sub>2</sub><sup>2+</sup> (eq. 8.13).



CV measurements were performed also to study the effect of positive potential on the reduction peak U<sup>5+</sup> to U<sup>4+</sup> (peak 2. in figure 8.18). It was clearly observed that scanning from more positive potentials that +0.3 V caused an increase in the reduction peak. The reason is that, when we scanned to more positive potentials, more uranyl species are oxidized and upon scanning in negative direction, more UO<sub>2</sub> precipitated onto electrode, which can be advantageous for uranium extraction.

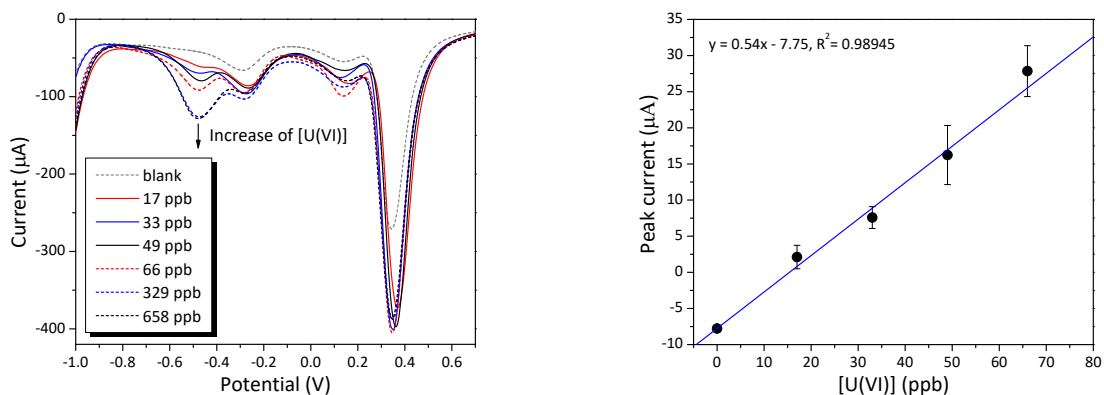


Figure 8.19: SW-CSV voltammograms and calibration curve built at various U(VI) concentrations (uranyl reduction peak raises with concentration) after **2 hours** adsorption at neutral pH. SW-CSV parameters:  $E_{dep} = +1.2$  V,  $t_{dep} = 300$  sec,  $f = 20$  Hz,  $E_{SW} = 30$  mV and  $\Delta E = 3$  mV.

SW-CSV parameters such as  $t_{dep}$ ,  $f$ ,  $E_{SW}$  and  $\Delta E$  were optimized as reported elsewhere [156]. The  $t_{dep}$  was determined by registering the highest current of the reduction peak at -0.5 V

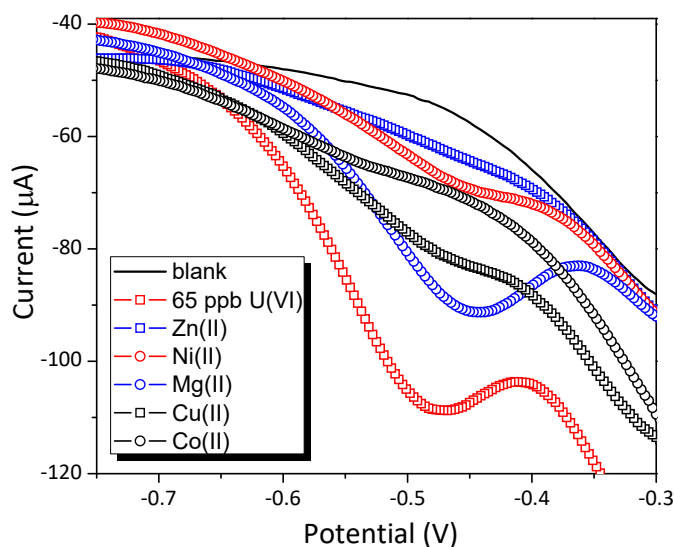


Figure 8.20: Interference with other metal ions.  $[U(VI)]=65$  ppb,  $[interfering\ metals]=650$  ppb.

at 10 ppm U(IV) in electrolyte and a deposition potential of +1.2 V. The optimal  $t_{dep}$  was found equal to 300 sec. The frequency was set at 20 Hz as it is a good compromise between peak height and its resolution.

Figure 8.19 shows SW-CSV voltammograms at set parameters after adsorption in aqueous solutions of various U(VI) concentrations and calibration curve for U(VI) reduction peak at ca. -0.5 V. The calibration curve demonstrates sensitivity of the sensor at ppb level. The LOD ( $3\sigma/slope$ ) of the PB2MP-g-PVDF membrane-electrodes of  $10^{10}$  cm<sup>-2</sup> fluence was found to be equal to 10 ppb, which is three times lower than that of recommended by WHO [237].

Interference with other metals has been studied at 65 ppb U(VI) concentration and 10-fold excess of Zn(II), Fe(II), Ni(II), Mg(II), Cu(II), Co(II) at neutral pH (figure 8.20). Apart from Mg(II), most of metal ions were found interfering with U(VI). As will be presented in section 8.4.2, uranyl is predominantly coordinated by phosphate group of PB2MP and do not ion-exchange. However, it does not mean that other earlier listed metal ions cannot ion-exchange with P-O<sup>-</sup> hindering therefore U(VI) coordination. Change in U(VI) speciation cannot be also excluded. The effect of Fe(II) is not shown in the figure because a broad and intense reduction peak is observed at close potential. Iron(II), however, possesses another problem: reduction of U(VI) to U(IV) in solution [238]. For this reason it is extensively used for UO<sub>2</sub> precipitation in water treatment technology.

#### 8.4.2 Time-resolved photoluminescence (TRPL) measurements

In order to get deeper understanding of uranyl complexation mechanism, time-resolved photoluminescence (TRPL) measurements have been performed on U(VI) adsorbed PB2MP-g-PVDF membranes using the set-up shown in figure 8.21.

Figure 8.22a depicts uranyl fluorescence emission spectra of PB2MP-g-PVDF membranes adsorbed at various U(VI) concentrations at neutral pH. TRPL spectra were recorded under an Indi Nd: YAG laser (Spectra-Physics) of 1.5 mJ energy at excitation wavelength of 355 nm. Detection is performed using an intensified charge-coupled device (ICCD) camera coupled with an Oriel monochromator with a 150 l/mm grating associated to a Stanford

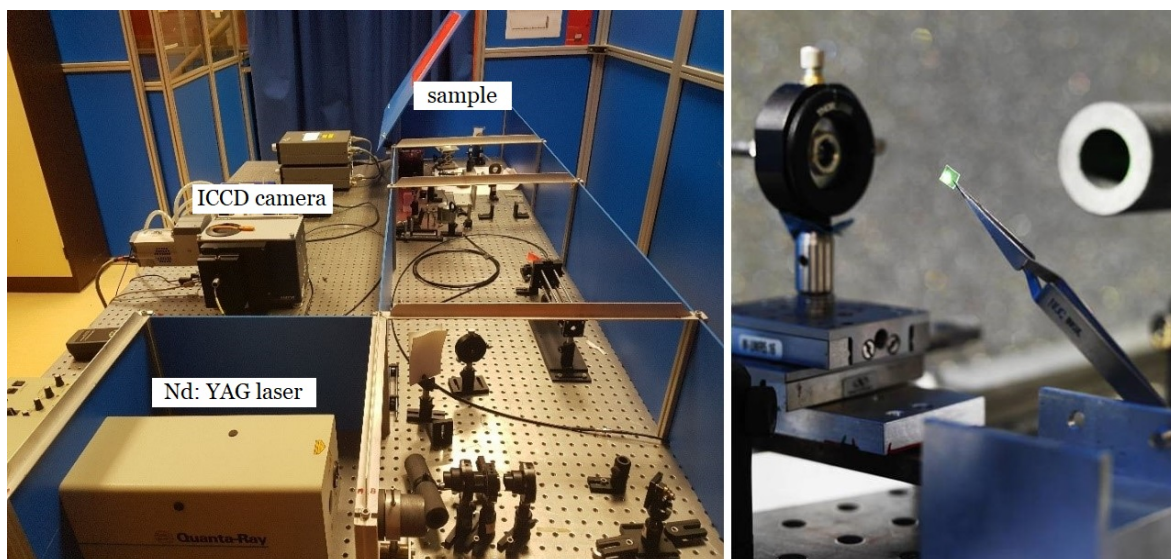


Figure 8.21: Set-up for TRPL measurements.

delay generator. The gate width of 10 ms and gate delay of 400 ns were set. For adsorption, PB2MP-g-PVDF membranes (GY=5 wt.%,  $10^{10} \text{ cm}^{-2}$  fluence) were immersed into stirred U(VI) solutions of various concentrations for 22 hours. Once adsorbed, the membranes were rinsed with deionized water to remove uranyl excess and dried at room temperature. For measurement, each membrane was sealed in quartz cuvette at fixed position. The emission band with four vibronic components at 496, 516, 539 and 565 nm is characteristic  $\text{UO}_2^{2+}$  emission band [239]. Increase of U(VI) concentration up to approximately 100 ppb, resulted in nearly linear increase of PL signal area (figure 8.22b). At higher U(VI) concentrations, the PL signal area levels off confirming the formation a monolayer of adsorbate, where saturatu-

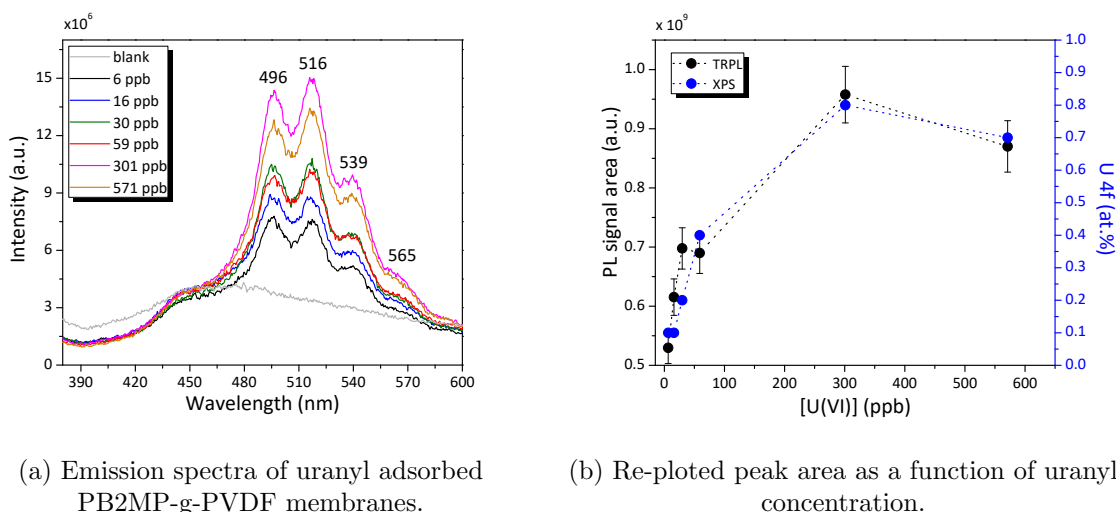


Figure 8.22: Photoluminescence measurements of uranyl adsorbed PB2MP-g-PVDF membranes. Fluence is  $10^{10} \text{ cm}^{-2}$ .

tion occurs. The amount of adsorbed U(VI) correlates with relative atomic concentration of uranium acquired by XPS (U 4f peak). It also demonstrates that PB2MP grafted inside the nanoporous structure of track-etched PVDF remains accessible for uranyl ions.

Attempts were made towards establishing a correlation between GY of PB2MP and U(VI) uptake. Two GYs were compared initially used 5 wt.% and 10 wt.%. It is reasonable to assume that higher GYs will result in higher uranyl uptakes. This is, however, did not work.

The PL signal of U(VI) was almost null even when PB2MP-g-PVDF of 10 wt.% GY were adsorbed in 1 ppm of U(VI). This is likely due to the small specific area of PB2MP contacted with adsorbing solution. It proves that the nanoporous structure plays a great role in pre-concentration.

Figure 8.23a represents the normalized intensities of fluorescence decay of 500 ppb U(VI) adsorbed PB2MP-g-PVDF. Uranyl lifetime was estimated to be 21  $\mu\text{s}$  (against 2  $\mu\text{s}$  of free

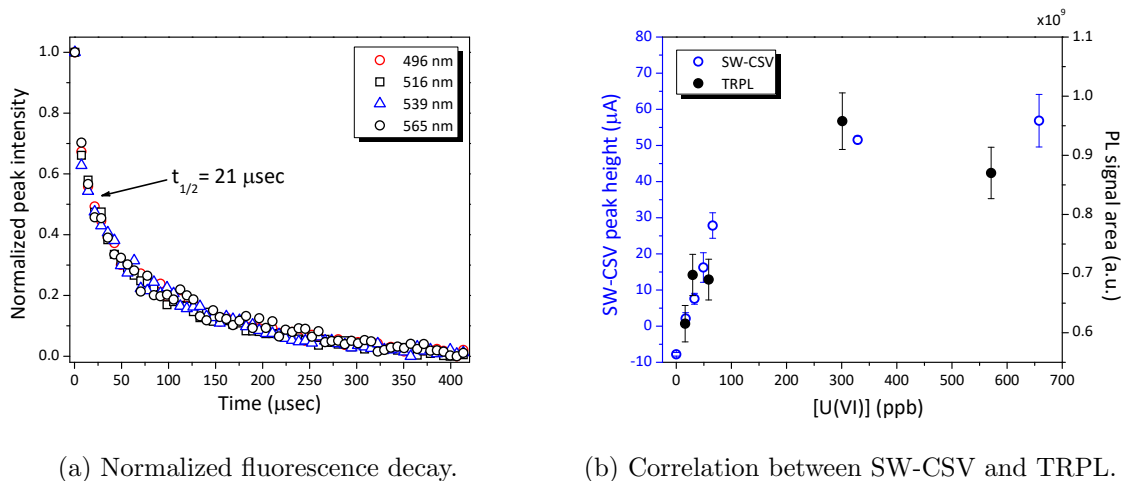


Figure 8.23: Photoluminescence kinetics of uranyl adsorbed PB2MP-g-PVDF membranes and correlation of TRPL with SW-ASV. Fluence is  $10^{10} \text{ cm}^{-2}$ .

$\text{UO}_2^{2+}$  in aqueous solutions [239, 240]) pointing out that i) U(VI) is coordinated, and ii) it is stabilized due to complexation with phosphate group of PB2MP. Scapolan et al. [241] attributed the lifetime of  $24 \pm 2 \mu\text{s}$  to the  $\text{UO}_2\text{PO}_4^-$  species having the vibronic components at 499, 520, 544 and 571 nm, which is in agreement with present results.

The efficiency of U(VI) adsorption was found to be pH dependent. Uranyl solutions prepared in 2%  $\text{HNO}_3$  caused total suppression of characteristic uranyl PL emission band. Indeed, low pHs were found affecting the SW-CSV results acquired by PB2MP-g-PVDF membrane-electrodes. Uranyl adsorption at  $\text{pH} < 4$  resulted in low peak currents whereas neutral and basic pHs consistently gave reproducible responses. As aforementioned in the text, the acidic phosphate groups are expected to bind uranyl ions through ion-exchange with  $\text{P}-\text{O}^-$  at  $\text{pH} \geq 1.5$  ( $\text{pK}_a$  of phosphate diestered 1.5) and coordination of neutral (anion associated) uranyl species at  $\text{pH} < 1.5$ . When acidified with  $\text{HNO}_3$ , uranyl associates with nitrate ions in solution. The absence of both PL and SW-CSV responses of U(VI) might be due to the fact that either nitrate substitution to phosphate does not take place, or there is no stable complex formation between uranyl and  $\text{P}=\text{O}$  because of unsatisfied coordination numbers. Vazquez et al. [242] reported that polyphosphate (polyP) binding energy rather than its coordination geometry may help to explain phosphate interaction with uranyl as a function of pH. In the case of polyP, the authors suggested that U(VI)-polyP forms soluble over a wide pH range complexes in contrast to  $\text{HPO}_4$  where uranyl precipitation takes place, and monodentate (at  $\text{pH} \leq 6$ ) and bidentate (at higher pH) bonding of uranyl with phosphate occurs. If so, then PL characteristic signature of uranyl would appear at low pH for uranyl adsorbed PB2MP-g-PVDF membranes. More probably, the geometrical constraint did not allow uranyl ions to bind with multiple  $\text{P}=\text{O}$  groups to satisfy their coordination numbers. Circumneutral pH favors the formation of positively charged uranyl hydroxide complexes,  $[(\text{UO}_2)(\text{OH})]^+$ , or  $[(\text{UO}_2)_2(\text{OH})_2]^{2+}$ , or  $[(\text{UO}_2)_3(\text{OH})_5]^+$ , or  $(\text{UO}_2)(\text{OH})_2$ , which are transformed into negatively charged at  $\text{pH} > 9$  (figure 8.15). At this pH range, hydrolyzed uranyl species can bind with acidic phosphate groups of PB2MP through mutual ion-exchange and coordination interaction with less hindering in terms of satisfaction of their coordination numbers. Similar to

present results specific uranyl adsorption behaviour was observed by Mhatre et al. [216] onto phosphate grafted teflon films.

Finally, figure 8.23b demonstrates a good correlation of the results obtained by stripping voltammetry and TRPL measurements. It is worth mentioning that consistently detected U(VI) concentration by PB2MP-g-PVDF membranes was as low as 6 ppb which can further be lowered. These results suggest that TRPL may be considered as a serious alternative to stripping voltammetry for U(VI) trace detection.

## Conclusion

This chapter reported on use of several functional polymers, PAA, P4VP and PB2MP, for Pb(II), Hg(II) and U(VI) preconcentration from aqueous solutions and their subsequent detection by stripping voltammetry. PAA-g-PVDF membrane-electrodes were used for Pb(II) and other divalent cation detection, namely Co(II), Ni(II), Cu(II), due to well known cation-exchange character of PAA. Therefore, these sensors can potentially be used for multi-ion analysis. Furthermore, a strong matrix was pointed out for PAA. Indeed, presence of salts affects swelling behaviour of ionized carboxyl groups of PAA. Based on the SW-ASV results, obtained for Cu(II) and Pb(II) adsorbed in simulated seawater solutions, it was suggested that ion-exchange between coordinated cations of salts and Cu(II) ions is favoured due to similar ionic radius, which facilitates stable complex formation compare to that of Pb(II). Nevertheless, these encouraging results require a complex study and might be a goal for further research, which is beyond the subject of present work.

The use of functional polymers, P4VP and PB2MP, containing donor atoms, seem to be the more successful way towards selective preconcentration and limiting matrix effect. P4VP-g-PVDF membrane-electrodes were found selective and sensitive to trace Hg(II) concentrations. Calibration curves obtained for two fluences ( $10^9$  and  $10^{10}$  cm<sup>-2</sup>) demonstrated that the sensor LOD can be lowered proportionally to the fluence. Specific peak broadening for Hg(II) concentrations higher than 10 ppb when stripping voltammetry is performed was attributed to membrane saturation, which is in accordance with adsorption isotherm results (see chapter 6). Mercury adsorption was found not affected by presence of salt of 0.01-35 g L<sup>-1</sup> concentration and other metals (except iron) enabling sensor application for real water analysis.

PB2MP-g-PVDF membrane-electrodes were, for the first time, used as electrochemical sensors for U(VI) detection. Cyclic voltammetry study was performed for acquiring qualitative information about overall redox reactions of uranyl at gold electrode surface. SW-CSV parameters were subsequently optimized. XPS confirmed the ability of phosphate groups of PB2MP to adsorb uranyl ions. Time-resolved photoluminescence (TRPL) measurements were exploited for acquiring the information about adsorbed U(VI) environment in PB2MP-g-PVDF membrane and was found to be an alternative technique to SW-CSV for trace uranyl determination. The lifetime of 21  $\mu$ sec was attributed to U(VI)-phosphate complex formation. Based on the obtained results, the mechanism of uranyl adsorption was proposed, where pH dependence of PB2MP of a crucial importance.

# General conclusion

In view of the growing demand for water quality monitoring due to a rapid progress in different industries, sensitive and portable techniques for determination of highly toxic metals are needed. Heavy metals are considered to be hazardous because of their accumulation effect in living tissues. It is therefore for this reason the tolerable limits are currently in a few  $\mu\text{g/L}$  (or, ppb) level.

Nanostructured materials nowadays are becoming extensively utilized in water treatment because of their large specific area enabling efficient preconcentration effect. Various types of inorganic, carbon-based, cellulose, *etc.* materials have been developed for toxic metal removal. Among them functional, or chelate, polymers possessing donor atoms (ligands) are being increasingly used primarily due to their enhanced selectivities. Besides conventional chemical modification, there are two main methods for preparing functional polymer materials – coating or radiation-induced grafting with a selective monomer onto the surface of a solid substrate. The radiation-induced grafting is a sophisticated technique to introduce functional polymers to chemically inert polymers such as poly(vinylidene fluoride) (PVDF) in form of films, fibers, or membranes by generation of free radicals under ionizing radiation. Because of its remarkable mechanical strength, high chemical resistance and thermal stability as well as good aging resistance, PVDF has found extensive industrial applications and research interest. Particularly, PVDF membranes are produced for separation and filtration in water purification processes. Swift heavy ion (SHI) irradiation and ion track etching allow the fabrication of membranes whose pore size, shape and density can be varied in a controllable manner so that required retention and transport characteristics can be produced. Track-etched membranes functionalised with functional polymers thus ensure the synergetic effect permitting the efficient preconcentration and high selectivities towards toxic metals in water.

In semicrystalline polymers, namely PVDF, ionizing radiation has an advantage of inducing the stable free radicals. The adsorbed dose is proportional to the number of active radical sites allowing a precise control of radical initiator concentration. Versatility of the radiation grafting technique is attributed to the ability to control the grafting yield (GY) by proper selection of irradiation and grafting conditions. By means of EPR spectroscopy, it has been demonstrated that amount and density of the radicals remained after track ion etching were sufficient to initiate graft polymerization in presence of vinyl monomers. The stability of these radicals is mainly attributed to semicrystalline structure of PVDF. The least stable radicals are located in the amorphous parts of PVDF and consumed quickly. While the crystalline phase contains the most stable and least accessible radicals. Properly chosen grafting conditions such as grafting temperature, monomer concentration, solvent, *etc.* can drastically influence not only the GY, but also the grafting location and density of polymer chains.

In present work, we have also shown how various functional polymers, such as polyacrylic acid (PAA), poly(4-vinylpyridine) (P4VP) and, applied for the first time, poly(bis[2-(methacryloyloxy)ethyl] phosphate) (PB2MP) can be introduced inside the nanoporous structure of track-etched PVDF membranes. These functional polymers were used for Pb(II), Hg(II) and U(VI) preconcentration from aqueous solutions. The radiation grafting conditions were studied first

using electron-beam irradiated PVDF films as the radicals produced by both electrons and ions have similar nature. The established grafting protocol was then subsequently applied to track-etched PVDF membranes. Previous works of our team have demonstrated by means of confocal laser scanning microscopy (CLSM) and double fluorescence labeling that the location of grafted PAA chains is inside the nanopores and does not spread out to the bulk of PVDF, confirming the fact that radical polymerization of AA monomer is initiated from the residual radicals present in the pore walls.

FESEM and FTIR were used for morphology characterization and monitoring the presence of functional groups inside of grafted track-etched PVDF. For the first time, non-conventional zeta-potential measurements were applied for characterization of nanopore surface state (chapter 5). It was demonstrated that the surface charge of the nanopore walls of track-etched PVDF is negative over all investigated pH range. It was mainly attributed to multiple oxidized species formed during ion track etching in strong oxidizing alkaline  $\text{KMnO}_4$  solutions (mainly fluorinated ones). Presence of grafted P4VP polymer, however, has completely inverted the negative charge from the track-etched PVDF into positive at low pH. The isoelectric point of P4VP-g-PVDF membrane at a given GY was reached at pH 5, which corresponds to the pKa of P4VP. These results pointed out that the coverage with P4VP is relatively dense all along the nanopore channels.

Toxic metal ion adsorption experiments performed in this work (chapter 6) confirmed that efficient uptakes of the grafted track-etched PVDF membranes are due to the presence of functional groups that facilitate coordination reactions. In case of PAA grafted membranes, the  $\text{Pb(II)}\cdot\text{PAA}$  interaction is governed mainly by complexation between ionized at pH close to neutral carboxylic groups and metal ions. If so, indirect interaction of adsorbed species, or adsorbed layer re-organization, cannot be excluded. Therefore, Freundlich and Temkin isotherm models appeared to describe better the adsorption of lead by PAA-g-PVDF membranes than Langmuir isotherm model at high concentrations (after exceeding 100 ppb). When functional polymers are used, namely P4VP and PB2MP, as no ion-exchange is involved,  $\text{Hg(II)}$  and  $\text{U(VI)}$  uptakes must be limited by the number of available adsorption sites (functional groups). This hypothesis was confirmed by experimental results, for which Langmuir isotherm model gave the most adequate fitting. Indeed, non-ionized P4VP chains at pH investigated can coordinate only with a particular amount of  $\text{Hg(II)}$ , and once adsorbed, no interaction between adsorbed species is expected. The  $\text{U(VI)}$  adsorption mechanism onto PB2MP, however, may differ from that of  $\text{Hg(II)}$  onto P4VP, since phosphate group of PB2MP can possess both ion-exchange character and chelating effect at pH close to neutral. Although the Langmuir isotherm model was proved to be the most appropriate for describing the experimental data among considered two-parameter isotherm models, it nevertheless may be more complex than a simple monolayer adsorption. To strengthen the latter observation, obtained Langmuir sorption equilibrium constants  $b$ , representing metal ion binding affinity to the given adsorption sites, can be compared between these three different complexation systems as follows:  $b(\text{Pb(II)}\cdot\text{PAA}) < b(\text{U(VI)}\cdot\text{B2MP}) < b(\text{Hg(II)}\cdot\text{P4VP})$ . The higher the  $b$  values, the greater affinity of the ions studied towards adsorbent. The ascending order demonstrates a transition from pure inherent to PAA electrostatic nature of interaction to metal-ligand coordination in case of P4VP and PB2MP complexation character in between. To find out the extent of two possible complexation mechanisms of uranyl and validate adsorption isotherm results, XPS and TRPL measurements were further performed.

For electrochemical detection, track-etched membranes grafted with functional polymers, were converted into electrodes by depositing a 35 nm thick gold layer onto each side through a mask. FESEM investigations revealed no considerable effect on nanopore radii. Despite the gold thickness of only 35 nm, a typical cyclic voltammetry profile of amorphous gold electrode was registered. Square wave anodic stripping voltammetry (SW-ASV) was exploited

for trace concentration detection of Pb(II) and Hg(II) by PAA-g-PVDF and P4VP-g-PVDF membrane-electrodes, respectively. Thanks to cation-exchange character of PAA, the PAA-g-PVDF membrane-electrodes have a potential for multi-ion detection. However, competitive co-adsorption phenomenon and strong matrix effect limit their application for real water analysis. Attempts were made to understand the adsorption process in simulated seawater solutions for Cu(II) and Pb(II) present separately and possible explanation was suggested. Perhaps, the  $\text{Cu}^{2+}$  superior affinity to carboxylates of PAA is assigned to similar ionic radii which allows to Cu(II) with less sterical hindrance to be coordinated. Indeed, salinity affects the PAA swelling behaviour. When counterbalanced with cations present in salted solution, chain shrinking takes place. Metal ions, even those having superior affinity like Cu(II), have to have comparable ionic radii for successful cation-exchange. Also, if a complex formation involves ligand substitution, in case when metal cation is associated with anions present in the solution, for certain metal cations the ligand substitution may be slow or unfavourable. The decrease of Pb(II) uptake can be due to Pb(II) chloride complex formation since the presence of salts in such concentrations changes its speciation compare to that in deionized water,  $\text{Pb}(\text{OH})_2$ , and interaction with carboxyl groups of PAA becomes unfavourable. Simultaneously, as pH is slightly more basic (due to  $\text{NaHCO}_3$ ), most carboxyl groups are ionized (deprotonated). The  $\text{K}^+$ ,  $\text{Na}^+$ ,  $\text{Mg}^{2+}$  and  $\text{Ca}^{2+}$  ions will be competitively attracted by  $-\text{COO}^-$  until reaching the equilibrium. Nevertheless, these encouraging results require a deeper study and might be a goal for further research, which is beyond the subject of present work.

In order to set the protocol for U(VI) detection using the innovative PB2MP-g-PVDF porous membrane-electrodes developed in the framework of this Ph.D project, a deeper cyclic voltammetry study was performed for acquiring qualitative and quantitative information about charge transfer reactions of uranyl with subsequent optimization of parameters for square wave cathodic stripping voltammetry (SW-CSV) detection (chapter 8). This study allowed to understand overall electrochemical reactions taking place in the system and revealed the peaks associated with one-electron reduction and oxidation of uranyl, reduction of  $\text{UO}_2^+$  to insoluble  $\text{UO}_2$  species as well as the two-electron oxidation of  $\text{UO}_2$  to  $\text{UO}_2^{2+}$ . The analyzed SW-CSV peak height was found linearly proportional to U(VI) concentration within 100 ppb range with limit of detection (LOD) of 10 ppb, which is three times lower than recommended value by World Health Organization (4th edition, 2011). It validates the proof of concept for U(VI) detection by PB2MP-g-PVDF membrane-electrodes. The interference with other toxic metals and pH effect were emphasized. Therefore, investigation of U(VI) speciation on adsorption by PB2MP-g-PVDF membranes is now needed for further sensor application.

Time-resolved photoluminescence (TRPL) measurements were performed, for the first time, for uranyl adsorbed PB2MP-g-PVDF membranes in order to understand deeper the U(VI)-PB2MP coordination mechanism (chapter 8). XPS confirmed the presence of phosphate groups and the binding energies of U 4f peaks indicated U(VI) interaction with phosphate groups. TRPL revealed the characteristic uranyl vibronic components increasing almost linearly with increase of U(VI) concentration up to approximately 100 ppb. Whereas at higher U(VI) concentrations, the PL signal area levelled off confirming adsorption isotherm results, where the membrane saturation occurs. The efficiency of U(VI) adsorption was found to be pH dependent. Uranyl solutions prepared in 2%  $\text{HNO}_3$  caused total suppression of characteristic uranyl PL emission band. Indeed, low pHs were found affecting the SW-CSV results acquired by PB2MP-g-PVDF membrane-electrodes. Uranyl adsorption at  $\text{pH} < 4$  resulted in low peak currents whereas neutral and basic pHs consistently gave reproducible responses. The acidic phosphate groups are expected to bind uranyl ions through ion-exchange with  $\text{P}-\text{O}^-$  at  $\text{pH} \geq 1.5$  ( $\text{pK}_a$  of phosphate diestered 1.5) and coordination of neutral (anion associated) uranyl species at  $\text{pH} < 1.5$ . When acidified with  $\text{HNO}_3$ , uranyl associates with nitrate ions in solution. The absence of both PL and SW-CSV responses of U(VI) might be due

to the fact that either nitrate substitution to phosphate does not take place, or there is no stable complex formation between uranyl and P=O because of unsatisfied coordination numbers. While circumneutral pH favors the formation of positively charged uranyl hydroxide complexes,  $[(\text{UO}_2)(\text{OH})]^+$ , or  $[(\text{UO}_2)_2(\text{OH})_2]^{2+}$ , or  $[(\text{UO}_2)_3(\text{OH})_5]^+$ , or  $(\text{UO}_2)(\text{OH})_2$ , which are transformed into negatively charged at  $\text{pH} > 9$  (figure 8.15). At this pH range, hydrolyzed uranyl species can bind with acidic phosphate groups of PB2MP through mutual ion-exchange and coordination interaction with less hindering in terms of satisfaction of their coordination numbers. Similar to present results specific uranyl adsorption behaviour was observed by Mhatre et al. [216] onto phosphate grafted teflon films. Finally, figure 8.23b demonstrates a good correlation of the results obtained by stripping voltammetry and TRPL measurements. It is worth mentioning that consistently detected U(VI) concentration by PB2MP-g-PVDF membranes was as low as 6 ppb which can further be lowered. These results suggest that TRPL may be considered as a serious alternative to stripping voltammetry for U(VI) trace detection.

To sum up, this work has demonstrated a powerful methodology for selective nanopore chemistry based on radiation-induced grafting, which can be applied not only for toxic metal retention, but also for biomedical applications or more fundamental research on transport properties, opening up a new route for the design of a new class of nanoporous functional materials.

# Bibliography

- [1] M. M. Monnin and G. E. Blanford. “Detection of charged particles by polymer grafting”. In: *Science* 181.4101 (1973), pp. 743–744 (cit. on p. 2).
- [2] R. L. Fleischer, P. B. Price, and R. M. Walker. *Nuclear tracks in solids: principles and applications*. University of California Press, 1975 (cit. on pp. 2, 9, 19).
- [3] G. Somogyi. “Processing of plastic track detectors”. In: *Nuclear Track Detection* 1.1 (1977), pp. 3–18 (cit. on p. 2).
- [4] M. Skupinski. “Nanopatterning by Swift Heavy Ions”. PhD thesis. Acta Universitatis Upsaliensis, 2006 (cit. on p. 9).
- [5] M. Toulemonde et al. “Atomic and cluster ion bombardment in the electronic stopping power regime: A thermal spike description”. In: *Nuclear Instruments and Methods in Physics Research Section B: Beam Interactions with Materials and Atoms* 112.1-4 (1996), pp. 26–29 (cit. on p. 9).
- [6] F. Seitz. “Displacement of atoms during irradiation”. In: *Solid State Physics*. 2 (1956), pp. 307–442 (cit. on p. 9).
- [7] S. Bouffard, B. Gervais, and C. Leroy. “Basic phenomena induced by swift heavy ions in polymers”. In: *Nuclear Instruments and Methods in Physics Research Section B: Beam Interactions with Materials and Atoms* 105.1-4 (1995), pp. 1–4 (cit. on p. 9).
- [8] S. A. Saleh and Y. Eyal. “Morphology of track cores and halos created by swift uranium ions in polycarbonate”. In: *Nuclear Instruments and Methods in Physics Research Section B: Beam Interactions with Materials and Atoms* 236.1-4 (2005), pp. 81–87 (cit. on pp. 9, 10).
- [9] S. Abu Saleh and Y. Eyal. “Porous tracks along wakes of swift uranium ions in polyimide”. In: *Applied physics letters* 85.13 (2004), pp. 2529–2531 (cit. on p. 9).
- [10] B. E. Fischer and R. Spohr. “Production and use of nuclear tracks: imprinting structure on solids”. In: *Reviews of Modern Physics* 55.4 (1983), p. 907 (cit. on p. 9).
- [11] Z. Chang and J. A. Laverne. “Hydrogen production in  $\gamma$ -ray and helium-ion radiolysis of polyethylene, polypropylene, poly(methyl-methacrylate), and polystyrene”. In: *Journal of Polymer Science Part A: Polymer Chemistry* 38.9 (2000), pp. 1656–1661 (cit. on pp. 10, 25).
- [12] N. Betz et al. “A FTIR study of PVDF irradiated by means of swift heavy ions”. In: *Journal of Polymer Science Part B: Polymer Physics* 32.8 (1994), pp. 1493–1502 (cit. on pp. 10, 51).
- [13] E. Balanzat et al. “Physico-chemical modifications induced in polymers by swift heavy ions”. In: *Nuclear Instruments and Methods in Physics Research Section B: Beam Interactions with Materials and Atoms* 91.1-4 (1994), pp. 140–145 (cit. on pp. 10, 14, 20).
- [14] E. Balanzat et al. “Effects of a dense electronic excitation in polyethylene”. In: *Nouvelles du GANIL* (1993), pp. 25–33 (cit. on p. 10).
- [15] M. Ferry et al. “Irradiation of atactic polystyrene: linear energy transfer effects”. In: *The Journal of Physical Chemistry B* 112.35 (2008), pp. 10879–10889 (cit. on p. 10).

- [16] S. Al-Assaf et al. *The Radiation Chemistry of Polysaccharides*. International Atomic Energy Agency: Vienna, Austria, 2016 (cit. on p. 10).
- [17] A. J. Lovinger. “Annealing of poly(vinylidene fluoride) and formation of a fifth phase”. In: *Macromolecules* 15.1 (1982), pp. 40–44 (cit. on p. 11).
- [18] B.-E. El Mohajir and N. Heymans. “Changes in structural and mechanical behaviour of PVDF with processing and thermomechanical treatments. 1. Change in structure”. In: *Polymer* 42.13 (2001), pp. 5661–5667 (cit. on p. 11).
- [19] S. Atchariyawut et al. “Effect of membrane structure on mass-transfer in the membrane gas-liquid contacting process using microporous PVDF hollow fibers”. In: *Journal of Membrane Science* 285.1-2 (2006), pp. 272–281 (cit. on p. 11).
- [20] S. Ray et al. “Structure and properties of melt-processed PVDF/PMMA/polyaniline blends”. In: *Materials Chemistry and Physics* 113.2-3 (2009), pp. 829–838 (cit. on p. 11).
- [21] D. C. Bassett. *Developments in crystalline polymers*. Vol. 1. Springer, 1982 (cit. on pp. 11, 12).
- [22] R. Hasegawa et al. “Crystal structures of three crystalline forms of poly(vinylidene fluoride)”. In: *Polymer Journal* 3.5 (1972), p. 600 (cit. on p. 11).
- [23] J. B. Lando, H. G. Olf, and A. Peterlin. “Nuclear magnetic resonance and x-ray determination of the structure of poly(vinylidene fluoride)”. In: *Journal of Polymer Science Part A-1: Polymer Chemistry* 4.4 (1966), pp. 941–951 (cit. on p. 11).
- [24] L. Li et al. “Studies on the transformation process of PVDF from  $\alpha$  to  $\beta$  phase by stretching”. In: *RSC Advances* 4.8 (2014), pp. 3938–3943 (cit. on p. 12).
- [25] V. Sencadas et al. “Relaxation dynamics of poly(vinylidene fluoride) studied by dynamical mechanical measurements and dielectric spectroscopy”. In: *The European Physical Journal E* 35.5 (2012), p. 41 (cit. on p. 13).
- [26] E. Adem et al. “Electron and proton irradiation of poly(vinylidene fluoride): characterization by electron paramagnetic resonance”. In: *Polymer degradation and stability* 81.1 (2003), pp. 75–79 (cit. on pp. 13, 27, 60).
- [27] J. S. Forsythe and D. J. T. Hill. “The radiation chemistry of fluoropolymers”. In: *Progress in Polymer Science* 25.1 (2000), pp. 101–136 (cit. on p. 13).
- [28] A. Fina et al. “Surface processes occurring on PVDF under energetic ion irradiation”. In: *Nuclear Inst. and Methods in Physics Research, B* 42.1 (1989), pp. 69–75 (cit. on p. 13).
- [29] L. Torrisi et al. “KeV-MeV ion irradiation of polyvinylidene fluoride (PVDF) films”. In: *Nuclear Instruments and Methods in Physics Research, Section B: Beam Interactions with Materials and Atoms* 116.1-4 (1996), pp. 473–477 (cit. on p. 13).
- [30] K. Makuuchi, M. Asano, and T. Abe. “Effect of evolved hydrogen fluoride on radiation-induced crosslinking and dehydrofluorination of poly(vinylidene fluoride)”. In: *Journal of Polymer Science: Polymer Chemistry Edition* 14.3 (1976), pp. 617–625 (cit. on pp. 13, 14).
- [31] N. Betz, E. Petersohn, and A. L. Moël. “Swift heavy ions effects in fluoropolymers: Radicals and crosslinking”. In: *Nuclear Instruments and Methods in Physics Research, Section B: Beam Interactions with Materials and Atoms* 116.1-4 (1996), pp. 207–211 (cit. on pp. 14, 27, 60).
- [32] J. Goslar, B. Hilczer, and H. Smogor. “ESR studies of fast electron irradiated ferroelectric poly(vinylidene fluoride)”. In: *Acta Physica Polonica-Series A General Physics* 108.1 (2005), pp. 89–94 (cit. on pp. 15, 28).

- [33] N. Betz. “Etude des effets d’irradiation et du radiogreffage, induits dans du polyfluorure de vinylidene, par des ions lourds rapides”. PhD thesis. Christiane Sciences appliquées Paris 6, 1992 (cit. on p. 14).
- [34] N. Betz, E. Petersohn, and A. Le Moël. “Free radicals in swift heavy ion irradiated fluoropolymers: An electron spin resonance study”. In: *Radiation Physics and Chemistry* 47.3 (1996), pp. 411–414 (cit. on p. 14).
- [35] V. Chailley, E. Balanzat, and E. Dooryhee. “Amorphization kinetics of poly(vinylidene fluoride) on high-energy ion irradiation”. In: *Nuclear Instruments and Methods in Physics Research Section B: Beam Interactions with Materials and Atoms* 105.1-4 (1995), pp. 110–114 (cit. on p. 14).
- [36] C. Trautmann, S. Bouffard, and R. Spohr. “Etching threshold for ion tracks in polyimide”. In: *Nuclear Instruments and Methods in Physics Research Section B: Beam Interactions with Materials and Atoms* 116.1-4 (1996), pp. 429–433 (cit. on p. 18).
- [37] J. F. Ziegler and J. P. Biersack. *The stopping and range of ions in matter*. Springer, 1985, pp. 93–129 (cit. on p. 18).
- [38] H. B. Lück. “Mechanism of particle track etching in polymeric nuclear track detectors”. In: *Nuclear Instruments and Methods in Physics Research* 202.3 (1982), pp. 497–501 (cit. on p. 18).
- [39] P. Yu. Apel et al. “Morphology of latent and etched heavy ion tracks in radiation resistant polymers polyimide and poly (ethylene naphthalate)”. In: *Nuclear Instruments and Methods in Physics Research Section B: Beam Interactions with Materials and Atoms* 185.1-4 (2001), pp. 216–221 (cit. on p. 18).
- [40] P. Apel. “Swift ion effects in polymers: industrial applications”. In: *Nuclear Instruments and Methods in Physics Research Section B: Beam Interactions with Materials and Atoms* 208 (2003), pp. 11–20 (cit. on p. 19).
- [41] D. O’Sullivan and A. Thompson. “The observation of a sensitivity dependence on temperature during registration in solid state nuclear track detectors”. In: *Nuclear Tracks* 4.4 (1980), pp. 271–276 (cit. on p. 19).
- [42] P. Yu. Apel et al. “Registration temperature effect in polymers: Physico-chemical aspects”. In: *Radiation measurements* 28.1-6 (1997), pp. 19–24 (cit. on p. 19).
- [43] P. Apel et al. “Tracks of very heavy ions in polymers”. In: *Nuclear Instruments and Methods in Physics Research Section B: Beam Interactions with Materials and Atoms* 131.1-4 (1997), pp. 55–63 (cit. on p. 19).
- [44] E. V. Benton and R. P. Henke. “Sensitivity enhancement of Lexan nuclear track detector”. In: *Nuclear Instruments and Methods* 70.2 (1969), pp. 183–184 (cit. on p. 19).
- [45] W. DeSorbo. “Ultraviolet effects and aging effects on etching characteristics of fission tracks in polycarbonate film”. In: *Nuclear Tracks* 3.1-2 (1979), pp. 13–32 (cit. on p. 19).
- [46] G. Guillot and F. Rondelez. “Characteristics of submicron pores obtained by chemical etching of nuclear tracks in polycarbonate films”. In: *Journal of Applied Physics* 52.12 (1981), pp. 7155–7164 (cit. on p. 19).
- [47] P. Wang et al. “Ultrafast ion sieving using nanoporous polymeric membranes”. In: *Nature Communications* 9.1 (2018) (cit. on p. 19).
- [48] P. Apel et al. “Tracks of very heavy ions in polymers”. In: *Nuclear Instruments and Methods in Physics Research Section B: Beam Interactions with Materials and Atoms* 131.1 (1997), pp. 55–63 (cit. on p. 19).
- [49] F.P. Petersen and D.E. Fairbrothers. “A serotaxonomic appraisal of the ”*Amen-tiferae.*””. In: *Bull. Torrey Bot. Club* 112 (1985). cited By 9, pp. 43–52 (cit. on p. 19).

- [50] S. P. Tretyakova and L. V. Jolos. “Heavy Particle Track Detector of Fluoropolymers”. In: *Prih. Tekh. Eksp.* 1 (1978), pp. 36–41 (cit. on p. 20).
- [51] Y. Komaki and S. Tsujimura. “Chemical etching of fission tracks in polyfluoro plastics”. In: *Science* 199.4327 (1978), pp. 421–422 (cit. on p. 20).
- [52] S. P. Tretyakova et al. “Polyvinylidene fluoride (PVF) as a charged particle detector”. In: *Nuclear Tracks and Radiation Measurements* 12.1-6 (1986), pp. 75–76 (cit. on p. 20).
- [53] M. Grasselli and N. Betz. “Making porous membranes by chemical etching of heavy-ion tracks in  $\beta$ -PVDF films”. In: *Nuclear Instruments and Methods in Physics Research Section B: Beam Interactions with Materials and Atoms* 236.1-4 (2005), pp. 501–507 (cit. on p. 20).
- [54] R. Rohani et al. “Enhancement of etch rate for preparation of nano-sized ion-track membranes of poly(vinylidene fluoride): Effect of pretreatment and high-LET beam irradiation”. In: *Nuclear Instruments and Methods in Physics Research Section B: Beam Interactions with Materials and Atoms* 267.3 (2009), pp. 554–557 (cit. on p. 20).
- [55] G. J. Ross et al. “Surface modification of poly(vinylidene fluoride) by alkaline treatment 1. The degradation mechanism”. In: *Polymer* 41.5 (2000), pp. 1685–1696 (cit. on p. 20).
- [56] M. B. Smith and J. March. *March’s advanced organic chemistry: reactions, mechanisms, and structure*. John Wiley & Sons, 2007 (cit. on p. 20).
- [57] O. Cuscito. “Fabrication of beta-PVDF membranes by track etching and specific functionalization of nano-pores”. PhD thesis. École Polytechnique, 2008 (cit. on pp. 21, 26, 29, 30, 50, 51).
- [58] A. Chapiro. “Radiation Chemistry of Polymeric Systems”. In: (1962) (cit. on pp. 23, 25–27).
- [59] M. Nasef and O. Güven. “Radiation-grafted copolymers for separation and purification purposes: Status, challenges and future directions”. In: *Progress in Polymer Science* 37.12 (2012), pp. 1597–1656 (cit. on p. 23).
- [60] A. Chapiro. “Chemical modifications in irradiated polymers”. In: *Nuclear Instruments and Methods in Physics Research Section B: Beam Interactions with Materials and Atoms* 32.1-4 (1988), pp. 111–114 (cit. on p. 23).
- [61] M. M. Nasef and E.-S. A. Hegazy. “Preparation and applications of ion exchange membranes by radiation-induced graft copolymerization of polar monomers onto non-polar films”. In: *Progress in Polymer Science* 29.6 (2004), pp. 499–561 (cit. on pp. 25, 26).
- [62] B. Gupta et al. “Preirradiation grafting of acrylonitrile onto polypropylene monofilament for biomedical applications: I. Influence of synthesis conditions”. In: *Radiation Physics and Chemistry* 75.1 (2006), pp. 161–167 (cit. on p. 25).
- [63] D. Binh and H. T. Huy. “The effect of concentration of acrylic acid, dose rates and temperature on preirradiated graft of natural rubber-based thermoplastic elastomer”. In: *Radiation Physics and Chemistry* 53.2 (1998), pp. 177–180 (cit. on p. 25).
- [64] B. Gupta, F. N. Büchi, and G. G. Scherer. “Cation exchange membranes by pre-irradiation grafting of styrene into FEP films. I. Influence of synthesis conditions”. In: *Journal of Polymer Science Part A: Polymer Chemistry* 32.10 (1994), pp. 1931–1938 (cit. on pp. 25, 27).
- [65] X. Ping, M. Wang, and X. Ge. “Radiation induced graft copolymerization of n-butyl acrylate onto poly(ethylene terephthalate)(PET) films and thermal properties of the obtained graft copolymer”. In: *Radiation Physics and Chemistry* 80.5 (2011), pp. 632–637 (cit. on p. 25).

- [66] G. Przybytniak et al. "Functionalization of polymer surfaces by radiation-induced grafting". In: *Nukleonika* 53.3 (2008), pp. 89–95 (cit. on p. 25).
- [67] C. Makhlof, S. Marais, and S. Roudesli. "Graft copolymerization of acrylic acid onto polyamide fibers". In: *Applied Surface Science* 253.12 (2007), pp. 5521–5528 (cit. on p. 25).
- [68] H. I. Nasr, K. M. Haggag, and E. A. El Kharadly. "Polyamides with improved moisture regain via  $\gamma$ -rays". In: *Radiation Physics and Chemistry (1977)* 16.6 (1980), pp. 447–449 (cit. on p. 25).
- [69] M. K. Chumakov et al. "Electron beam induced grafting of N-isopropylacrylamide to a poly(ethylene-terephthalate) membrane for rapid cell sheet detachment". In: *Radiation Physics and Chemistry* 80.2 (2011), pp. 182–189 (cit. on p. 25).
- [70] N. I. Zhitariuk and N. I. Shtanko. "Influence of some factors on radiation grafting of styrene on poly(ethylene terephthalate) nuclear membranes". In: *European Polymer Journal* 26.8 (1990), pp. 847–851 (cit. on p. 25).
- [71] M. Walo et al. "Radiation-induced graft polymerization of N-vinylpyrrolidone onto segmented polyurethane based on isophorone diisocyanate". In: *Radiation Physics and Chemistry* 84 (2013), pp. 85–90 (cit. on p. 25).
- [72] P. Alves et al. "Surface modification and characterization of thermoplastic polyurethane". In: *European Polymer Journal* 45.5 (2009), pp. 1412–1419 (cit. on p. 25).
- [73] J. F. Madrid and L. V. Abad. "Modification of microcrystalline cellulose by gamma radiation-induced grafting". In: *Radiation Physics and Chemistry* 115 (2015), pp. 143–147 (cit. on p. 25).
- [74] L. Wojnárovits, C. M. Földváry, and E. Takács. "Radiation-induced grafting of cellulose for adsorption of hazardous water pollutants: A review". In: *Radiation Physics and Chemistry* 79.8 (2010), pp. 848–862 (cit. on p. 25).
- [75] L. Gubler, S. A. Gürsel, and G. G. Scherer. "Radiation grafted membranes for polymer electrolyte fuel cells". In: *Fuel Cells* 5.3 (2005), pp. 317–335 (cit. on p. 25).
- [76] J. Qiu et al. "Radiation grafting of styrene and maleic anhydride onto PTFE membranes and sequent sulfonation for applications of vanadium redox battery". In: *Radiation Physics and Chemistry* 76.11-12 (2007), pp. 1703–1707 (cit. on p. 25).
- [77] G. M. Estrada-Villegas and E. Bucio. "Comparative study of grafting a polyampholyte in a fluoropolymer membrane by gamma radiation in one or two-steps". In: *Radiation Physics and Chemistry* 92 (2013), pp. 61–65 (cit. on p. 25).
- [78] H. P. Ferreira, D. F. Parra, and A. B. Lugao. "Radiation-induced grafting of styrene into poly(vinylidene fluoride) film by simultaneous method with two different solvents". In: *Radiation Physics and Chemistry* 81.9 (2012), pp. 1341–1344 (cit. on p. 25).
- [79] M.-Cl. Clochard et al. "Tailoring bulk and surface grafting of poly(acrylic acid) in electron-irradiated PVDF". In: *Polymer* 45.26 (2004), pp. 8683–8694 (cit. on pp. 26, 49–51).
- [80] R. G. Compton, C. H. Bamford, and C. F. H. Tipper. *Degradation of polymers*. Vol. 14. Elsevier, 1975 (cit. on p. 26).
- [81] K. Makuuchi and S. Cheng. *Radiation processing of polymer materials and its industrial applications*. John Wiley & Sons, 2012 (cit. on p. 26).
- [82] Z. Lin, T. Xu, and L. Zhang. "Radiation-induced grafting of N-isopropylacrylamide onto the brominated poly(2, 6-dimethyl-1, 4-phenylene oxide) membranes". In: *Radiation Physics and Chemistry* 75.4 (2006), pp. 532–540 (cit. on p. 26).
- [83] S. Phadnis et al. "Proton exchange membranes by grafting of styrene-acrylic acid onto FEP by preirradiation technique. I. Effect of synthesis conditions". In: *Journal of Applied Polymer Science* 90.9 (2003), pp. 2572–2577 (cit. on p. 26).

- [84] J. Dobo, A. Somogyi, and T. Czvikovszky. *Grafting of styrene onto Teflon and polyethylene by preirradiation*. Tech. rep. Research Inst. for the Plastics Industry, Budapest, 1963 (cit. on p. 26).
- [85] G. Ellinghorst, J. Fuehrer, and D. Vierkotten. “Radiation initiated grafting on fluoro polymers for membrane preparation”. In: *Radiation Physics and Chemistry* 18.5-6 (1981), pp. 889–897 (cit. on p. 26).
- [86] G. Ellinghorst, A. Niemöller, and D. Vierkotten. “Radiation initiated grafting of polymer films-an alternative technique to prepare membranes for various separation problems”. In: *Radiation Physics and Chemistry (1977)* 22.3-5 (1983), pp. 635–642 (cit. on p. 26).
- [87] G. Yun-Peng. “Preparation of charged micro-mosaic membrane via radiation-induced grafting of styrene and methyl methacrylate onto Teflon FEP films”. In: *Desalination* 62 (1987), pp. 265–273 (cit. on p. 27).
- [88] T. R. Dargaville et al. “High energy radiation grafting of fluoropolymers”. In: *Progress in Polymer Science* 28.9 (2003), pp. 1355–1376 (cit. on p. 27).
- [89] A. Oshima, T. Seguchi, and Y. Tabata. “ESR study on free radicals trapped in crosslinked polytetrafluoroethylene (PTFE)”. In: *Radiation physics and chemistry* 50.6 (1997), pp. 601–606 (cit. on p. 27).
- [90] D. J. T. Hill et al. “An ESR study of the radiation chemistry of poly(tetrafluoroethylene-co-hexafluoropropylene) at 77 and 300 K”. In: *Radiation Physics and Chemistry* 59.3 (2000), pp. 295–302 (cit. on p. 27).
- [91] T. R. Dargaville, D. J. T. Hill, and A. K. Whittaker. “An ESR study of irradiated poly(tetrafluoroethylene-co-perfluoropropyl vinyl ether)(PFA)”. In: *Radiation physics and chemistry* 62.1 (2001), pp. 25–31 (cit. on p. 27).
- [92] T. Seguchi et al. “Radiation effects on poly(vinylidene fluoride). III. Electron spin resonance study on irradiated poly(vinylidene fluoride)”. In: *Chem. Soc. Jpn. Chem. Ind. Chem.* 7 (1974), pp. 1309–1315 (cit. on p. 27).
- [93] M.-C. Clochard et al. “Ion track grafting: A way of producing low-cost and highly proton conductive membranes for fuel cell applications”. In: *Journal of Power Sources* 195.1 (2010), pp. 223–231 (cit. on p. 27).
- [94] M. Barsbay and O. Güven. “Grafting in confined spaces: Functionalization of nanochannels of track-etched membranes”. In: *Radiation Physics and Chemistry* 105 (2014), pp. 26–30 (cit. on p. 27).
- [95] S. Deshayes et al. “Synthesis of specific nanoparticles for targeting tumor angiogenesis using electron-beam irradiation”. In: *Radiation Physics and Chemistry* 79.3 (2010), pp. 208–213 (cit. on p. 27).
- [96] Y. Komaki et al. “Radicals in heavy ion-irradiated polyvinylidene fluoride”. In: *Radiation Measurements* 26.1 (1996), pp. 123–129 (cit. on pp. 27, 60).
- [97] D. Suryanarayana and L. Kevan. “Peroxy spin probe studies of motion in poly(vinylidene fluoride)”. In: *Journal of the American Chemical Society* 104.23 (1982), pp. 6251–6254 (cit. on p. 28).
- [98] J. Goslar, B. Hilczer, and H. Smogor. “Radiation-induced modification of P(VDF/TrFe) copolymers studied by ESR and vibrational spectroscopy”. In: *Applied Magnetic Resonance* 34.1-2 (2008), pp. 37–45 (cit. on p. 28).
- [99] C. Aymes-Chodur, S. Esnouf, and A. Le Moël. “ESR studies in  $\gamma$ -irradiated and PS-radiation-grafted poly(vinylidene fluoride)”. In: *Journal of Polymer Science Part B: Polymer Physics* 39.13 (2001), pp. 1437–1448 (cit. on p. 28).

- [100] Le Bouëdec A. et al. “Swift heavy ion irradiation effects in  $\alpha$  poly (vinylidene fluoride): spatial distribution of defects within the latent track”. In: *Nuclear Instruments and Methods in Physics Research Section B: Beam Interactions with Materials and Atoms* 151.1-4 (1999), pp. 89–96 (cit. on p. 28).
- [101] C. Aymes-Chodur et al. “A FTIR and SEM study of PS radiation grafted fluoropolymers: influence of the nature of the ionizing radiation on the film structure”. In: *Nuclear Instruments and Methods in Physics Research Section B: Beam Interactions with Materials and Atoms* 151.1-4 (1999), pp. 377–385 (cit. on pp. 28, 29).
- [102] G. Gebel et al. “Structural study of polystyrene grafted in irradiated polyvinylidene fluoride thin films”. In: *Nuclear Instruments and Methods in Physics Research Section B: Beam Interactions with Materials and Atoms* 105.1-4 (1995), pp. 145–149 (cit. on p. 28).
- [103] N. Betz. “Ion track grafting”. In: *Nuclear Instruments and Methods in Physics Research Section B: Beam Interactions with Materials and Atoms* 105.1-4 (1995), pp. 55–62 (cit. on p. 28).
- [104] R. Mazzei et al. “Swift heavy ion induced graft polymerization in track etched membranes’ submicroscopic pores”. In: *Nuclear Instruments and Methods in Physics Research Section B: Beam Interactions with Materials and Atoms* 226.4 (2004), pp. 575–584 (cit. on p. 29).
- [105] O. Cuscito et al. “Nanoporous  $\beta$ -PVDF membranes with selectively functionalized pores”. In: *Nuclear Instruments and Methods in Physics Research Section B: Beam Interactions with Materials and Atoms* 265.1 (2007), pp. 309–313 (cit. on pp. 29, 48, 52, 59).
- [106] M. Barsbay et al. “Nanopore size tuning of polymeric membranes using the RAFT-mediated radical polymerization”. In: *Journal of membrane science* 445 (2013), pp. 135–145 (cit. on pp. 30, 52, 59).
- [107] R. N. Adams. *Electrochemistry at solid electrodes*. Tech. rep. M. Dekker, 1969 (cit. on p. 32).
- [108] A. J. Bard et al. *Electrochemical methods: fundamentals and applications*. Vol. 2. Wiley New York, 1980 (cit. on p. 33).
- [109] D. M. Kolb. “Electrochemical surface science”. In: *Angewandte Chemie International Edition* 40.7 (2001), pp. 1162–1181 (cit. on p. 33).
- [110] J. O. M. Bockris and A. K. N. Reddy. *Modern electrochemistry 2B: electrodics in chemistry, engineering, biology and environmental science*. Vol. 2. Springer Science & Business Media, 2000 (cit. on p. 34).
- [111] C. M. A. Brett and A. M. O. Brett. “Electroanalysis Oxford University Press”. In: (1998) (cit. on p. 35).
- [112] C. R. Martin et al. “Electroanalytical Chemistry”. In: (1999) (cit. on p. 35).
- [113] D. A. C. Brownson and C. E. Banks. *The handbook of graphene electrochemistry*. Springer, 2014 (cit. on p. 36).
- [114] V. Mirceski, S. Skrzypek, and L. Stojanov. “Square-wave voltammetry”. In: *Chem-Texts* 4.4 (2018), p. 17 (cit. on p. 37).
- [115] J. Wang. *Analytical electrochemistry*. Wiley-VCH, Hoboken, 2006 (cit. on p. 38).
- [116] V. Mirceski, S. Komorsky-Lovric, and M. Lovric. *Square-wave voltammetry: theory and application*. Springer Science & Business Media, 2007 (cit. on p. 38).
- [117] V. Mirceski et al. “Square-wave voltammetry: a review on the recent progress”. In: *Electroanalysis* 25.11 (2013), pp. 2411–2422 (cit. on p. 38).

- [118] V. Mirceski and R. Gulaboski. “Recent achievements in square-wave voltammetry (a review)”. In: *Macedonian Journal of Chemistry and Chemical Engineering* 33.1 (2014), pp. 1–12 (cit. on p. 38).
- [119] J. Wang. “Stripping Analysis: Principles”. In: *Instrumentation and Applications, VCH, Deerfield Beach, FL* (1985), p. 30 (cit. on pp. 38, 40).
- [120] T. R. Copeland and R. K. Skogerboe. “Anodic stripping voltammetry”. In: *Analytical Chemistry* 46.14 (1974), 1257A–1268a (cit. on p. 38).
- [121] C. Du et al. “Rotating disk electrode method”. In: (2014), pp. 171–198 (cit. on p. 38).
- [122] Nürnberg H. W. Sipos L., P. Valenta, and M. Branica. “The reliable determination of mercury traces in sea water by subtractive differential pulse voltammetry at the twin gold electrode”. In: *Analytica chimica acta* 115 (1980), pp. 25–42 (cit. on pp. 39, 71).
- [123] H. Huiliang, D. Jagner, and L. Renman. “Simultaneous determination of mercury(II), copper(II) and bismuth(III) in urine by flow constant-current stripping analysis with a gold fibre electrode”. In: *Analytica chimica acta* 202 (1987), pp. 117–122 (cit. on p. 39).
- [124] E. P. Gil and P. Ostapczuk. “Potentiometric stripping determination of mercury(II), selenium(IV), copper(II) and lead(II) at a gold film electrode in water samples”. In: *Analytica chimica acta* 293.1-2 (1994), pp. 55–65 (cit. on pp. 39, 71).
- [125] I. Švancara et al. “Carbon paste electrodes plated with a gold film for the voltammetric determination of mercury(II)”. In: *Electroanalysis* 9.11 (1997), pp. 827–833 (cit. on pp. 39, 40, 71).
- [126] J. Inukai, S. Sugita, and K. Itaya. “Underpotential deposition of mercury on Au(111) investigated by in situ scanning tunnelling microscopy”. In: *Journal of Electroanalytical Chemistry* 403.1-2 (1996), pp. 159–168 (cit. on p. 40).
- [127] M. Brand, I. Eshkenazi, and E. Kirowa-Eisner. “The silver electrode in square-wave anodic stripping voltammetry. Determination of Pb(II) without removal of oxygen”. In: *Analytical Chemistry* 69.22 (1997), pp. 4660–4664 (cit. on p. 40).
- [128] Kirowa-Eisner, M. E. Brand, and D. Tzur. “Determination of sub-nanomolar concentrations of lead by anodic-stripping voltammetry at the silver electrode”. In: *Analytica chimica acta* 385.1-3 (1999), pp. 325–335 (cit. on p. 40).
- [129] Y. Bonfil, M. Brand, and E. Kirowa-Eisner. “Determination of sub- $\mu\text{g l}^{-1}$  concentrations of copper by anodic stripping voltammetry at the gold electrode”. In: *Analytica chimica acta* 387.1 (1999), pp. 85–95 (cit. on p. 40).
- [130] R. C. Alkire et al. *Advances in electrochemical science and engineering*. Wiley Online Library, 2002 (cit. on p. 40).
- [131] V. Sudha and M. V. Sangaranarayanan. “Underpotential deposition of metals – Progress and prospects in modelling”. In: *Journal of Chemical Sciences* 117.3 (2005), pp. 207–218 (cit. on p. 40).
- [132] N. Mayet et al. “Probing the Surface of Noble Metals Electrochemically by Underpotential Deposition of Transition Metals”. In: *Surfaces* 2.2 (2019), pp. 257–276 (cit. on p. 40).
- [133] Y. Bonfil, M. Brand, and E. Kirowa-Eisner. “Trace determination of mercury by anodic stripping voltammetry at the rotating gold electrode”. In: *Analytica chimica acta* 424.1 (2000), pp. 65–76 (cit. on p. 40).
- [134] O. Abollino et al. “Determination of Mercury by Anodic Stripping Voltammetry with a Gold Nanoparticle-Modified Glassy Carbon Electrode”. In: *Electroanalysis: An International Journal Devoted to Fundamental and Practical Aspects of Electroanalysis* 20.1 (2008), pp. 75–83 (cit. on p. 40).

- [135] A. Mandil, L. Idrissi, and A. Amine. “Stripping voltammetric determination of mercury(II) and lead(II) using screen-printed electrodes modified with gold films, and metal ion preconcentration with thiol-modified magnetic particles”. In: *Microchimica Acta* 170.3-4 (2010), pp. 299–305 (cit. on p. 40).
- [136] Y. Oztekin, A. Ramanaviciene, and A. Ramanavicius. “Electrochemical Determination of Cu(II) Ions by 4-Formylphenylboronic Acid Modified Gold Electrode”. In: *Electroanalysis* 23.7 (2011), pp. 1645–1653 (cit. on p. 40).
- [137] G. March, T. Nguyen, and B. Piro. “Modified electrodes used for electrochemical detection of metal ions in environmental analysis”. In: *Biosensors* 5.2 (2015), pp. 241–275 (cit. on p. 40).
- [138] T. Ahuja, I. A. Mir, and D. Kumar. “Biomolecular immobilization on conducting polymers for biosensing applications”. In: *Biomaterials* 28.5 (2007), pp. 791–805 (cit. on p. 40).
- [139] D. T. McQuade, A. E. Pullen, and T. M. Swager. “Conjugated polymer-based chemical sensors”. In: *Chemical Reviews* 100.7 (2000), pp. 2537–2574 (cit. on p. 40).
- [140] K. Zinoubi et al. “Determination of trace heavy metal ions by anodic stripping voltammetry using nanofibrillated cellulose modified electrode”. In: *Journal of Electroanalytical Chemistry* 799 (2017), pp. 70–77 (cit. on p. 40).
- [141] P. Guan et al. “The preparation of a flexible AuNP modified carbon cloth electrode and its application in electrochemical detection of Hg(II) by continuous flow in environmental water”. In: *Analyst* 143.18 (2018), pp. 4436–4441 (cit. on p. 40).
- [142] Y. B. Mollamahale et al. “Application of 3D gold nanotube ensembles in electrochemical sensing of ultra-trace Hg(II) in drinkable water”. In: *Surfaces and Interfaces* 10 (2018), pp. 27–31 (cit. on p. 40).
- [143] A. Becker et al. “Detection of uranium(VI) in aqueous solution by a calix[6]arene modified electrode”. In: *Journal of Electroanalytical Chemistry* 621.2 (2008), pp. 214–221 (cit. on pp. 40, 71, 85).
- [144] Y. Peled et al. “Electrochemical determination of low levels of uranyl by a vibrating gold microelectrode”. In: *Analytical chemistry* 87.1 (2014), pp. 768–776 (cit. on pp. 40, 71, 86).
- [145] O. A. Farghaly and M. A. Ghandour. “Cathodic adsorptive stripping voltammetric determination of uranium with potassium hydrogen phthalate”. In: *Talanta* 49.1 (1999), pp. 31–40 (cit. on p. 40).
- [146] P. Metilda, J. M. Gladis, and T. P. Rao. “Influence of binary/ternary complex of imprint ion on the preconcentration of uranium(VI) using ion imprinted polymer materials”. In: *Analytica chimica acta* 512.1 (2004), pp. 63–73 (cit. on p. 41).
- [147] M. Sonoda et al. “Super uranophile, water-soluble calixarenes: Their metal complexes, stability constants and selective reactivity to uranyl ion”. In: *Analytical sciences* 15.12 (1999), pp. 1207–1213 (cit. on p. 41).
- [148] Q. Lu, J. H. Callahan, and G. E. Collins. “The selective detection of uranium(VI) on a microchip using a derivatized 4-sulfonic calix[6]arene”. In: *Chemical Communications* 19 (2000), pp. 1913–1914 (cit. on p. 41).
- [149] C. Blake, C. Baes, and K. Brown. “Solvent extraction with alkyl phosphoric compounds”. In: *Industrial & Engineering Chemistry* 50.12 (1958), pp. 1763–1767 (cit. on p. 41).
- [150] D. L. Manning, J. R. Stokely, and D. W. Magouyrk. “Uranyl organophosphorus compounds in a poly(vinyl chloride) (PVC) matrix as ion sensors for uranium”. In: *Analytical Chemistry* 46.8 (1974), pp. 1116–1119 (cit. on p. 41).

- [151] I. Goldberg and D. Meyerstein. “Influence of ion exchanger and diluent structure on uranyl ion selective electrode response”. In: *Analytical Chemistry* 52.13 (1980), pp. 2105–2108 (cit. on p. 41).
- [152] C. S. Luo, F. C. Chang, and Y. C. Yeh. “Uranyl selective electrode based on organophosphorus compounds”. In: *Analytical Chemistry* 54.13 (1982), pp. 2333–2336 (cit. on p. 41).
- [153] G. J. Moody, J. M. Slater, and J. D. R. Thomas. “Poly(vinyl chloride) matrix membrane uranyl ion-selective electrodes based on organophosphorus sensors”. In: *Analyst* 113.5 (1988), pp. 699–703 (cit. on p. 41).
- [154] A. Becker, H. Tobias, and D. Mandler. “Electrochemical determination of uranyl ions using a self-assembled monolayer”. In: *Analytical chemistry* 81.20 (2009), pp. 8627–8631 (cit. on pp. 41, 71, 84).
- [155] U. Pinaeva et al. “Early Warning Sensors for Monitoring Mercury in Water”. In: *Journal of hazardous materials* (2019) (cit. on pp. 45, 57, 60, 66, 82).
- [156] U. Pinaeva et al. “Bis[2-(methacryloyloxy) ethyl]phosphate radiografted into track-etched PVDF for uranium(VI) determination by means of cathodic stripping voltammetry”. In: *Reactive and Functional Polymers* 142 (2019), pp. 77–86 (cit. on pp. 45, 58, 87).
- [157] H. Bessbousse et al. “Poly(4-vinyl pyridine) radiografted PVDF track etched membranes as sensors for monitoring trace mercury in water”. In: *Radiation Physics and Chemistry* 118 (2016), pp. 48–54 (cit. on pp. 48, 52, 81, 82).
- [158] C. Aymes-Chodur. “Radiogreffage de fluoropolymères en vue de l’obtention de surfaces hémocompatibles : étude comparative de l’influence des ions lourds rapides ( $E > 1$  MeV/uma) et des rayonnements gamma”. PhD thesis. Charles Sciences biologiques et médicales. Biologie - Santé Bordeaux 2, 1998 (cit. on p. 49).
- [159] R. G. W. Norrish and R. R. Smith. “Catalysed polymerization of methyl methacrylate in the liquid phase”. In: *Nature* 150.3803 (1942), p. 336 (cit. on p. 50).
- [160] V. E. Trommsdorff, H. Köhle, and P. Lagally. “Zur polymerisation des methacrylsäuremethylestern”. In: *Die Makromolekulare Chemie* 1.3 (1948), pp. 169–198 (cit. on p. 50).
- [161] A. Chapiro and J. Dulieu. “Influence of solvents on the molecular associations and on the radiation initiated polymerization of acrylic acid”. In: *European Polymer Journal* 13.7 (1977), pp. 563–577 (cit. on pp. 50, 51).
- [162] M. Grasselli and N. Betz. “Electron-beam induced RAFT-graft polymerization of poly(acrylic acid) onto PVDF”. In: *Nuclear Instruments and Methods in Physics Research Section B: Beam Interactions with Materials and Atoms* 236.1-4 (2005), pp. 201–207 (cit. on p. 51).
- [163] G. Socrates. *Infrared and Raman characteristic group frequencies: tables and charts*. John Wiley & Sons, 2004 (cit. on p. 53).
- [164] L. Franck-Lacaze, P. Sizat, and P. Huguet. “Determination of the pKa of poly(4-vinylpyridine)-based weak anion exchange membranes for the investigation of the side proton leakage”. In: *Journal of Membrane Science* 326.2 (2009), pp. 650–658 (cit. on pp. 53, 57).
- [165] Y. Wang et al. “Highly swellable ultrathin poly(4-vinylpyridine) multilayer hydrogels with pH-triggered surface wettability”. In: *Soft Matter* 9.39 (2013), pp. 9420–9429 (cit. on p. 53).
- [166] M. Elimelech, W. H. Chen, and J. J. Waypa. “Measuring the zeta (electrokinetic) potential of reverse osmosis membranes by a streaming potential analyzer”. In: *Desalination* 95.3 (1994), pp. 269–286 (cit. on p. 54).

- [167] D. O. Jordan and A. J. Taylor. “The electrophoretic mobilities of hydrocarbon droplets in water and dilute solutions of ethyl alcohol”. In: *Transactions of the Faraday Society* 48 (1952), pp. 346–355 (cit. on p. 54).
- [168] H. A. Abramson. “Electrokinetic phenomena and their application to biology and medicine.” In: *The Journal of Physical Chemistry* 38.8 (1934), pp. 1128–1129 (cit. on p. 54).
- [169] J. Stachurski and M. Michałek. “The zeta potential of emulsion droplets of the aliphatic hydrocarbons in aqueous solutions”. In: *Colloids and surfaces* 15 (1985), pp. 255–259 (cit. on p. 54).
- [170] L. P. Voegtli and C. F. Zukoski IV. “Adsorption of ionic species to the surface of polystyrene latexes”. In: *Journal of colloid and interface science* 141.1 (1991), pp. 92–108 (cit. on p. 54).
- [171] M. Elimelech and C. R. O’Melia. “Effect of electrolyte type on the electrophoretic mobility of polystyrene latex colloids”. In: *Colloids and Surfaces* 44 (1990), pp. 165–178 (cit. on p. 54).
- [172] J. R. Goff and P. Luner. “Measurement of colloid mobility by laser Doppler electrophoresis: the effect of salt concentration on particle mobility”. In: *Journal of colloid and interface science* 99.2 (1984), pp. 468–483 (cit. on p. 54).
- [173] H.-J. Jacobasch and J. Schurz. “Characterization of polymer surfaces by means of electrokinetic measurements”. In: (1988), pp. 40–48 (cit. on p. 54).
- [174] H.-J. Jacobasch, G. Bauböck, and J. Schurz. “Problems and results of zeta-potential measurements on fibers”. In: *Colloid and Polymer Science* 263.1 (1985), pp. 3–24 (cit. on p. 54).
- [175] W. Stumm, L. Sigg, and B. Sulzberger. *Chemistry of the solid-water interface: processes at the mineral-water and particle-water interface in natural systems*. John Wiley & Son Inc., 1992 (cit. on p. 54).
- [176] R. J. Hunter. *Zeta potential in colloid science: principles and applications*. Vol. 2. Academic press, 2013 (cit. on p. 55).
- [177] J. Westall and H. Hohl. “A comparison of electrostatic models for the oxide/solution interface”. In: *Advances in Colloid and Interface Science* 12.4 (1980), pp. 265–294 (cit. on p. 55).
- [178] B. Metayer. “Activation acide ou superacide: synthèse de nouveaux composés azotés fluorés et polycycliques”. PhD thesis. Poitiers, 2014 (cit. on p. 56).
- [179] K.-U. Goss. “The pKa values of PFOA and other highly fluorinated carboxylic acids”. In: *Environmental science & technology* 42.2 (2007), pp. 456–458 (cit. on p. 56).
- [180] H. Wang, I. H. Lee, and M. Yan. “A general method to determine ionization constants of responsive polymer thin films”. In: *Journal of colloid and interface science* 365.1 (2012), pp. 178–183 (cit. on p. 57).
- [181] A. A. L. Gonçalves et al. “Synthesis and characterization of high performance super-absorbent hydrogels using bis[2-(methacryloyloxy) ethyl] phosphate as crosslinker”. In: *Express Polymer Letters* 10.3 (2016), p. 248 (cit. on pp. 57, 60).
- [182] B. Oktay, M. H. Uğur, and N. K. Apohan. “Preparation of poly(bis [2-(methacryloyloxy) ethyl] phosphate) crosslinked polymer brushes on Poly(vinylidene fluoride) nanofibers”. In: *Materials Chemistry and Physics* 217 (2018), pp. 168–174 (cit. on p. 58).
- [183] C. Vilela et al. “Poly(bis[2-(methacryloyloxy) ethyl] phosphate)/bacterial cellulose nanocomposites: Preparation, characterization and application as polymer electrolyte membranes”. In: *Applied Sciences* 8.7 (2018), p. 1145 (cit. on p. 58).

- [184] H. Bessbousse et al. “Mercury removal from wastewater using a poly(vinylalcohol)/poly(vinylimidazole) complexing membrane”. In: *Chemical Engineering Journal* 164.1 (2010), pp. 37–48 (cit. on p. 66).
- [185] H. Bessbousse et al. “Novel metal-complexing membrane containing poly(4-vinylpyridine) for removal of Hg(II) from aqueous solution”. In: *The Journal of Physical Chemistry B* 113.25 (2009), pp. 8588–8598 (cit. on p. 66).
- [186] C. Djelloula, A. Hasseineb, and O. Hamdaouic. “Adsorption of cationic dye from aqueous solution by milk thistle seeds: isotherm, kinetic and thermodynamic studies”. In: *Desalination and water treatment* 78 (2017), pp. 313–320 (cit. on p. 67).
- [187] H. Bessbousse et al. “Functionalized nanoporous track-etched  $\beta$ -PVDF membrane electrodes for lead (II) determination by square wave anodic stripping voltammetry”. In: *Analytical Methods* 3.6 (2011), pp. 1351–1359 (cit. on pp. 73, 76, 77).
- [188] R. G. Pearson. “Hard and soft acids and bases”. In: *Journal of the American Chemical Society* 85.22 (1963), pp. 3533–3539 (cit. on pp. 74, 75).
- [189] C. Mbareck et al. “Elaboration, characterization and application of polysulfone and polyacrylic acid blends as ultrafiltration membranes for removal of some heavy metals from water”. In: *Journal of Hazardous Materials* 171.1-3 (2009), pp. 93–101 (cit. on p. 75).
- [190] Y. Zheng and A. Wang. “Removal of heavy metals using polyvinyl alcohol semi-IPN poly (acrylic acid)/tourmaline composite optimized with response surface methodology”. In: *Chemical Engineering Journal* 162.1 (2010), pp. 186–193 (cit. on p. 75).
- [191] R. Roma-Luciw, L. Sarraf, and M. Morcellet. “Complexes of poly(acrylic acid) with some divalent, trivalent and tetravalent metal ions”. In: *European polymer journal* 37.9 (2001), pp. 1741–1745 (cit. on pp. 75, 79).
- [192] A. S. Michaels and O. Morelos. “Polyelectrolyte adsorption by kaolinite”. In: *Industrial & Engineering Chemistry* 47.9 (1955), pp. 1801–1809 (cit. on p. 75).
- [193] M. Wiśniewska and S. Chibowski. “Influence of temperature and purity of polyacrylic acid on its adsorption and surface structures at the  $ZrO_2$ /polymer solution interface”. In: *Adsorption Science & Technology* 23.8 (2005), pp. 655–667 (cit. on p. 75).
- [194] T. Tomida et al. “Binding properties of a water-soluble chelating polymer with divalent metal ions measured by ultrafiltration. Poly(acrylic acid)”. In: *Industrial & engineering chemistry research* 40.16 (2001), pp. 3557–3562 (cit. on p. 75).
- [195] J. Karppi et al. “Adsorption of metal cations from aqueous solutions onto the pH responsive poly(vinylidene fluoride grafted poly(acrylic acid) (PVDF-PAA) membrane”. In: *Journal of polymer research* 17.1 (2010), p. 71 (cit. on p. 78).
- [196] L. Furlan, V. T. de Fávère, and M. C. M. Laranjeira. “Adsorption of calcium ions by graft copolymer of acrylic acid on biopolymer chitin”. In: *Polymer* 37.5 (1996), pp. 843–846 (cit. on p. 78).
- [197] N. Sebastian, B. George, and B. Mathew. “Metal complexes of poly(acrylic acid): synthesis, characterization and thermogravimetric studies”. In: *Polymer degradation and stability* 60.2-3 (1998), pp. 371–375 (cit. on p. 79).
- [198] V. Antochshuk et al. “Benzoylthiourea-modified mesoporous silica for mercury(II) removal”. In: *Langmuir* 19.7 (2003), pp. 3031–3034 (cit. on p. 79).
- [199] B. J. Hathaway et al. “Comprehensive coordination chemistry”. In: *The synthesis, reactions, properties and applications of coordination compounds* 5 (1987), pp. 533–774 (cit. on p. 79).
- [200] A. C. Hiremath and A. S. R. Murthy. “Zink(II), Cadmium(II) and mercury(II) complexes with substituted thioureas”. In: *Chemischer Informationsdienst* 8.34 (1977) (cit. on p. 79).

- [201] A. K. Sengupta, Y. Zhu, and D. Hauze. "Metal(II) ion binding onto chelating exchangers with nitrogen donor atoms: some new observations and related implications". In: *Environmental science & technology* 25.3 (1991), pp. 481–488 (cit. on p. 79).
- [202] R. R. Navarro et al. "Mercury removal from wastewater using porous cellulose carrier modified with polyethyleneimine". In: *Water Research* 30.10 (1996), pp. 2488–2494 (cit. on p. 79).
- [203] P. Braunstein et al. "Competing metal-metal bonding in heterometallic complexes of gold and mercury. Synthesis of contrasting iron-gold-gold-iron and iron-mercury-iron complexes". In: *Inorganic Chemistry* 31.18 (1992), pp. 3685–3687 (cit. on p. 81).
- [204] F. Okçu et al. "Anodic stripping voltammetric behavior of mercury in chloride medium and its determination at a gold film electrode". In: *Turkish Journal of Chemistry* 29.4 (2005), pp. 355–366 (cit. on p. 83).
- [205] O. Ordeig et al. "Trace Detection of Mercury(II) Using Gold Ultra-Microelectrode Arrays". In: *Electroanalysis: An International Journal Devoted to Fundamental and Practical Aspects of Electroanalysis* 18.6 (2006), pp. 573–578 (cit. on p. 83).
- [206] P. Ugo, L. Sporni, and L. M. Moretto. "Ion-exchange voltammetry of trace mercury(II) at glassy carbon electrodes coated with a cationic polypyrrole derivative. Application to pore-waters analysis". In: *Electroanalysis* 9.15 (1997), pp. 1153–1158 (cit. on p. 83).
- [207] J.-M. Zen and M.-J. Chung. "Square-wave voltammetric stripping analysis of mercury(II) at a poly(4-vinylpyridine)/gold film electrode". In: *Analytical Chemistry* 67.19 (1995), pp. 3571–3577 (cit. on p. 83).
- [208] M. Ravichandran. "Interactions between mercury and dissolved organic matter – a review". In: *Chemosphere* 55.3 (2004), pp. 319–331 (cit. on p. 83).
- [209] J. M. Boncella. "Inorganic chemistry: Uranium gets a reaction". In: *Nature* 451.7176 (2008), p. 250 (cit. on p. 84).
- [210] R. V. Davies et al. "Extraction of uranium from sea water". In: *Nature* 203.4950 (1964), pp. 1110–1115 (cit. on p. 84).
- [211] H. Egawa and H. Harada. "Recovery of uranium from sea water by using chelating resins containing amidoxime groups". In: *Nippon Kagaku Kaishi* 1979.7 (1979), pp. 958–959 (cit. on p. 84).
- [212] M. Tamada. "Current status of technology for collection of uranium from seawater". In: *International Seminar On Nuclear War And Planetary Emergencies-42nd Session*. World Scientific. 2010, pp. 243–252 (cit. on p. 84).
- [213] S. Das et al. "Chemical aspects of uranium recovery from seawater by amidoximated electron-beam-grafted polypropylene membranes". In: *Desalination* 232.1-3 (2008), pp. 243–253 (cit. on p. 84).
- [214] S. Girgin, N. Acarkan, and A. A. Sirkeci. "The uranium(VI) extraction mechanism of D2EHPA-TOPO from a wet process phosphoric acid". In: *Journal of radioanalytical and nuclear chemistry* 251.2 (2002), pp. 263–271 (cit. on p. 84).
- [215] A. M. Mhatre et al. "Thin film of poly(bis[2-(methacryloyloxy)ethyl] phosphate) grafted on surface of poly(ether sulfone) membrane for plutonium(IV)-selective alpha tracks registration in CR-39 detector". In: *Journal of Radioanalytical and Nuclear Chemistry* 314.1 (2017), pp. 187–196 (cit. on p. 84).
- [216] A. M. Mhatre et al. "Phosphate functionalized radiation grafted Teflon for capturing and quantifications of U(VI) and Pu(IV) ions at ultra-trace concentration in aqueous samples". In: *Journal of Radioanalytical and Nuclear Chemistry* 317.2 (2018), pp. 1141–1149 (cit. on pp. 84, 91, 96).
- [217] G. R. Choppin. "Soluble rare earth and actinide species in seawater". In: *Marine Chemistry* 28.1-3 (1989), pp. 19–26 (cit. on p. 84).

- [218] D. M. Spori et al. "Influence of alkyl chain length on phosphate self-assembled monolayers". In: *Langmuir* 23.15 (2007), pp. 8053–8060 (cit. on p. 85).
- [219] G. C. Allen et al. "X-ray photoelectron spectroscopy of some uranium oxide phases". In: *Journal of the Chemical Society, Dalton Transactions* 12 (1974), pp. 1296–1301 (cit. on p. 85).
- [220] E. Ordóñez-Regil et al. "Sorption of uranium(VI) onto lanthanum phosphate surfaces". In: *Langmuir* 18.21 (2002), pp. 7977–7984 (cit. on p. 85).
- [221] Y. Al-Salik, I. Al-Shankiti, and H. Idriss. "Core level spectroscopy of oxidized and reduced  $Ce_{x}U_{1-x}O_{2}$  materials". In: *Journal of Electron Spectroscopy and Related Phenomena* 194 (2014), pp. 66–73 (cit. on p. 85).
- [222] Z. Huang et al. "Interaction mechanism of uranium(VI) with three-dimensional graphene oxide-chitosan composite: Insights from batch experiments, IR, XPS, and EXAFS spectroscopy". In: *Chemical Engineering Journal* 328 (2017), pp. 1066–1074 (cit. on p. 85).
- [223] J. Liu et al. "Adsorption behavior of U(VI) on doped polyaniline: the effects of carbonate and its complexes". In: *Radiochimica Acta* 106.6 (2018), pp. 437–452 (cit. on p. 85).
- [224] C. Zhao et al. "Characteristics of uranium biosorption from aqueous solutions on fungus *Pleurotus ostreatus*". In: *Environmental Science and Pollution Research* 23.24 (2016), pp. 24846–24856 (cit. on p. 85).
- [225] A. Gładysz-Płaska, E. Grabias, and M. Majdan. "Simultaneous adsorption of uranium(VI) and phosphate on red clay". In: *Progress in Nuclear Energy* 104 (2018), pp. 150–159 (cit. on p. 85).
- [226] A. Kowal-Fouchard et al. "Use of spectroscopic techniques for uranium(VI)/montmorillonite interaction modeling". In: *Environmental science & technology* 38.5 (2004), pp. 1399–1407 (cit. on p. 85).
- [227] L. Tan et al. "Removal of uranium(VI) ions from aqueous solution by magnetic cobalt ferrite/multiwalled carbon nanotubes composites". In: *Chemical Engineering Journal* 273 (2015), pp. 307–315 (cit. on p. 85).
- [228] L. Ai et al. "Biosorption behaviors of uranium(VI) from aqueous solution by sunflower straw and insights of binding mechanism". In: *Journal of Radioanalytical and Nuclear Chemistry* 298.3 (2013), pp. 1823–1834 (cit. on p. 85).
- [229] T. N. Filippov et al. "Photocatalytic and photochemical processes on the surface of uranyl-modified oxides: an in situ XPS study". In: *Applied Catalysis A: General* 558 (2018), pp. 81–90 (cit. on p. 85).
- [230] E. S. Ilton and P. S. Bagus. "XPS determination of uranium oxidation states". In: *Surface and Interface Analysis* 43.13 (2011), pp. 1549–1560 (cit. on p. 85).
- [231] M. Schindler et al. "XPS spectra of uranyl minerals and synthetic uranyl compounds. I: The U 4f spectrum". In: *Geochimica et Cosmochimica Acta* 73.9 (2009), pp. 2471–2487 (cit. on p. 85).
- [232] R. Drot et al. "Structural environment of uranium(VI) and europium(III) species sorbed onto phosphate surfaces: XPS and optical spectroscopy studies". In: *Journal of colloid and interface science* 205.2 (1998), pp. 410–416 (cit. on p. 85).
- [233] J. Kuuta and E. Yeager. "The study of the charge transfer reaction of the U(VI)-U(V) couple on the rotating gold disc electrode". In: *Journal of Electroanalytical Chemistry and Interfacial Electrochemistry* 31.1 (1971), pp. 119–127 (cit. on p. 86).

- [234] J. Kuuta and E. Yeager. “Regeneration of a substance undergoing an electrode reaction by disproportionation at a rotating electrode: II. Disproportionation of uranium(V) at a gold electrode”. In: *Journal of Electroanalytical Chemistry and Interfacial Electrochemistry* 46.2 (1973), pp. 233–241 (cit. on p. 86).
- [235] H. G. Heal. “Electrochemistry of uranium”. In: *Nature* 157.3982 (1946), p. 225 (cit. on p. 86).
- [236] A. J. Bard, R. Parsons, and J. Jordan. “Standard Potentials in Aqueous Solution”. In: *M. Dekker* (1985) (cit. on p. 86).
- [237] 4th Edition. “Guidelines for drinking-water quality”. In: *WHO chronicle* 38.4 (2011), pp. 104–8 (cit. on p. 88).
- [238] S. Regenspurg et al. “Removal of uranium(VI) from the aqueous phase by iron(II) minerals in presence of bicarbonate”. In: *Applied Geochemistry* 24.9 (2009), pp. 1617–1625 (cit. on p. 88).
- [239] C. Moulin et al. “Uranium speciation in solution by time-resolved laser-induced fluorescence”. In: *Analytical Chemistry* 67.2 (1995), pp. 348–353 (cit. on pp. 89, 90).
- [240] C. Moulin et al. “Time-resolved laser-induced fluorescence as a unique tool for low-level uranium speciation”. In: *Applied Spectroscopy* 52.4 (1998), pp. 528–535 (cit. on p. 90).
- [241] S. Scapolan et al. “Investigations by time-resolved laser-induced fluorescence and capillary electrophoresis of the uranyl–phosphate species: application to blood serum”. In: *Journal of alloys and compounds* 271 (1998), pp. 106–111 (cit. on p. 90).
- [242] G. J. Vazquez, C. J. Dodge, and A. J. Francis. “Interactions of uranium with polyphosphate”. In: *Chemosphere* 70.2 (2007), pp. 263–269 (cit. on p. 90).



# Appendix





## Early warning sensors for monitoring mercury in water

U. Pinaeva<sup>a</sup>, D. Lairez<sup>a,b</sup>, O. Oral<sup>a</sup>, A. Faber<sup>a</sup>, M-C. Clochard<sup>a,\*</sup>, T.L. Wade<sup>a</sup>, P. Moreau<sup>c</sup>, J-P. Ghestem<sup>c</sup>, M. Vivier<sup>d</sup>, S. Ammor<sup>d</sup>, R. Nocua<sup>e</sup>, A. Soulé<sup>e</sup>

<sup>a</sup> Laboratoire des Solides Irradiés, CNRS-CEA-Université Paris-Saclay, UMR7642, Ecole polytechnique, 91128 Palaiseau Cedex, France

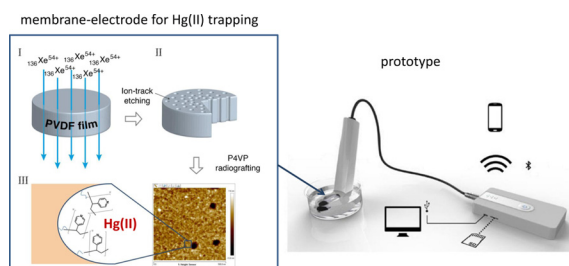
<sup>b</sup> Laboratoire Léon Brillouin, CNRS-CEA-Université Paris-Saclay, CEA-Saclay, 91191 Gif-sur-Yvette Cedex, France

<sup>c</sup> BRGM, 3 avenue Claude-Guillemin, BP 36009, 45 060 Orléans, France

<sup>d</sup> SGS France, Technopole du Madrillet, 65 rue Ettore Bugatti, BP 90014, 76 801 St-Etienne du Rouvray Cedex, France

<sup>e</sup> VALOTEC, Villejuif Bio Park, 1 mail du Professeur Georges Mathé, 94 800 Villejuif, France

### GRAPHICAL ABSTRACT



### ARTICLE INFO

#### Keywords:

Mercury  
Anodic stripping voltammetry  
Membranes  
Nanopores  
Radiografting

### ABSTRACT

Poly-4-vinylpyridine grafted poly(vinylidene difluoride) (P4VP-g-PVDF) nanoporous polymer electrodes were found to be sensitive for Hg(II) analysis. The fabrication and characterization of functionalized nanoporous membrane-electrodes by FESEM and FTIR are presented. Functionalized nanopore charge state versus a large range of pH (1–10) was investigated by registering the streaming potential. This isoelectric point is achieved at the pKa of P4VP (pH = 5). Mercury adsorption at solid-liquid interface obeys a Langmuir law. A protocol for accurate Hg(II) analysis at ppb level was established. Calibration curves were performed and different real water samples (mineral water, ground water, surface water) were spiked and analyzed. The resulting sensor is intended to be integrated into existing systems or used standalone as portable devices. A first generation prototype exhibiting its own integrated potentiostat, its software and set of membrane-electrode pads is presented.

### 1. Introduction

The need for water quality monitoring, in different environmental and health context required by European and national regulations, is increasing. It gives rise to large sampling campaigns with spot sampling, handling, preserving, shipping, storing samples and then time consuming laboratory analysis. The trend for some applications is toward real-time, on-site or *in situ* analyses to improve the reliability of monitoring regarding, for example, the representativity of sampling,

faster information and increasing the capacity of real time warning systems. Quality standards are now in the very low  $\mu\text{g/L}$  (ppb) or  $\text{ng/L}$  range. The objective of getting on site or *in situ* information requires fast, portable, low-cost, environmentally friendly and sensitive instruments; however, few options are available. Among all monitored pollutants, mercury is one of the priority substances identified by the Water Framework Directive (Directive 2000/60/EC) for which discharges have to be stopped before 2020. However, in some historical industrial context or illegal activities (gold panning) mercury

\* Corresponding author.

<https://doi.org/10.1016/j.jhazmat.2019.05.023>

Received 25 January 2019; Received in revised form 30 April 2019; Accepted 11 May 2019

Available online 14 May 2019

0304-3894/ © 2019 Elsevier B.V. All rights reserved.

contamination subsists. Electrochemical mercury sensors allow *in situ* detection but suffer from a lack of repeatability due to memory effects resulting from the difficult removal of mercury from the working electrode [1]. This serious drawback limits their implementation in standard laboratories. Laboratory analyses are still based on expensive equipments such as atomic adsorption (AAS) or atomic fluorescence spectroscopy (AFS) or inductively coupled plasma mass spectroscopy (ICP-MS).

Based on Anodic Stripping Voltammetry (ASV) detection, our team has already proposed functionalized nanoporous polymer electrodes sensitive and selective for heavy metal analysis [2]. With their 3D nanostructure, which allows *in situ* sampling, these membrane-electrodes are ideal for self-monitoring of metals directly on-site. The manufacturing of these membrane-electrodes is so cheap that they can be used as disposable products. This technology relies on gold coated ion-track etched nano-functionalized membranes made of bio-compatible polyvinylidene fluoride (PVDF). Gold electrodes have already shown a remarkable stability toward Hg(II) ASV determination [3–5]. The actual trend for the development of new electrochemical sensors for mercury is the nanostructuring of electrodes as it significantly reduces the Hg (II) detection limit [6–10]. The proposed nanoporous electrodes mix not only the gold electrode nanostructuring but also the functionalization inside of the cylindrical nanopores to collect and pre-concentrate Hg(II) ions by passive adsorption. Poly-4-vinyl pyridine (P4VP), well-known to complex heavy metals such as Cu(II), Co(II), Cr(VI), [11–13] has a special affinity for Hg(II) [14–16]. The pyridinium cycle therefore boots Hg(II) preconcentration [17]. The selectivity for mercury ions was also reported for P4VP grafted PVDF track-etched membranes [18]. The resulting sensors measure mercury well below the limitations imposed by existing norms for landfill and soil leachate. In this field, there is a need for portable and reliable non-certified sensors which can act as early warning sensors to alert in the case of pollution events. The sensors should warn if the mercury level in soil leachate exceeds a threshold of 200 ppb from class 2 non dangerous to class 2 dangerous and 10 ppb from class 2 non dangerous to class 3 inert -EU directive of the 15 march 2006-) making them competitive. Nevertheless, considering the ability of mercury for non-specific adsorption on solid surfaces [20], the understanding of mercury adsorption at the solid-liquid interface inside the P4VP functionalized nanoporosity has to be studied. As the objective is to integrate these Hg(II) sensors in a portable device, the establishment on a robust protocol to obtain reliable results is necessary.

To address these issues, the present publication reports not only on the fabrication and characterization of functionalized nanoporous P4VP-g-PVDF membranes-electrodes by Field Emission Scanning Electron Microscopy (FESEM) and Fourier transformed infra-red (FTIR), but also, on functionalized nanopore charge state versus a large range of pH (1–10). The latter study was performed by registering the streaming potential through the nanopores. To go deeper in the understanding of mercury adsorption at solid-liquid interface, a Langmuir model was investigated. A protocol for mercury analysis at ppb level using these innovative disposable membrane-electrodes has been determined. A performance evaluation on a set of natural water samples was also performed to look at possible interferences. Finally, a first generation prototype exhibiting its own integrated potentiostat, its software and a set of single-use membrane-electrode pads is herein presented.

## 2. Materials and methods

### 2.1. Irradiation

Bi-oriented and polarized PVDF films were purchased from PIEZO-TECH SA (thickness: 9  $\mu\text{m}$ ). Swift Heavy Ions (SHI) irradiations were performed at GANIL, France. Films were irradiated at room temperature with  $\text{Xe}^{54+}$  at energy of 5.9  $\text{MeV}\cdot\text{amu}^{-1}$  under He atmosphere.

Fluence was equal to  $10^9 \text{ cm}^{-2}$ .

### 2.2. Track-etching

Chemical attack is performed at 65 °C in a solution of KOH 10 N and  $\text{KMnO}_4$  0.25 N. The final diameter depends on the etching time. To obtain a pore diameter of 50 nm, 30 min of etching were required. Afterwards, etched PVDF films were first washed in potassium disulfite solution (15%) and then 3 times rinsed with deionized water.

### 2.3. Radiografting and gold sputtering

Remaining radicals present in the pore walls were used to initiate a radical polymerization in presence of 4-vinylpyridine following a reported method [18]. 4-Vinylpyridine was purchased from Sigma-Aldrich without further purification. Pure liquid 4-vinylpyridine monomer solution was added. A bubbling under nitrogen gas was performed for 15 min before radiografting. The radiografting reaction temperature was set at 65 °C. Reaction time was 15 min. The resulting P4VP-g-PVDF nanoporous membranes were rinsed in deionized water, then immersed in ethanol. Finally, they were put in HCl solution at pH 2 for 48 h. The membranes were dried gently at room temperature for 24 h.

A gold layer of 35 nm was sputtered on both side of the nanoporous membrane through a mask to form membrane-electrodes. The design of the mask was adapted to the electrochemical probe which was shaped as a clip for practical use. A circular electrode was preferred to fit with the demonstrator clip (two dimensions were used 4 mm and 8 mm of diameter) while a square one ( $1 \text{ cm}^2$ ) was more appropriate according to prototype pad design.

### 2.4. Zeta potential measurements

The flow of water through porous membranes comes with the flow of ions in solutions. In case pore-walls are electrically charged, the global electric neutrality necessarily implies that the flowing solution is not neutral, but contains an excess of charges of opposite sign to that of the pore-walls. Thus, the liquid flow causes an electric current named streaming current. In the framework of: 1) the Gouy-Chapman-Stern theory for the electric double-layer that neutralizes the surface; and 2) the Poiseuille's law for laminar flow; one obtains for the streaming current  $I_{\text{str}}$ :

$$I_{\text{str}} = -\zeta \epsilon \frac{\pi r^2 \Delta P}{\eta l} \quad (1)$$

where  $\epsilon$  is the electric permittivity,  $r$  the hydrodynamic radius of the pore,  $l$  its length,  $\eta$  the viscosity of the solution,  $\Delta P$  the difference of hydrostatic pressure between the two extremities of the pore and  $\zeta$  (zeta) the electric potential at a distance from the pore-wall at which the fluid velocity becomes zero. Eq. (1) cannot be directly used to measure  $\zeta$ , e.g. by measuring  $I_{\text{str}}$  as a function of  $\Delta P$ , because the current would be cancelled by the potential  $U_{\text{str}}$  due to the accumulation of charges it produces itself:  $U_{\text{str}} = I_{\text{str}}/G$ , where  $G = \sigma \pi r^2/l$  is the pore conductance and  $\sigma$  the conductivity of the solution. With Eq. (1) one gets

$$U_{\text{str}} = -\zeta \times \frac{\epsilon \Delta P}{\sigma \eta}, \quad (2)$$

where all geometric parameters vanish. It is actually this potential that is measured by applying a feedback transmembrane voltage  $U = -U_{\text{str}}$  allowing the electric current to be maintained at zero once a pressure difference  $\Delta P$  is applied. From the slope of  $U$  versus  $\Delta P$ , one gets  $\zeta$  for a salt solution with known  $\sigma$ ,  $\eta$  and  $\epsilon$ .

Measurements were performed by means of a home made device. The membrane is trapped between two compartments with Ag/AgCl electrodes and containing a 0.1 M KCl solution. One compartment

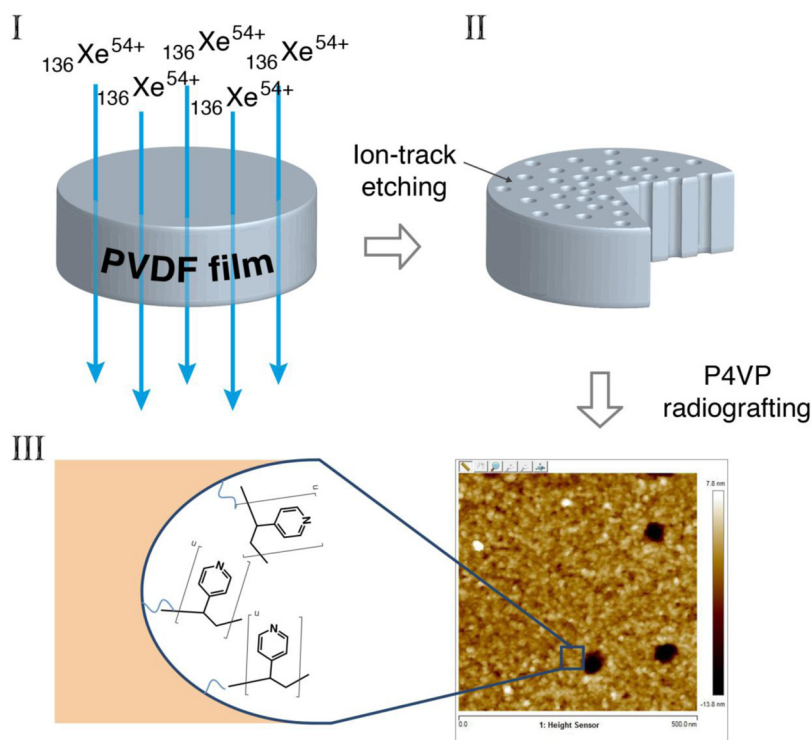


Fig. 1. Fabrication steps to create P4VP-g-PVDF nanoporous membrane: I. swift heavy-ion irradiation of PVDF thin film; II. creation of cylindrical nanopore by ion-track etching; III. functionalization by radiografting inside the nanopores; IV. AFM 2D picture of P4VP-g-PVDF nanoporous membrane and scheme of pore interior.

experiences a varying pressure coming from a syringe-pump, whereas the other remains at the atmospheric pressure. The pressure difference ranging between  $\pm 0.3$  bar is measured with a differential-pressure transducer whereas the feedback voltage is automatically applied, and so measured, using an Axopatch-200B amplifier working in the “I=0” mode.

## 2.5. ASV measurements

Once Au-sputtered, functionalized track-etched P4VP-g-PVDF nanoporous sensors were put in Hg(II)-spiked aqueous solutions for adsorption. For adsorption/exposition tests, the sensors were immersed in Hg(II)-spiked aqueous solutions. Adsorption was passive meaning that application of potential was not needed. During adsorption step, orbital shaker or ping-pong stirrer (250 rpm) were used for stirring Hg(II) polluted solutions. During this step, solvated mercury ions were pre-concentrated inside the P4VP functionalized nanopores.

### 2.5.1. Exposition of the sensors to tested waters (natural and spiked)

Atomic Absorption Spectroscopy stock solution of Hg(II) (1 g/L) was purchased from Alfa Aesar. Nitric acid (65%) and NaCl were purchased from Sigma–Aldrich. For calibration, dilutions in milliQ water were realized in volumetric flasks to obtain final concentrations of 0.5, 1, 2, 5 ppb. For real samples analysis, an intermediate dilution was prepared in volumetric flask in milliQ water and a final dilution was performed in a 250 mL volumetric flask using tested water. Exposition of each membrane-electrode was performed with the same protocol for calibration and real samples analysis: one membrane-electrode (also called sensor) was added in glass containers of 125 mL, 2/3 filled with the tested solution. The flasks were closed and agitated for 4h at room temperature ( $20 \pm 5$  °C) otherwise specified. For each condition (concentration, water type) 3 replicates of each flask were prepared. 12 real water samples have been used for recovery tests: 2 bottled mineral waters (MW), 3 ground waters (GW) and 7 river waters (SW). GWs and SWs were sampled in France, in different locations. 2 ppb of mercury was added to each sample. The final concentration of mercury in spiked

waters was monitored by Atomic Fluorescence Spectroscopy (AFS) applying NF EN ISO 17852. The preparation of the solutions and the analysis of the sensors were done simultaneously with a calibration curve. One trial was performed at lower temperature in milliQ water. For this trial, the water was left in a refrigerator (4 °C) for 1 night before preparing the solutions and the exposition was performed in a cool box

### 2.5.2. Electrochemical analysis

After exposition of the sensors, they were placed into a voltammetric cell for electrochemical analysis. Square Wave Anodic Stripping Voltammetry (SW-ASV) was used for qualitative determination of adsorbed species. Analysis protocol was established as follows: electro-deposition time of 50 seconds at -0.8 V, voltage scanning from -0.8 V to + 1 V at 75 Hz, 3 mV step and 30 mV amplitude. The electrolyte for the analysis was 10 mM HNO<sub>3</sub> and 10 mM NaCl. Two potentiostats were used for SW-ASV measurements. The first, PalmSens (The Netherlands), completed by a home-made clip device was used for lab-scale tests. The clip ensured a connection between the membrane-electrode and the potentiostat. Two gold wires were used for contact with gold coated parts of the membrane, silver wire was used as pseudo-reference electrode. The second potentiostat was a first generation prototype device made by ValoTec (France). A special pad was used for strongly anchoring the membrane-electrode inside ensuring good electrical contact. Sputtered silver electrode was used as pseudo-reference electrode. The pad was then plugged to a pad holder, which was connected to the potentiostat. The design of this prototype was done to allow on-site and *in situ* analyses.

## 3. Results and discussion

### 3.1. Fabrication and characterization of functionalized nanoporous membranes

The fabrication steps are summarized in Fig. 1. Once the PVDF thin films have been irradiated by swift heavy ions at the desired fluence of  $10^9$  cm<sup>-2</sup> (step I), they were chemically etched by a strong alkaline

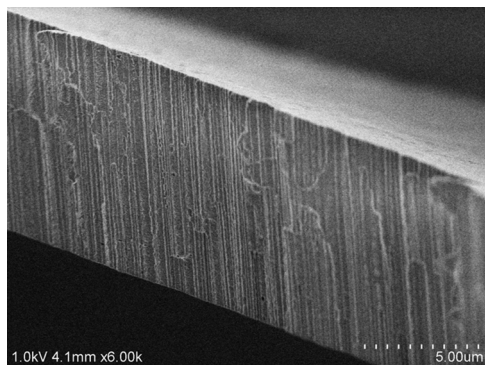


Fig. 2. FESEM cryo-section of PVDF track-etched membranes of  $10^9$  nanopores. $\text{cm}^{-2}$  ( $\text{Kr}^{34+}/^{36+}$  of 10 MeV/mau irradiation performed at GANIL, France)-membrane thickness of 9  $\mu\text{m}$ , pore diameter of 50 nm.

solution containing oxidative species (step II). The ion-track etched PVDF membrane results in a membrane with well-defined cylindrical nanopores (Fig. 2). Track-etched PVDF nanopore walls are rich with radicals. These radicals have been created during ion-beam pre-treatment. The radicals, which were located in the crystalline areas, kept trapped and could not diffuse nor recombine [2]. Freshly etched PVDF membranes with pore diameters of 60 nm were then immersed in 4-vinyl pyridine (4-VP) monomer solution. Heating the system to 65  $^\circ\text{C}$  gave sufficient energy to the remaining radicals to initiate the 4-VP polymerization from the pore walls (step III).

The functionalized P4VP-g-PVDF nanoporous membranes were characterized by FTIR (Fig. 3). The FTIR spectrum predominantly exhibits the characteristic absorption bands of PVDF with its doublet corresponding to  $\text{CH}_2$  vibrations at 2985 and 3025  $\text{cm}^{-1}$ , a multiplet with spectral bands at 1453, 1424, 1403 and 1385  $\text{cm}^{-1}$  attributed to a mixture of  $\text{CH}_2$  and C-C vibrations, the two most intense bands for  $\text{CF}_2$  absorption at 1211 and 1183  $\text{cm}^{-1}$  and the PVDF skeleton vibration region between 900 and 400  $\text{cm}^{-1}$ . The last region contains well-organized spectral bands. It reflects the conformation of the PVDF chains and gives access to information concerning the crystalline nature. As we have chosen a bi-stretched PVDF film, the signature of  $\beta$ -phase content is shown by the peak presence at 840  $\text{cm}^{-1}$ . The pyridinium cycle absorption band at 1600  $\text{cm}^{-1}$  (inset of Fig. 3) shows the P4VP presence. Its intensity is very small due to the low radio-grafting yield of 1 wt%. The radiografting reaction was intentionally stopped at its early stage (15 min of reaction) to limit the P4VP grafting to the sole pore wall surface and to avoid any pore blockage. The pyridinium cycle displays absorption bands with a main peak at 1600  $\text{cm}^{-1}$  surrounded by two satellite peaks at 1560 and 1640  $\text{cm}^{-1}$  as previously described [18]. The homogeneity of the grafting on the large treated membranes of  $4 \times 20 \text{ cm}^2$  was also checked by FTIR comparing the pyridinium cycle absorption band intensity at 1600  $\text{cm}^{-1}$  on three very different points.

To complete the characterization of grafted P4VP onto the PVDF nanopore walls, we have investigated the quality of the nanopore coverage with P4VP chains by determining the charge state at the solid surface all along the cylindrical nanopores. To do so, a pressure-driven flow of electrolyte solution through the nanopores (or nanochannels)

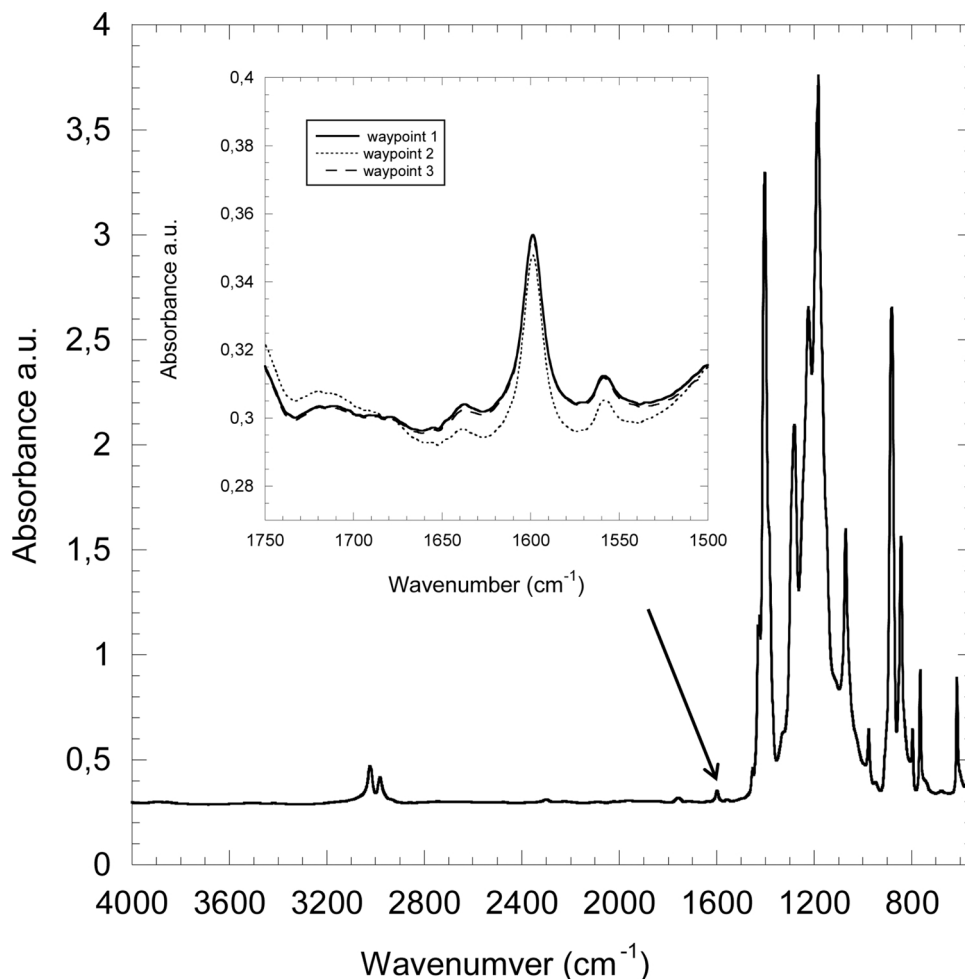
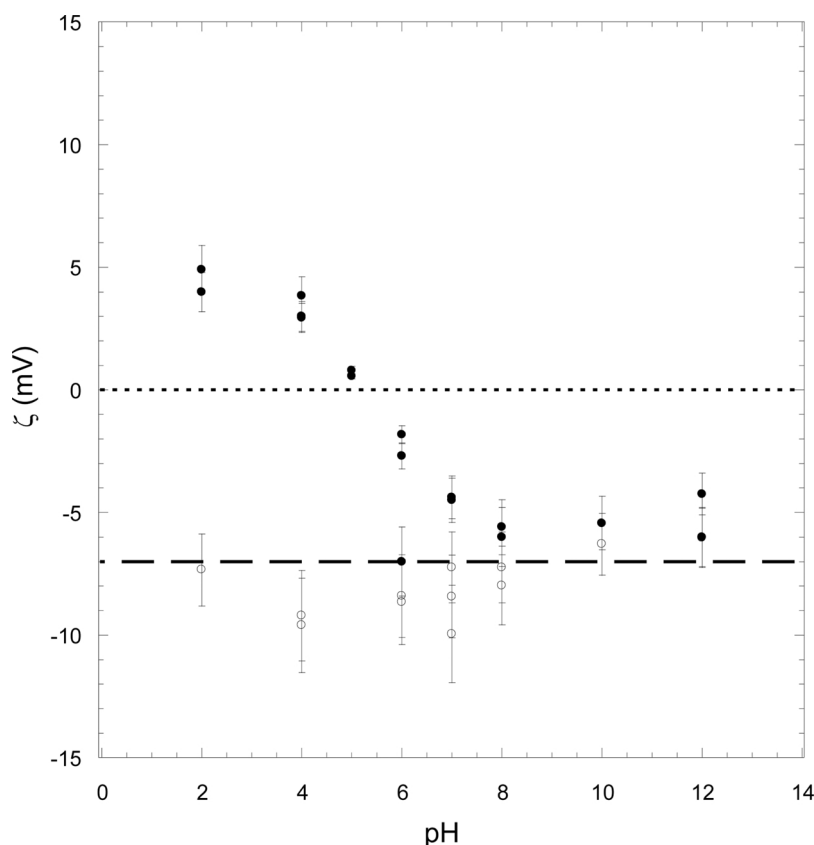


Fig. 3. FT-IR spectra in transmission mode of P4VP-g-PVDF nanoporous membrane registered at 3 different points on the same film.



**Fig. 4.** Zeta potential of PVDF nanoporous membranes against pH of aqueous solutions. (●) P4VP grafted PVDF nanoporous membrane; (○) non-grafted PVDF nanoporous membrane.

was applied to create an electric streaming current due to the movement of ions in the bulk and electrical double layer at solid–liquid interface. Accumulation of ions downstream generated an electric streaming potential that depends on surface charge, electrolyte concentration, and channel dimensions [21]. With these factors, streaming potential measurements can be used to calculate the zeta potential of pore walls.

Fig. 4 displays the zeta potential of P4VP grafted and non-grafted PVDF nanopores. Ungrafted PVDF nanopores were negatively charged. The negative charges correspond to the presence of oxidative species formed at the nanopore surface during the alkaline etching process. The mean zeta potential of -7 mV was roughly constant whatever the pH of the solution. P4VP grafted PVDF nanopores exhibited a different behaviour. The nanopore charges were completely inverted into positive charges for very acidic pH. The isoelectric point was reached at pH 5 which corresponds to the pKa of P4VP. [22] It shows that the zeta potential determination via the streaming potential is a powerful technique to accurately characterize the charge state of functionalized organic nanopores. It also gives information on the coverage completion of the nanopores walls by the grafted polymer chains. Effectively, the P4VP protonation in acidic pH was sufficient to completely counterbalance the underneath negative charges of PVDF nanoporous membrane. It means that the grafting coverage is uniform and relatively dense all along the nanopores.

### 3.2. Mercury detection by ASV

To transform radiografted P4VP-g-PVDF nanoporous membranes into membrane-electrodes, a thin gold layer is sputtered on both membrane surfaces (Fig. 5a). The gold layer should be thin enough to not block the pore entry and thick enough to ensure a good conductivity (Fig. 5c).

The first step is the passive adsorption of Hg(II) ions by complexation with P4VP functionalities. The membranes were immersed into the Hg(II) solution to analyze for 4 h and 24 h. The concentration range was 0 to 0.05  $\mu\text{mol.L}^{-1}$  corresponding to 0–10 ppb. After adsorption, both gold layers were connected to a potentiostat. One gold layer served as working electrode and the second one, as counter electrode. The pseudo-reference electrode was made of chlorinated Ag wire. Applied potential of -0.8 V during 50 s promotes Hg(II) migration to the working electrode, where Hg(II) were reduced into Hg(0). After electrodeposition, a potential scan from -0.8 V to 1 V permitted to oxidize again from Hg(0) atoms into Hg(II) ions when reaching Hg(II) redox potential at +0.5V as shown in Fig. 5b.

The calibration curves displayed on Fig. 5d summarize the mean results obtained from measurements in membrane triplicate of 3 different batches. The obtained calibration shows a deviation from the linearity at 10 ppb. The linearity can be proposed only for a 0 to 5 ppb range. A power curve fit was found more appropriate to describe the results considering a larger range (Fig. 5d).

The mean error of each set of measurements was 21% at 4 h of adsorption against 45% at 24 h of adsorption (Fig. 6).

It was also found that the stirring is of crucial importance for result reproducibility. A ping-pong stirring, set at 200–250 rpm equivalent, gave better results than rotating stirring.

To further explore the sources of error, various calibration curves were performed by three of involved teams from 0.5 to 5 ppb using sensors fabricated at different dates of the year and belonging to 4 different batches of P4VP-g-PVDF membrane-electrodes (Fig. 7 left). The calibration curves presented good linearity. However, they could not be superimposed. The variability of peak height might diverge as 2 to 3 times, i.e. for the 5 ppb concentration, the measured current peak heights vary from 35 to 115  $\mu\text{A}$ . Note that the obtained data with the batch 1 showed higher peak heights than those obtained with other

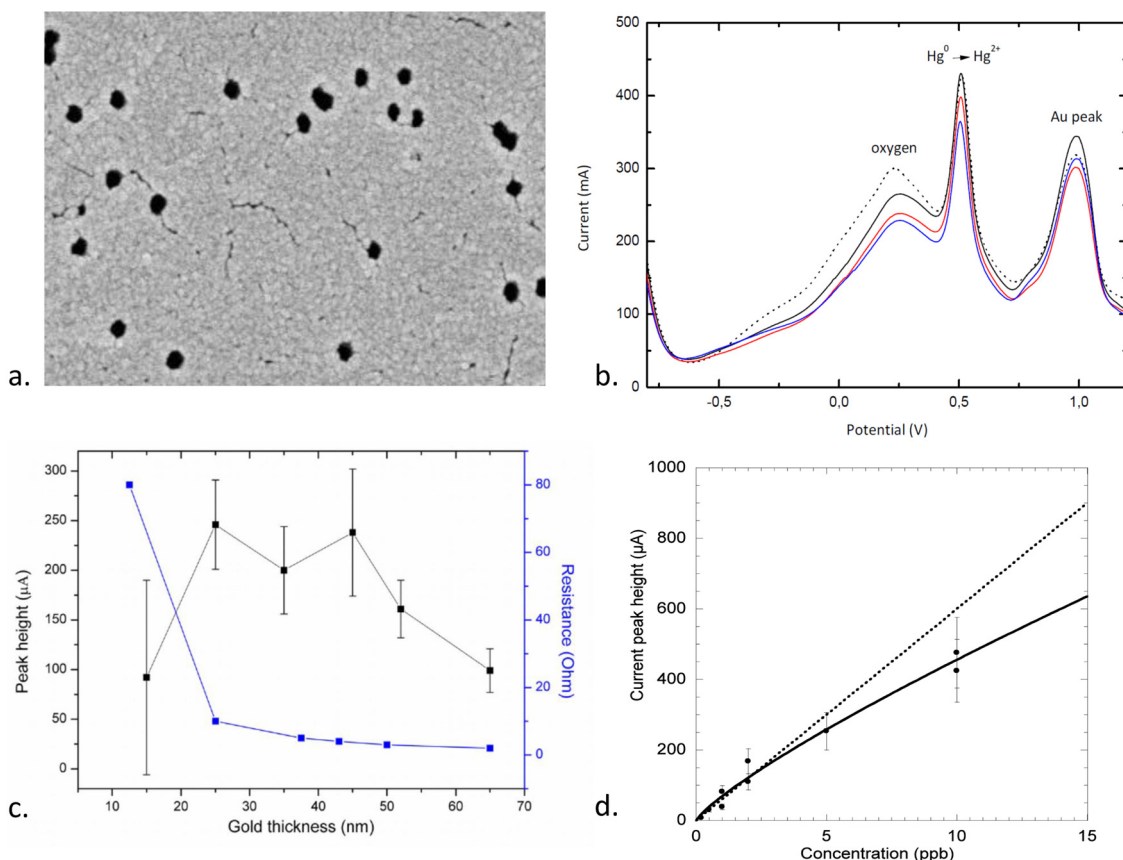


**Fig. 5.** a. FESEM image of the surface of Au-sputtered P4VP-g-PVDF nanoporous membrane; b. ASV voltammograms of Hg(II) adsorbed into P4VP-g-PVDF nanopores - Hg(II) solution concentration of 25 ppb - frequency 25 Hz-, adsorption time of 4h, stirring rate of 250 rpm; c. effect of gold layer thickness on the conductivity; d. Calibration curve grouping results obtained on 3 different membrane-electrode batches and registered using circular electrode of 4 mm diameter and pore density of  $10^9 \text{ cm}^{-2}$  - adsorption time of 4h, stirring rate of 200 rpm - linear fit:  $y = 60x$ ; power fit:  $y = 69x^{0.82}$ .

batches. This very high sensitivity is sometimes due to a better contact with the demonstrator clip and the Au electrode layer. Considering only batches 2, 3 and 4, the mean values were in the 40–74  $\mu\text{A}$  range.

Taking into account such inter-batch variability, not only triplicates were systematically done for all concentrations and water samples but also, calibration curves were plotted at each analytical sequence with the same batch of membrane-electrodes. As the repeatability for a batch is rather good (20% on average), the user protocol would mention the calibration of the sensor by a three point calibration curve registered the same day.

The effect of temperature was also studied for a given calibration curve (Fig. 7 right). A 3 points calibration curve (1, 2, 5 ppb) was performed at 25°C and another at lower temperature (10°C) in MilliQ water. The signal is lower at low temperature. Dispersion seems not to be affected by temperature. This result suggests a thermodynamical equilibrium between Hg(II) and P4VP entities grafted inside the nanopores.

### 3.3. Sorption of Hg(II) study in P4VP grafted nanopores

To better understand Hg complexation inside P4VP grafted nanopores, we have studied the equilibrium sorption of Hg(II) in aqueous solutions. Experiments were thus carried out at pH 7 on MilliQ solutions of Hg(II) with initial concentrations  $c_0$  ranging from 0.1 ppb to 100 ppb. The measurements were performed at room temperature after 4 h of P4VP-g-PVDF nanoporous membrane immersion in the Hg(II) solution. The uptake of Hg(II) ions by the P4VP-g-PVDF nanoporous membrane has been evaluated by calculating the variation of Hg(II) concentration of the surrounded solution,  $c_{eq}$ , before and after membrane immersion.

The Hg(II) uptake can be described in the form of sorption isotherm. Fig. 8 displays the molar mass  $q$  of mercury sorbed at equilibrium per gram of membrane ( $\text{mol.g}^{-1}$ ) versus the equilibrium concentration  $c_{eq}$ . A maximum mass of  $0.55 \mu\text{mol.g}^{-1}$  of sorbed Hg(II) was reached. It corresponds to the mercury saturation of the membrane. It is worth noting that the mercury saturation starts at  $c_{eq}$  equals to  $0.05 \mu\text{mol.L}^{-1}$  corresponding to 10 ppb which explains the observed deviation from the linearity of Hg(II) calibration curves (Fig. 5d).

To fit the experimental data, a Langmuir model was used. The Langmuir equation is written as follows (eq. 3):

$$q = \frac{q_{\max} b c_{\text{eq}}}{1 + b c_{\text{eq}}} \quad (3)$$

where  $q_{\max}$  and  $b$  are the maximum sorbed mass at saturation ( $\mu\text{mol.L}^{-1}$ ) and the sorption coefficient ( $\text{L} \cdot \mu\text{mol}^{-1}$ ) respectively. To validate the Langmuir formalism, the linearized form (eq. 4) of eq. 3, known as Hanes–Woolf treatment, was plotted (inset of Fig. 8). The thermodynamic equilibrium behaviour is in agreement with previous work [15] for P4VP/Hg(II) complexes at solid-liquid interface.

$$\frac{c_{\text{eq}}}{q} = \frac{c_{\text{eq}}}{q_{\max}} + \frac{1}{b q_{\max}} \quad (4)$$

### 3.4. Interference in presence of metal ions and high salt content

In the presence of numerous metallic cations (Ni(II), Zn(II), Cd(II), Cu(II), Mg(II), Pb(II) and Ca(II)), the Hg(II) peak potential did not exhibit any interference (Fig. 9a). Neither Hg peak area nor peak height was affected within experimental error, except in presence of Fe(II)

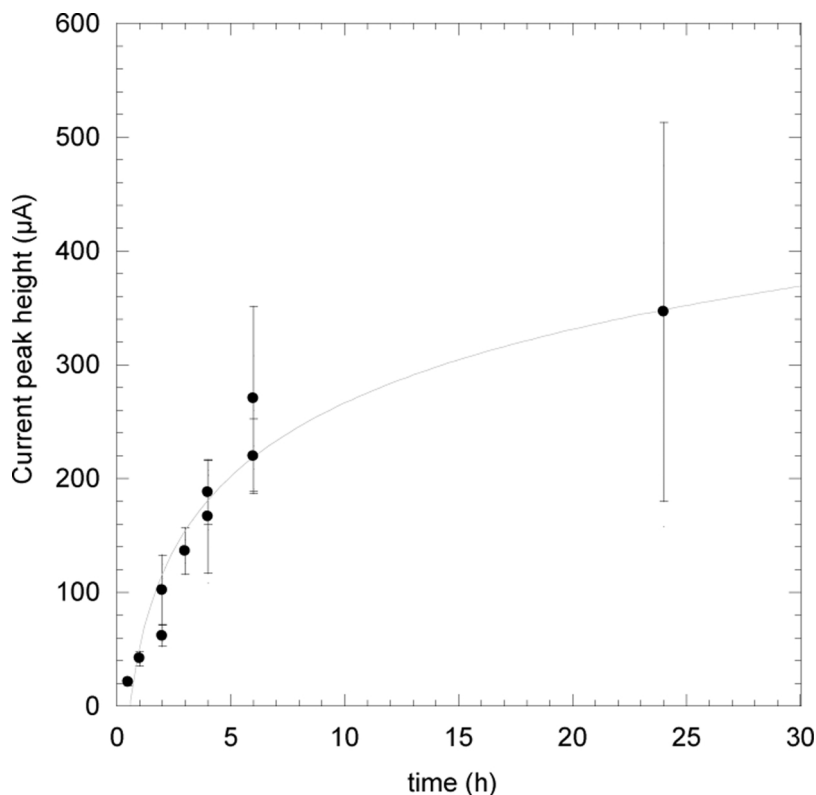


Fig. 6. Measured ASV peak height against adsorption time of 2ppb Hg(II) in presence of P4VP-g-PVDF nanoporous membrane; milliQ water, 4 mm circular electrodes, logarithm fit:  $y = 51.54 + 215\log(x)$ .

ions. The interference with Fe(II) ions confirmed a previous study [18]. It is due to a well-known complex formation between Fe and Hg species in the solution [19]. As a matter of fact, this complex formation decreased the Hg(II) content prior the sorption step by the P4VP-g-PVDF membrane-electrode. The pH effect was already reported in the range from 3 to 9 [18] and no impact on peak intensity was noticed.

The effect of salt content from 0.01 to 35 g.L<sup>-1</sup> was also investigated (Fig. 9b). The concentration of 35 g.L<sup>-1</sup> of NaCl was herein chosen to simulate seawater. The increase of salt content slightly shifts the Hg peak to more positive potentials. A 0.05 V variation of Hg peak potential was observed in salted aqueous solutions from 0.01 to 35 g.L<sup>-1</sup>. This variation of potential is due to slight fluctuations of the pseudo-reference (chlorinated Ag wire). Such small variations of

potential are not a problem as far as the Hg(II) peak height and area are preserved. An automatic correction was always applied by peak searching mode associated with potentiostat software. These results suggest that the high selectivity of P4VP toward Hg(II) ions allows an Hg detection compatible to seawater environment.

### 3.5. Measurements in natural waters

The results are presented in Table 1 together with natural water samples characteristics such as organic carbon or ion content depending the locations from where these samples were taken (see supplementary information). After adding 2 ppb Hg(II) in water samples, mercury concentrations were both measured by ASV and Atomic Fluorescence

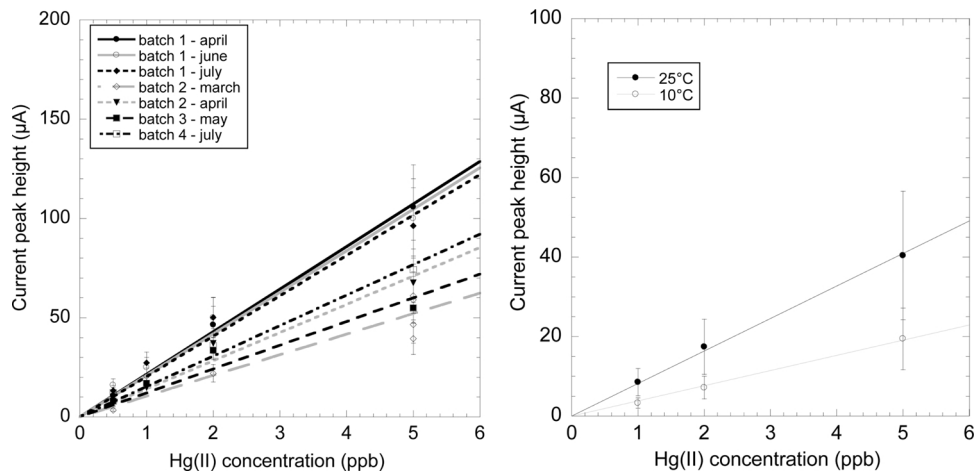


Fig. 7. Linear calibration curves for Hg(II) trapped inside P4VP-g-PVDF nanoporous membranes registered using circular electrodes of 8 mm diameter and pore density of 10<sup>9</sup> cm<sup>-2</sup> at: (left) different dates and (right) two temperatures.

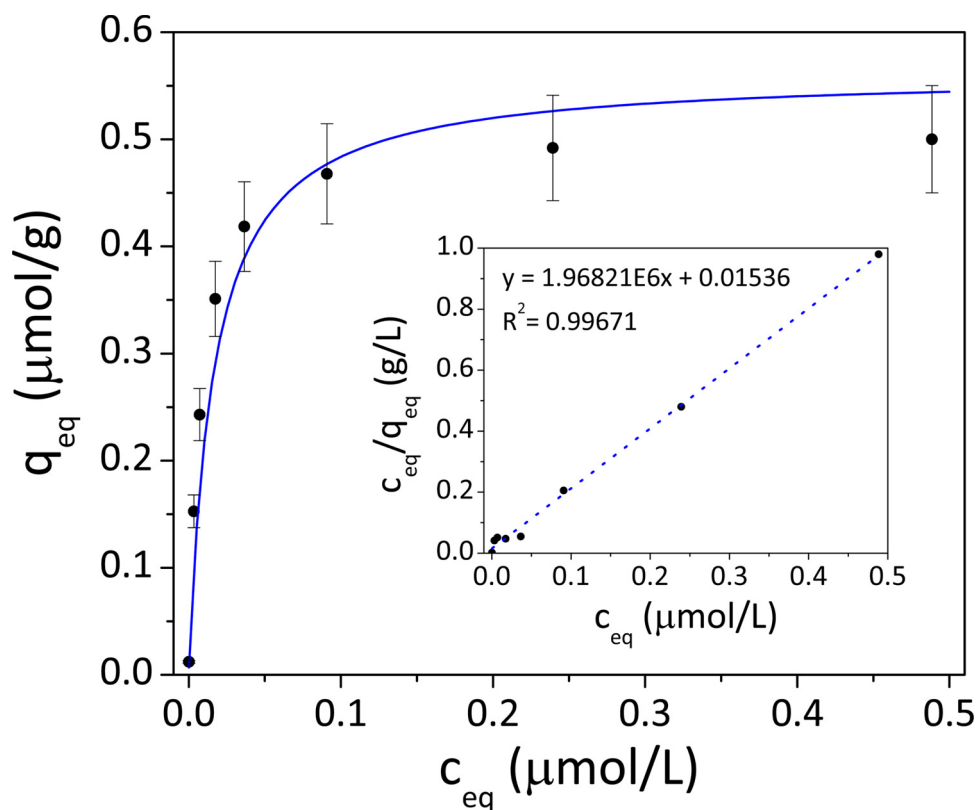


Fig. 8. Sorbed Hg(II) concentration versus equilibrium concentration: (•) experimental data, (line) Langmuir model; (inset) linearization to assess the Langmuir model towards the experimental data.

Spectroscopy (AFS). Recovery levels were calculated as the ratio of Hg (II) concentrations measured by ASV with the sensor and the total concentration of Hg in the spiked sample measured by AFS. It was shown by ASV that high salt content did not affect mercury adsorption in P4VP-g-PVDF nanoporous membrane-electrodes. The Hg(II) recoveries obtained in the mineral (MW) and ground (GW) waters are higher than 100%, except for sample GW-3 for which no signal was identified. The latter result was confirmed by a second trial with the same experimental conditions and a different membrane batch. It seems that no interferences occur in mineralized water. In contrast, the Hg(II)

recoveries are dramatically decreased when the tests are performed in surface waters (SW). In some SW samples, the signal was totally missing (SW-5 for example). As suspended particulate matters may affect  $Hg^{2+}$  sorption, surface water samples were studied as filtrated samples (filter cut-off of 0.7 μm) before the trials. In these samples, the recovery is lower than the one obtained in MW and GW samples. It does not seem to be directly correlated to ion content. The effect of dissolved organic carbon content seems more probable as the Hg(II) concentration decreases as dissolved organic carbon increases.

When SW samples were used raw (without filtration), the mercury

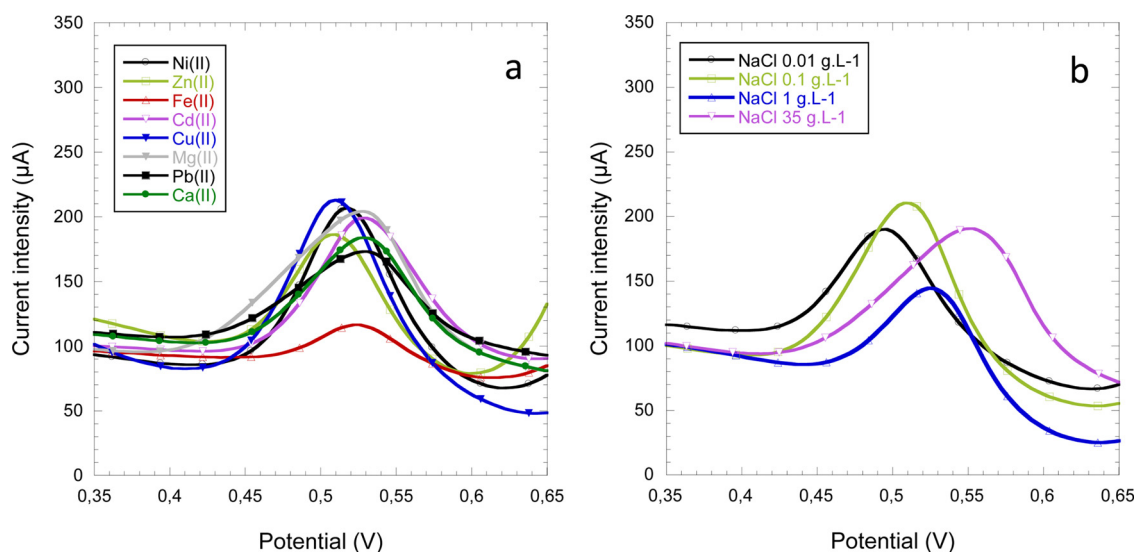


Fig. 9. 5 ppb Hg(II) in presence of: 0.1 g.L<sup>-1</sup> of Ni(II), Zn(II), Fe(II), Cd(II), Cu(II), Mg(II), Cu(II) and 1 mg.L<sup>-1</sup> of Pb(II) standard solution; b) NaCl at various concentrations: 0.01, 0.1 and 35 g.L<sup>-1</sup>.

**Table 1**  
Measured Hg(II) concentrations by P4VP-g-PVDF nanoporous membrane-electrodes in 2 ppb Hg(II) artificially polluted natural waters.

Water type	Suspended matter (mg/L)	Total organic carbon (mg/L)	pH	Conductivity ( $\mu$ S/cm)	Measured Hg(II) concentration (ppb)	Recovery <sup>*</sup> (%)
GW-1	< 2	< 0.5	7.9	327	3.0 $\pm$ 0.23	147.6
GW-2	< 2	< 0.5	7.6	419	3.4 $\pm$ 0.88	174.0
GW-3	< 2	0.8	8.3	597	No peak	No peak
MW-1	< 2	-	7.4	-	2.5 $\pm$ 0.38	138.4
MW-2	< 2	0.7	7.2	-	2.7 $\pm$ 1.61	164.7
SW-1 (filtrated)	< 2	0.6	7.8	99	1.3 $\pm$ 0.44	62.2
SW-2 (filtrated)	< 2	1.6	8.1	419	1.6 $\pm$ 1.28	82.2
SW-3 (filtrated)	< 2	3.0	8.4	507	1.0 $\pm$ 0.38	49.7
SW-4 (filtrated)	< 2	3.5	7.5	198	0.1 $\pm$ 0.07	8.4
SW-5 (filtrated)	< 2	4.5	7.8	249	No peak	No peak
SW-4 (raw)	10.0	3.7	7.5	204	0.3 $\pm$ 0.05	16.7
SW-5 (raw)	8.0	4.8	7.8	249	No peak	No peak
SW-6 (raw)	21.0	4.3	7.5	249	-0.3 $\pm$ 0.40	0.0
SW-7 (raw)	21.0	9.3	8.2	666	No peak	No peak

\* Ratio of Hg(II) concentrations measured by ASV and by Atomic Fluorescence Spectroscopy(AFS).

recoveries were almost null for these samples. Two SW samples were studied after filtration and as raw samples (SW-4 and SW-5). For SW-4 and SW-5 the trials on filtrated samples and raw samples were performed the same days. For both samples, either filtrated or raw, the recovery was very low. It means that the ASV signal extinction is not due to suspended matter, but rather to the matrix composition and notably the total dissolved organic carbon. A high organic carbon content may favor sorption of Hg(II) dramatically decreasing the Hg(II) ion content. The sensors reported herein are only sensitive to free dissolved Hg<sup>2+</sup> ions. This result suggests that the sorption of Hg(II) with dissolved organic species changes the mercury speciation.

### 3.6. Prototype fabrication and function

A first generation prototype exhibiting its own integrated potentiostat, its software and set of membrane-electrode pads has been built (Fig. 10). The manufacturing of membrane-electrode pads is cheap enough to use them as disposable products. A single-use avoids any memory effect of polluted membranes after Hg sampling. The

membrane-electrode pads are thus consumables, well-adapted to be inserted by a simple clip to the probe. The prototype probe is composed of a ladel-like support and a measurement device driven by a dedicated software application.

Regarding the measurement device, it is composed by seven sub-modules (Fig. 11). The power supplies module is used to provide electronics needed power supplies, while the excitation module is used to generate the voltage, in the range from -2 V to 2 V, to be applied to the working electrode. An additional voltage measurement module is used to measure the voltage at the reference electrode. The current measurement module serves to measure the current between the working electrode and the counter electrode in the range from nA to mA. The central unit and acquisition module allows the configuration of the voltage to be applied by the excitation module and also the data acquisition of the measurements of the voltage and current needed to make the voltammogram measurement. A data storage module is included to simply store the acquired data through a micro SD card. Finally, the communication module permits to send the data to a computer or to a smartphone application to visualize the data.



**Fig. 10.** Photograph of the prototype showing, immersed in a 125 mL glass beaker container, a support holding the membrane-electrode pad. Membrane-electrode pads are connected to the measurement device via the support cable -inset: pad components, the membrane-electrode is sandwiched in middle where the open windows allow a permanent contact with the electrolyte. A dedicated software drives the overall system.

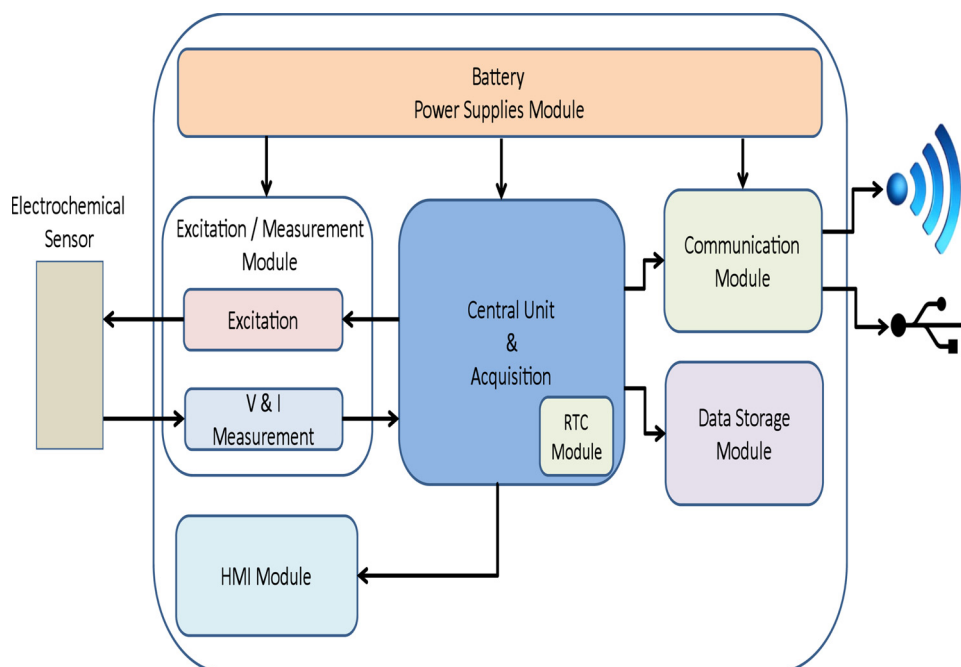


Fig. 11. Scheme of sub-modules composing the measurement system of the prototype.

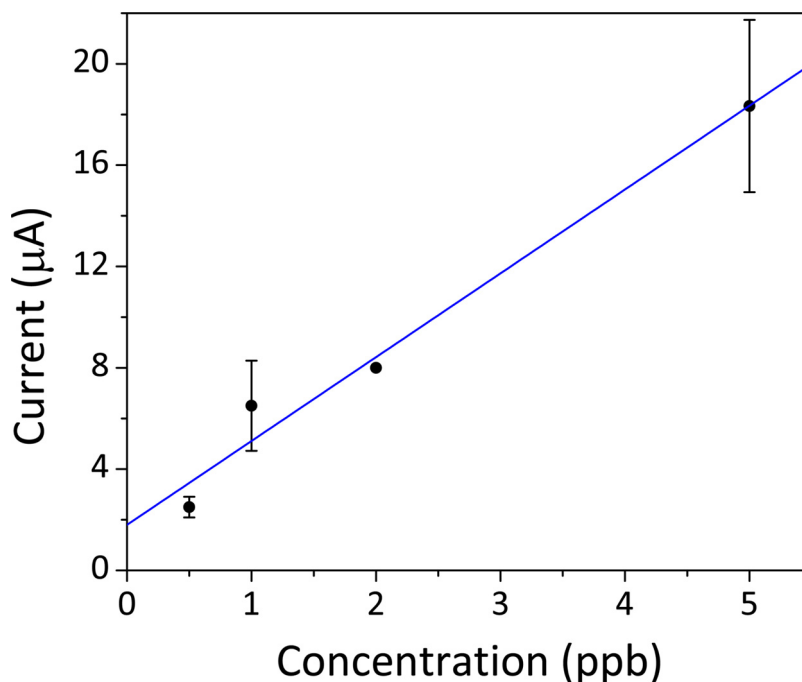


Fig. 12. Calibration curve of Hg(II) using the prototype.

Among devices available on the market, this specific device has the advantage to be portable and offer the possibility to perform on-site measurements. The device is simple to use and allows the registration of the voltammograms in few minutes. End-users only have to plug the sensor to the device, power it on, open the software and click to start the measurement. A blue LED on the device turns on during the measurement, then end-users can obtain a voltammogram, save it as figure or export it as data table. Fig. 10 shows the results obtained for Hg(II) detection using the device for different concentrations of Hg(II) and the Au-sputtered P4VP-g-PVDF membrane inserted in the pad (inset of Fig. 8). Prior to measurement, the P4VP-g-PVDF membrane-electrodes have been immersed in diluted Hg(II) standard solutions following the

aforementioned established protocol. As observed, the complete system presented a linear response *versus* Hg(II) concentration solution in ppb range (Fig. 12).

### 3.7. Conclusions

Functionalized P4VP-g-PVDF nanoporous membrane-electrodes for anodic stripping voltammetry have been successfully fabricated and have exhibited a good sensitivity toward Hg(II) in deionized and natural waters. Membranes were fully characterized by FTIR and by zeta potential determination. The zeta potential determination *via* the streaming potential was found to be a powerful technique to accurately

characterize the charge state of functionalized organic nanopores. The isoelectric point of PVDF-g-P4VP nanoporous membranes was reached at pH 5 which corresponds to the pKa of P4VP.

To transform the radiografted P4VP-g-PVDF nanoporous membranes into electrodes, a thin gold layer of 35 nm was sputtered on both membrane surfaces. The 3D nanostructuring of membrane-electrodes allowed a pre-concentration of mercury prior ASV measurement. Hg(II) adsorption isotherm displayed a Langmuir shape confirming that the adsorption of Hg(II) and P4VP was an equilibrium at room temperature. Using membrane-electrodes with a density of nanopores of  $10^9 \text{ cm}^{-2}$ , an adsorption time of 4 h into Hg(II) spiked deionized water, it resulted in a limit of detection of 0.1 ppb and mean precision of 20%. It is important to mention that the membrane-electrodes are consumables and should be thrown away after use for quantitative results.

These membrane-electrodes coupled with ASV sensing showed a good mercury recovery in mineral waters and ground waters. However Hg(II) recoveries in surface waters were very low, even in filtrated samples. A relationship with total carbon content was pointed out. The sensors reported herein are only sensitive to free dissolved  $\text{Hg}^{2+}$  ions. Future work should be done to cross our results with other techniques to understand how Hg(II) reacts with dissolved organic species and changes its speciation.

From the demonstrator home-made system, a first generation prototype exhibiting its own integrated potentiostat, its software and set of membrane-electrode pads was built. A calibration for Hg(II) in the range of 0-5 ppb was easily obtained with a reliable linearity.

## Acknowledgements

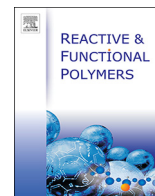
This work belongs to CAPTOT project supported by the French National Agency for Research, ANR -Agence National de la Recherche (grant ANR-15-CE04-13). The authors want to warmly thank the EMIR committee to have accepted their irradiation proposal and allow GANIL experiments. Notably, the strong implication of Dr. E. Balanzat and Dr. Y. Ngono-Ravache during swift heavy ion irradiations is herein acknowledged. The authors are also grateful to Sébastien Ceste from Centre Polymedia of the Ecole Polytechnique (France) for its graphic work implication.

## Appendix A. Supplementary Data

Supplementary data associated with this article can be found, in the online version, at <https://doi.org/10.1016/j.jhazmat.2019.05.023>.

## References

- [1] D. Martin-Yerga, M.B. Gonzalez-Garcia, A. Costa-Garcia, Electrochemical determination of mercury: A review, *Talanta* 116 (2013) 1091–1104, <https://doi.org/10.1016/j.talanta.2013.07.056>.
- [2] M. Barsbay, O. Guven, T.L. Wade, M.-C. Clochard, Functionalized membrane electrodes (FMEs) by RAFT-mediated radical polymerization inside synthetic nanochannels, *J. Membr. Sci.* 445 (2013) 135–145, <https://doi.org/10.1016/j.memsci.2013.05.029>.
- [3] Y. Bonfil, M. Brand, E. Kirova-Eisner, Trace determination of mercury by anodic stripping voltammetry at the rotating gold electrode, *Analyt. Chim. Acta* 424 (2000) 65–76, [https://doi.org/10.1016/S0003-2670\(00\)01074-6](https://doi.org/10.1016/S0003-2670(00)01074-6).
- [4] A. Giacomino, O. Abollino, M. Malandrino, E. Mentasti, Parameters affecting the determination of mercury by anodic stripping voltammetry using a gold electrode, *Talanta* 75 (2008) 266–273, <https://doi.org/10.1016/j.talanta.2007.11.015>.
- [5] A. Mandil, L. Idriissi, A. Amine, Stripping voltammetric determination of mercury (II) and lead(II) using screen-printed electrodes modified with gold films and metal pre-concentration with thiol-modified magnetic particles, *Microchim. Acta* 170 (2010) 299–305, <https://doi.org/10.1007/s00604-010-0329-x>.
- [6] K. Zinoubi, H. Majdoub, H. Barhoumi, S. Boufi, N. Jaffrezic-Renault, Determination of trace heavy metal ions by anodic stripping voltammetry using nanofibrillated cellulose modified electrode, *J. Electroanal. Chem.* 799 (2017) 70–77, <https://doi.org/10.1016/j.jelechem.2017.05.039>.
- [7] P. Guan, P.R. Guo, N. Liu, F. Zhang, Y.Q. Lei, The preparation of a flexible AuNP modified carbon cloth electrode and its application in electrochemical detection of Hg(II) by continuous flow in environmental water, *Analyst* 143 (18) (2018) 4436–4441, <https://doi.org/10.1039/c8an01284a>.
- [8] Y. Mollamahale, M. Ghorbani, A. Dolati, M.M. Ghalkhani, Application of 3D gold nanotube ensembles in electrochemical sensing of ultra-trace Hg(II) in drinkable water, *Surf. Interfaces* 10 (2018) 27–31, <https://doi.org/10.1016/j.surfin.2017.11.001>.
- [9] F. Tan, L. Cong, N.M. Saucedo, J. Gao, X. Li, A. Mutchandani, An electrochemically reduced graphene oxide chemiresistive sensor for sensitive detection of  $\text{Hg}^{2+}$  ion in water samples, *J. Hazard. Mater.* 320 (2016) 226–233, <https://doi.org/10.1016/j.jhazmat.2016.08.029>.
- [10] A.M. Ashrafi, Z. Koudelkova, E. Sedlackova, L. Richtera, V.V. Adam, Review - Electrochemical sensors and biosensors for determination of mercury ions, *J. Electrochem. Soc.* 165 (16) (2018) B824–B834, <https://doi.org/10.1149/2.038181jes>.
- [11] W.Q. Tang, L.H. Mao, Z.F. Zhou, C.F. Wang, Q.L. Chen, S.S. Chen, Facile synthesis of 4-vinylpyridine-based hydrogels via laser-ignited frontal polymerization and their performance on ion removal, *Colloid. Polym. Sci.* 292 (2014) 2529–2537, <https://doi.org/10.1007/s00396-014-3279-8>.
- [12] D.D. Maksin, S.O. Klajajavic, M.B. Dolic, J.P. Markovic, B.M. Ekmesic, A.E. Onjia, A.B. Nastasovic, Kinetic modeling of heavy metal sorption by vinyl pyridine based copolymer, *Hem. Ind.* 66 (6) (2012) 795–804, <https://doi.org/10.2298/HEMIND121002112M>.
- [13] P. Viel, S. Palacin, F. Descours, C. Bureau, Electropolymerized poly-4-vinylpyridine for removal of copper from wastewater, *Appl. Surf. Sci.* 212–213 (2003) 792–796, [https://doi.org/10.1016/S0169-4332\(03\)00105-3](https://doi.org/10.1016/S0169-4332(03)00105-3).
- [14] H. Bessbousse, J.-F. Verchere, L. Lebrun, Increase in permeate flux by porosity enhancement of a sorptive UF membrane designed for the removal of mercury(II), *J. Membr. Sci.* 364 (2010) 167–176, <https://doi.org/10.1016/j.memsci.2010.08.018>.
- [15] H. Bessbousse, T. Rhalou, J.-F. Verchere, L. Lebrun, Novel metal-complexing membrane containing poly(4-vinylpyridine) for removal of Hg(II) from aqueous solution, *J. Phys. Chem. B* 113 (2009) 8588–8598, <https://doi.org/10.1021/jp900863f>.
- [16] B.L. Rivas, H.A. Maturana, M. Luna, Selective binding of mercury ions by poly(4-vinylpyridine) hydrochloride resin, *J. Appl. Polym. Sci.* 74 (1999) 1557–1562, [https://doi.org/10.1002/\(SICI\)1097-4628\(19991107\)74:6 < 1557::AID-APP30 > 3.0.CO;2-2](https://doi.org/10.1002/(SICI)1097-4628(19991107)74:6 < 1557::AID-APP30 > 3.0.CO;2-2).
- [17] Z. Li, S. Xia, J. Wang, C. Bian, J.J. Tong, Determination of trace mercury in water based on N-octylpyridinium ionic liquids preconcentration and stripping voltammetry, *J. Hazard. Mater.* 301 (2016) 206–213, <https://doi.org/10.1016/j.jhazmat.2015.08.061>.
- [18] H. Bessbousse, N. Zran, J. Fauléau, B. Godin, V. Lemée, T. Wade, M.-C. Clochard, Poly(4-vinylpyridine) radiografted PVDF track etched membranes as sensors for monitoring trace mercury in water, *Rad. Phys. Chem.* 118 (2016) 48–54, <https://doi.org/10.1016/j.radphyschem.2015.03.011>.
- [19] P. Braunstein, M.T. Camellini, Competing Metal-Metal bonding in heterometallic complexes of gold and mercury. Synthesis of contrasting Fe-Au-Au-Fe and Fe-Hg-Fe complexes, *Inorg. Chem.* 31 (1992) 3685–3687, <https://doi.org/10.1021/ic0004a002>.
- [20] J.L. Parker, N.S. Bloom, Preservation and storage techniques for low-level aqueous mercury speciation, *Sci. Total Environ.* 337 (1) (2005) 253–263, <https://doi.org/10.1016/j.scitotenv.2004.07.006>.
- [21] M.B. Andersen, H. Bruus, J.P.J.P. Bardhan, S.S. Pennathur, Streaming current and wall dissolution over 48 h in silica nanochannels, *J. Colloid Interface Sci.* 360 (2011) 262–271, <https://doi.org/10.1016/j.jcis.2011.04.011>.
- [22] H. Wang, I.H. Lee, M. Yan, A general method to determine ionization constants of responsive polymer thin films, *J. Colloid Interface Sci.* 365 (2012) 178–183, <https://doi.org/10.1016/j.jcis.2011.08.081>.



# Bis[2-(methacryloyloxy)ethyl] phosphate radiografted into track-etched PVDF for uranium (VI) determination by means of cathodic stripping voltammetry

U. Pinaeva<sup>a</sup>, T.C. Dietz<sup>b</sup>, M. Al Sheikhy<sup>b</sup>, E. Balanzat<sup>c</sup>, M. Castellino<sup>d,e</sup>, T.L. Wade<sup>a</sup>, M.C. Clochard<sup>a,\*</sup>

<sup>a</sup> Laboratoire des Solides Irradiés, CEA/DRF/IRAMIS, Ecole Polytechnique, CNRS Institut Polytechnique de Paris, 91128 Palaiseau, France

<sup>b</sup> Laboratory for Radiation and Polymer Science, Department of Materials Science and Engineering A. J. Clark School of Engineering, University of Maryland, College Park, MD 20742 – 2115, USA

<sup>c</sup> CIMAP, GANIL, 14000 Caen Cedex, France

<sup>d</sup> Department of Applied Science and Technology, DISAT, Politecnico di Torino, Corso Duca degli Abruzzi 24, 10129 Torino, Italy

<sup>e</sup> Istituto Italiano di Tecnologia, IIT@Polito, Via Livorno 60, 10144 Torino, Italy



## ARTICLE INFO

### Keywords:

Uranyl  
Track-etched membrane  
Radiation grafting  
Stripping voltammetry

## ABSTRACT

We report the radiation grafting of bis[2-(methacryloyloxy)ethyl] phosphate (B2MP) through electron-beam onto PVDF films and through swift heavy ions (SHI) irradiations into the pores of track-etched PVDF membranes. Radiolytically produced radicals were studied using EPR. To adapt the radiation grafting protocol inside the nanopores of track-etched membranes, the electron-beam irradiated films at varying monomer concentrations, doses and solvent mixtures were first studied. It was found that track-etched membranes, even after 1 h of chemical treatment, do not require a post-etching irradiation to initiate free-radical polymerization of B2MP from remaining radiation-induced radicals. The presence of functional groups inside the nanopores of the membrane were examined using FTIR and XPS. After exposure of B2MP-g-PVDF membranes to a uranyl solution, XPS was also exploited to evidence of  $O_2UO_2^{2+}$  trapping inside the membrane nanoporosity by tracking the presence of U 4f peak. The B2MP-g-PVDF membranes were converted into electrodes by depositing 35 nm of gold on each side through a mask. Detection of ppb concentrations (from 20 to 100 ppb) of uranyl by B2MP-g-PVDF membrane electrodes was demonstrated by means of square wave cathodic stripping voltammetry (SW-CSV). The limit of detection (LOD) was estimated to be 17 ppb ( $3\sigma - / \text{slope}$ ).

## 1. Introduction

The International Guidelines for Drinking Water Quality of the World Health Organization (4th edition, 2011) has recommended a value for uranium of 30 ppb (or  $\mu\text{g L}^{-1}$ ) for waters intended for human consumption [1]. However, this limit may not protect specifically sensitive populations, such as children and people with predispositions for hypertension or osteoporosis [2,3]. Common analytical techniques involve ICP-MS [4] and radio-metric analyses [5]. However, these methods are neither accessible nor suitable for daily field work and tests. Additionally, they are expensive and not portable. Thus, removal and accurate analysis of low uranium concentrations in drinking water are necessary.

Uranium is a natural element that exists in various oxidation states, namely +2, +3, +4, +5, and +6. The most common and

thermodynamically stable form of dissolved uranium is uranyl ion,  $^{VI}O_2U^{VI}O_2^{2+}$ . The uranyl ion has a linear structure with two non-reactive double uranium-oxygen bonds, and it tends to create a complex with six ligands at the most, leaving the  $U = O$  bonds unaltered [6]. Being a hard Lewis acid, uranyl has more affinity for hard bases. The compounds, containing oxygen or nitrogen atoms, as well as phosphate or carbonate anions, are good candidates for uranium trapping [7–14]. Recently developed oxalate-based adsorbents made by radiation grafting of diallyl oxalate onto polyamide 6 fabrics maintain high uranium capacity comparable with amidoximated resins [15]. Five years ago, a polymeric chelating resin was prepared by growing third generation poly(amido)amine (PAMAM) dendron on the surface of styrene divinylbenzene (SDB) [16]. The main advantage of a dendron structure is that it contains a significant quantity of nitrogen and oxygen atoms from the amino and amide groups, which produce a strong chelating

\* Corresponding author.

E-mail address: [marie-claude.clochard@polytechnique.edu](mailto:marie-claude.clochard@polytechnique.edu) (M.C. Clochard).

effect. PAMAM modified poly(SDB) adsorbent, carrying phosphorus functional groups, has exhibited superior adsorption characteristics with high complexation rates, capacity and selectivity [17]. Indeed, the poly(ethylene glycol methacrylate phosphate) macroporous membranes made by means of radiation grafting onto poly(propylene) fibrous sheets have shown a high pre-concentration effect due to the presence of phosphate groups [18]. In nature, phosphates have been found complexed with uranium in ore deposits [19,20]. It is also well known that di-(2-ethylhexyl) phosphoric acid and trioctylphosphine oxide are used for uranium extraction from liquid acidic solutions [21]. Thus, phosphate containing materials have already proved their efficacy in extracting uranium from aqueous solutions.

Electrochemical analysis has a major advantage over aforementioned methods, as it allows speciation of uranium in solution by direct measurement. Also, voltammetry is an easy-to-use, sensitive, fast, portable and relatively cheap technique, enabling the performance of on-site analysis. There are not many reports about electrochemical detection of uranium. Peled et al. report the determination of uranyl using gold microelectrodes by anodic stripping voltammetry [22]. Another technique among the few is to use a gold electrode chemically modified by  $\text{POCl}_3$  capable quantifying  $\mu\text{M}$  uranyl concentrations [23]. Recently, nanostructured materials are becoming a trend in heavy metal extraction from water due to the improved trapping properties. Nevertheless, there is no method for uranyl determination by means of functionalized nanoporous membrane electrodes. Bis[2-(methacryloyloxy)ethyl] phosphate (B2MP),  $[\text{H}_2\text{C}=\text{C}(\text{CH}_3)\text{CO}_2\text{CH}_2\text{CH}_2\text{O}]_2\text{P}(\text{O})\text{OH}$ , is one among a few commercially available phosphate containing monomers which might be used for uranium extraction. Additionally, the availability of two vinyl groups allows B2MP to be grafted onto an irradiated polymer.

The current study presents radiation grafting of B2MP onto electron-beam irradiated polyvinylidene fluoride (PVDF) films and inside the nanopores of track-etched PVDF membrane. The goal is to show the capability of such a nanostructured material to preconcentrate uranyl from aqueous solutions and its ability to be analyzed using voltammetry. Our study is one of the few reports relating to on-site uranyl sensing. The B2MP-g-PVDF membrane electrodes were fabricated according to the previous works of our team [24,25]. Electron paramagnetic resonance spectroscopy (EPR) was used to analyze radiolytically produced radicals. Field-emission scanning electron microscopy (FESEM) was used to examine morphology of the PVDF track-etched membrane surface. Fourier-transform infrared spectroscopy (FTIR) and X-ray photoelectron spectroscopy (XPS) were utilized to verify the presence of functional groups inside the nanopores of the membrane. Square-wave cathodic stripping voltammetry (SW-CSV) was used to plot a calibration curve and to demonstrate sensitivity toward trapped  $\text{O}_2\text{UO}_2^{2+}$  in trace level (LOD is 17 ppb).

## 2. Experimental section

### 2.1. Materials and instruments

Semi-crystalline  $\beta$ -polyvinylidene fluoride (PVDF) films of 9  $\mu\text{m}$  thickness (about 40% crystallinity) were provided by PiezoTech SA. Potassium hydroxide, potassium permanganate, Mohr's salt ( $(\text{NH}_4)_2\text{Fe}(\text{SO}_4)_2 \cdot 6\text{H}_2\text{O}$ ), sodium metabisulphite ( $\text{Na}_2\text{S}_2\text{O}_5$ ), bis[2-(methacryloyloxy)ethyl] phosphate (B2MP), ethanol were purchased from Sigma-Aldrich. Uranyl acetate (Polysciences, Inc.) was used in the preparation  $\text{O}_2\text{UO}_2^{2+}$ -spiked water. Acetate buffer was prepared using acetic acid (glacial, 100% unhydrous, Merck) and anhydrous sodium acetate (Alfa Aesar). Deionized water was used for preparing all the solutions. The orbital shaker (Heidolph) was used to perform the B2MP-g-PVDF membrane electrodes adsorption. A PalmSens potentiostat (The Netherlands) was used for all voltammetric tests.

### 2.2. Irradiation

Swift-heavy ion (SHI) irradiations were performed at GANIL, France. PVDF films were irradiated at room temperature with  $^{136}\text{Xe}^{48+}$  ( $7.46 \text{ MeV} \cdot \text{amu}^{-1}$ ) under He atmosphere. The films ( $4 \text{ cm} \times 30 \text{ cm}$ ) were anchored on movable sample holders. Fluence was adjusted taking into account number of passages and the ion beam flux. For all the results the fluence was  $10^{10} \text{ cm}^{-2}$ . Conversion of the fluence to adsorbed dose in the polymer was calculated by formula:

$$\text{Dose (Gy)} = 1.6 \cdot 10^{-7} \cdot f \cdot \frac{dE}{dx}, \quad (1)$$

where  $f$  is ion fluence,  $\text{cm}^{-2}$ ,  $\frac{dE}{dx}$  is the massic stopping power,  $\text{MeV} \cdot \text{mg}^{-1} \cdot \text{cm}^2$ ,  $1.67 \cdot 10^{-7}$ ,  $\text{J} \cdot \text{mg} \cdot \text{MeV}^{-1} \cdot \text{kg}^{-1}$ , is a conversion constant. For instance, the ion fluence of  $10^9 \text{ cm}^{-2}$  for SHI irradiated films corresponds to 7.6 kGy dose.

Electron-beam irradiations were performed at the SIRIUS facility (Laboratoire des Solides Irradiés, Ecole Polytechnique, France). Films were irradiated at room temperature under He atmosphere with accelerating voltage of 2.5 MeV and machine current of 1.4  $\mu\text{A}$ . Doses were 5, 7.5, 10, 50 and 100 kGy. All the irradiated samples were immediately stored at  $-20^\circ\text{C}$  under anaerobic conditions to prevent from oxidation.

### 2.3. Chemical etching

$\beta$ -PVDF SHI irradiated films were chemically etched using 10 M KOH and 0.25 M  $\text{KMnO}_4$  solutions at  $65^\circ\text{C}$  for 25 min. The etched membranes were washed with aqueous solution of  $\text{Na}_2\text{S}_2\text{O}_5$  (7.5 wt%) to reduce the remaining active  $\text{KMnO}_4$ , followed by rigorous rinsing by deionized water. The diameter of obtained cylindrical nanopores depends on the etching duration. After 25 min etching of films exposed to a  $10^{10} \text{ cm}^{-2}$  fluence the resulting mean pore diameter was  $60 \pm 5 \text{ nm}$ .

### 2.4. Radiation grafting of B2MP

The electron-beam irradiated films or track-etched PVDF membranes were placed in purgeable glass tubes containing B2MP monomer solutions. To avoid undesired homopolymerization reaction, we followed indirect grafting. However, Mohr's salt (632 mg/100 mL) was used in each radiation grafting procedure to suppress possible gel formation, and thereby to increase the grafting yields onto the surface of PVDF. The purgeable glass tubes were then connected to a Schlenk line for oxygen elimination. After 15 min of  $\text{N}_2$  purging at room temperature, they were then sealed and put into a thermostat water bath at  $65^\circ\text{C}$  for various times. The grafted films were washed with ethanol and dried at room temperature. Gravimetric grafting yields (GY) were calculated by formula (2).

$$\text{GY} = \frac{m_{\text{final}} - m_{\text{initial}}}{m_{\text{initial}}} \times 100\%, \quad (2)$$

where  $m_{\text{initial}}$  and  $m_{\text{final}}$  are masses of film weighed before and after radiation grafting respectively.

### 2.5. Characterization of B2MP-g-PVDF membranes

Electron paramagnetic resonance spectroscopy (EPR) was used to examine radiation-induced changes in PVDF films. The measurements were carried out at room temperature using a Bruker EMX spectrometer with 9.85 GHz at 18.4 mW power and 100 kHz field modulation frequency. The radical consumption was determined through the ratio of signal intensity and the receiver gain multiplied by the mass of the sample. Membranes topologies were checked after each fabrication step using Field-Emission Scanning Electron Microscopy (FESEM). FESEM micrographs were acquired with Hitachi S-4800 microscope at 1 kV accelerating voltage and 7  $\mu\text{A}$  current. B2MP grafting was followed by

Fourier-Transform InfraRed spectroscopy (FTIR) and X-ray Photoelectron Spectroscopy (XPS). FTIR spectra were obtained with the Nicolet iS50 FT-IR spectrometer (Thermo scientific). Spectra were recorded in absorption mode by cumulating of 64 scans with resolution of  $2\text{ cm}^{-1}$ . XPS spectra were conducted on a PHI 5000 VersaProbe (Physical Electronics) instrument. An Al K- $\alpha$  (1486.6 eV) monochromatic X-ray source was used. A 187.85 eV pass energy value was used for survey spectra and 23.5 eV for high resolution (HR) peaks. Charge compensation was accomplished with a combined electron and Ar neutralizer system. The binding energies were calibrated by fixing the C 1s binding peak to 284.5 eV. XPS spectra also allowed the detection of trapped U(VI) in B2MP-g-PVDF membranes. The P2p signal has been acquired during 10–15 min (around 50 scans) for undoped samples and during 30–40 min (roughly 150 scans) for U(VI) doped samples.

## 2.6. Voltammetry

rack-etched B2MP-g-PVDF membranes were converted into electrochemical nanoporous sensors by depositing 35 nm of gold on each side of the membrane through a mask. The gold on one side of the membrane serves as working electrode while the other one serves as counter electrode. Both gold surfaces ( $0.8\text{ cm}$  of diameter =  $0.502\text{ cm}^2$ ) were connected to a potentiostat. A chlorinated Ag wire acts as pseudo-reference electrode. A cyclic voltammogram (CV) was first performed on a B2MP-g-PVDF membrane electrode in a blank solution of acetate buffer (50 mM) and  $0.1\text{ M}$   $\text{KNO}_3$  (pH 3) (Fig. 1). Despite the thin Au layer, a typical profile of amorphous Au electrode was registered. Integration of reduction peak at  $0.62\text{ V}$  corresponding to one monolayer of Au oxide formed during the positive scan leads to a charge of around  $300\text{ }\mu\text{C}$ . Taking in account the charge of gold monolayer of  $482\text{ }\mu\text{C}\cdot\text{cm}^{-2}$  [26], an electroactive surface area of  $0.622\text{ cm}^2$  was found.

The sensors were then immersed in the aqueous solutions of uranyl acetate to adsorb uranyl. During stirring, the solvated  $\text{UO}_2^{2+}$  ions are complexed with phosphate groups of B2MP in the subporous region of the membrane, thus the trapped ions can be analyzed by means of voltammetry. Applying a potential of  $+1.2\text{ V}$  during 300 s permits oxidation of adsorbed species on the cathode. After this deposition time, quantitative analysis was performed by registering the charge of  $\text{UO}_2^{2+}$  reduction peak when applying square-wave cathodic stripping voltammetry (SW-CSV). The potential was negatively scanned from  $+1.2\text{ V}$  to  $-1.2\text{ V}$  with step potential of  $3\text{ mV}$ , frequency of  $20\text{ Hz}$  and amplitude of  $30\text{ mV}$ . A mixture of  $50\text{ mM}$  acetate buffer and  $0.1\text{ M}$   $\text{KNO}_3$  (pH 3) was used as electrolyte. Each current peak height of U(VI)

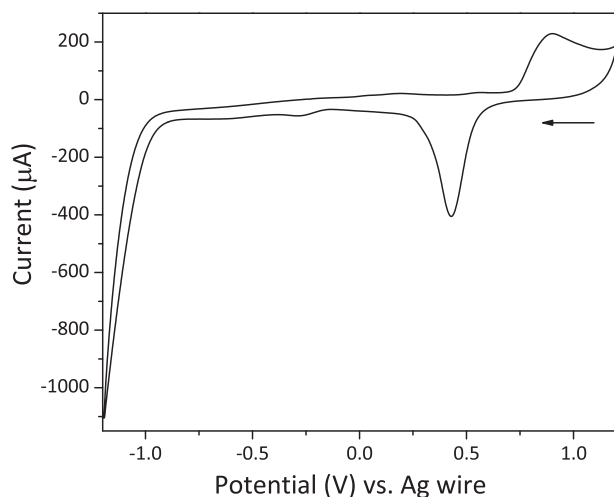


Fig. 1. CV of B2MP-g-PVDF membrane-electrode of  $0.8\text{ cm}$  of diameter recorded in  $50\text{ mM}$  acetate buffer and  $100\text{ mM}$   $\text{KNO}_3$  (pH 3) electrolyte at a scan rate of  $100\text{ mV}\cdot\text{s}^{-1}$ .

reduction peak corresponds to an average value of 3 registered SW-CSV measurements referred to 3 distinct B2MP-g-PVDF membrane-electrodes from the same batch.

## 3. Results and discussion

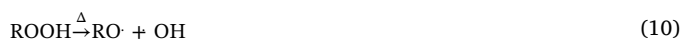
### 3.1. Radiation-induced radical polymerization in PVDF films

Whatever the irradiation process (electrons or ions), the irradiation of PVDF films,  $-\text{[CH}_2-\text{CF}_2\text{]}_n-$ , yields  $\text{H}_2$  and HF gas release [27], crosslinking, double bond formation (for example,  $-\text{CF}_2-$ ,  $\text{CH}=\text{CF}_2$ ,  $-\text{CH}=\text{CF}-$ ) [28], in addition to the formation of alkyl radicals [29,30]. These free radicals are  $-\text{CF}_2-\text{C}\cdot\text{H}_2$ ,  $-\text{CH}_2-\text{C}\cdot\text{F}_2$ ,  $-\text{CF}_2-\text{C}\cdot\text{H}-\text{CF}_2$ ,  $-\text{CH}_2-\text{C}\cdot\text{F}-\text{CH}_2$  [31]. The radicals react with molecular oxygen to produce the corresponding peroxy radicals ( $\text{ROO}\cdot$ ). There is thus the co-existence of two types of radicals, alkyl and peroxy, present in the irradiated PVDF films.

Due to the semi-crystalline structure of PVDF of about 40%, there is still a considerable amount of radicals trapped in the crystallites, and at the interfaces between the crystalline and amorphous regions [32]. The addition of the alkyl radicals to the double bonds of B2MP monomer initiates the polymerization reaction. Simultaneously, the peroxy radicals also initiate, to some extent, the polymerization reaction. Trapped radicals, formed by breaking lateral bonds of polymer, initiate polymerization reaction in presence of monomer (Eq. (4)). After the initiation, the propagation of monomer chains takes place (Eq. (5)). The process continues until the growing macro-radicals meet each other (recombination) and thus terminate the chain growth (Eq. (6)).



When the polymer substrate is irradiated under an oxygen (or air) atmosphere or was exposed to air after irradiation, peroxides or hydroperoxides due to oxidation of alkyl radicals are formed (Eqs. (7)–(9)). At elevated temperature, the peroxide bonds decompose on alkoxy and hydroxy radicals (Eq. (10)). The alkoxy radicals can then initiate the polymerization reaction when put in contact with monomer solution (Eq. (11)).



### 3.2. Electron-beam induced grafting of B2MP onto PVDF

In order to determine the optimal radiation grafting parameters, the electron-beam irradiated films at various doses were first grafted with B2MP. During electron beam irradiation, the energy is randomly deposited in polymer bulk and subsequent radio-grafted copolymer chains are also homogeneously distributed. Fig. 2 shows the EPR spectra of radiation-induced species in the electron-beam irradiated PVDF films at 5, 7.5 and  $10\text{ kGy}$  doses [25,32,33]. It should be mentioned, precautions were made to ensure the absence of oxygen during irradiation. After irradiation, the samples were exposed to oxygen during transferring allowing the formation of the peroxy radicals.

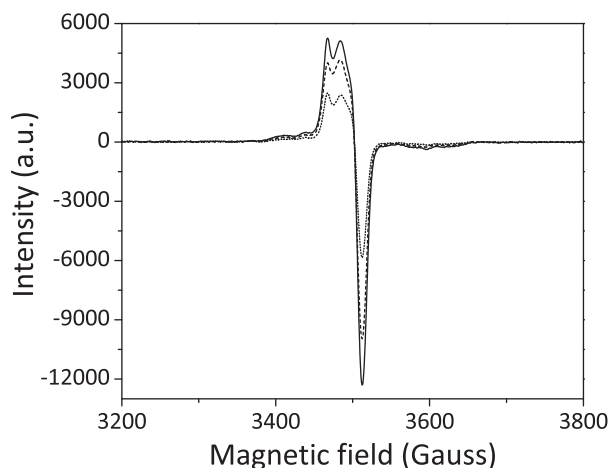


**Fig. 2.** EPR spectra of electron-beam irradiated 9  $\mu\text{m}$  thickness PVDF films at different doses: 5 kGy (dotted line), 7.5 kGy (dashed line), 10 kGy (solid line). Calculated  $g$ -value equals to 2.008 for central field of 3502.7 G.

As shown in Fig. 3a, the grafting yield (GY) increases up to 7 wt% as a function of B2MP concentration. However, the GY starts decreasing for the higher B2MP concentrations. This can be interpreted by the fact that after exceeding of 100 mM B2MP, the electron transfer reactions between the growing grafting chains and the monomer become predominant, leading to termination of the graft polymerization reaction.

As mentioned earlier, the homopolymerization reaction is not expected to occur in our experimental conditions. The role of the solvent is to enhance the solid polymer swelling during radical polymerization through the growing grafted polymer chains. Consequently, a good solvent should be both a good solvent for the monomer and its polymer facilitating the monomer accessibility to radical sites. The use of good-swelling solvent results in bulk and homogeneous grafting. A mixture of 50 vol% water and 50 vol% ethanol was used as a solvent.

The grafted B2MP-g-PVDF films were washed with ethanol, weighed and analyzed by FTIR. A FTIR peak at  $1725\text{ cm}^{-1}$  associated with a carbonyl group of B2MP was measured each time to confirm the presence of functional polymer onto PVDF surface. For a given dose, 100 kGy, 100 mM B2MP concentration and the solvent composition of 50 vol% water and 50 vol% ethanol were found to give the highest GY (Fig. 3b). The same procedure was carried out for the electron-beam irradiated PVDF films at different doses. GYs should vary proportionally with the dose as the radical content gradually increases as shown in Fig. 2. Gravimetric yield was found linearly increasing with dose (Fig. 3c).

### 3.3. B2MP radiation grafting into track-etched PVDF membranes

The fabrication procedure is comprised of several steps. Firstly, PVDF films were bombarded by SHI of  $^{136}\text{Xe}^{48+}$  under He atmosphere. The ions, passing through the solid polymer film, induce continuous trails of excitations and ionizations along their pathways leading to the formation of latent tracks. Contrary to electrons, the deposited energy is

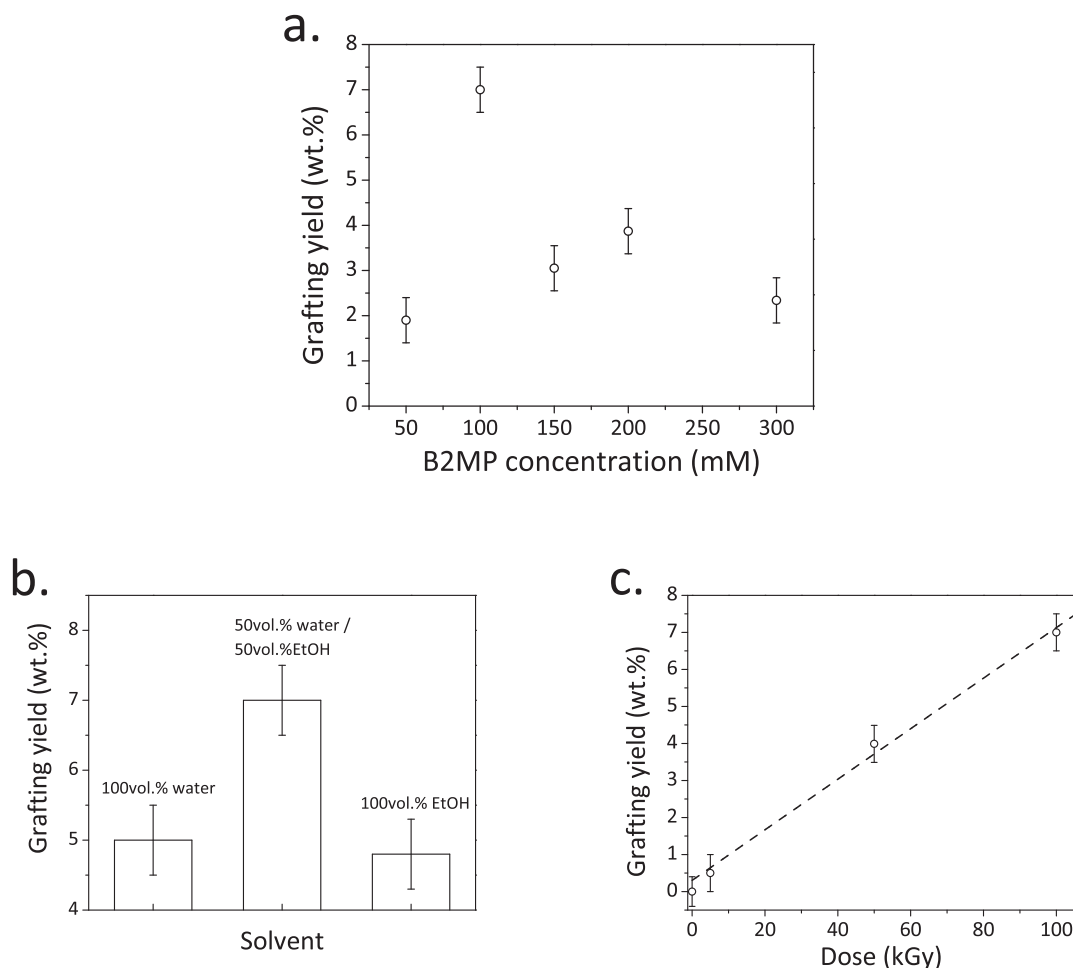


**Fig. 3.** GY of electron-beam irradiated PVDF films depending on the (a) B2MP concentration at 100 kGy dose, 50 vol% water and 50 vol% ethanol solvent, (b) solvent at 100 kGy dose, 100 mM B2MP, and (c) GY versus dose, 100 mM B2MP, 50 vol% water and 50 vol% ethanol solvent; PVDF film thickness is 9  $\mu\text{m}$ .

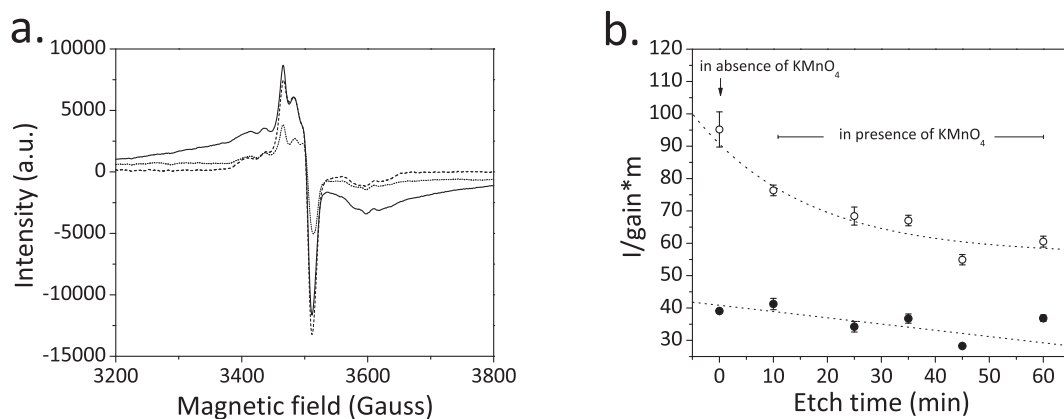


**Fig. 4.** EPR spectra of track-etched PVDF membrane (a) before and after the radiation grafting, fluence  $10^{10} \text{mcm}^{-2}$ : 25 min of etching (solid line), 25 min etching and 1 h grafting (dotted line), no etching (dashed line); (b) the radical consumption by grafting: (°) Etched during various times, (•) etched during various times and grafted within 1 h.

highly localized along the ion trails [28]. Secondly, latent tracks are revealed by selective ion track etching in a highly oxidizing solution of KOH and  $\text{KMnO}_4$  resulting in the formation of cylindrical nanopores. The etching process does not remove all the radicals. Despite the fact that the remaining radical amount is relatively low, a localized radiografting occurs from the nanopore walls [32,33]. Once the radiation grafting parameters have been established for electron-beam irradiated PVDF films which are rich of radicals, the same grafting protocol (i.e. 50 vol% water and 50 vol% ethanol as solvent, 100 mM B2MP concentration,  $65^\circ\text{C}$  grafting temperature, 18 h grafting time) was directly applied to the fabrication of B2MP-g-PVDF nanoporous membranes.

Fig. 4a shows the EPR spectra of the PVDF track-etched membranes exposed to a  $10^{10} \text{mcm}^{-2}$  fluence before and after grafting with B2MP. Fig. 4b displays the radical decay due to the addition of the B2MP. Since the addition of PVDF radicals to the B2MP gives a rise to the formation of the growing free radicals, it is expected that there is no change in a total radical concentration. However, as shown in Fig. 4b, there is tremendous decrease of the free radical concentration after addition of the B2MP. This may be explained by the fact that the decay of the PVDF radicals undergoes through various competing reactions. Since the GY is only about 3.5 wt%, it seems that the reaction of B2MP addition is not a predominant one. To explain a disappearance of the free radicals in the absence of  $\text{KMnO}_4$ , one would expect the PVDF radicals undergo either crosslinking or disproportionating reactions favored by temperature of the reaction. Nevertheless, in the presence of  $\text{KMnO}_4$ , the disappearance of the free radicals of PVDF may be additionally due to the oxidation reactions through an electron transfer to potassium permanganate.

Table 1 shows GYs under various irradiation conditions. As clearly demonstrated in the table, the optimal conditions were archived at 300 mM B2MP concentration, 50 vol% water and 50 vol% ethanol as a solvent.

Fig. 5 shows the chemical structure and of the B2MP and

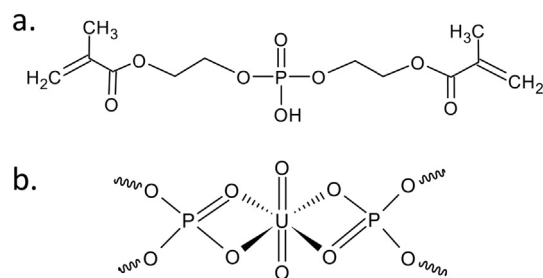


**Fig. 5.** (a) Chemical structure of B2MP and (b) proposed configuration of uranyl coordination by phosphate groups of B2MP according to the ref. [14].

configuration of uranyl coordination by phosphate groups of B2MP [14].

FESEM was used to analyze the surface morphology of functionalized track-etched membranes. In microphotographs (Fig. 6) are shown a top view and cross section of B2MP-g-PVDF membrane exposed to a  $10^9 \text{mcm}^{-2}$  fluence. Increasing the ion fluence from  $10^9 \text{mcm}^{-2}$  to  $10^{10} \text{mcm}^{-2}$  leads to the statistical overlapping of some pores. However, at higher pore density, more B2MP is exposed toward uranyl enabling the enhancement of loading capacity of the membranes. Therefore, the membranes exposed to a fluence of  $10^{10} \text{mcm}^{-2}$  had been used for sensor's fabrication in this work. Cryofracture was made in order to study the cross section of the membranes and to verify their openness after chemical etching. FESEM imaging of the cryofractured membrane showed that pores extended completely through the membrane and not blocked inside.

The presence of functional polymer inside cylindrical nanopores was verified by FTIR (Fig. 7a). The FTIR spectrum primarily demonstrates the characteristic absorption bands of PVDF [40] with a doublet corresponding to the  $\text{CH}_2$  vibrations at  $2985$  and  $3025 \text{cm}^{-1}$ , a multiplet with spectral absorption bands at  $1453$ ,  $1424$ ,  $1403$  and  $1385 \text{cm}^{-1}$  attributed to a mixture of  $\text{CH}_2$  and  $\text{C}-\text{C}$  vibrations, two of the most intense absorption bands of  $\text{CF}_2$  at  $1211$  and  $1183 \text{cm}^{-1}$  and PVDF skeleton vibration region between  $900$  and  $400 \text{cm}^{-1}$ . The latter region is attributed to the crystalline structure. The well-defined peak at  $840 \text{cm}^{-1}$  represents  $\beta$ -phase of PVDF. Additional absorbance peaks were caused by B2MP presence. [41]

Notably, the absorbance peak at ca.  $1725 \text{cm}^{-1}$  associated with the  $-\text{C}=\text{O}$  vibration of the esters was clearly observed (inset in Fig. 7a). The absorption bands corresponding to the stretching vibrations of the  $-\text{P}=\text{O}$ , that typically appear at  $1350$ – $1250 \text{cm}^{-1}$  are not observable due to the overlap between these and PVDF absorption bands. The  $1725 \text{cm}^{-1}$  peak increase with the grafting time is in coherence with quantitative GY results obtained by gravimetry (Fig. 7b). GYs rapidly

**Table 1**

GYs of track-etched PVDF under various grafting conditions.

Fluence	Grafting time	B2MP concentration	Solvent mixture	GY
$\text{cm}^{-2}$	h	mM		wt. %
$10^9$	18	100	EtOH/water	0.08
		300		1.04
		600		0.63
$10^{10}$	1	300	EtOH/water	3.53
		2		4.4
		5		6.2
		18		10.6

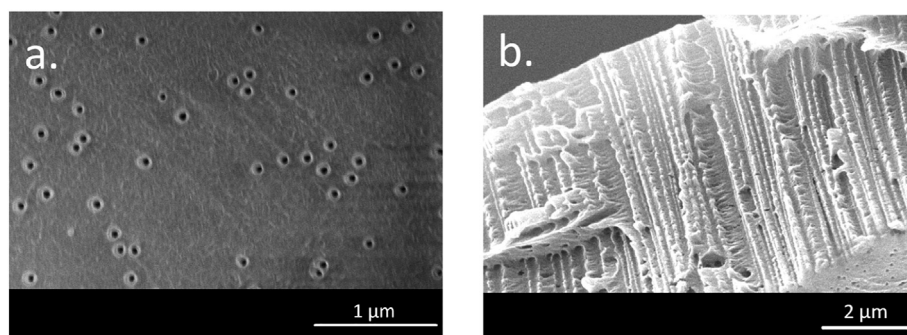


Fig. 6. FESEM photo of (a) top view and (b) cross section of PVDF membrane after chemical etching, fluence  $10^9 \text{mcm}^{-2}$ .

increase within 4 h and reach a plateau after 16–18 h due to the diminution of monomer diffusion through the amorphous part of the PVDF.

XPS was used to confirm the presence of phosphate groups after radiation grafting of B2MP and its capability to trap uranyl ions. Fig. 8 shows XPS spectra of the B2MP-g-PVDF membranes exposed to a fluence of  $10^{10} \text{mcm}^{-2}$  before and after adsorption of uranyl. An intense peak in the survey spectrum of F 1 s arises from PVDF (Fig. 8a). The C 1 s peak at ca. 285 eV can be curved-fitted with six peaks (Fig. 9). Two main peaks with binding energies (BE) of 285.6 eV and 290.1 eV for  $\text{CH}_2$  and  $\text{CF}_2$  species, respectively, assigned to the PVDF main chains. Others, less intense, arise from C-C/H,  $-\text{C}=\text{O}$ ,  $-\text{C}-\text{O}$  and  $-\text{O}-\text{C}=\text{O}$  groups of grafted B2MP. The revealed peak at 133 eV (Fig. 8b) confirms the presence of the phosphate groups of B2MP whose position is in agreement with previous studies [34,35]. Evidently, no signal of uranyl was observed before uranyl adsorption (Fig. 8c). For the adsorption, the B2MP-g-PVDF membrane was immersed into a 2 mM uranyl acetate solution for 18 h. After the adsorption, oxygen atoms from the uranyl ion shield the phosphate group as they are more electronegative than phosphorus, causing a decrease of the P 2p peak intensity (Fig. 8d) and thus affirming  $\text{UO}_2^{2+}$ -B2MP complexation. Fig. 8e shows the U 4f XPS spectrum of uranyl after the B2MP-g-PVDF membrane adsorbed uranyl ions. The two peaks of U assigned to the U  $4f_{7/2}$  and U  $4f_{5/2}$  possessing spin orbit splitting of 10.9 eV were detected [36–38]. Deconvolution of U  $4f_{7/2}$  peak revealed two satellites at higher binding energies of 389.7 eV and 386.1 eV. It agrees with previously published data and can be attributed to  $\text{U}^{5+}$  and  $\text{U}^{6+}$  in the uranyl cation [39,42–44].

### 3.4. Electrochemical detection

The first step in developing an electroanalytical method was

selecting the working electrode. In this work, a gold electrode was chosen as it is frequently used for low concentrations measurements of uranyl in aqueous solutions [35,45,46]. Another important choice was an electrolyte and pH as both parameters affect on redox mechanism of uranyl. Peled et al. report that 50 mM acetate buffer (pH 3) with 100 mM  $\text{KNO}_3$  is the best medium for the detection of low concentration of uranyl in water [22].

To connect the membrane electrodes to a potentiostat, a home-made clip device was used for all voltammetric measurements (Fig. 10). The clip was made of Plexiglas (PMMA) with gold wires inserted in the clip to provide an electrical contact. A silver wire was used as a pseudo-reference electrode.

For the adsorption, membranes were placed in glass bottles containing polluted solutions and stirred using an orbital shaker for various times (from 30 min to 7 days). 2 h of adsorption were found sufficient to get reproducible responses. During adsorption, uranyl, being a hard Lewis acid, tends to form a complex with phosphate ligands of B2MP. Proposed configuration of this  $\text{UO}_2^{2+}$ -B2MP complex according to the reference [14] is shown in Fig. 5b. Adsorbed uranyl ions were then analyzed by SW-CSV using acetate buffer (50 mM) and 100 mM  $\text{KNO}_3$  (pH 3) electrolyte. Cyclic voltammetry measurements were firstly performed in order to understand the reactions taking place in the system. Fig. 11 shows B2MP-g-PVDF membrane-electrode CV curves in presence of electrolyte (black dotted) and electrolyte spiked with U(VI) at 3, 10 and 20 ppm. It can be seen that a reduction wave appears at  $-0.003$  V and an oxidation one at 0.54 V versus Ag wire pseudo-reference. These signals are associated with one-electron reduction and oxidation of uranyl (1. and 3. in Fig. 11) [47]. The second reduction wave, corresponding to the reduction of  $\text{UO}_2^+$  to insoluble species  $\text{UO}_2$  (2. in Fig. 11), is observed at ca.  $-0.5$  V. A second oxidation wave at ca. 0.6 V is related to the direct two-electron oxidation of  $\text{UO}_2$  to  $\text{UO}_2^{2+}$

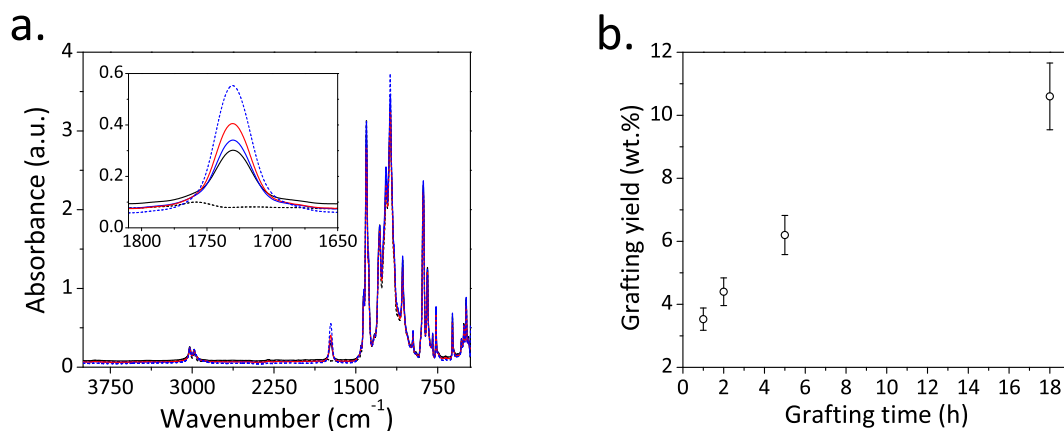
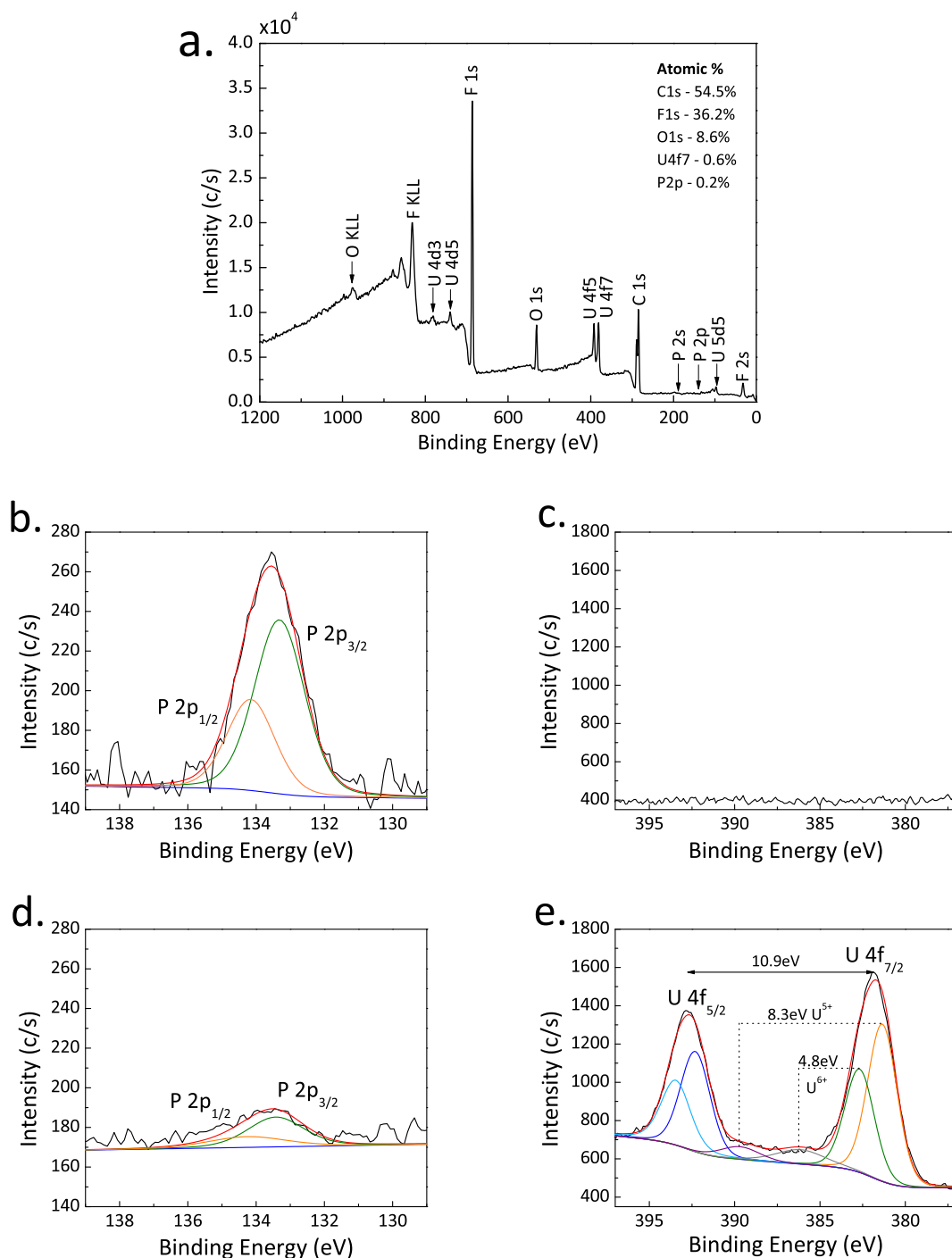


Fig. 7. Functionalized B2MP-g-PVDF track-etched membranes analyses at various grafting times: (a) FTIR spectra of B2MP-g-PVDF: no grafting (dashed line), 1 h, 2 h, 5 h and 18 h of grafting (ascending in grafting time); (b) radiation grafting kinetics - grafting conditions: 300 mM B2MP concentration in 50:50 vol% ethanol/water solutions, fluence  $10^{10} \text{cm}^{-2}$ .



**Fig. 8.** XPS spectra of B2MP-g-PVDF membrane of  $10^{10} \text{cm}^{-2}$  fluence (GY of 3.5 wt%) (a) Survey spectrum of B2MP-g-PVDF membrane after immersion into 2 mM uranyl acetate solution for 18 h. (b, d) P 2p peak of B2MP before and after uranyl adsorption respectively. (c, e) U 4f peak of uranyl before and after adsorption respectively.

species (4. in fig. 11).

Several parameters such as deposition time, frequency, kinetic of adsorption were investigated. Registering the highest current of the reduction peak at  $-0.5 \text{ V}$  (reaction 2.) for a given U(IV)-spiked electrolyte (10 ppm) and a deposition potential of  $+1.2 \text{ V}$ , the optimal deposition time on the cathode side of B2MP-g-PVDF membrane-electrode was found equal to 300 s and was further used for all the measurements. The chosen frequency was set at 20 Hz (Fig. 12 (left)) as it is a good compromise between current intensity optimization and reproducibility. Fig. 12 (right) displays kinetics of adsorption registering

the peak current intensity of U(VI) reduction peak.

As displays on Fig. 13a, the peak currents obtained from the first reduction peak at  $-0.5 \text{ V}$  were used to plot a calibration curve (Fig. 13b). The repeatability is 20% in average showing a good reproducibility between membrane-electrode batches. No problem of stability was observed after 2 h adsorption at neutral pH.

B2MP-g-PVDF nanoporous electrodes with a GY of 3.5 wt.% were tested by SW-CSV for calibration curve establishment. It was shown that these functionalized membranes were sufficiently reactive toward U (VI) trapping and electrochemical detection (Fig. 13). Hence, it is

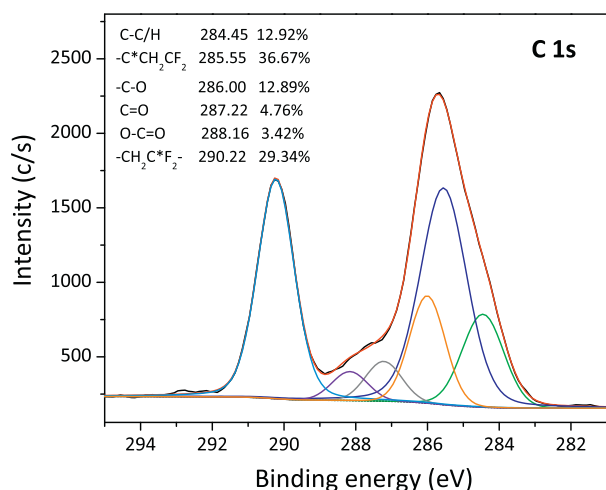


Fig. 9. C1s peak deconvolution from XPS spectrum of B2MP-g-PVDF membrane of  $10^{10}\text{mcm}^{-2}$  fluence (GY of 3.5 wt%).

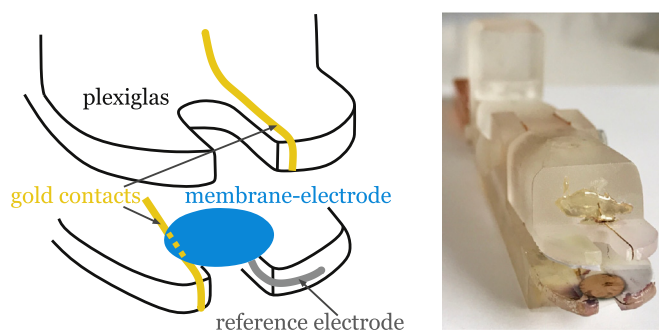


Fig. 10. (a) Scheme of the clip set-up used for voltammetric measurements. (b) Photo of the clip with membrane electrode placed inside.

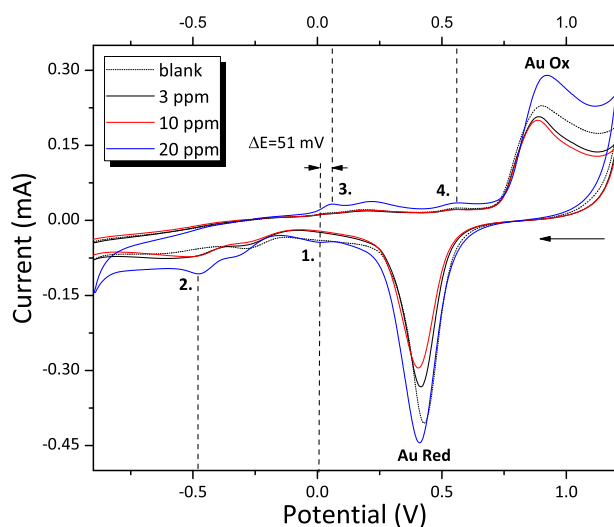


Fig. 11. CV curves of B2MP-g-PVDF membrane-electrode in 50 mM acetate buffer and 100 mM KNO<sub>3</sub> electrolyte spiked with U(VI) reaching 3, 10 and 20 ppm (black, red, blue curves respectively). Reactions marked 1., 2., 3. and 4. are discussed in the text. (For interpretation of the references to colour in this figure legend, the reader is referred to the web version of this article.)

recommended to limit the GY to facilitate ionic transport. The obtained calibration curve demonstrates sensitivity at the ppb-level. The limit of detection ( $3\sigma$ -slope) of the B2MP-g-PVDF membrane electrodes of  $10^{10}\text{mcm}^{-2}$  equals to 17 ppb, with a quantification limit (LOQ) of

51 ppb.

The interferences of trapped U(VI) in B2MP-g-PVDF membrane-electrode with other metal ions during adsorption are shown in Fig. 14. The uranyl concentration equals to 100 ppb, while the concentrations of other metals is in 10-fold excess. Apart Mg(II), most of metal ions were found to interfere with U(VI). This result suggests a high instability of  $\text{UO}_2^+$  ions, which can disproportionate to more stable species in presence of other salts leading to the  $-0.5$  V reduction peak suppression. More investigations are needed to pursue this study.

#### 4. Conclusions

We have successfully developed a novel U(VI) electrochemical sensor based on radiation-induced grafting methodology of B2MP onto PVDF. The radiolytically produced C-centered free radicals of the PVDF initiate graft polymerization of the B2MP onto internal surface of cylindrical nanopores. Based on the relatively low grafting yield and the decay of C-centered free radicals of PVDF, our results suggest that there are different competitive reactions occurring during grafting. These competing reactions are radical-radical interactions, PVDF +  $\text{KMnO}_4$  electron transfer, and PVDF-B2MP $\cdot$  chain growing reactions.

While the radical-radical interactions take place, crosslinking and disproportionation reactions occur, while at the same time the electron transfer from PVDF to  $\text{KMnO}_4$  as a result of chemical etching cannot be underestimated. All these termination reactions explain a 60% radical decay observed by EPR after radiation grafting. Our results thus suggest that desired graft polymerization PVDF + B2MP may be not the predominant one. Despite these considerations, limiting the GY to low values (around 3.5 wt%) was found to produce advantageous membrane detection performance as this GY allowed the B2MP polymer to cover the inner surface of the cylindrical nanopores without blocking them.

The efficient uranyl uptake of B2MP-g-PVDF membranes points out that the geometry of the cylindrical nanopores provides a confinement that facilitates the coordination reaction between phosphate groups of the grafted B2MP and uranyl ions. In addition, the nanopores increase the surface area of the membrane which leads to higher loading capacities by increasing the amount of B2MP exposed to uranyl. The higher loading capacities validated the construction of a novel electrochemical sensor capable of monitoring uranyl in water through the conversion of the membrane into an electrode.

To validate the proof of concept for U(VI) sensing, a calibration plot obtained by means of SW-CSV demonstrates a ppb-level sensitivity of the sensors toward dissolved uranyl ions (LOD is 17 ppb). The LOD might be lowered using more efficient agitation during adsorption.

As a prospective goal, the B2MP-g-PVDF membranes might also be used in nanofiltration for uranium removal. However, our results have demonstrated that the presence of high salt concentration in water strongly affects the U(VI) electrochemical response. Deeper electrochemical studies on U(VI) speciation in real waters are needed.

#### Acknowledgements

Authors acknowledge the IDI Ph.D. funding of the Université Paris Saclay for financial support of this work. We like to thank the USA-Department of Energy-Nuclear Energy University Program (USA-DOE-NEUP) for the financial support through grant number DE-NE0000723. The authors are grateful to the EMIR committee, SIRIUS team of LSI and CIMAP team at GANIL for their strong implication in irradiation experiments. The authors would also thank Bruno Boizot for his encouraging assistance in EPR measurements and Marco Sangermano for XPS consultancy.

#### Appendix A. Supplementary data

Supplementary data to this article can be found online at <https://>

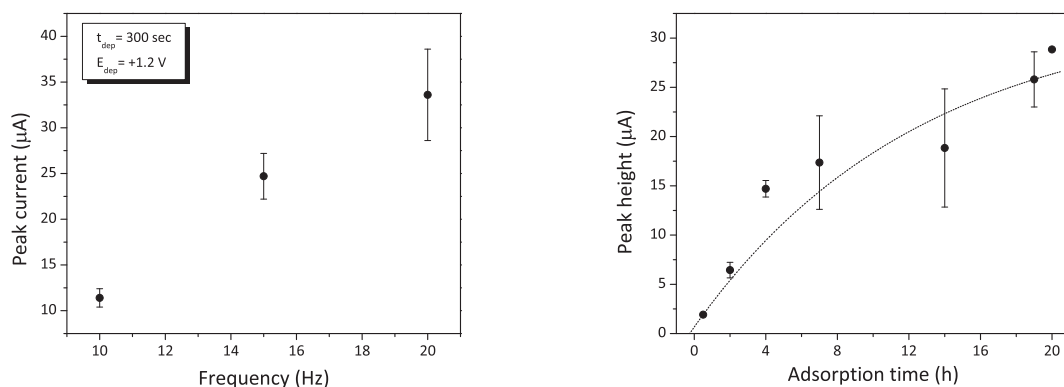


**Fig. 12.** SW-CSV optimization of B2MP-g-PVDF membrane-electrodes doped with U(VI) ions: (left) frequency against current intensity of U(VI) reduction peak (500 ppb U(VI) concentration); (right) kinetics of adsorption as function of U(VI) reduction peak height (50 ppb U(VI) concentration). - deposition time: 300 s; deposition potential: +1.2 V; GY of 3.5 wt%.

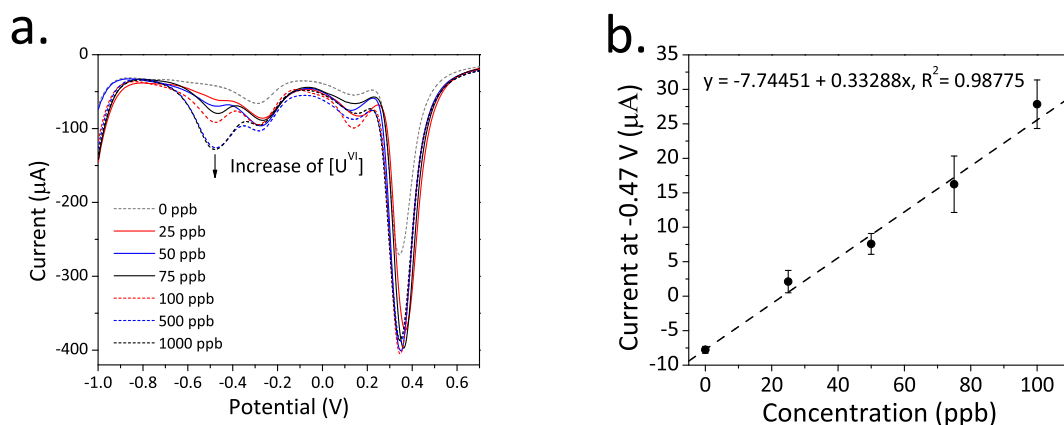


**Fig. 13.** (a) SW-CSV curves recorded at various concentrations of uranyl: 0, 25, 50, 75, 100, 500, 1000 ppb (uranyl reduction peak raises with concentration) in acetate buffer (50 mM) and 100 mM  $\text{KNO}_3$  (pH 3) electrolyte at a deposition potential of +1.2 V and deposition time of 300 s, (b) calibration curve after 2 h of adsorption at neutral pH.

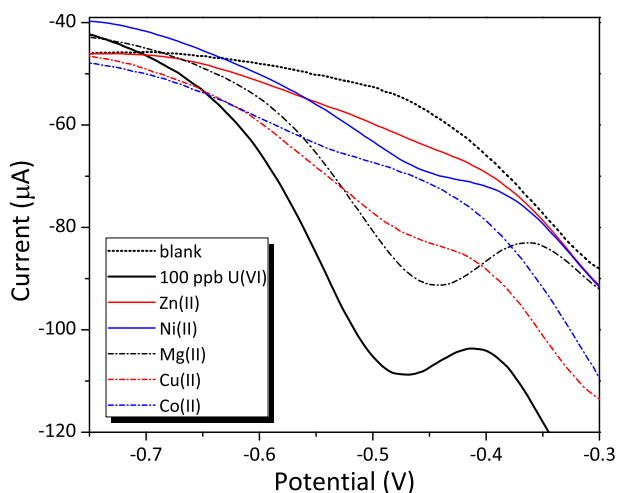


**Fig. 14.** Interferences with some metal ions after 7 h of adsorption in 10-fold excess ion concentration (100 ppb U(VI) concentration).

[doi.org/10.1016/j.reactfunctpolym.2019.06.006](https://doi.org/10.1016/j.reactfunctpolym.2019.06.006).

## References

- [1] F. Edition, Guidelines for drinking-water quality, WHO chronicle 38 (4) (2011) 104–108.
- [2] P. Kurttio, A. Auvinen, L. Salonen, H. Saha, J. Pekkanen, I. Mäkeläinen, S.B. Väisänen, I.M. Penttilä, H. Komulainen, Renal effects of uranium in drinking water, *Environ. Health Perspect.* 110 (4) (2002) 337.
- [3] S.H. Frisbie, E.J. Mitchell, B. Sarkar, World health organization increases its drinking-water guideline for uranium, *Environmental Science: Processes & Impacts* 15 (10) (2013) 1817–1823.
- [4] J.H. Aldstadt, J.M. Kuo, L.L. Smith, M.D. Erickson, Determination of uranium by flow injection inductively coupled plasma mass spectrometry, *Anal. Chim. Acta* 319 (1–2) (1996) 135–143.
- [5] D. Soltatie, P. Carbol, P. Peerani, M. Betti, Investigation of separation/purification methodologies for the determination of  $^{232}\text{U}$  and  $^{236}\text{U}$  in solution of spent nuclear fuels by  $\alpha$ -spectrometry, *Radiochim. Acta* 89 (9) (2001) 551–556.
- [6] J.M. Boncella, *Inorganic chemistry: uranium gets a reaction*, *Nature* 451 (7176) (2008) 250.
- [7] E. Billo, *Modern Inorganic Chemistry* (Jolly, William L.), (1985).
- [8] R. Davies, J. Kennedy, R. McIlroy, R. Spence, K. Hill, Extraction of uranium from sea water, *Nature* 203 (4950) (1964) 1110–1115.
- [9] H. Egawa, H. Harada, Recovery of uranium from sea water by using chelating resins containing amidoxime groups, *Nippon Kagaku Kaishi* 1979 (7) (1979) 958–959.
- [10] A. Mellah, S. Chegrouche, M. Barkat, The removal of uranium (vi) from aqueous solutions onto activated carbon: kinetic and thermodynamic investigations, *J. Colloid Interface Sci.* 296 (2) (2006) 434–441.
- [11] M. Tsezos, Recovery of uranium from biological adsorbents: desorption equilibrium, *Biotechnol. Bioeng.* 26 (8) (1984) 973–981.
- [12] M. Tamada, Current status of technology for collection of uranium from seawater, *International Seminar On Nuclear War And Planetary Emergencies* 42nd Session, World Scientific, 2010, pp. 243–252 1em plus 0.5em minus 0.4em.
- [13] N. Seko, A. Katakai, S. Hasegawa, M. Tamada, N. Kasai, H. Takeda, T. Sugo, K. Saito, Aquaculture of uranium in seawater by a fabric-adsorbent submerged system, *Nucl. Technol.* 144 (2) (2003) 274–278.
- [14] S. Das, A. Pandey, A. Athawale, V. Kumar, Y. Bhardwaj, S. Sabharwal, V. Manchanda, Chemical aspects of uranium recovery from seawater by amidoximated electron-beam-grafted polypropylene membranes, *Desalination* 232 (1–3) (2008) 243–253.
- [15] T.C. Dietz, C.E. Tomaszewski, Z. Tsinas, D. Poster, A. Barkatt, M. Adel-Hadadi, F.B. Bateman, L.T. Cumberland, E. Schneider, K. Gaskell, et al., Uranium removal from seawater by means of polyamide 6 fibers directly grafted with diallyl oxalate

- through a single-step, solvent-free irradiation process, *Ind. Eng. Chem. Res.* 55 (15) (2015) 4179–4186.
- [16] P. Ilaiyaraja, A.K.S. Deb, K. Sivasubramanian, D. Ponraju, B. Venkatraman, Adsorption of uranium from aqueous solution by pamam dendron functionalized styrene divinylbenzene, *J. Hazard. Mater.* 250 (2013) 155–166.
- [17] Q. Cao, Y. Liu, C. Wang, J. Cheng, Phosphorus-modified poly (styrene-co-divinylbenzene)-pamam chelating resin for the adsorption of uranium (vi) in aqueous, *J. Hazard. Mater.* 263 (2013) 311–321.
- [18] S. Das, A.K. Pandey, A.A. Athawale, V. Natarajan, V.K. Manchanda, Uranium pre-concentration from seawater using phosphate functionalized poly (propylene) fibrous membrane, *Desalin. Water Treat.* 38 (1–3) (2012) 114–120.
- [19] D. Beltrami, G. Cote, H. Mokhtari, B. Courtaud, B.A. Moyer, A. Chagnes, Recovery of uranium from wet phosphoric acid by solvent extraction processes, *Chem. Rev.* 114 (24) (2014) 12 002–12 023.
- [20] T.C. Dietz, C.E. Tomaszewski, Z. Tsinas, D. Poster, A. Barkatt, M. Adel-Hadadi, F.B. Bateman, L.T. Cumberland, E. Schneider, K. Gaskell, J. LaVerne, M. Al-Sheikhly, Uranium removal from seawater by means of polyamide 6 fibers directly grafted with diallyl oxalate through a single-step, solvent-free irradiation process, *Indust. Eng. Chem. Res.* 55 (154) (2015) 179–4186.
- [21] S. Girgin, N. Acarkan, A.A. Sirkeci, The uranium (vi) extraction mechanism of d2ehpa-topo from a wet process phosphoric acid, *J. Radioanal. Nucl. Chem.* 251 (2) (2002) 263–271.
- [22] Y. Peled, E. Krent, N. Tal, H. Tobias, D. Mandler, Electrochemical determination of low levels of uranyl by a vibrating gold microelectrode, *Anal. Chem.* 87 (1) (2014) 768–776.
- [23] A. Becker, H. Tobias, D. Mandler, Electrochemical determination of uranyl ions using a self-assembled monolayer, *Anal. Chem.* 81 (20) (2009) 8627–8631.
- [24] H. Bessbousse, I. Nandhakumar, M. Decker, M. Barsbay, O. Cuscito, D. Lairez, M.-C. Clochard, T.L. Wade, Functionalized nanoporous track-etched  $\beta$ -pvdf membrane electrodes for lead (ii) determination by square wave anodic stripping voltammetry, *Anal. Methods* 3 (6) (2011) 1351–1359.
- [25] H. Bessbousse, N. Zran, J. Fauléau, B. Godin, V. Lemée, T. Wade, M.-C. Clochard, Poly (4-vinyl pyridine) radiografted pvdf track etched membranes as sensors for monitoring trace mercury in water, *Radiat. Phys. Chem.* 118 (2016) 48–54.
- [26] J.C. Hoogvliet, M. Dijkstra, B. Kamp, W.P. van Bennekom, Electrochemical pre-treatment of polycrystalline gold electrodes to produce a reproducible surface roughness for self assembly : a study in phosphate buffer pH 7.4, *Anal. Chem.* 72 (9) (2000) 2016–2021.
- [27] A. Fina, A. Lemoel, J.P. Duraud, M.T. Valin, C. Legressus, E. Balanzat, J.M. Ramillon, C. Darnez, Surface processes occurring on PVDF under energetic ion irradiation, *Nucl. Inst. and Meth. in Physics Research, B* 42 (1) (1989) 69–75.
- [28] E. Balanzat, S. Bouffard, A. Lemoel, N. Betz, Physico-chemical modifications induced in polymers by swift heavy ions, *Nucl. Inst. and Meth. in Physics Research*, vol. 91, 1994, pp. 140–145.
- [29] E. Adem, G. Burillo, E. Munoz, J. Richards, L. Cota, M. Avalos-Borja, Electron and proton irradiation of poly(vinylidene fluoride): characterization by electron paramagnetic resonance, *Polymer Degradation and Stability*, B 81 (1) (2003) 75–79.
- [30] J.S. Forsythe, D.J.T. Hill, The radiation chemistry of fluoropolymers, *Prog. Polym. Sci.* 25 (1) (2000) 101–136.
- [31] C. Aymes-Chodur, S. Esnouf, A. Lemoel, ESR studies in  $\gamma$ -irradiated and PS-radiation grafted poly(vinylidene fluoride), *J. Polym. Sci. B Polym. Phys.* 39 (13) (2001) 1437–1448.
- [32] M. Barsbay, O. Güven, H. Bessbousse, T.L. Wade, F. Beuneu, M.-C. Clochard, Nanopore size tuning of polymeric membranes using the raft-mediated radical polymerization, *J. Membr. Sci.* 445 (2013) 135–145.
- [33] O. Cuscito, M.-C. Clochard, S. Esnouf, N. Betz, D. Lairez, Nanoporous  $\beta$ -pvdf membranes with selectively functionalized pores, *Nucl. Instrum. Methods Phys. Res., Sect. B* 265 (1) (2007) 309–313.
- [34] D.M. Spori, N.V. Venkataraman, S.G. Tosatti, F. Durmaz, N.D. Spencer, S. Zürcher, Influence of alkyl chain length on phosphate self-assembled monolayers, *Langmuir* 23 (15) (2007) 8053–8060.
- [35] A. Becker, H. Tobias, Z. Porat, D. Mandler, Detection of uranium (vi) in aqueous solution by a calix [6] arene modified electrode, *J. Electroanal. Chem.* 621 (2) (2008) 214–221.
- [36] G.C. Allen, J.A. Crofts, M.T. Curtis, P.M. Tucker, D. Chadwick, P.J. Hampson, X-ray photoelectron spectroscopy of some uranium oxide phases, *J. Chem. Soc. Dalton Trans.* (12) (1974) 1296–1301.
- [37] E. Ordonez-Regil, R. Drot, E. Simoni, J. Ehrhardt, Sorption of uranium (vi) onto lanthanum phosphate surfaces, *Langmuir* 18 (21) (2002) 7977–7984.
- [38] Y. Al-Salik, I. Al-Shankiti, H. Idriss, Core level spectroscopy of oxidized and reduced ceu1-xo2 materials, *J. Electron Spectrosc. Relat. Phenom.* 194 (2014) 66–73.
- [39] T. Filippov, D. Svintsitskiy, I. Chetyrin, I. Prosvirin, D. Selishchev, D. Kozlov, Photocatalytic and photochemical processes on the surface of uranyl-modified oxides: an in situ xps study, *Appl. Catal. A Gen.* 558 (2018) 81–90.
- [40] N. Betz, A. Le Moel, E. Balanzat, J.M. Ramillon, J. Lamotte, J.P. Gallas, G. Jaskierowicz, A FTIR study of PVDF irradiated by means of swift heavy ions, *J. Polym. Sci. B Polym. Phys.* 32 (1994) 1493–1502.
- [41] A.A.L. Goncalves, A.C. Fonseca, I.G.P. Fabela, J.F.J. Coelho, A.C. Serra, Synthesis and characterization of high performance superabsorbent hydrogels using bis (2-(methacryloyloxy) ethyl) phosphate as crosslinker, *Express Polym Lett* 10 (3) (2016) 248–258.
- [42] E.S. Ilton, P.S. Bagus, Xps determination of uranium oxidation states, *Surf. Interface Anal.* 43 (13) (2011) 1549–1560.
- [43] M. Schindler, F. Hawthorne, M. Freund, P. Burns, Xps spectra of uranyl minerals and synthetic uranyl compounds. I: the u 4f spectrum, *Geochim. Cosmochim. Acta* 73 (9) (2009) 2471–2487.
- [44] S.A. McMaster, R. Ram, F. Charalambous, M.I. Pownceby, J. Tardio, S.K. Bhargava, Synthesis and characterisation of the uranium pyrochlore betafite [(ca, u) 2 (ti, nb, ta) 2o7], *J. Hazard. Mater.* 280 (2014) 478–486.
- [45] G. Billon, C.M. van den Berg, Gold and silver micro-wire electrodes for trace analysis of metals, *Electroanalysis* 16 (19) (2004) 1583–1591.
- [46] R.K. Shervedani, S.A. Mozaffari, Preparation and electrochemical characterization of a new nanosensor based on self-assembled monolayer of cysteamine functionalized with phosphate groups, *Surf. Coat. Technol.* 198 (1–3) (2005) 123–128.
- [47] H.G. Heal, Electrochemistry of uranium, *Nature* 157 (3982) (1946) 225.



**Titre :** Membrane-électrodes en PVDF fonctionnalisées pour la détection des métaux toxiques dans l'eau

**Mots clés :** PVDF ; irradiation ; traces attaquées ; radio-greffage ; adsorption sélective ; métaux toxiques

**Résumé :** Le greffage radio-induit de polymères fonctionnels, tels que le poly(acide acrylique) (PAA), la poly(4-vinyl pyridine) (P4VP) et le poly(bis[2-(methacryloyloxy)ethyl] phosphate (PB2MP), dans la structure nanoporeuse de membranes en poly(fluorure de vinylidène) (PVDF) à traces attaquées est ici rapporté, l'objectif étant la pré-concentration sélective des ions Pb(II), Hg(II) et U(VI) en solution dans l'eau. Les membranes en PVDF à traces attaquées sont fabriquées par irradiation aux ions lourds rapides suivie par la révélation chimique des traces. Les membranes nanoporeuses en PVDF ainsi créées sont ensuite fonctionnalisées dans la porosité grâce à la présence de radicaux résiduels à la paroi des nanopores. La spectroscopie RPE a été utilisée pour déterminer la quantité et la réactivité des radicaux piégés, notamment dans le cas d'une fonctionnalité nouvelle comme le PB2MP. Il a été montré que ces radicaux, alkyles et peroxy, étaient en quantité suffisante pour initier une polymérisation radicalaire en présence des trois monomères étudiés. Le FESEM, le FTIR et une méthode moins conventionnelle comme le potentiel Zeta ont permis la caractérisation des groupes fonctionnels. Dans le cas du greffage de la P4VP dans les nanopores, la me-

sure des états de charges à la surface des nanopores *versus* le pH a montré que le greffage était relativement dense tout au long des canaux poreux. L'objectif de ce travail étant de développer des capteurs électrochimiques innovants pour la détection des métaux toxiques, une étude en adsorption a confirmé des capacités de sorption très efficaces des membranes à traces en PVDF greffées dont les groupes fonctionnels facilitent les réactions de coordination partant d'une interaction électrostatique pure inhérente au PAA à la complexation chélatante avec la P4VP en passant par celle du PB2MP. L'effet complexant modéré du PB2MP dans le cas de l'adsorption de l'U(VI) est dû à la co-existence de groupements échangeurs d'ions et chélatants dans la structure du PB2MP. Pour la détection électrochimique, les membranes en PVDF nanoporeuses radio-greffées sont converties en électrodes. La pré-concentration de métaux toxiques adsorbés dans la nanoporosité permet de diminuer la limite de sensibilité de la voltammétrie à redissolution à des concentrations sub-ppb ( $\mu\text{g/L}$ ). Les données acquises en photoluminescence résolue en temps (TRPL) et en XPS ont approfondi la compréhension du mécanisme de coordination du complexe U(VI)·PB2MP.

**Title :** Functionalised track-etched PVDF membrane-electrodes for toxic metal detection in water

**Keywords :** PVDF ; irradiation ; track etching ; radiation grafting ; selective adsorption ; toxic metals

**Abstract :** Present work reports on radiation grafting of poly(acrylic acid) (PAA), poly(4-vinyl pyridine) (P4VP) and poly(bis[2-(methacryloyloxy)ethyl] phosphate) (PB2MP) functional polymers inside nanoporous structure of track-etched poly(vinylidene fluoride) (PVDF) membranes for selective preconcentration of Pb(II), Hg(II) and U(VI) from aqueous solutions. Track-etched PVDF membranes were made by swift heavy ion (SHI) irradiation followed by ion track revealing. The resulting nanoporous PVDF membranes were then functionalised through remained radicals trapped in the nanopore walls. EPR spectroscopy was used to examine the amount and reactivity of radical species, notably towards a novel functional PB2MP polymer. It was found out that these radicals, alkyl and peroxy ones, were sufficient to initiate free-radical polymerization in presence of three studied monomers. FESEM, FTIR and a less conventional zeta-potential measurements were utilized for examination of functional group presence. In case of P4VP grafting, the measured nanopore surface charge *versus* pH demonstrated relatively dense grafting all along

the nanopore channels. As the objective of this work is to develop innovative electrochemical sensors for toxic metal detection in water, sorption experiments were performed to investigate adsorption characteristics. The results confirmed that efficient uptakes of the grafted track-etched PVDF membranes are due to the presence of functional groups that facilitate complex formation through either inherent to PAA electrostatic interaction or metal coordination with P4VP, and PB2MP complexation character in between. The moderate interaction effect in case of U(VI) adsorption by PB2MP is due to co-existence of ion-exchange and chelating groups. For electrochemical detection, membranes functionalised with abovementioned functional polymers were converted into electrodes. Toxic metal preconcentration inside the nanoporous structure permitted to below stripping voltammetry sensitivity limits to sub-ppb ( $\mu\text{g/L}$ ) level. Time-resolved photoluminescence (TRPL) measurements accompanied with XPS were performed on uranyl adsorbed PB2MP-g-PVDF membranes in order to understand deeper the U(VI)·PB2MP mechanism.

